UNIVERSITÀ DEGLI STUDI DI CAMERINO

School of Advanced Studies

Doctoral course in:

Chemical and Pharmaceutical Sciences and Biotechnology – Pharmaceutical Sciences

Cycle XXXVI

Tackling trypanosomiasis:

innovative synthetic and natural approaches

PhD candidate:

Cecilia Baldassarri

Supervisors:

Prof. Riccardo Petrelli

Prof.ssa Loredana Cappellacci

Coordinator:

Prof. Sauro Vittori

2020-2024

TABLE OF CONTENTS

LIST OF PUBLICATIONS

Publications included in the thesis:

Baldassarri, C., Falappa, G., Mazzara, E., Acquaticci, L., Ossoli, E., Perinelli, D.R., Bonacucina, G., Dall'acqua, S., Cappellacci, L., Maggi, F., Ranjbarian, F., Hofer, A., Petrelli, R. (2021). Antitrypanosomal activity of *Anthriscus nemorosa* essential oils and combinations of their main constituents. Antibiotics, 10(11), 1413.

Marchetti, F., Tombesi, A., Di Nicola, C., Pettinari, R., Verdicchio, F., Crispini, A., Scarpelli, F., **Baldassarri, C**., Marangoni, E., Hofer, A., Galindo, A., Petrelli, R. (2022). Zinc (II) Complex with pyrazolone-based hydrazones is strongly effective against *Trypanosoma brucei* which causes African sleeping sickness. Inorganic Chemistry, 61(34), 13561-13575.

Baldassarri, C., Spinozzi, E., Ferrati, M., Rossi, P., Maggi, F., Petrelli, R. (2023). Editorial for the Special Issue "Antiprotozoal Activity of Natural Products". Antibiotics, 12(12), 1650.

Publications not included in the thesis:

Spinozzi, E., **Baldassarri, C.**, Acquaticci, L., Del Bello, F., Grifantini, M., Cappellacci, L., Riccardo, P. (2021). Adenosine receptors as promising targets for the management of ocular diseases. Medicinal Chemistry Research, 30, 353-370.

Perinelli, D. R., Pavela, R., Bonacucina, G., **Baldassarri, C.**, Spinozzi, E., Torresi, J., Petrelli, R., Morshedloo, M.R., Maggi, F., Benelli, G., Canale, A. (2022). Development, characterization, insecticidal and sublethal effects of *Bunium persicum* and *Ziziphora clinopodioides*-based essential oil nanoemulsions on *Culex quinquefasciatus*. Industrial Crops and Products, 186, 115249.

Spinozzi, E., Ferrati, M., **Baldassarri, C.**, Cappellacci, L., Marmugi, M., Caselli, A., Benelli, G., Maggi, F., Petrelli, R. (2022). A review of the chemistry and biological activities of *Acmella oleracea* ("jambù", Asteraceae), with a view to the development of bioinsecticides and acaricides. Plants, 11(20), 2721.

Wandjou, J.G.N., **Baldassarri, C.**, Ferrati, M., Maggi, F., Pavela, R., Tsabang, N., Petrelli, R., Ricciardi, R., Desneux, N., Benelli, G. (2022). Essential oils from Cameroonian aromatic plants as effective insecticides against mosquitoes, houseflies, and moths. Plants, 11(18), 2353.

Giordani, C., Spinozzi, E., **Baldassarri, C.**, Ferrati, M., Cappellacci, L., Santibañez Nieto, D., Pavela, R., Ricciardi, R., Benelli, G., Petrelli, R., Maggi, F. (2022). Insecticidal activity of four essential oils extracted from Chilean Patagonian plants as potential organic pesticides. Plants, 11(15), 2012.

Baldassarri, C., Giorgioni, G., Piergentili, A., Quaglia, W., Fontana, S., Mammoli, V., Minazzato, G., Marangoni, E., Gasparrini, M., Sorci, L., Raffaelli, N., Cappellacci, L., Petrelli, R., Del Bello, F. (2023). Properly Substituted Benzimidazoles as a New Promising Class of Nicotinate Phosphoribosyltransferase (NAPRT) Modulators. Pharmaceuticals, 16(2), 189.

Ferrati, M., Spinozzi, E., **Baldassarri, C.**, Maggi, F., Pavela, R., Canale, A., Petrelli, R., Cappellacci, L. (2023). Efficacy of *Mentha aquatica* L. Essential Oil (Linalool/Linalool Acetate Chemotype) against Insect Vectors and Agricultural Pests. Pharmaceuticals, 16(4), 633.

Spinozzi, E., Ferrati, M., **Baldassarri, C.**, Maggi, F., Pavela, R., Benelli, G., Aguzzi, C., Zeppa, L., Cappellacci, L., Palmieri, A., Petrelli, R. (2023). Synthesis of carlina oxide analogues and evaluation of their insecticidal efficacy and cytotoxicity. Journal of Natural Products, 86(5), 1307-1316.

Spinozzi, E., Zeni, V., Di Giovanni, F., Marmugi, M., **Baldassarri, C.**, Mazzara, E., Ferrati, M., Ricciardi, R., Canale, A., Lucchi, A., Petrelli, R., Maggi, F., Benelli, G. (2023). Aniseed, Pimpinella anisum, as a source of new agrochemicals: phytochemistry and insights on insecticide and acaricide development. Agriculture Communications, 100003.

ABSTRACT

Trypanosomiases are a class of pathologies caused by the protozoan parasite Trypanosoma. Among them, the only two affecting humans are Chagas disease and Human African Trypanosomiasis (HAT). Specifically, HAT is a tropical neglected disease caused by the parasite *Trypanosoma brucei*. It is present mainly in sub-Saharan regions of the African continent and especially in Congo. Two parasites' subspecies are responsible for two forms of the disease, *gambiense* and *rhodesiense* HAT, but the *gambiense* form is the most widespread. The main vector of the parasite is the tse tse fly, a hematophagous fly that populates wet areas and that infects the hosts through the injection of saliva when biting. HAT manifests itself in two stages; in the hemolymphatic stage more unspecific symptoms appear that are mistakable with malaria; in the late stage, in which the parasite affects the nervous central system, and encephalopathy, mental changes, a constant somnolent state and other more severe symptoms show up. The continuous variation of surface glycoproteins by the parasite poses an overwhelming challenge in developing an effective preventive measure. For this reason, the production of a vaccine remains elusive. On the other hand, the conventional therapy by existing drugs is highly toxic, and impractical for oral administration. Moreover, the local population's reluctance towards synthetic drugs, coupled with the parasite's demonstrated resistance, exacerbates the treatment dilemma. In light of these challenges my PhD research was focused on exploring both natural and synthetic innovative strategies for the development of new and promising alternatives to commercially available drugs.

In detail, Chapter 2 reports the study of both essential oils (EOs) and extracts from *Anthriscus nemorosa*, an aromatic plant from the Apiaceae family which is spread in Europe and in Asia. EOs from aerial parts and roots of *A. nemorosa* were analyzed through GC-MS analysis, and tested on *T. brucei* together with their single main constituents, to evaluate their antitrypanosomal activity *in vitro*. The most interesting data came from the tests of the single components; among all, *β*-ocimene and farnesene resulted to be strongly active. In order to better understand synergistic effects of the different components in the *A. nemorosa* EO, a compound elimination assay was carried out, obtaining 11 blends that were subsequently tested on the parasite. Results were compared with Wadley's formula to assess the synergy among the constituents. Limonene, *β*-ocimene, *p*-cymene and farnesene resulted as the EO's major antitrypanosomal constituents and when alternatively present, showed a synergistic effect. Nanoemulsions of the aerial parts EO were also prepared and tested, affording an improved safety profile. The study proceeded by working on extracts. Two different methods of extraction were adopted (digestion with stirring and maceration with ultrasounds) using

methanol as solvent for both aerial parts and roots. Resulting extracts were tested on the parasite demonstrating a mild activity for roots, with a very low selectivity index. In order to obtain potentially less toxic fractions, a liquid-liquid partition of the root extract was performed using different solvents at growing polarity and subsequently testing them on *T. brucei*. Methanolic fraction resulted to be the most active and was characterized through HPLC-MS^n analysis. Fourteen compounds were identified and, after performing a preparative HPLC, sub-fractions A, B, C and three pure compounds were obtained. All of them were tested *in vitro* and anthriscusin emerged as a moderate antitrypanosomal agent, being considerably potentiated by other components of the sub-fraction from which it was isolated.

In Chapter 3 my research focused on *Cannabis sativa* as source of antiparasitic products. *Cannabis sativa*, belonging to the Cannabaceae family, has lately risen great interest in many fields and in particular in the pharmaceutical one, because of its wide and varied composition. Both EOs and hydrophilic extracts (HEs) from thirteen cultivars of *C. sativa* developed by crossbreeding selected varieties and provided by Everweed company were evaluated. Nine of these were CBD-rich varieties while the remaining four were CBG-rich ones. EOs were analyzed through GC-MS analysis and their antitrypanosomal potential assessed. HEs were prepared by lyophilization of the residual water used for the hydrodistillation, in order to obtain a product rich in water-soluble compounds, excluding, in this way, all phytocannabinoids. The antiprotozoal activity of these extracts was also evaluated, obtaining interesting results for one of the CBD-rich varieties extracts, Gorilla glue HE. Its composition was investigated performing an HPLC-DAD-MS^n analysis that allowed to identify eleven main compounds. Gorilla glue HE was then fractioned in four fractions, and the most active against *T. brucei* was subsequently purified through preparative HPLC to afford pure Cannflavin A. The flavonoid was characterized and tested against the parasite, providing the first report of the antiprotozoal activity for Cannflavin A.

Lastly, Chapter 4 reports the synthesis and the antitrypanosomal evaluation of three series of pyrazolone-based hydrazones (PbH**1-36**), and metal complexes of the most promising among them. All compounds from the three series (phenyl, thiophene, and benzyl series) were synthesized and preliminary tested on wild type *T. brucei* cells. The thiophene series resulted practically inactive and cytotoxic; the phenyl series demonstrated good activity with most of the analogs with EC_{50} values below 10 µM; however, the two most active compounds among all three series resulted to be PbH**26** and PbH**27** from the benzyl series. These two analogs were selected as ligands for the synthesis of Zn(II) and Cu(II) complexes, affording four complexes, **C1-4**. Three of them demonstrated good antitrypanosomal activity, with **C2** as the most active one (EC_{50} value = 0.084 µM). PbH**26**, PbH**27**,

C1, and **C2** were selected for the investigation of the mechanism of action. Specifically, cross-resistance with commercially available antitrypanosomal drugs was excluded; then, the trypanocidal or trypanostatic behavior of selected compounds was determined at different concentrations. Subsequently, the reversibility of the antitrypanosomal activity and cell cycle abnormalities were assessed through flow cytometry and fluorescence microscopy. Finally, variations in nucleotide metabolism after treatment were detected through HPLC analysis, allowing to hypothesize an enzymatic target for the drugs.

CHAPTER 1

Trypanosomiases: a global issue

CHAPTER 1 Outline

1.1 Trypanosomal diseases

Trypanosomiases are a group of parasitic pathologies included in the WHO (World Health Organization) NTD list (neglected tropical diseases' list), representing an important global health issue (Fig. 1). All of them are caused by different species of the genus *Trypanosoma*, belonging to the protozoan subkingdom (Fig. 2). Each species is responsible for different pathologies which are spread in specific countries and regions. Infections can occur through two ways: the stercoraria subspecies reach the hosts *via feces*, while salivaria subspecies parasites affect the target organism through vectors infected saliva.

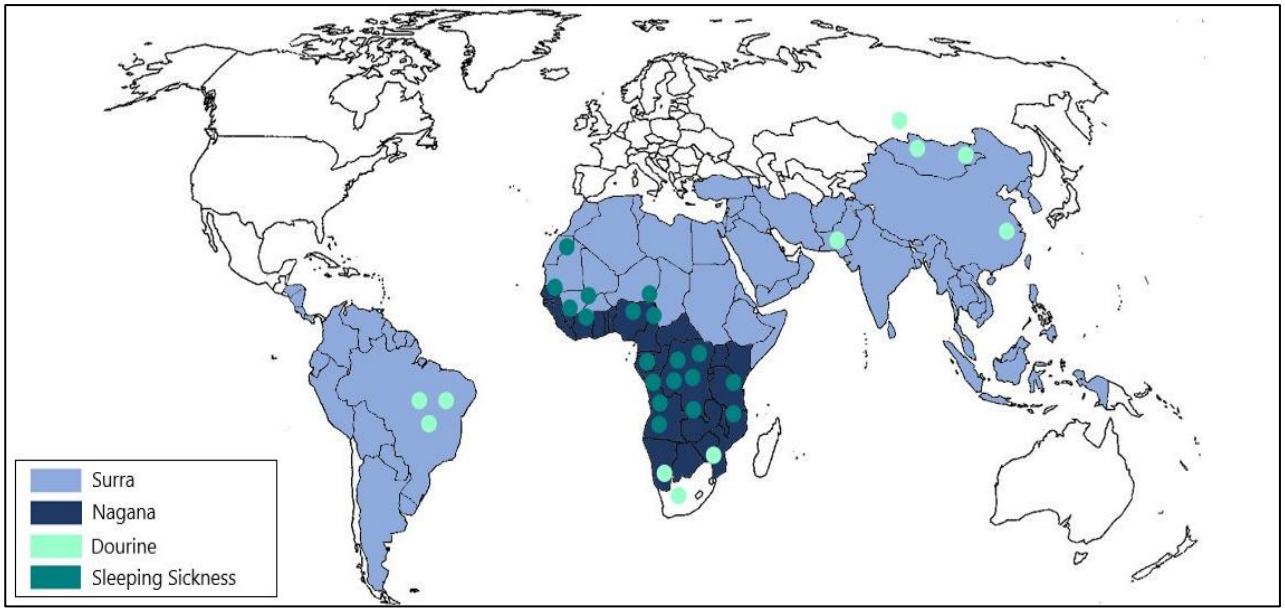

Figure 1. Diffusion of different trypanosomiases around the world.

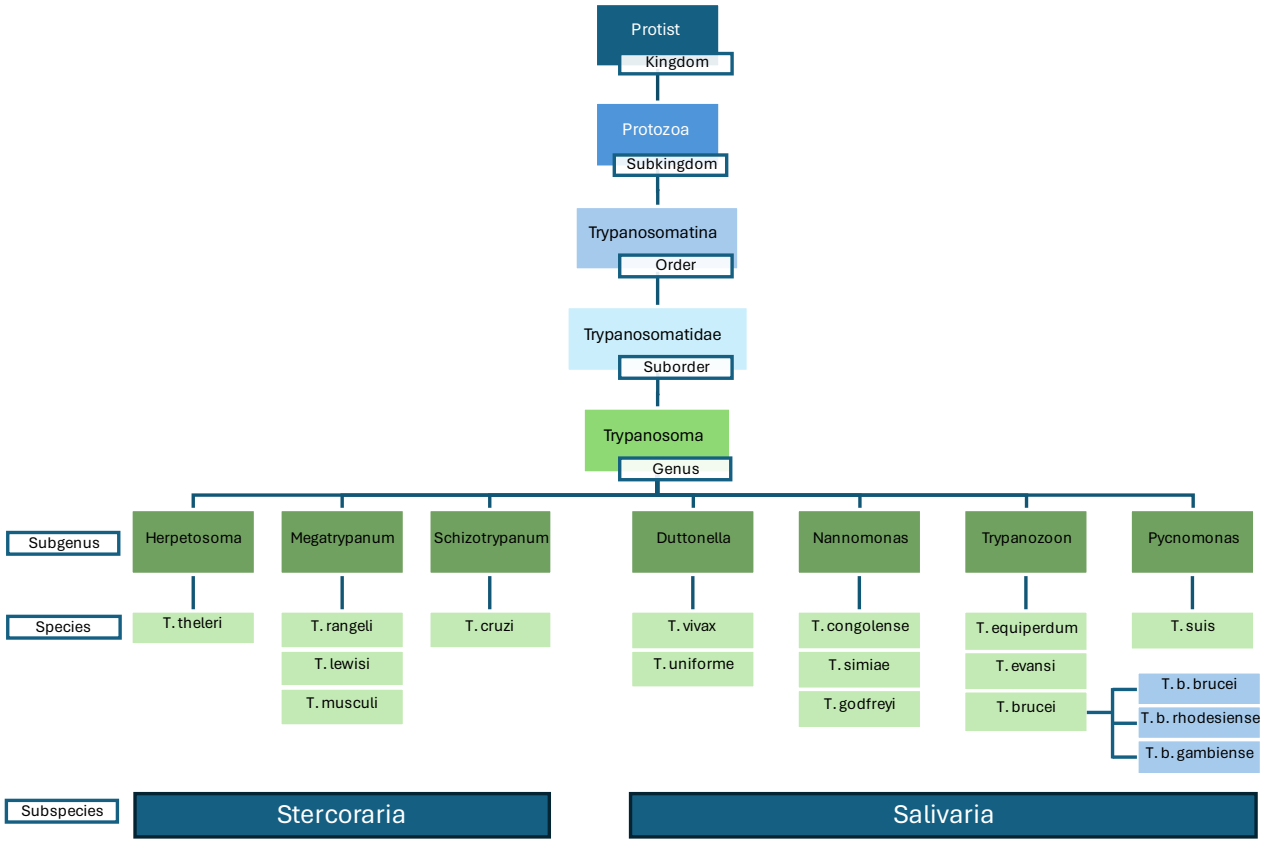

Figure 2. Classification of trypanosomes.

1.1.1 Veterinary pathologies

Some Trypanosoma species only cause pathologies in animal hosts; specifically, *T. brucei brucei*, *T. congolense*, *T. vivax*, *T. evansi*, and *T. equiperdum* are responsible for the most spread animal trypanosomiases (Table 1). All of them belong to the Salivaria subspecies and cause only apparently similar diseases; indeed, symptoms often overlap, but they substantially differ for way of transmission, vectors, host species, and causative agents' biology.

Table 1. *Trypanosoma* species and taxonomy of hosts (Kapo et al., 2023).

Group	Subgenus	Species	Taxonomy of host	Vector
Salivaria	*Trypanozoon*	***T. brucei brucei***	Bovidae, Girafidae, Hippopotamidae, Pantherinae, Rhinocerotidae	*Glossina* spp.
		T. b. rhodesiense	Bovidae, Suidae, Equidae, Cephalophinae, Aepycerotinae	*Glossina* spp.
		T. b. gambiense	Cercopithecinae	*Glossina* spp.
		T. evansi	Bovidae, Girafidae, Elephantidae, Hippopotamidae, Suidae Equidae, Pantherinae, Hyaenidae, Cervidae, Tayassuidae, Chiroptera	Tabanids
		T. equiperdum	Equidae	None
	Nannomonas	*T. simiae*	Suidae	*Glossina* spp.
		T. godfreyi	Suidae, Canidae	*Glossina* spp.
		T. congolense	Bovidae, Elephantidae, Hippopotamidae, Suidae, Pantherinae, Cephalophinae, Aepycerotinae, Hyaenidae, Cercopithecinae	*Glossina* spp.
	Duttonella	***T. vivax***	Bovidae, Girafidae, Elephantidae, Hippopotamidae, Suidae, Cephalophinae, Aepycerotinae, Crocodylinae	*Glossina* spp., Tabanidae, and *Stomoxys*
	Pycnomonas	*T. suis*	Suidae	*Glossina* spp.
Stercoraria	*Schizotrypanum*	*T. cruzi*	Canidae, Felidae, Suidae, Pteropodidae, Tayassuidae, Chiroptera	Triatominae, *Rhodnius*, and *Panstrongylus*
		T. vespertilionis	Chiroptera	Biological
		T. dionisii	Chiroptera	Biological

Group	Subgenus	Species	Taxonomy of host	Vector
	Trypanosomes with unspecified subgenus	*T. theileri*	Bovidae, Cervidae	Tabanidae
	Trypanosomes with unspecified subgenus	*T. (Megatrypanum) pestanai*	Mustelidae	Unknown
	Megatrypanum	*T. melophagium*	Bovidae	*Melophagus ovinus*
	Herpetosoma	*T. lewisi*	Muridae, Heteromyidae	*Nosopsyllus fasciatus, Xenopsylla cheopis*

1.1.1.1 Nagana

Animal African Trypanosomiasis (AAT), also called Nagana, is endemic in 37 of the 54 African countries, thus involving a very wide area (approximately 10 million km^2) (Fig. 3) and affecting the productivity of hundreds of million cattle (Leigh et al., 2015; Nyimba et al., 2015).

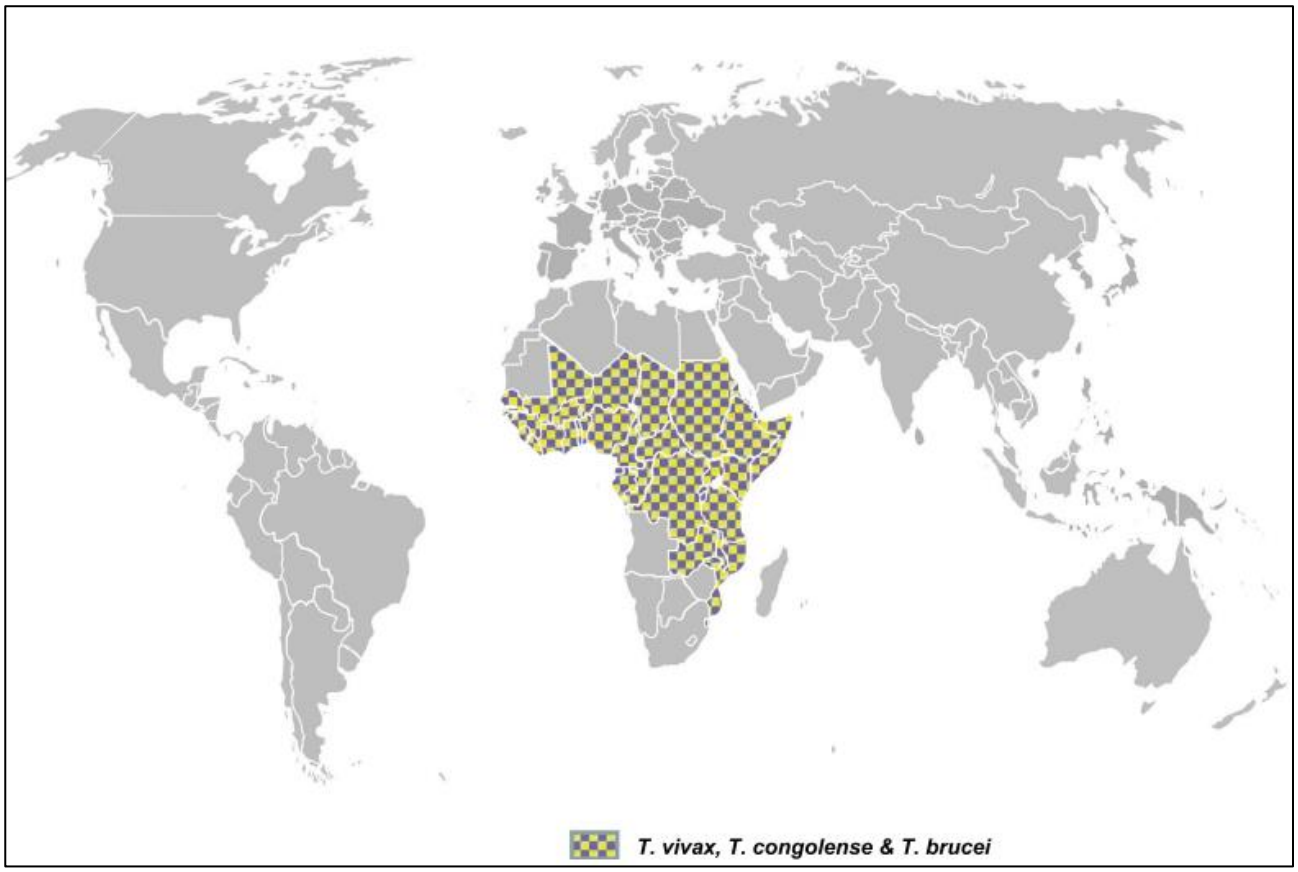

Figure 3. Geographical distribution of the Nagana complex (Desquesnes et al., 2022).

In the last years, the disease has become a serious problem for both the economic and health of the African scenario: in 2015 it was estimated that Nagana caused more than US$ 4.58 billion dollars losses in the agricultural sector (Dagnachew and Bezie, 2015). Not coincidentally, 21 of the 37 countries in which Nagana is endemic are listed as the world's poorest countries (Shaw, 2015).

The wide distribution of the disease in the African continent is due to the abundance of its main transmitting vector in the involved regions: the tsetse fly. These flies exclusively develop and breed in the African continent and specifically in the "flies" belt (Fig. 4).

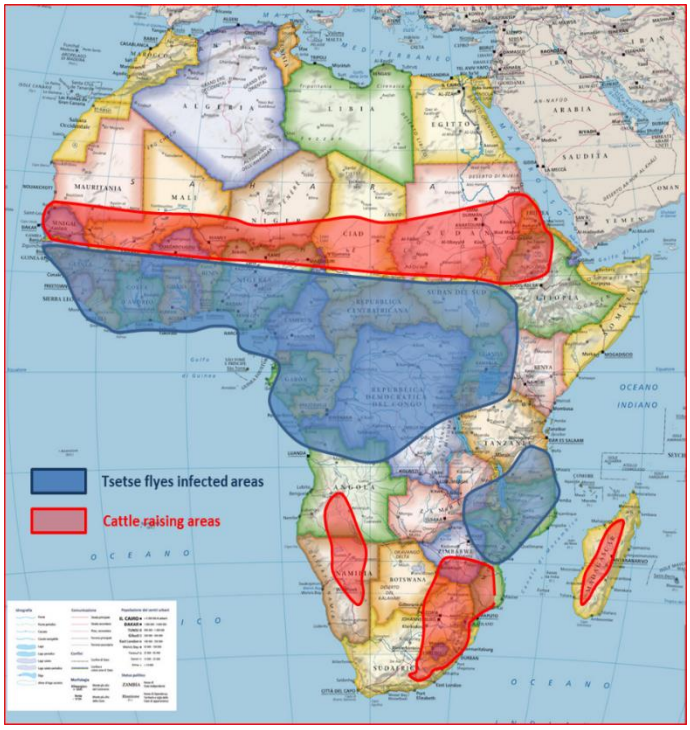

Figure 4. The "flies belt": distribution of tsetse and infected cattle-raising area in Africa

The pathology manifests itself in chronic or acute form depending on the parasite species invading the host. *Trypanosoma congolense* causes a chronic disease while *T. vivax* and *T. brucei* are responsible for the acute form (Taylor, 2022). The most common symptoms are weakness, anaemia, ataxia, intermittent fever, and loss of appetite and body condition, which lead to weight loss and a reduction in fertility and milk production of the affected animal.

1.1.1.2 Surra

Trypanosoma evansi is the causative agent for Surra, a disease that affects animal health leading to considerable morbidity and mortality. Both wild and domestic animals can be reservoirs for the disease and in particular, camels, horses, water buffalos, donkeys, mules, deer, goats, sheep, cattle, pigs, dogs, cats, donkeys, rodents, and Indian elephants (Kapo et al., 2023; Habila et al., 2012; Eberhardt et al., 2014). Among all trypanosomes, this parasite also presents the widest geographical spread, and its diffusion generates severe issues because of its negative influence on meat and milk production (Fig. 5).

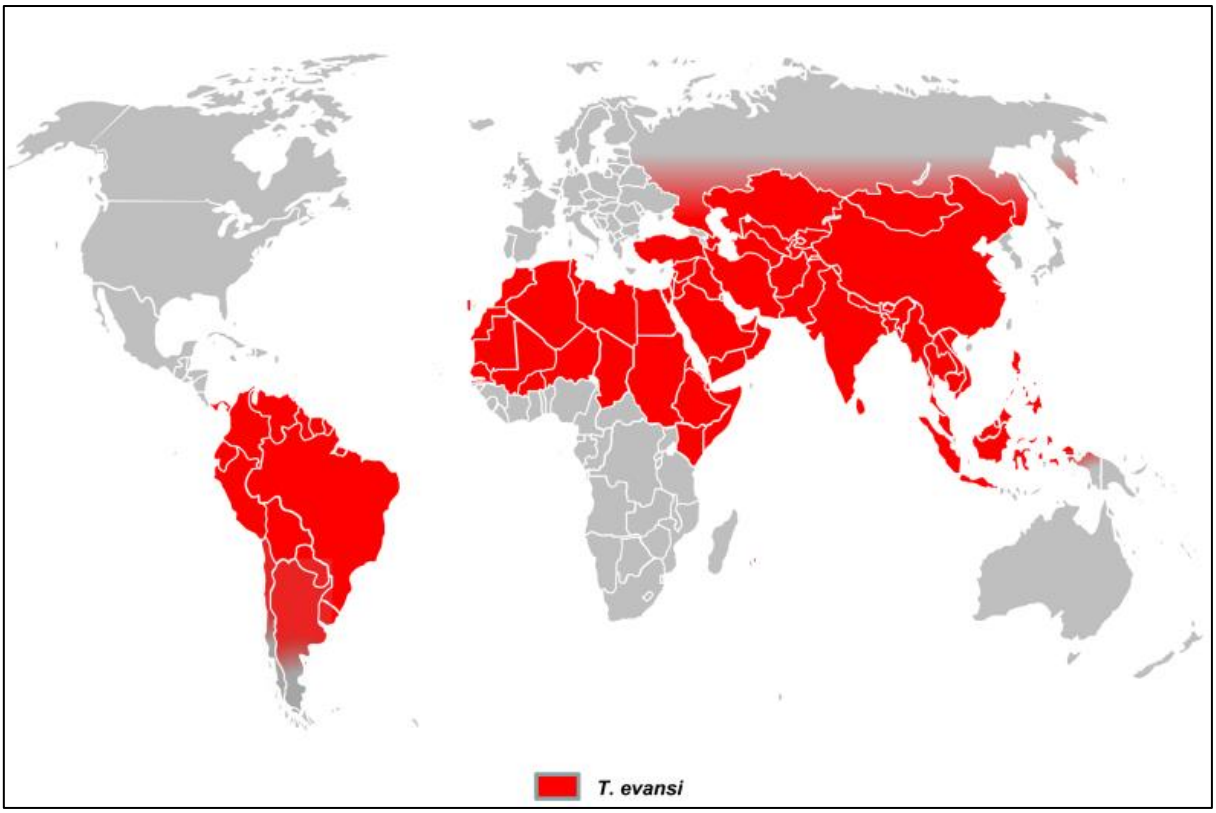

Figure 5. Geographical distribution of *T. evansi* in the world (Desquesnes et al., 2022)

The most affected areas are tropical and subtropical regions; there the transmission is eased by the presence of a great number of vectors carrying *T. evansi*, e.g., biting flies of genera *Tabanus*, *Stomoxys*, *Haematopoda Chrypsos*, and *Lyperosia* but also vampire bats, or carnivores (Luckins, 1988; Gutierrez et al., 2010; Desquesnes et al., 2013). The variety of vectors conveying the pathogen finds an explanation in the mechanical nature of the transmission of the parasite, substantially differing from the classical cyclical transmission; indeed, *T. evansi* evolutionarily diverged from *T. brucei* that only rely on the exploitation of tsetseflies' life cycle (Brun et al., 1998; Borst et al., 1987). Moreover, *T. evansi* can also be transmitted sexually, through milk consumption or through ingestion of freshly killed infected animals (Habila et al., 2012) (Fig. 6).

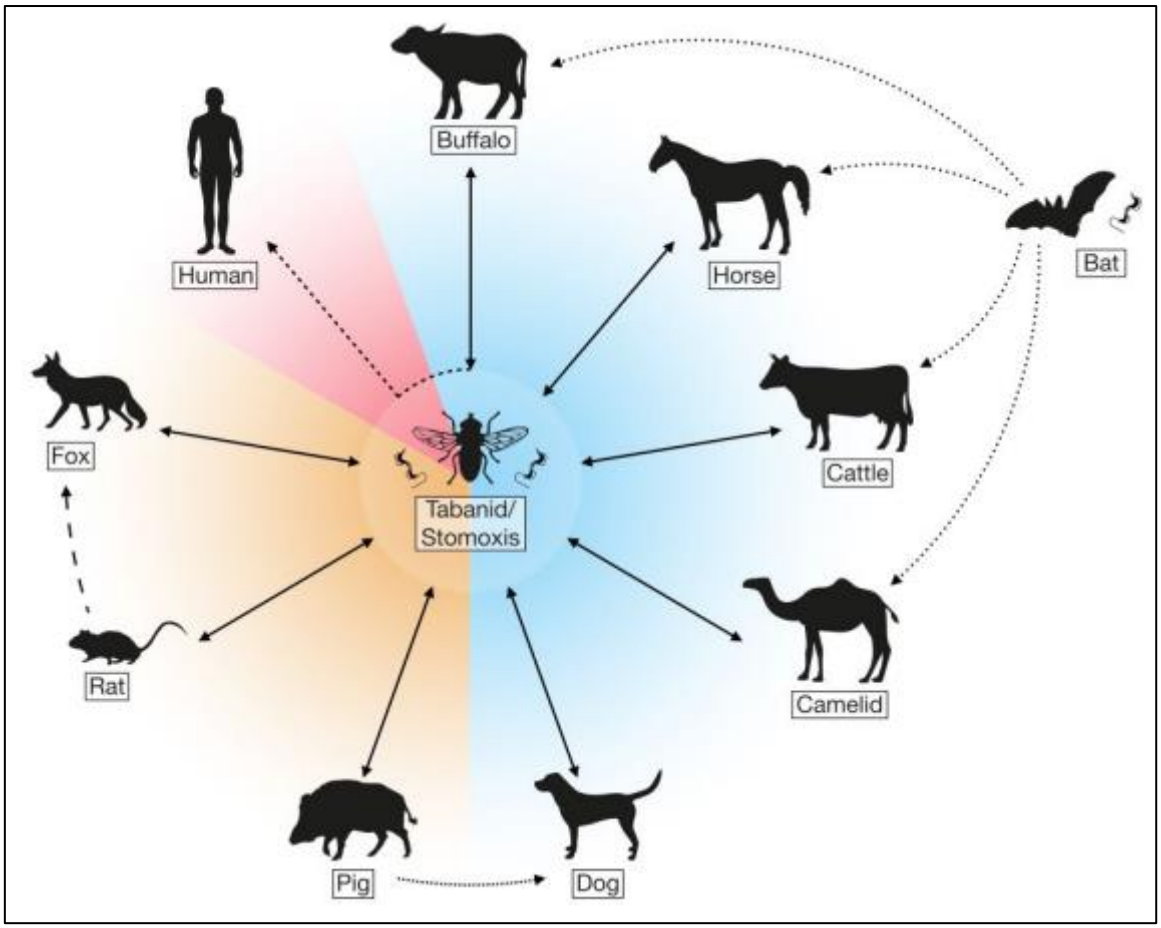

Figure 6. *T. evansi* transmission. A variety of mammals are mainly infected by biting flies. The host species depend on geographical location and are livestock, domestic, and wild animals. The south American vampire bat *Desmodus rotundus* acts as both a reservoir host and vector. Human infections occasionally occurred in people living in close proximity to infected animals (Kim et al., 2024).

Symptoms are severe and, if not treated, the pathology relentlessly results in progressive weakness, depletion, lymph node enlargement, and eventually, death (Saleh et al., 2009; Herrera et al., 2002).

Due to the wide spread of the pathology both in terms of geographic areas and animal host species, Surra represents an important issue that has both an economic and a social impact. Nonetheless, it is neglected in many parts of the world, leading to a continuous evolution and dramatic progression of the disease itself.

1.1.1.3 Dourine

Dourine differs from other animal trypanosomiases because of its venereal transmission. The disease, which mainly affects equids, is indeed almost exclusively transmitted by coitus, and results to be widespread in Asia, Africa, South America, Southern and Eastern Europe, Mexico, Venezuela, and Russia (Sidney et al., 2013). Its peculiar way of transmission makes it difficult to be diagnosed

because of the impossibility of detecting the parasites in blood samples (Gizaw et al., 2017). Indeed, even if it is morphologically identical to *T. brucei* and *T. evansi*, *T. equiperdum* is a primarily tissue parasite, meaning that it rarely invades the blood. Moreover, not being influenced by the presence of a specific vector or climatic conditions, the pathology is likely to occur in many parts of the world, and it currently represents an important economic issue because of its impact on the transport of equids (Chin et al., 2013).

Swelling of the genitalia, cutaneous plaques, and neurological signs are the most common symptoms of the disease, and they usually appear gradually, in a three stages pattern (Claes et al. 2005). The incubation period goes from 1-2 weeks to even after several years from the infection (William and Steven, 2007). The severity of these conditions varies with multiple factors e.g., virulence of the strain, nutritional status, and stress of the animal. In more than 50% of the cases, the pathology is ultimately fatal (Sidney et al., 2013).

The criticality of the treatment of dourine lies in the fact that animals can clinically improve, but they still behave as carriers of the parasite (OIE, 2013). *In vitro* tests from older literature indicate suramin, diminazene, quinapyramine, and cymelarsan as effective potential drugs (Zhang et al. 1992; Brun & Lun 1994). Nevertheless, there are no current approved drugs for dourine.

1.1.2 Human pathologies

Some trypanosoma subspecies also affect humans; *Trypanosoma cruzi* and *Trypanosoma brucei* are the responsible parasites for Chagas disease and Human African Trypanosomiasis (HAT), respectively. Although these pathologies are spread in different geographic areas and show different symptoms and clinical courses, they do present some significant similarities; moreover, they are considerably neglected, mostly affecting poor and marginalized populations.

1.1.2.1 Chagas disease

Trypanosoma cruzi can be geographically located in southern America, where it causes the Chagas disease (Fig. 7). This pathology is spread through bugs belonging to the subfamily Triatominae in the family Reduviidae, and specifically *Triatoma infestans*, *Rhodnius prolixus*, and *Panstrongylus megistus* are the main vectors (Barrett et al., 2003).

Differently from *T. brucei*, *T. cruzi* belongs to the stercoraria subspecies, meaning that its transmission takes place *via feces*, which contain metacyclic forms of trypanosomes. Once the feces are deposited on the host's skin during the insect's feeding, the individual is led to scratch because of

the itching, mechanically introducing trypanosomes into the organism through skin abrasions (Miles, 2003; Prata, 2001).

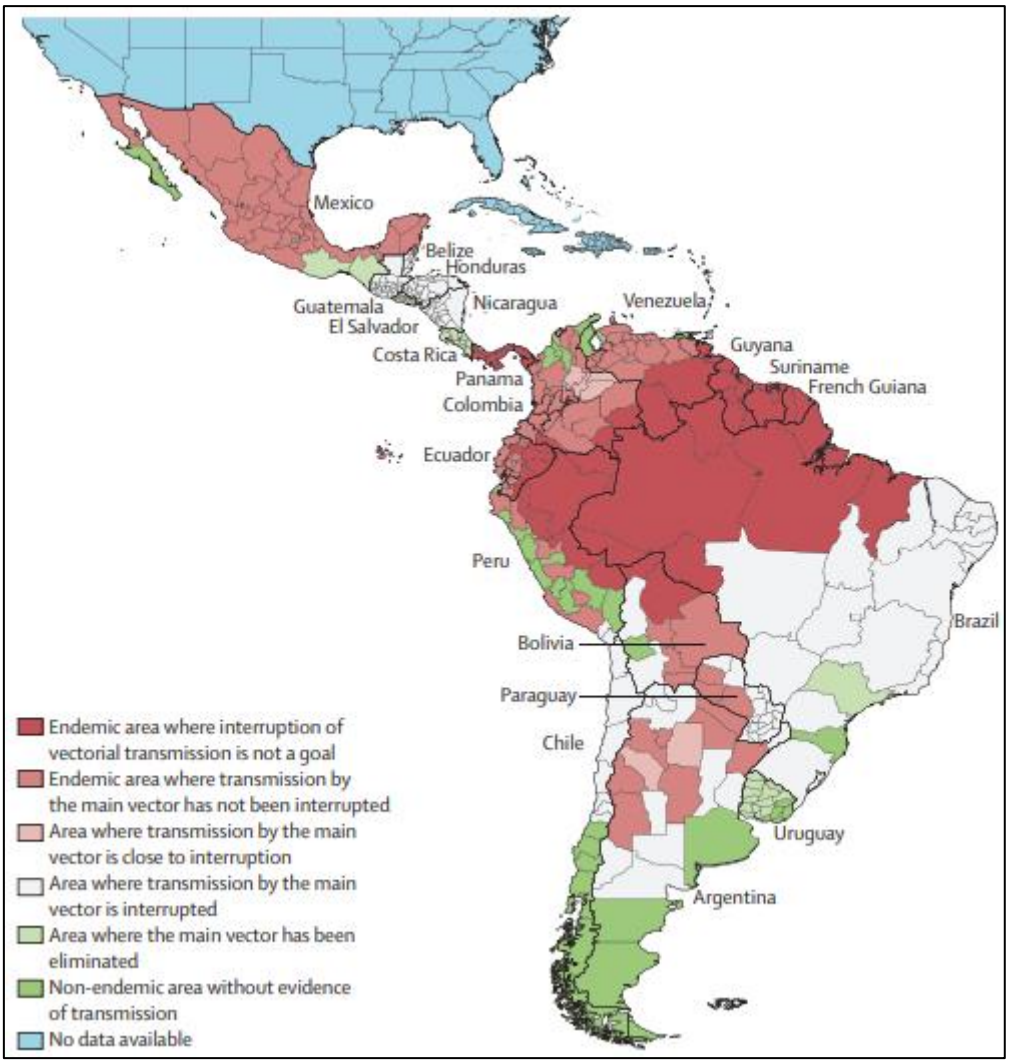

Figure 7. Diffusion of Chagas disease by the main vector, Triatominae. Updated in September 2014 (Perez Molina et al., 2018).

The clinical evolution of the disease is peculiar: it consists of two stages, an acute and a chronic one. The acute phase occurs 6-10 days after the first contact with the parasite and usually lasts 1-2 months. In this period, the host shows inflammation in the site of infection, resulting in an oedematous swelling called chagoma; plus, Romaña's sign can appear, i.e. a swelling of the eyelids characteristic of the disease that often eases the diagnosis (Miles, 2003). Death can occur even in the acute stage of Chagas, due to cardiac complications; in this phase the electrocardiogram shows abnormalities with concomitant tachycardia, prolongation of atrio-ventricular interval, and primary T-wave changes (Rassi et al., 2000).

The chronic stage occurs in 15-30% cases, even after long years after the disappearance of symptoms of the first phase. This second step of the pathology is characterized by severe cardiac, digestive, and nervous symptoms that often lead to the sudden death of the patient (Miles, 2003).

The two main drugs used against Chagas' disease are nifurtimox and benznidazole. Unfortunately, both the heterocyclic drugs are not always effective and induce severe side effects, and for this reason the need for new drugs is urgent (Sosa Estani et al., 1998).

1.1.2.2 Human African Trypanosomiasis

Sleeping sickness is a human trypanosomiasis spread in the sub-Saharan regions of the African continent (Fig. 8). In the next paragraph we will deepen this complex and severe pathology.

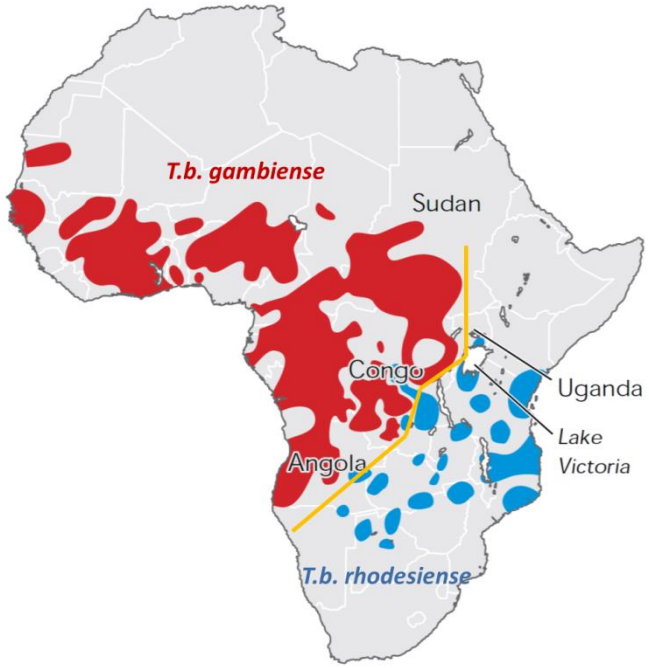

Figure 8. Geographical distribution of *T. brucei gambiense* and *T. brucei rhodesiense* in the African continent (Lundkvist et al., 2004).

1.2 A focus on sleeping sickness

1.2.1 Epidemiology

Human African Trypanosomiasis (HAT), also known as sleeping sickness, is one of the two human pathologies caused by trypanozoons. The two responsible parasites for this disease are from the species *T. brucei*, namely *Trypanosoma brucei gambiense* and *Trypanosoma brucei rhodesiense*.

T. b. gambiense is responsible for about 98% of the cases in humans (Franco et al., 2014).

In this stage parasites circulate in the bloodstream, and first symptoms show up, such as fever and swollen lymph nodes. These symptoms are generic, and therefore the sickness is often mistaken for malaria and treated wrongly. The second stage occurs in a few months, when trypanosomes cross the blood brain barrier (BBB) and affect the central nervous system (CNS). In this phase symptoms become severe, including encephalopathies, mental changes, coma, and in 2-10 years it can be fatal (Brun et al., 1999).

Rhodesian HAT is instead caused by *T. b. rhodesiense*. This pathology is less common (it rarely affects humans) and mainly spread around Lake Victoria. Its clinical course is shorter, and thus it is considered an acute zoonotic disease which leads to death within months (Odiit et al., 1997).

Adult population is the main target of this parasitic disease, and there is an evident correlation with the type of activity carried out by the patients; for example, fishermen who are in close contact with the vector appeared to be more prone to infection (Büscher et al., 2017).

The affected areas are rural and confined in specifica areas called "foci"; most of them are in Sub-Saharan Africa on a 1,55 million Km^2 area, between 14°N and 20°S latitude (Fig. 8) (Simarro et al., 2012). Currently, almost 70 milion people are estimated to be at risk of sleeping sickness (57 milion of these 70 milion are exposed to gambiense parasite), as well as 50 milion cattle (Keating et al., 2015; WHO, 2013).

In the last century, three main epidemics occurred: the first one was between 1896 and 1906, mostly in Uganda and the Congo Basin; in the 1920s, another epidemic was spread in several sub-Saharan countries and by the mid-1960s was maintained below 5.000 cases per year; the last great wave occurred between 1970 and the late 1990s, with peaks of almost 40.000 cases, amidst an estimated 300.000 undetected and untreated cases. More than 50% of them were reported in several villages in Angola, the Democratic Republic of Congo (DRC), and South Sudan. HAT resulted to be the greatest cause of mortality in those communities (WHO, 2023a).

Thanks to the efforts of WHO, national control programs, and non-governmental organizations, the increasing trend was reversed, and WHO itself fixed for 2020 the elimination of HAT as a public health problem, and for 2030 its total eradication (zero cases) (Fig. 9).

Although HAT occurrence reached a historic low already in 2017 and maintained a decreasing trend over the following years (Fig. 10), only 6 of the 24 countries in which the disease is spread managed to eliminate gambiense HAT as a public health problem, namely Côte d'Ivoire (2020), Togo (2020), Benin (2021), Equatorial Guinea (2022), Uganda (2022), and Ghana (2023) (WHO, 2023b).

DRC still represents the most affected country accounting for 61% of 837 total cases in 2022 (mean 522 cases/year), and many other countries have not declared or have only partially declared cases for over a decade, making the estimation of risk and the diffusion control not completely accurate.

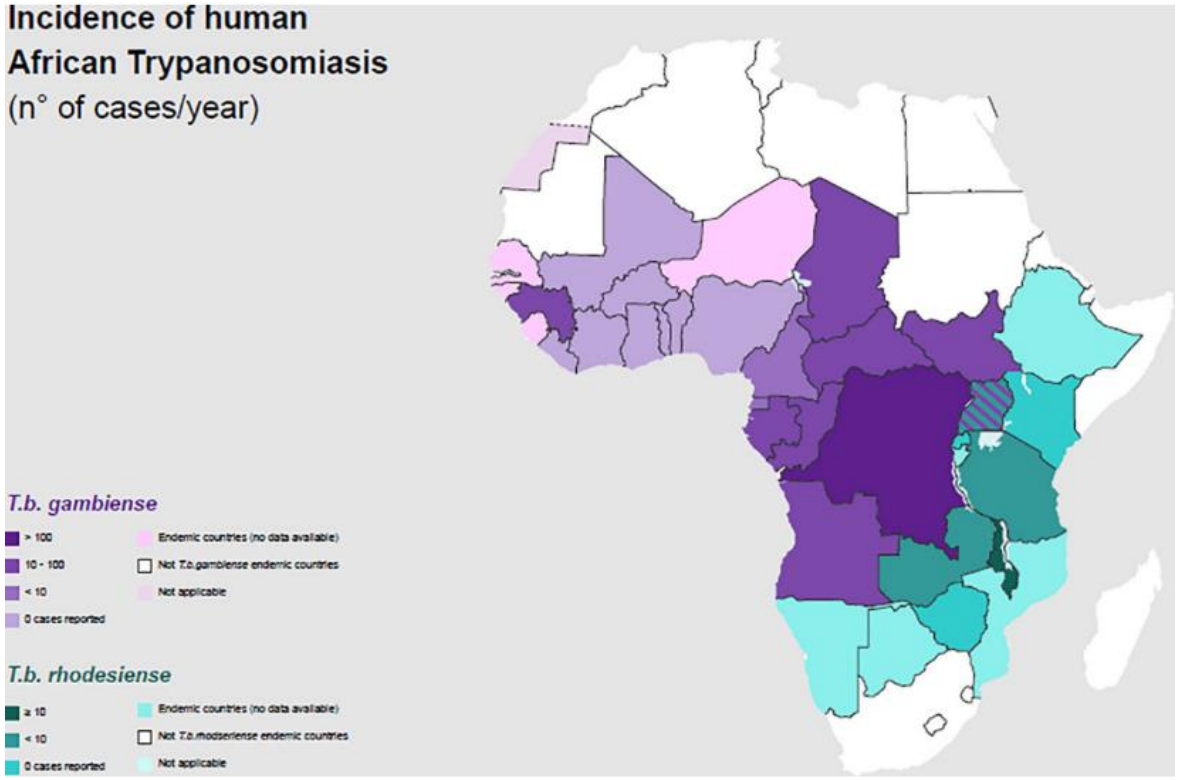

Figure 9. Incidence of Human African Trypanosomiasis: *T. b. gambiense* and *T. b. rhodesiense* (number of newly reported cases of HAT per year) and geographical distribution in 2020 (Papagni et al., 2023).

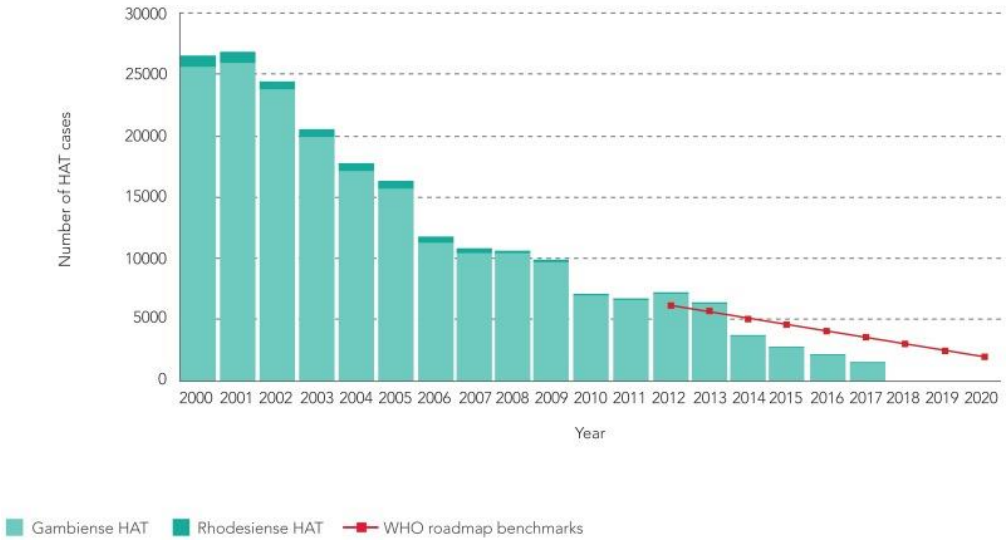

Figure 10. Total number of reported cases of HAT (gambiense and rhodesiense) per year (WHO, 2019).

Based on these considerations, estimations of trends and case detections must be interpreted cautiously; number of cases are strongly related to the quality and the amount of screening efforts.

Thus, the risk of future epidemics of HAT shouldn't be underrated, also considering the absence of vaccines and the limits of current approved treatments (Simarro et al., 2010).

1.2.2 History

Phylogenetic studies proved that trypanosomes developed in central Africa almost 180 million years ago, and only subsequently, the pathogens split between Salivaria and Stercoraria subspecies and became gut parasites of some prehistoric insects. Tsetse flies, instead, only appeared 35 million years ago, becoming the main vectors of trypanosomes in mammals (Haag et al., 1998). Being in constant contact with these flies, it is not surprising that most parts of African wild animals developed resistance to trypanosomes; on the other hand, domestic animals didn't show tolerance to the parasites and became the main target of the animal disease.

1.8 million years ago, hominids started migrating to the savannah area (East Africa) coming into direct contact with the flies. At the beginning, the serum sensitivity to *T. brucei* protected humans from infection, but after a prolonged exposure the parasite started mutating, evading the hosts' immune system and managing to survive in human organisms (Steverding, 2008).

The first written report of trypanosomiasis dates to 2000 BC in ancient Egypt. The Veterinary Papyrus of the Kahun Papyri described an animal illness highly similar to Nagana called Ushau, which was treated at that time with a bird-derived oil (Fig. 11) (Steverding, 2008).

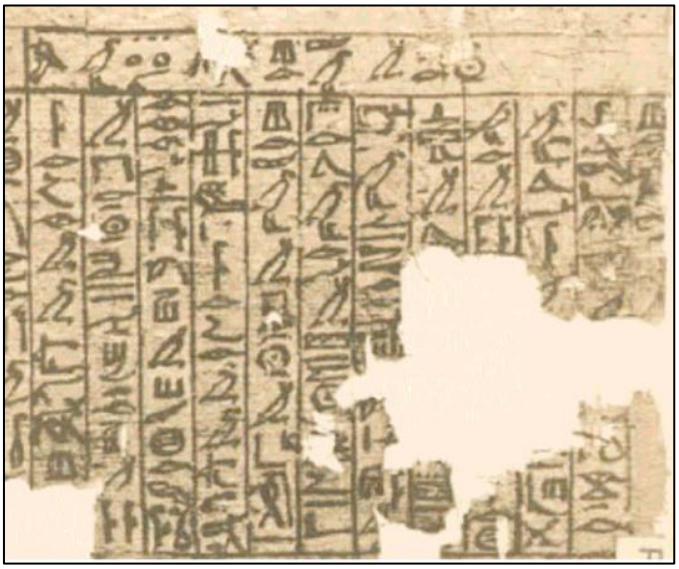

Figure 11. A section of a veterinary papyrus about a cattle disease from the 2nd millennium BC (Steverding et al. 2008).

In the Middle Ages, some records of Arabic traders and writers witnessed the diffusion of a disease affecting both humans and domestic animals, and the described symptoms matched with current trypanosomiasis symptoms. The geographer Abu Abdallah Yaqut (1179–1229), during his African journey found in the "Country of Gold" (Wangara) a village whose “inhabitants and even their dogs were just skin and bones and asleep”; another famous writer from the 14th century, Ibn Khaldun, reported the king of Mali’s death caused by a sickness resembling human trypanosomiasis.

In the following centuries, trypanosomiasis became intimately related to colonial slavery. Around the 18th century, sleeping sickness caused several losses in slaves, and slave-traders financially supported the study of the disease (Headrick, 2014). In 1734, John Aktins published the first medical report of HAT that included an accurate description of the neurological late-stage symptoms (Cox, 2004).

It was only in 1895, when the first big epidemics of the modern age occurred, that the microbiologist David Bruce discovered the causative pathogen of Nagana in the blood of infected cattle and horses. Six years later, in 1901, the British surgeon Forde observed trypanosomes for the first time in the blood of a HAT patient; but only in 1902 the parasites were identified as the protozoa *T. b. gambiense*, thanks to the physician Joseph E. Dutton, who gave them this name because of the Gambian colony in which the pathogen was discovered (Headrick, 2014).

T. congolense and *T. vivax* were discovered a few years later by Alphonse Broden and Hans Ziemann, respectively (Broden, 1904; Ziemann, 1905). Finally, in 1910, Stephens and Fantham identified *T. b. rhodesiense*, the second human pathogenic trypanosome (Stephens and Fantham, 1910). In those years the first studies for mechanisms of infection, life cycle, and chemotherapy were conducted, and the first drug was developed, namely Atoxyl, an arsenical compound used for the treatment of first-stage HAT.

Unfortunately, during the second great epidemic of the 20th century (1920-1940), arsenical drugs revealed to be highly toxic, and the need for safer drugs pushed the research to explore different chemical patterns. A viable alternative was found only in the second half of the century, when Pentamidine was introduced into the market by the English chemist Ewins (Eperon et al., 2014); with the discovery of pentamidine, a decrease in HAT cases was registered by the mid-1960s. For this reason, and after the decolonizing processes, the control of HAT and the screening programs that kept the disease under control were also stopped.

Therefore, in the mid-1970s a new epidemic’s wave occurred, being even more dramatic than the previous ones, due to the development of resistance mechanisms of the parasite to the drugs used at

the time. The situation started improving with the discovery of Eflornithine, that revealed to be a valid therapy for second stage gambiense HAT (gHAT) (Van Nieuwenhove et al., 1985).

Currently, as already mentioned, thanks to the coordinated efforts of WHO and other non-profit and non-governmental organizations, the situation seems to be under control. However, due to the lack of a proper health system and control in the affected areas, the urge for new therapies and control systems is not to be underrated.

1.2.3 Economic and social impact

Tsetse flies are spread in sub-Saharan regions of Africa in 37 countries (32 of which are ranked as the poorest in the world) and covering almost 10 million km^2, corresponding to one third of the entire continent (Meyer et al., 2016; Mattioli et al., 2004). This wide diffusion is the reason why trypanosomiasis remains a significant global health challenge, affecting not only humans but also domesticated and wild animals (Kasozi et al., 2021).

Livestock and agriculture represent the main source of profit and nutrition supply for sub-Saharan areas, and, concomitantly, they are the two most affected sectors by trypanosomiasis.

Abro and colleagues reported that trypanosomiasis potentially reduces production of meat and milk by 36% and 34%, respectively (Abro et al., 2021) and lowers the productivity of cattle by 20% to 40%, being of considerable impact and causing an estimated loss of billions of dollars per year (Devisser et al., 2010). Moreover, the conditions in which the farmers are compelled to work increase the likelihood of exposure to tsetse bites (Gashururu et al., 2021). Many areas, even if fertile and potentially good sources of profit, are also underutilized because of their infestation with tsetse flies (Cecchi et al., 2014). Sokwa and Durra regions in Nigeria constitute a clear example of this problem: being infested with both *Glossina morsitans* and *Glossina tachinoides*, farmers were discouraged to start cultivation and livestock in these areas, that were therefore abandoned (Putt & Shaw, 1982).

In this regard, vector control constitutes an important tool to counteract the spread of the disease. In a study by Swallow (1999), a sample of farmers were interrogated before and after tsetse control measures were applied in their areas. The livestock owners witnessed that, after the control campaign, there was a great reduction in cattle mortality (from 63% in 1994 to 7% in 1995) (Shaw, 1999).

However, treatment and control campaigns have high costs. Most involved countries governments currently spend US$ 44 million to control the disease, and supply 70 million doses of treatments per year (Abro et al., 2021; Kulohoma et al., 2020). Besides, secondary expenses are not to be overlooked: transport costs, visits, loss of occupation time and income (Bukachi et al., 2017).

Trypanosomiasis affects, although to a lesser extent, tourists; from 2000 to 2010, 94 HAT cases were registered in non-endemic countries, discouraging National Parks and Reserve tourism in a great number of African countries (Simarro et al., 2012; Gamba et al., 2021). In local populations, HAT represents a heavy burden especially for families; the disease mainly affects young adults that become unable to work because of its debilitating nature. This results in increased crimes, unemployment, and low life expectancy (Njenga, 2007).

The initiation of Pan African Tsetse and Trypanosomiasis Eradication Campaign (PATTEC) in 2000 by the African Heads of State and Government contributed to provide financial and institutional support. Despite the fact that HAT is currently kept under control in most of the affected areas, the disease remains a serious threat to the economic and social stability of countries already challenged by many constraints; climate change is one among many that may potentially increase the diffusion of tsetse flies even in non-endemic areas.

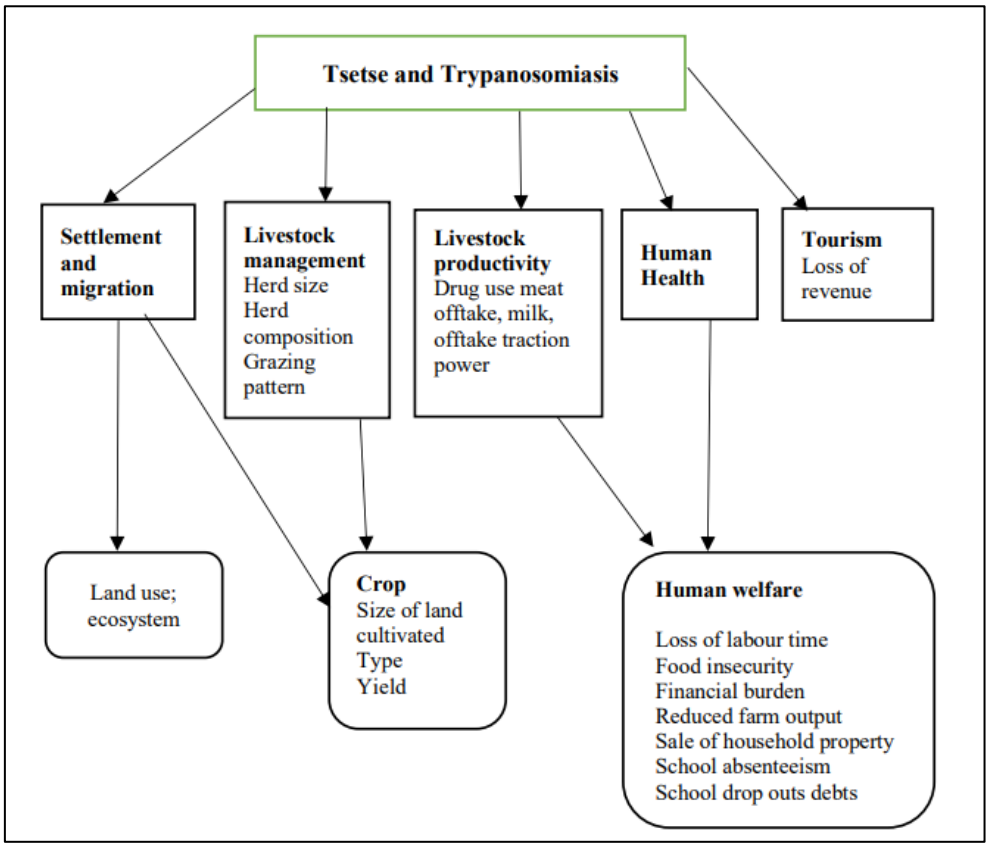

Figure 12. Social and economic impacts of tsetse and trypanosomiasis (Kikwai and Ngeiywa, 2022).

1.2.4 Clinical features

The parasite subspecies, the host immune system response, and the stage of the disease are factors that strongly influence HAT symptoms. For instance, gHAT determines a chronic infection whereas *rhodesiense* HAT (rHAT) is acute. rHAT is characterized by a fast progression and death can occur from few weeks to 6 months, even in the early stage. On the contrary, gHAT takes at least 3 years to be fatal (Büscher et al., 2017).

The very first symptom of the disease appears at the site of the tsetse fly bite with a local reaction, which is called trypanosomal chachre (Fig. 13). Subsequent to this sign, which is typical of *rhodensiense* infections, other unspecific symptoms manifest, such as fever, headache, muscle ache, and joint pain. This early stage is sometimes mistaken for malaria, and not properly treated (Brun et al., 1999).

Subsequently, HAT evolves through clinically distinct stages, with a fatal outcome if left untreated.

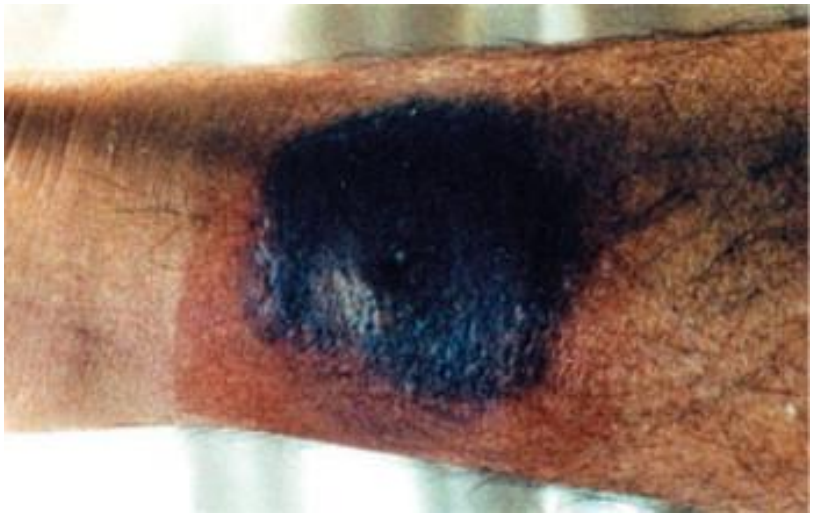

Figure 13. Trypanosomal chancre on a patient affected by gHAT (Malvy and Chappuis, 2011).

1.2.4.1 First stage

A general infection characterizes the first stage of HAT. Fever appears and its pattern results irregular over the weeks, reflecting progressive waves of parasites multiplying in the blood (Stich et al., 2002). Some central symptoms can be noticeable in this stage, e.g., cranial nerve palsies, urinary incontinence, somnolence, tremor, and abnormal gait. In particular, they were detected in patients with early-stage *T. b. rhodesiense* disease in two distinct regions of Uganda (Kennedy and Rodgers, 2019).

Nonetheless, the most common symptoms for West African trypanosomiasis are usually milder. Lymphadenopathy, especially in the posterior triangle of the neck (Winterbottom's sign) (Fig. 14), is characteristic and helps the diagnosis.

Figure 14. Winterbottom's sign on the neck of a patient affected from gHAT (infectionlandscapes.org, 2011).

1.2.4.2 Late stage

When trypanosomes start invading CNS, late stage occurs. Specifically, for rHAT this phase begins within some weeks, while for gHAT it can take months. Mogk and colleagues suggested that the passage of parasites through the BBB is immune-mediated and takes place when a high concentration of trypanosomes in the blood is detected (Mogk et al., 2014). This stage of the disease is characterized by chronic encephalopathy, headache, and mental changes. Moreover, patients demonstrate difficulty in concentration, reduction of mental functions, and alienation from reality, and eventually they enter a terminal somnolent state, from which the disease takes its name (Stich et al., 2002). Mobility and sensory disturbances are also common, as well as difficulties in focusing. Plus, cardiac disorders also emerge, noticeable from electrocardiogram abnormalities, e.g. perimyocarditis (Büscher et al., 2017).

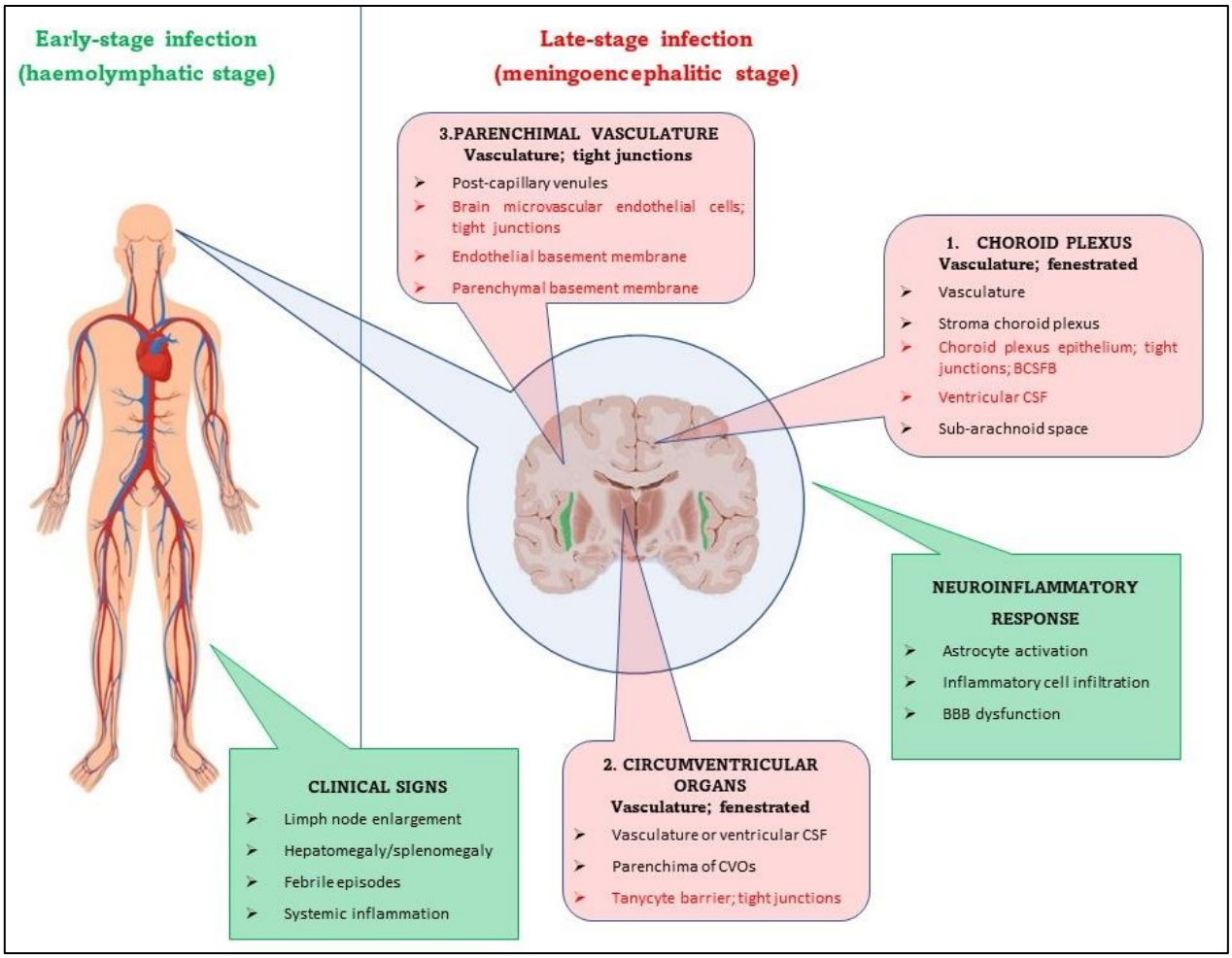

Figure 15. Clinical features of HAT in the two stages of the disease.

1.2.5 Diagnosis

A timely establishment of a HAT diagnosis is pivotal to program a prompt intervention. As soon as the first symptoms show up, an appropriate treatment has to be set up, especially in view of the progression of the pathology in its second-stage, for which the chemotherapy becomes more problematic. Indeed, possibilities of survival are higher if HAT is treated in its early stage, and safer drugs can be adopted, being late stage drugs characterized by several side effects and relevant toxicity

First, the staging of the disease needs to be determined (Fig. 14). The two main criteria for the differentiation of stage I and II are essentially the direct detection of parasites and the number of white blood cells (WBC) per µL. Specifically, WHO indicates a count of more than 5 WBC/µL and a concomitant presence of parasites in the cerebrospinal fluid (CSF) as diagnostic criteria for the late stage (Bonnet et al., 2015). Nonetheless, the presence of WBC in the CSF is not peculiar to HAT, being also common in other pathologies, such as meningitis.

1.2.5.1 Antibody detection

Positive specific diagnosis for *T. b. gambiense* usually needs to be performed by serological methods. The Card Agglutination Test for Trypanosomiasis (CATT) turned out to be the best diagnosis method and is mostly used in regions where there is a high prevalence of the disease. Unfortunately, it has a high incidence of false-positive results which makes it particularly problematic in areas where the number of cases is low (Brun et al., 2010; Kennedy and Rodgers, 2019).

The test is based on the antigen type LiTat 1.3, and its sensitivity and specificity vary between 68.8–100 and 83.5–99.3 (Bonnet et al., 2015). Although its cost is affordable, it is a very delicate technique, susceptible to heat and packed in 50-dose format, with consequent loss of non-used doses.

During the last 7 years, rapid diagnostic tests (RDT) were developed based on the antigens LiTat 1.3 and 1.5 and Second- generation RDTs based on recombinant antigens. They seem to be better than CATT and more suitable for population screening (Sternberg et al., 2014).

1.2.5.2 Parasite detection

Unfortunately, a satisfactory test that confirms parasite detection in fluids is not currently available. For this reason, a combination of a number of different tests is used, including lymphnode aspirates in suspects with cervical adenopathy, capillary tube centrifugation (CTC), quantitative buffy coat (QBC), and the mini anion-exchange centrifugation technique (mAECT). mAECT, in particular, is the most sensitive test that consists in isolating the parasites from venous blood using anion exchange mini columns, and concentrating them. Blood cells become negatively charged while parasites remain neutral, and an anion-exchange chromatography at pH 8 allows to separate them efficiently (Bonnet et al., 2015).

1.2.5.3 Stage diagnosis

Once the diagnosis of sleeping sickness is certain, the stage of the disease has to be assessed through the examination of the CSF trhrough lumbar puncture. If parasites are detectable through microscopy in the CSF, stage II is confirmed, although this kind of analysis is not highly sensitive nor reproducible. Indeed, the number of circulating trypanosomes can be very low and hard to be detected, generating false-negative results. Thus, the late-stage HAT diagnosis mostly depends on the abovementioned WHO criteria, requiring, beside the presence of parasite in the CSF, a WBC count of more than 5 cells per µL (Brun et al., 2010).

In some cases, a higher WBC count threshold is adopted for the diagnosis of gHAT (20 cells/µL), but the optimum WBC count for staging the disease was suggested to be 10 cells/µL (Sehkar et al., 2014). The measurement of CSF IgM concentration is another tool to give a confirmation of the late-stage diagnosis, being enhanced earlier than WBC as soon as trypanosomes enter the CNS.

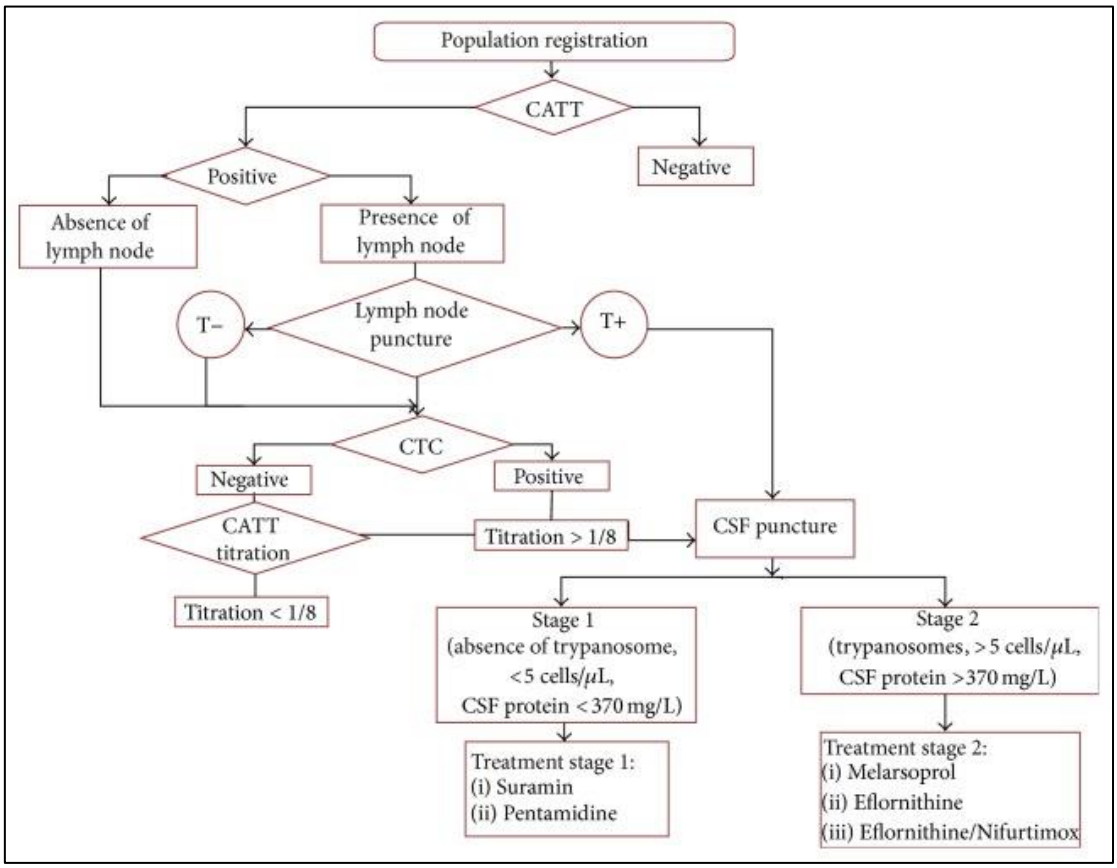

Figure 16. Decision tree of HAT stage diagnosis (Bonnet et al., 2015). CTC = Capillary Tube Centrifugation; CSF = cerebrospinal fluid.

1.2.6 Transmission

The transmission of HAT depends on the form of disease itself.

Indeed, rHAT commonly affect wild animals and cattle, and rarely human hosts. Rare cases of rHAT were reported in National Parks, where the environment doesn't allow to control HAT diffusion at all. Due to the exponential growth of the African population, a great number of wild animals have been decimated because of the massive hunting and for this reason, domestic animals are the most important reservoirs of the disease. Most infective animals resulted to be pigs and cattle, probably because they freely roam in humid and shady areas where they are more exposed to tsetse flies (N'Djetchi et al., 2017).

A recent study run in Busoga has demonstrated that *T. b. rhodesiense* HAT can be transmitted five/six times more likely through a cattle-fly-human cycle than by a human-fly-human cycle (Hide et al., 2007).

On the other hand, *T. b. gambiense* HAT is mostly transmitted by the human-tsetse fly-human cycle. The parasite is transmitted across the placenta or by blood transfusion only in some rare cases.

Despite debates about the animal reservoir involvement in *T. b. gambiense* HAT, recent studies conducted using modern molecular tools have confirmed the presence of the parasite in pigs in Cameroon and Ivory Coast, and the infection was also detected in several primates (Jamonneau et al., 2004; Nkinin et al., 2002).

The disease is spread in humans and in general in mammalian hosts by Tsetse flies of the genus *Glossina*. The commonly called tsetse fly belongs indeed to the order of Diptera and is categorized as member of the superfamily Hippoboscidea, the family of Glossinidae. Over 20 species of tsetse flies exist, and they are classified into three species groups: *palpalis* group (Nemorhina), *morsitans* group (Glossina) and *fuscipes* group (Austenina) (Franco et al., 2014) (Fig. 17).

Although there are several species of tsetse flies, they are not all equally important for transmission. The species of the *fuscipes* and the *palpalis* groups are mainly implicated in the transmission of *T. b. gambiense*, while species of the *morsitans* group are involved in the transmission of *T. b. rhodesiense* (Geiger et al., 2004).

All the insects are characterized by a recognizable proboscis, antenna with branched arista hairs and wings that fold and have a characteristic “hatchet” cell (Fig. 18).

These flies are hematophagous (blood-feeding), and they inject saliva when biting their mammalian prey before they start to suck blood. If the tsetse fly is infected by Trypanosome, they release it through saliva.

Tsetse flies acquire parasites while feeding on infected animals. In the flies’ digestive tract, the parasites undergo a 3-to-4-week developmental cycle before they reach the salivary gland, and the fly becomes infective. The salivary gland infection rate is low; through dissection and microscopy it was possible to state the infection rate in the field below 1% (Abdi et al., 2017; Wamwiri and Changasi, 2016). However, a tsetse fly feeds every 3 days and can infect several people during its lifetime. The pathogens can be harbored by humans and both domestic and wild animals which then act as reservoirs for the disease. While domestic animals can show symptoms, wild animals remain healthy (Brun et al., 1999).

Vector-control is considered an important strategy to improve human and animal health and consequently increase agricultural production and ensure food security by the local authorities. Since the 1970s many institutions have encouraged projects and programs, some of which were research-oriented, for trypanosomiases control, achieving good results. One of these is certainly the Pan-African Tsetse and Trypanosomosis Eradication Campaign (PATTEC), launched in 2001 (Diarra et al., 2019).

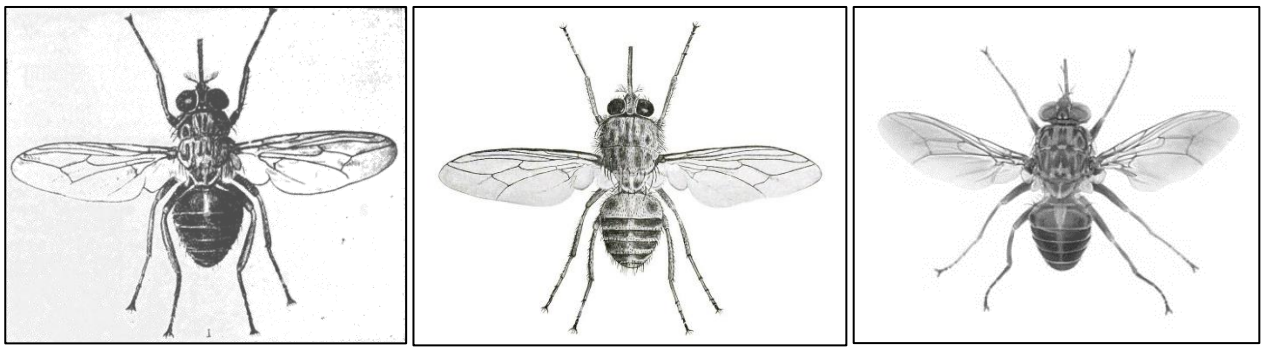

Figure 17. Principal vectors of HAT. From the right: *Glossina palpalis*, *Glossina morsitans* and *Glossina fuscipes.*

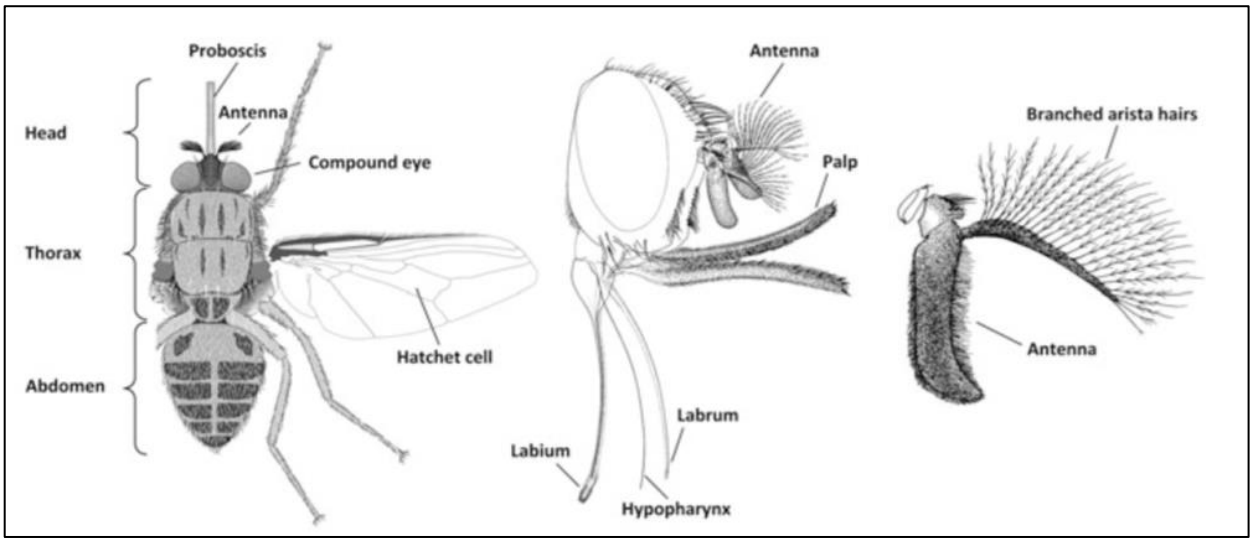

Figure 18. Anatomy of the tsetse fly (Magez and Radwanska, 2014).

1.2.7 The responsible parasite: Trypanosoma brucei

Trypanosomes belong to Kinetoplastida, one of the most ancient eukaryotes' classes, including *T. Brucei*, *T. Cruzi*, and various species of *Leishmania*, all of them switching between a mammalian and an insect host (Vickerman et al., 1976). These parasites are characterized by a unique organelle called kinetoplast, which behaves as a mitochondrion and is is constituted by a network of thousands of

small interlocking circular DNAs divided into mini and maxi-circles (Donelson et al., 1999). It is located near the basal body of the flagellum, a sort of "tail" which is attached to the cell body along most of its length and it is essential for the parasite mobility (Fig. 19).

The cell is elongated and shaped by the presence of a microtubules network (cytoskeleton) following the longitudinal axis of the parasite (Mc Kean, 2003). The cytoskeleton comprises the nucleus, the Golgi apparatus and the endoplasmic reticulum. The nucleus is located in the central region of the cell and contains 11 diploid pairs of megabase chromosomes, and approximately 100 minichromosomes (Akiyoshi et al., 2013).

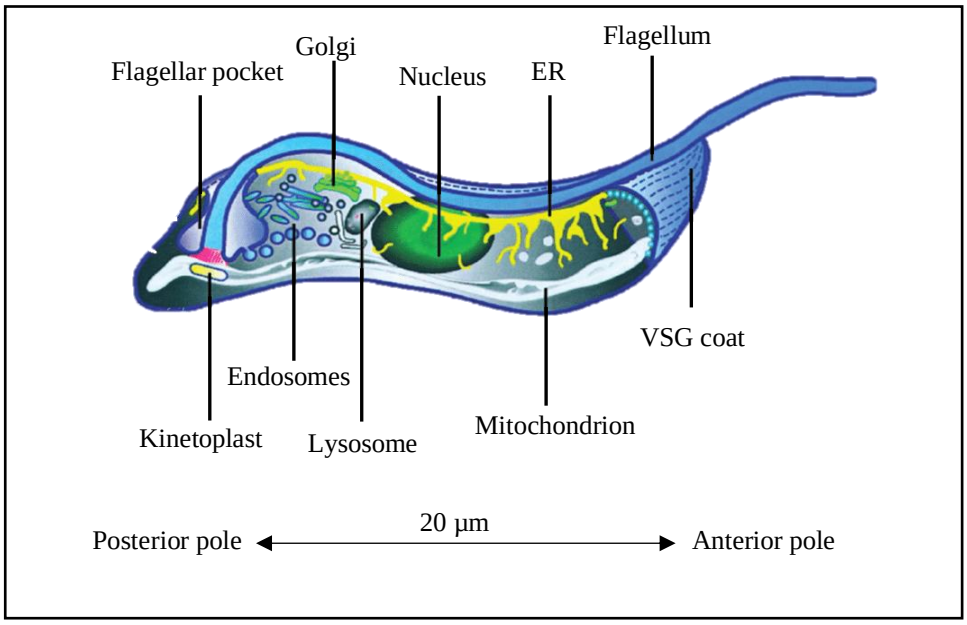

Figure 19. Schematic representation of bloodstream form of *T. brucei*.

1.2.7.1 DNA replication and nucleotide metabolism

Trypanosomes, differently from many eukaryotes, possess two unit-genomes; one is nuclear, and the other one is mitochondrial, and is located in the kinetoplast. The first description of *T. brucei* peculiar DNA synthetic periods of nucleus and mitochondrion was provided by Woodward and Gull in 1990 (Woodward and Gull, 1990). The two researchers performed a DAPI fluorescence assay that allowed to detect the nucleus and kinetoplast behavior over time defining a pattern of replication for both (Fig. 20). From this study it was possible to divide the cell cycle in four morphological distinct periods, in which cells are defined as: 1N1K (1 nucleus, 1 kinetoplast, C from Fig. 20), 1N2K (I from Fig. 20), mitoticN2K (L from Fig. 20), and 2N2K (O from Fig. 20). Replication for nucleus and kinetoplast clearly have different timings, however they seem related to each other, suggesting a unique regulation within the parasite cell cycle. The segregation of the two genomes occurs in a specific

chronological order by interaction with microtubule-based structures, the spindle for nuclear DNA and the flagellum basal bodies for the kinetoplast DNA (Gull, 2002).

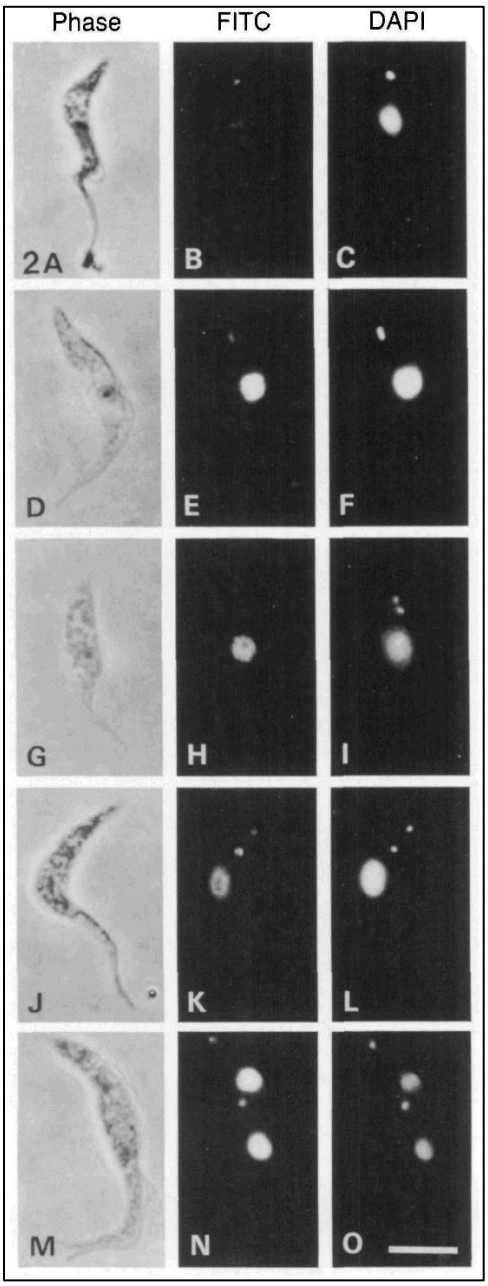

Figure 20. The DAPI fluorescence indicates cells at progressive stages in the *T. brucei* cell cycle. Nucleus and kinetoplast replication stages are reported in C (1N1K), I (1N2K), L (mitoticN2K), and O (2N2K).

Several components of the DNA replication apparatus are unique to kinetoplastids, thus making this system a potential target for drug development (Klingbeil et al., 2002; Sinha et al., 2004). For instance, the purine and pyrimidine metabolism of *T. brucei* show some peculiarities with respect to the corresponding mammalian metabolism. In a review from Hofer (2023), the nucleotide metabolism for the parasite was elucidated (Fig. 21).

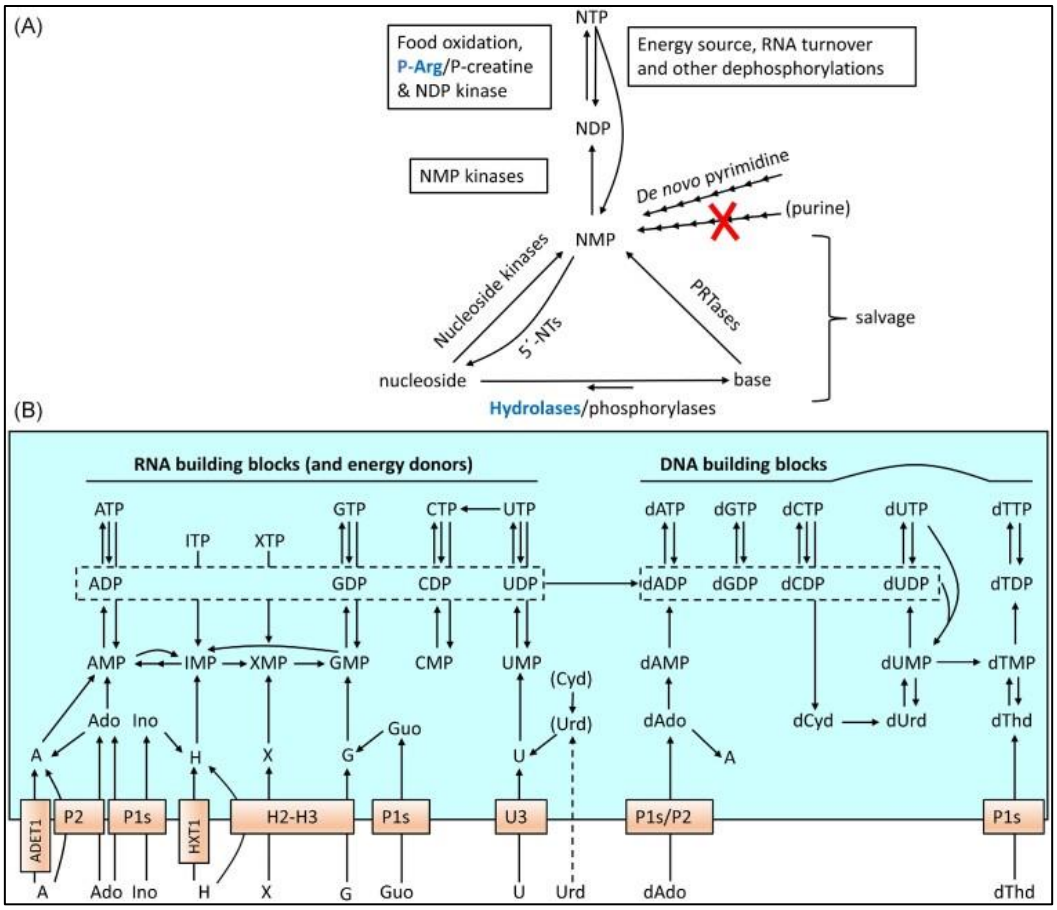

Figure 21. Nucleotide metabolism in *T. brucei*. A) Intracellular nucleotide metabolism of *T. brucei*. Differences in mechanisms inside the parasite with respect to mammalian cells are marked in blue and followed by the mammalian alternative in black. B) Nucleotide biosynthesis in *T. brucei*. Abbreviations: PRTases, phosphoribosyltransferases; NMP/NDP/NTP, nucleoside mono-, di-, or triphosphate; P-Arg, phosphoarginine; P-creatine, phosphocreatine; X, xanthine; H, hypoxanthine.

Briefly, purine pools only rely on salvage pathways, completely lacking *de novo* mechanisms (Fig. 22). Salvage reactions are both cytosolic and glycosomal. Several interconversion enzymes between AMP, IMP, and GMP consent to the parasites to survive on any purine source; for this reason, targeting these enzymes singularly wouldn't be a successful strategy.

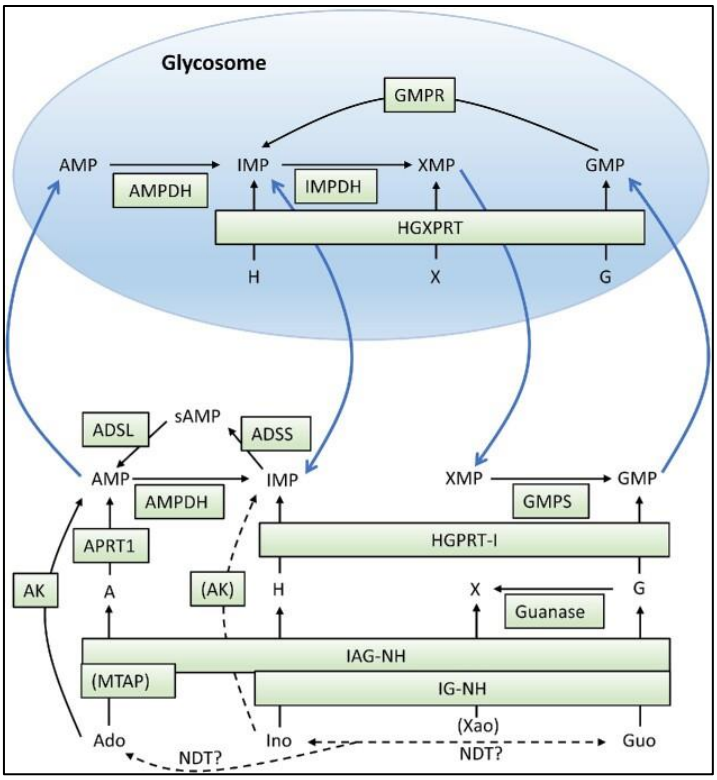

Figure 22. Purine salvage and interconversion reactions in *T. brucei*. Abbreviations: IMPDH, IMP dehydrogenase; GMPR, GMP reductase; sAMP, succinyladenylate; AK, adenosine kinase; APRT1, adenine phosphoribosyltransferase 1 (cytosolic isoform); HGXPRT, hypoxanthine-guanine-xanthine phosphoribosyltransferase; IAG-NH, inosine-adenosine-guanosine-nucleoside hydrolase; IG-NH, inosine-guanosine-nucleoside hydrolase; ADSL, adenosylsuccinatelyase; ADSS, adenylosuccinate synthase; GMPS, GMP synthase; AMPDH, AMP dehydrogenase; HGPRT-I, hypoxanthine-guanine phosphoribosyltransferase 1 (cytosolic isoform); MTAP, methylthioadenosine phosphorylase; NDT, nucleoside deoxyribosyltransferase.

Purine uptake in trypanosomatids instead, is dependent on high-affinity active transporters, such as P1 and P2, that have been selected as preferential targets for drug development. Specifically, many adenosine analogs were found to exploit these two transport mechanisms resulting in a high antitrypanosomal efficacy.

Concerning pyrimidines, UTP is generally synthesized *de novo*, although it can be salvaged via uracil/uridine. dTTP synthesis is dependent on an entirely new mainly mitochondrial pathway, whereas other dNTPs can be made via RNR. Finally, CTP cannot be acquired from the host and its production exclusively relies on the transformation of UTP in CTP catalyzed by CTP synthetase (CTPS) (Fig. 23). RNR, CTPS, and probably thymidine kinase, are considered as essential nucleotide metabolism enzymes in *T. brucei*. Therefore, they represent good drug targets for new chemotherapies.

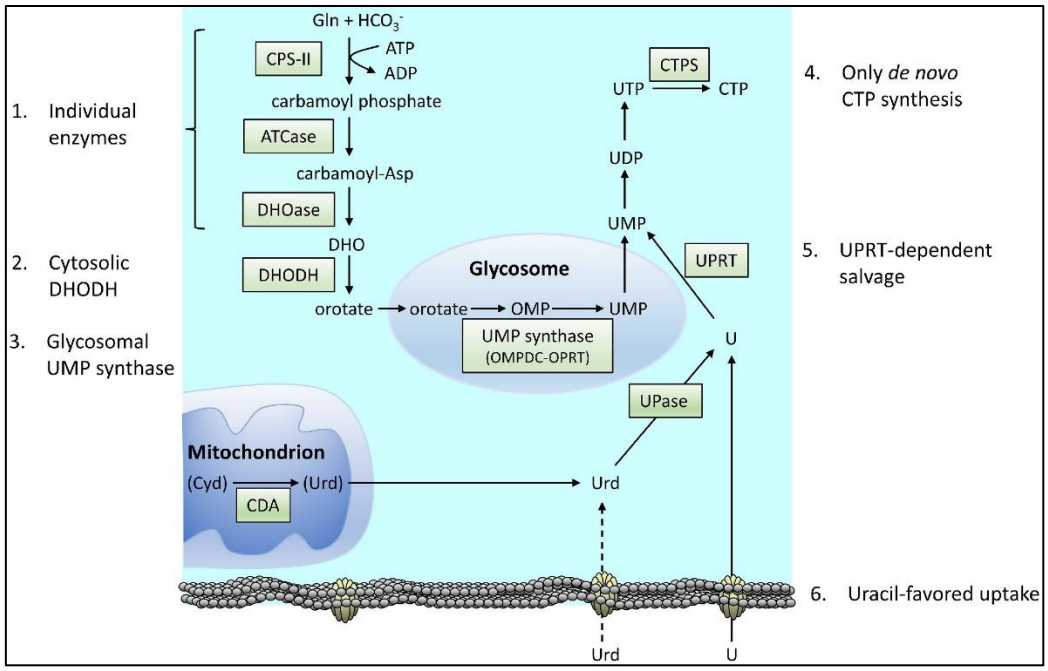

Figure 23. Pyrimidine metabolism in *T. brucei*. Differences from mammalian cells are reported from 1 to 6. Abbreviations: CPS-II, carbamoyl phosphate synthase II; ATCase, aspartate transcarbamoylase; DHOase, dihydroorotase; DHOHD, dihydroorotate dehydrogenase; OMPDC, OMP decarboxylase; OPRT, orotate phosphoribosyltransferase; CDA, cytidine deaminase; UPase, uridine phosphorylase; UPRT, uracil phosphoribosyltransferase; CTPS, CTP synthetase.

1.2.7.2 T. brucei life cycle

Trypanosome life cycle is very complex with two stages in its mammalian host and three stages in the insect (Fig. 24).

As soon as the parasites enter the blood of a mammal (1), they transform into a long slender trypomastigote (2) which is able to divide (3) and is covered by a variable surface glycoprotein (VSG) coat. By changing continuously, this VSG protects the parasite from getting eliminated by the immune system of the host. The parasites are also able to transform into short trypomastigotes which don't divide but that are transmittable to a new tsetse fly. When the tsetse fly takes a blood meal from an infected host (5), *T. brucei* enters in the insect organism and transforms into procyclic form in the guts (6); they replace their VSG coat with a coat of procyclin, start to proliferate and mutate their metabolism in order to use amino acids instead of glucose as energy source. The kinetoplast (which has the same function as the mitochondrion in human beings) increases in size to accommodate for this change. Then, procyclics start to migrate from the midgut to the proboscis transforming into epimastigotes and passing from the food channel to the channel leading to the salivary gland (7). Being a long and difficult process, only 1% of infected tsetse flies get salivary gland infection.

However, in salivary glands, the epimastigotes multiply (8) and, after that, they transform into a non-dividing metacyclic form that acquires a VSG coat. After this last transformation, trypanosomes can be transmitted to another mammal (Matthews, 2005).

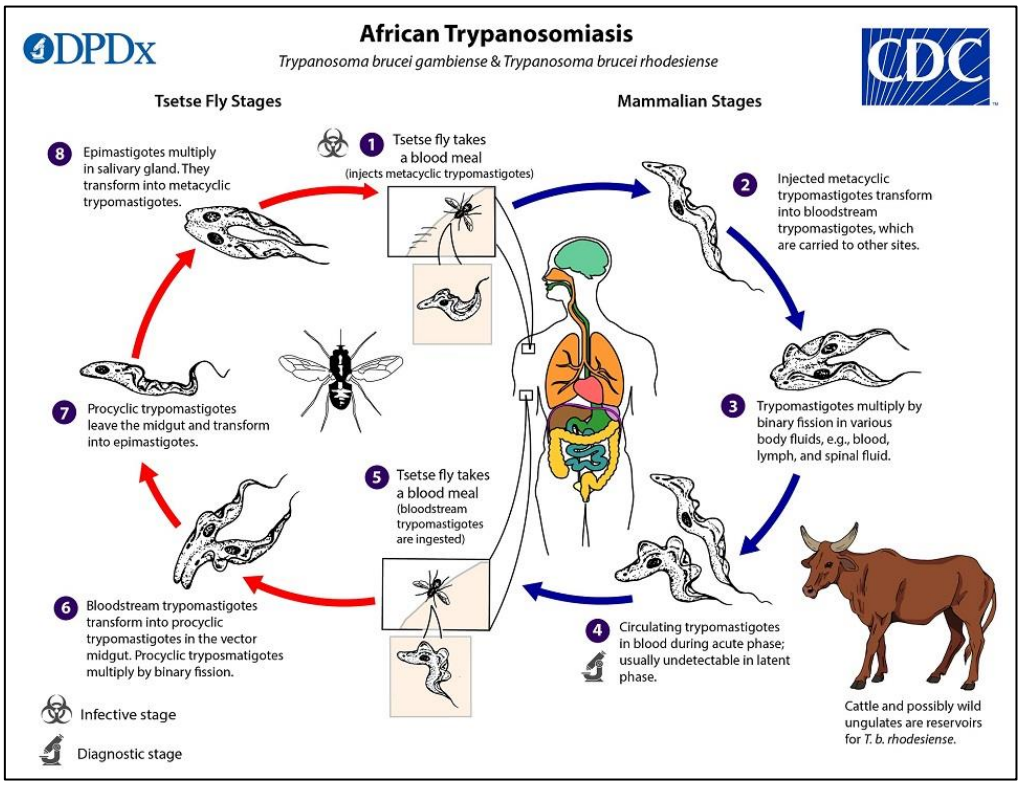

Figure 24. Life cycle of Trypanosoma (CDC, 2019).

The complexity of *T. brucei* life cycle is not surprising in a protozoan which exploits different organisms for its own propagation, since it needs to adapt to several hostile conditions. Procyclic and bloodstream form of the parasite are indeed characterized by different features to better fit to the environment in which they grow. For instance, bloodstream form of *T. brucei* possess a simple tubular mitochondrion with low mitochondrial activity since it has the availability of blood glucose as an abundant source of energy; on the other hand, procyclic trypanosomes are equipped with a more complex and active mitochondrion that is fundamental for energy production and survival of the parasites in the vector guts (Parsons, 2004). Although both procyclic and bloodstream forms of *T. brucei* are harvestable *in vitro*, most drug assays are conducted on bloodstream forms of the parasite, since it is the form in which they are detectable in mammalian hosts.

1.2.8 Current drugs

Since Trypanosome is able to evade the host immune system, a vaccine is not an appropriate approach to the treatment of the disease. For this reason, the research until now has always focused on chemotherapy.

Nevertheless, most of the drugs currently available for HAT treatment are highly toxic and their administration is difficult. Furthermore, parasite resistance is always a risk.

Currently, only six drugs are registered for the treatment of human African trypanosomiasis: pentamidine, eflornithine, nifurtimox, fexinidazole, suramin and melarsoprol (Table 2). However, all of them have a certain level of toxicity.

New WHO treatment guidelines, issued in 2019, divide gHAT and rHAT drugs.

In particular, gHAT therapy comprises pentamidine, eflornithine, nifurtimox and fexinidazole. Pentamidine is administered through intramuscular way and is used in the first phase of the disease; eflornithine and nifurtimox are used in the second phase of HAT. Eflornithine is intravenous while nifurtimox is an oral drug. However, eflornithine can be used alone, while nifurtimox, even if its administration results easier, is useful only in association with eflornithine (NECT therapy). Fexinidazole is used instead both in the first and in the second stage of gHAT.

For rhodesiense trypanosomiasis, suramin and melarsoprol are the preferred drugs, both administered intravenously and useful for the treatment of first and second stages, respectively. Unfortunately, they cause severe side effects including nephrotoxicity, allergic reactions, and encephalopathy (WHO, 2023b).

Table 2. Characteristics of HAT treatments (Papagni et al., 2023).

DRUG	MODE OF ACTION	INDICATION	DOSAGE	ADVERSE EFFECTS	RESISTANCE
Pentamidine	- Prevention of replication and transcription in the kinetoplast and/or in the nucleus - Inhibition of the plasma-membrane Ca2+-ATPase - Collapse of the mitochondrial membrane potential	First stage of gHAT, if fexinidazole is controindicated	4 mg/kg i.m. once a day for 7 days	- Hypotension (if administered iv) - Nausea and vomit - Hyperazotemia - Diabetes mellitus	- Caused by mutations of genes encoding membrane transporters (P2; TbAQP2) - Melarsoprol cross-resistance - Low rate of therapeutic failure
Suramin	Inhibition of various enzymes: dihydropholate reductase, thymidine kinases, glycolytic enzymes, and many others	First stage rHAT	Test dose of S. at 4-5 mg/kg on day 1, followed by injections of 20 mg/kg every 7 days for 5 weeks	Nephrontoxicity, usually reversible	Expression of the variant surface glycoprotein (VSGsur)
Melarsoprol	Formation of toxic adducts with trypanothione and to alteration of the parasite's mitotic processes through action on multiple kinases	- First choice in second stage rHAT - Treatment of recurrent relapse after first-line and rescue treatments of gHAT	2.2 mg/kg iv once daily for 10 days + prednisolone 1 mg/kg for 12 days with dose tapering in the last 3 days	-encephalopathic syndrome - heart failure	- Caused by mutations of genes encoding membrane transporters (P2; TbAQP2) - Pentamidine cross-resistance - High rate of therapeutic failure - The only clinically relevant resistance

Eflornithine	Suicide inhibitor of ornithine decarboxylase (ODC), inhibition of polyamine biosynthesis	Alone only in second-stage gHAT when NECT is not feasible because nifurtimox is unavailable or contoindicated and when fexinidazole cannot be given.	100 mg/kg e.v. every 6 h for 14 days	- Itching - Fever - Headache - Abdominal pain, nausea, vomiting, diarrhea - Myelosuppression	Loss of a membrane transporter for amino acids (TbAAT6)
NECT	Nifurtimox: unknown mechanism, perhaps through the generation of free radicals. Eflornithine: see above	- First choice in severe second stage gHAT - Early second stage gHAT if fexinidazole if contraindicated	Nifurtimox: 5 mg/kg every 8 hours for 10 days. Eflornithine: 200 mg/kg iv every 12 hours for 7 days.	- frequent (>50%) but mild gastrointestinal symptoms - headache	Nifurtimox: probably type 1 nitroreductase mutations possibly cross-resistance with fexinidazole Eflornithine: see above
Fexinidazole	production of reactive amines and other metabolites with toxic effect on trypanosome.	First and early second stage of gHAT (Only if patient is > 6 years and body weight > 20 kg)	body weight >35 kg: loading dose 1800 mg orally for 4 days, then 1200 for 6 days body weight 20-34 kg: loading dose 1200 mg orally for 4 days, then 600 for 6 days	- vomit and nausea - asthenia - prolongation of QT interval	Probably type 1 nitroreductase mutations, possibly cross-resistance with Nifurtimox
Oxaboroles		Both stages of gHAT	Single oral dose		

1.2.8.1 Early-stage drugs

Pentamidine

Pentamidine was registered in 1950 as pentamidine mesylate but has been used against trypanosomiasis and leishmaniasis since 1937 and 1940, respectively. The drug was reevaluated and commercialized in its actual isothionate form in 1984, and in 1987 its effect on *Pneumocystis carinii* was evidenced by Goa and Campoli-Richards (Goa and Campoli-Richards, 1987).

Pentamidine efficacy against *T. b. gambiense* is around 90-95%, while it is very limited for *rhodesiense* infection treatment (Büscher et al., 2017).

The active molecule is an aromatic diamine and its mechanism of action is unknown, but it appears to be taken up and concentrated within microorganisms where it inhibits DNA, RNA and protein synthesis (Wilson et al., 2005). Recent studies revealed that pentamidine uptake occurs by endocytosis with the specific aquaglyceroporin TbAQP2 acting as a high-affinity receptor (Munday et al., 2014; Song et al., 2016).

Pentamidine is not orally well absorbed and is available in aerosol forms (300 mg) under the brand name of Nebupent and as a solution for injection under the name Pentam 300. Pentamidine therapy is well tolerated but some side effects of intravenous therapy can occur, including nausea, abdominal discomfort, dizziness, hypotension, tachycardia, headache, rash, fever, hypoglycemia, hyponatremia; nephrotoxicity and allergic reactions, including Stevens Johnson syndrome were rarely detected (Livertox, 2014).

After the pentamidine discovery, researchers have focused on finding diamines with improved efficacy, oral bioavailability, and BBB penetration. Furamidine showed good *in vitro* and *in vivo* activities on *Trypanosoma*. Unfortunately, it had poor oral bioavailability (Midgley et al., 2007). Furamidine prodrugs were synthesized to overcome this issue. In 2000, the methamidoxime prodrug, parafuramidine, was selected by the consortium for parasitic drug development (CPDD) for clinical development. The first phase of clinical trials, conducted in 2000, was successful. The second lasted 6 years and was conducted on patients at the first stage of the disease. In the end, the third phase aimed to assess the efficacy and safety of the compound compared to pentamidine maleate for the treatment of first-stage sleeping sickness. Unfortunately, although a better safety profile, some renal post-treatment toxicities obliged to stop the development of the drug in 2008 (Pohlig et al., 2016).

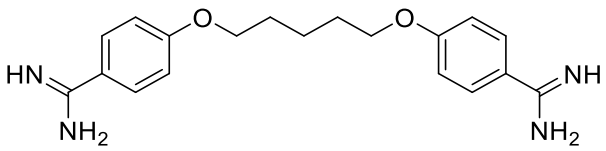

Pentamidine

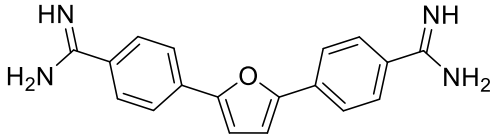

Furamidine

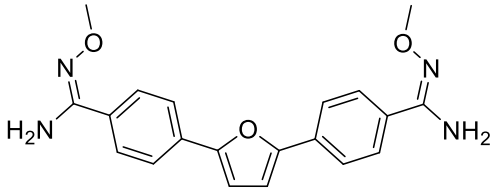

Parafuramidine

Suramin sodium

Suramin is a polysulphonated naphthylamine-based compound discovered by the Bayer pharmaceutical company of Germany. Paul Ehrlich, a major investigator within the synthetic dyestuff industry, described a compound called Trypan blue, which was shown to have trypanocidal properties, but was a coloured dye and thus unacceptable for use in humans. The pharmaceutical industry thus decided to synthesize a completely colorless naphthalene derivative. In 1917 a compound was shown to cure trypanosomiasis in both animal and human individuals. The new molecule was first named Bayer 205 and subsequently given its current name, suramin. Suramin was first used in 1922 (Babokhov et al., 2013).

It is mainly used in *rhodesiense* but is also active on *gambiense* form of the disease. However, it is not used in g*ambiense* therapy because of the high risk of co-infection with onchocerciasis in endemic areas that could lead to allergic reactions due to the rapid killing of the microfilariae (Büscher et al., 2017). In these cases, pentamidine therapy is preferred, being easier and less risky.

Suramin treatment involves five intravenous injections of 20 mg/kg of the drug, every 3–7 days over a total period of 4 weeks. Unfortunately, intravenous injection is the only effective way of getting suramin into the body because of the poor oral bioavailability and of local irritation at the site of injection with intramuscular administration. Once in the blood, it has very long duration of action; it stays in the body for weeks (around 44–54 days) thanks to its 99.7% affinity for serum proteins (Barrett, 2007).

The specificity of Suramin for Trypanosome was attributed to the parasite's enzymes peculiarity; these enzymes were found to have higher (basic) isoelectric points than mammalian cells, and, for this reason, suramin (that is negatively charged) resulted able to bind them preferentially. Glycolytic

enzymes are the most affected, as well as thymidine kinase and dihydrofolate reductase (Bacchi, 2009, Wang et al., 1995). Other trypanosomal enzymes inhibited by suramin are enzymes of the pentose phosphate pathway, e.g., 6-phosphogluconate dehydrogenase. Suramin most likely enters trypanosomes by way of receptor-mediated endocytosis. Vansterkenburg and colleagues hypothesized that suramin exploited its high affinity to serum proteins such as low-density lipoprotein (LDL) to enter *T. b. rhodesiense*'s bloodstream-form parasites (Vansterkenburg et al., 1993); however, in 2002 this theory was disproved by Pal and colleagues, that found out that Suramin and LDL exploited distinct pathways to enter cells (Pal et al., 2002).

The multiple targets mechanism of action of suramin may help to explain the low development of resistance. However, a study published in 2018 has revealed the involvement of VSG in the development of resistance to suramin (Wiedemar et al., 2018).

Suramin's treatment concerns only HAT first stage, since it is unable to pass through the BBB, due to the large size of the molecule, the presence of a number of tight junctions near the endothelial membrane and the lack of transport vesicles. This explains the low concentrations of suramin in the CSF (y1%) when compared to the serum (Babokhov et al., 2013). However, studies in murine models induced with second-stage HAT, showed that the co-administration of suramin with late-stage drugs resulted in higher cure rates in mice. The main hypothesis states that these high cure rates were in part due to the suramin's inhibition of the P-glycoprotein, preventing the expulsion of stage II drugs from the CNS (Sanderson et al., 2007).

Suramin causes some adverse effects such as heavy proteinuria, stomal ulceration, exfoliative dermatitis, severe diarrhea, prolonged high fever, and prostration. Lighter symptoms, which are common, include tiredness, anorexia, malaise, polyuria, increased thirst and tenderness of the palms and soles (WHO, 2002). Hence, the main treatment of the first stage HAT remains pentamidine.

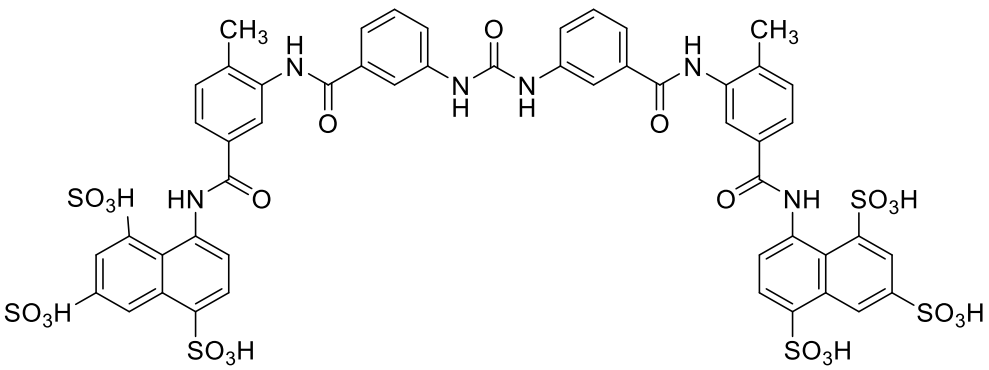

Suramin

1.2.8.2 Late-stage drugs

Melarsoprol

The organic arsenical drug melarsoprol was introduced in 1949 and became the most commonly used treatment against HAT until the introduction of the nifurtimox-eflornithine combination treatment in 2009. This drug is derived from the melamine arsenical melarsen. Melarsen was first synthesized in 1938 in Switzerland. In 1939, an analogue to melarsen called melarsen oxide was synthesized. This synthesis was based on the premise that melarsen oxide (trivalent compound) was a more potent trypanocide than the pentavalent compound from which it was derived. Unfortunately, it showed higher toxicity. To reduce the toxic effects, a disulfide chelating agent was added (dimercaprol or British 'anti-Lewisite' (BAL)) to mitigate the arsenical group's negative effects. Melarsoprol was the resulting compound, and it was found to be less toxic and still potent (Babokhov et al., 2013).

Melarsoprol has been used in the treatment of confirmed second stage cases of *T. b. gambiense* or *T. b. rhodesiense*. Relapse occurs in less than 5% of cases, however, in certain endemic areas, the rate of relapses is much higher (up to 20%). Because of the occurrence of occasional drug-induced fatalities, only hospitals and specialized treatment centers are allowed to administer melarsoprol (Babokhov et al., 2013).

Moreover, melarsoprol is not homogeneously absorbed from the gastrointestinal tract and its vehicle is too irritant for intramuscular administration: being insoluble in water, it must be dissolved in propylene glycol, which is highly irritating to tissues. As a result, the administration of melarsoprol is exclusively intravenous and very painful. However, the compound is liposoluble and for this reason can cross the BBB (Nok, 2003). It enters the CNS in sufficiently high quantities to kill the trypanosomes and it is largely metabolized to nontoxic pentavalent compounds.

The specific trypanocidal mechanisms of melarsoprol are currently unknown but some studies suggest inhibition of the trypanosomal enzymes pyruvate kinase, phosphofructokinase, fructose-2,6-bisphosphatase and trypanothione reductase (Denise et al., 1999).

Also, the bloodstream forms of trypanosomes are highly dependent on glycolytic and redox processes and any dysregulation of these factors may lead to cell lysis due to lack of ATP. Other studies report that melarsoprol uptake takes place through the purine nucleotide transporter P2 and arsenical-resistant trypanosomes lack those transporters (Carter and Fairlamb, 1993).

Melarsoprol causes a variety of adverse reactions, but the most serious is post-treatment reactive encephalopathy (PTRE) with seizures, high fever, headaches, nausea, vomiting and dizziness. The exact causes of PTRE are currently unknown, but one possible explanation is the presence of

propylene glycol in the treatment mixture (Balasegaram et al., 2009). The incidence of this complication varies from 1.5% to 28% of all melarsoprol treatments, with a median associated fatality rate of 50% (Seixas, 2005).

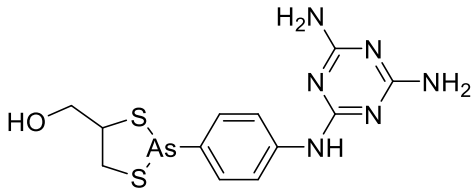

Melarsoprol

Eflornithine

Eflornithine (diethylfluoromethylornithine or DFMO), initially evaluated for the treatment of cancer, is an antitrypanosomal monotherapy introduced in 1990 for the treatment of second-stage human African trypanosomiasis.

Its antitrypanosomal properties were first observed by biologist Cyrus Bacchi in 1980. He demonstrated that eflornithine was able to cure *T. b. brucei* infected mice with no signs of side effects. DFMO was then subjected to extensive human clinical trials in Africa.

The drug has a trypanostatic effect inhibiting the parasite's ornithine decarboxylase (ODC), an enzyme needed for the synthesis of polyamines, themselves involved in cell multiplication and differentiation (Priotto et al., 2008). Eflornithine was found to be effective only on *T. b. gambiense* and not on *rhodesiense*. The most likely reason for this selectivity is that *T. b. rhodesiense* has a very rapid ODC turnover rate (about 4.3 hours), making the drug less able to inhibit ODC activity (Babokhov et al., 2013).

Eflornithine was a great discovery because of its better activity against *T. b. gambiense* when compared to melarsoprol. Additionally, the new drug seemed to have a lower fatality rate, i.e. 1.4% versus up to 5% for melarsoprol (Bacchi, 2009).

DMFO has several disadvantages too. First of all, the treatment is time-consuming and complex. The mean half-life of eflornithine is between 1.5 and 5 hours and 80% of it is excreted in the urine in its unaltered form 24 hours post-injection. Moreover, there is little protein binding to eflornithine in the plasma indicating that prolonged intravenous infusion is needed to keep the drug actively working during the treatment process. The 14-day slow infusion was found to be the only effective way to administer eflornithine. The standard administration of DMFO involves 56 intravenous infusions at 100 mg/kg for adults and 150 mg/kg for children every 6 hours for 7 days. Another additional

disadvantage of eflornithine is that its penetration of the BBB is more limited than previously thought (Babokhov et al., 2013).

Since the drug has a trypanostatic activity it also needs a functional immune system to be effective, which means that it is ineffective on HIV/AIDS affected patients (or other immune-suppressive diseases).

DMFO is generally a safe drug; the most common adverse effects detected include diarrhoea, anaemia, leukopenia, thrombocytopenia, and convulsions. Impaired hearing has also been reported. Less commonly, vomiting, anorexia, alopecia, abdominal pain, headache, facial oedema, eosinophilia, and dizziness have occurred. These effects are reversible on withdrawal of the drug (Coin Jr, 2001).

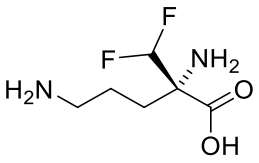

Eflornithine

NECT

HAT chemotherapy research progressed with the introduction of nifurtimox-eflornithine combination therapy (NECT), which is currently the first line for the treatment of second-stage HAT.

The therapy is strongly recommended by WHO and has been included in the WHO Essential Medicine List in 2009.

Nifurtimox is a 5-nitrofuran derivative developed by Bayer in 1960 and registered for Chagas disease therapy in 1967. It has been successfully used for the treatment of melarsoprol-refractory *T. b. gambiense* infection.

Its mechanism of action is unknown, but its activity relies on the membrane and DNA binding of free radicals generated by nitrofuran reduction (Bisser et al. 2007). Nitroreductases (NTR) and trypanothione reductases are the enzymes involved.

Unfortunately, the impairment of type I nitroreductase in *T. cruzi* conferred resistance to nifurtimox (Wilkinson et al., 2008). Additionally, its activity against trypanosomal infections showed limits against late-stage HAT because of the low concentration in the CNS compared to the plasma (Bisser et al., 2007).

However, compared to other treatments, NECT has been an improvement in HAT therapy's research because of the lower costs and the easier administration: the treatment consists of three daily oral

doses of nifurtimox for a total of 10 days and 14 infusions of eflornithine for a total of 7 days. This was significantly lower than the 56 doses over 14 days required for the eflornithine treatment. Medical personnel previously trained for eflornithine administration could use the combination treatment much faster and more efficiently. A single NECT kit weighs 30 kg, has a volume of 100 dm^3, is useful for four treatments and costs 288€ for a single treatment, instead of 554€ corresponding to the estimated cost of a single treatment with eflornithine (Babokhov et al., 2013).

There are side effects such as vomiting, nausea, headaches, abdominal pain, joint pains, seizures, and insomnia. Fortunately, they are less severe than the ones caused by previous drugs.

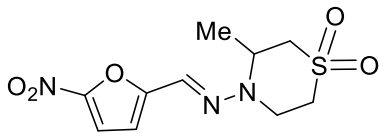

Nifurtimox

Fexinidazole

Fexinidazole is a 5-nitroimidazole derivative first discovered by Hoechst AG (now part of Sanofi) and identified by the Drugs for Neglected Diseases initiative (DNDi) in 2005 as having activity against *T. b. gambiense* and *T. b. rhodesiense*.

In 2010, Torreele and colleagues conducted a study to assess the *in vitro* and *in vivo* antitrypanosomal activities of fexinidazole and its metabolites fexinidazole sulphoxide and fexinidazole sulphone (Torreele et al., 2010).

Fexinidazole and its metabolites showed moderate activities *in vitro* against *T. b. gambiense* and *T. b. rhodesiense* with an IC_{50} value ranging from 0.16 and 0.93 µg/mL. They also showed no cytotoxicity on L-6 rat myoblast cells with $IC_{50} > 90$ µg/mL and a selectivity index always above 97. Fexinidazole showed an almost similar activity to eflornithine and nifurtimox but was less active compared to melarsoprol and pentamidine ($IC_{50} = 0.003$ µg/mL). The best feature of fexinidazole is its good absorption with absolute oral bioavailability of 41, 30 and 10% in mice, rats, and dogs, respectively (Torreele et al., 2010).

Phase I clinical trials were performed in 2011 and 1800 mg/day was the suitable dose for the first 4 days and 1200 mg/day for 6 other days. Based on these results, the phase II/III trials started in 2012 on stage II *gambiense* HAT patients compared to NECT.

Between October 2012 and November 2016, more than half a million people were screened to identify 419 pre-screened patients. Of these, ten (2%) patients were not eligible. Of the 409 eligible patients, 15 patients were not included because they did not meet all inclusion criteria. Therefore, 394 patients were randomly assigned, 264 of whom were assigned to fexinidazole and 130 to nifurtimox eflornithine combination therapy. After 18 months of observation, fexinidazole was 7% less successful than the NECT (91% *vs* 98%) (Mesu et al., 2018).

The 7% deficit of efficacy compared with nifurtimox-eflornithine combination therapy was likely to be more than compensated by increased access to treatment, especially in remote or unstable settings: home-based treatment is an attractive and cost-saving option for both the patients and the health system. Fexinidazole can also contribute to simplifying the diagnostic approach. Results of a parallel study run by the same investigators assessing fexinidazole in 230 patients with stage 1 or early stage 2 g-HAT were presented in 2017 at the 10th European Congress on Tropical Medicine and International Health, showing high efficacy (>98% success rate at 18 months), and adequate safety. Since fexinidazole works in both disease stages, lumbar puncture for CSF examination (an invasive procedure disliked by patients and communities) is no longer necessary (Chappuis, 2018).

Because of the good results in phase III clinical trials, fexinidazole has been granted a positive opinion by the EMA in November 2018 under Article 58 of Regulation (EC) no. 726/2004 (a regulatory

mechanism for reviewing new medicines destined for use outside of the EU), for the treatment of both the first stage and second stage of gHAT in adults and children aged ≥ 6 years and weighing ≥ 20 kg (Deeks, 2019). This positive opinion facilitated and supported marketing authorization applications in endemic countries such as the Democratic Republic of Congo, where the drug was approved on January 2019; after that, on July 2019, WHO added Fexinidazole to the Essential Medicines List (DNDi, 2019).

The discovery of Fexinidazole is certainly a revolutionary step for the Neglected Disease's research, but it is still not sufficient. Despite the drug can help to eradicate HAT in poor areas, it still holds some critical drawbacks making the need for safer drugs urgent.

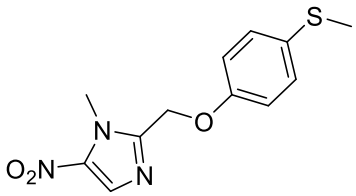

Fexinidazole

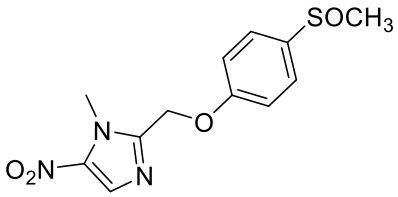

Fexinidazole sulfoxide

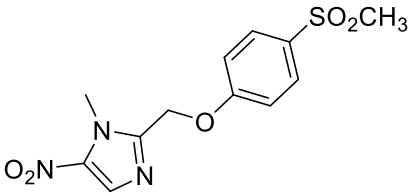

Fexinidazole sulfone

Acoziborole – SCYX-7158

A screening of benzoxaboroles conducted by Anacor Pharmaceuticals led to the identification of SCYX-7158 (Acoziborole) that was optimized by Scynexis and seemed to have parasitical activity against *T. b. gambiense*. It was found to be effective in *in vitro* trypanocidal assays and it seemed to have interesting physicochemical and ADME properties. In animal models of HAT, SCYX-7158 exhibited significant activity following oral administration of 7 days at a dose of 25 mg/kg. The *in vivo* pharmacokinetic characterization of SCYX-7158 revealed that this compound can cross the BBB to achieve therapeutically relevant concentrations in the brain and cerebrospinal fluid. Acoziborole enters the parasite cells and is metabolized into the SCYX-3109 diol through oxidative deboronation. The diol has the nuclear-localized cleavage and polyadenylation specific factor 3 (CPSF3) as target, an mRNA processor (Wall et al., 2018; Jacobs et al., 2011). CSPF3 is an important parasitic factor because of its involvement in the pre-mRNA cleavage before poly(A) tail coupling (Dominski et al., 2005; Mandel et al., 2006).

Based on these properties, SCYX-7158 has been selected to enter IND-enabling preclinical studies and it entered in phase I clinical trials in 2011 (Jacobs et al., 2011).

The Phase I study, conducted in France, assessed the safety, tolerability, pharmacokinetics, and pharmacodynamics of SCYX-7158 after single oral ascending doses in 128 healthy human volunteers of sub-Saharan origin. It allowed for the therapeutic dose to be determined at 960 mg administered once as three tablets, with a good safety profile. As the drug has a long half-life (400 hours), the study was extended to ensure extensive safety monitoring of the healthy volunteers up to 210 days. Phase I results confirm that the drug enters the CNS, a pivotal advantage for the treatment of the late stage of the disease. Based on the outcomes of this study, DNDi and partners decided to proceed to Phase IIb/III in 2016 in the Democratic Republic of the Congo (DRC), which is the most affected country (News medical, 2015). Currently the drug has progressed phase III trials (Jamabo et al., 2023).

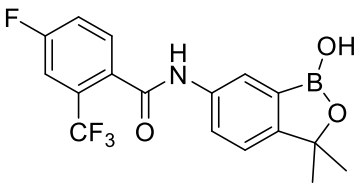

Acoziborole - SCYX-7158

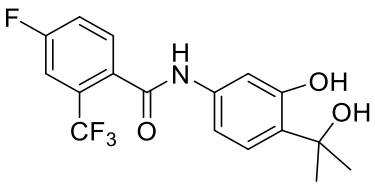

SCYX-3109

1.2.9 Treatment issues

HAT therapy is hindered by many factors. First, the impossibility of formulating a vaccine, which would be the first line approach for a disease of this extent, greatly limits the treatment. Unfortunately, due to the wide spread of the disease and the characteristic continuously changing VSG of the parasite, a vaccine would become almost immediately obsolete. For this reason, the research efforts are restricted to vector control, chemoprophylaxis, and chemotherapy. Even in chemotherapy, as already mentioned, constraints are not neglectable: side effects, high costs and administration issues are important challenges that need to be faced. Moreover, social and cultural discrepancies strongly influence the compliance of patients being treated; a decreased compliance was noticed in parasitic diseases treated patients. Basically, patients don't follow dosages, schedules and administration guidelines and result in inefficacy of the therapy, preferring being cured with traditional local remedies, that are often more easily affordable and potentially efficacious but not properly developed and studied (Tagboto and Townson, 2001). The massive and incorrect use of trypanocides over time also generates genome mutations in the parasite, because of the significant selection pressure put on drug-targeted trypanosome genes. This relentlessly results in resistance development, which represents another obstacle to the eradication of trypanosomiasis. The lack of new accessible drugs in the last 50 years has led to the abuse of the available drugs, resulting in the emergence of drug-resistances and consequent inefficacy of the therapies (Giordani et al., 2016). Specifically, trypanosomes already demonstrated resistance towards suramin, nifurtimox, eflornithine, melarsoprol, and pentamidine. Melarsoprol and diamidines resistances are related to the loss of P2 transporters activity, a class of aminopurine transporters encoded by the *Tb*AT1 gene (Munday et al., 2015; de Koning, 2020). Diamidines resistance is also strengthened by deletions, mutations, and chimeric rearrangements of *Tb*AQP2 and *Tb*AQP3 genes (Quintana et al., 2020). On the other hand, nifurtimox and eflornithine resistances are due to single point mutations of nitroreductase enzymes' genes (NTRs) and *Tb*AAT6 gene, respectively, while trypanosomes endurance to suramin is caused by loss of function of the surface suramin receptor (ISG75) present on the parasites VSG (Wilkinson et al., 2008; Vincent et al., 2010; Zoltner et al., 2015; Wyllie et al., 2016).

1.2.10 Natural products: a source for drug candidates

Treatment complexity led the researchers to explore new and innovative alternatives to synthetic and traditional chemotherapy. Natural matrices have been thoroughly investigated in the last 30 years as sources for new drug candidates, giving promising results. Antiparasitic activity of natural products has raised great interest in current research. In a review from Kayser and colleagues, the antiparasitic potential of different classes of plant-derived products was highlighted (Kayser et al., 2003). Alkaloids, terpenes and phenolics were identified and extensively investigated through both *in vitro* and *in vivo* studies.

Among alkaloids, a class of very active but also toxic compounds, some products demonstrated good antiprotozoal activity. Fournet and colleagues (Fournet et al., 1993a; Fournet et al., 1993b), isolated a series of 2-substituted quinolines (**1**-**6** Fig. 25) and tested it against *Leishmania amazonensis* (the causative agent of cutaneous leishmaniasis) both *in vivo* and *in vitro*, with resulting EC_{50} values of 25-50 µg/mL and a good efficacy in mice with 100 mg/kg/day dosages over 14 days. Antiprotozoal quinolines came from different families such as Annonaceae, Berberidaceae, Menispermaceae and Hernandiaceae; berberine and its derivatives demonstrated to be the most promising candidates as antiparasitic alkaloids (**7** Fig. 25). Berberine was tested against various subspecies of *Leishmania*, and even some derivatives of the molecule were tested not only on *Leishmania* but also on *Trypanosoma* genus, showing encouraging results (El-On et al., 1988; Vennerstrom et al., 1990). Dioncophyllaceae as well demonstrated to be good sources of antiparasitic products, with dioncophylline B and C (**8** and **9** Fig 25), both exerting considerable antiplasmodial, antileishmanial, and antitrypanosomal activity (Francois et al., 1997a; Francois et al., 1997b).

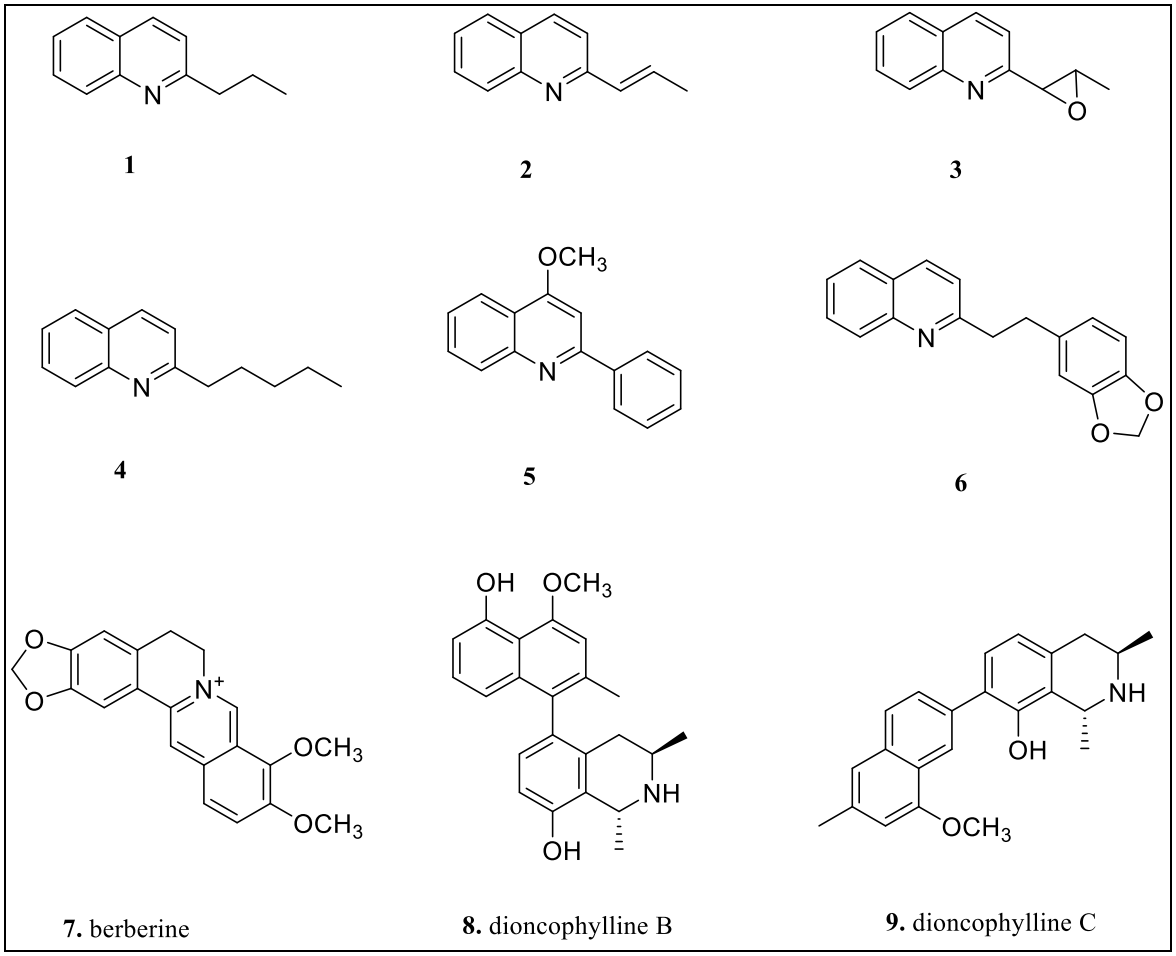

Figure 25. Structures of the main antiparasitic alkaloids.

Another promising class of compounds that can be employed in antiparasitic treatments is that of terpenes. The discovery of the antimalarial Artemisinin (**1** Fig. 26), extracted and isolated from *Artemisia annua* L. (Asteraceae), paved the way for the study of other bioactive terpenes; axisonitrile (**2** Fig. 26) was isolated from the sponge *Acanthella klethra* Pulitzer-Finali, and resulted active against malaria without showing cytotoxicity (Angerhofer et al., 1992). Tanshinones (**3-6** Fig. 26) were isolated from iranian *Perovskia abrotanoides* Kar. and exhibited both antileishmanial and antimalarial activities with IC_{50} values ranging from 5 to 47 mM (Sairafianpour et al., 2001).

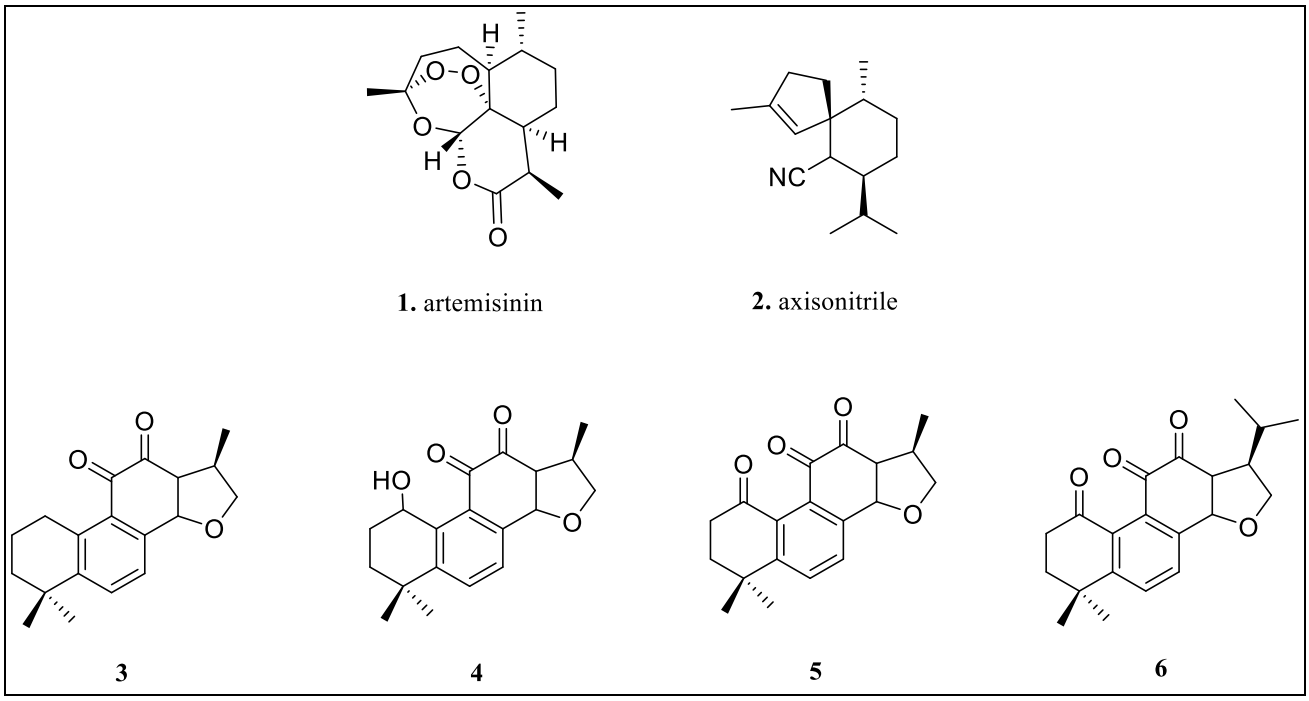

Figure 23. Structures of the main antiparasitic terpenes.

Flavonoids are another class of plant secondary metabolites characterized by a great antiparasitic potential. After the discovery of the synergistic activity of artemetin and casticin (**1** and **2** Fig. 27) with artemisinin, there was a growing interest in studying this class of compounds for antiprotozoal purposes (Elford et al., 1987). A review from Fotie (2008), highlighted the crucial role that flavonoids acquired in those years describing the antimalarial, antileishmanial, antitrypanosomal and antiamebial properties of many plant-derived flavonoids (Fotie, 2008).

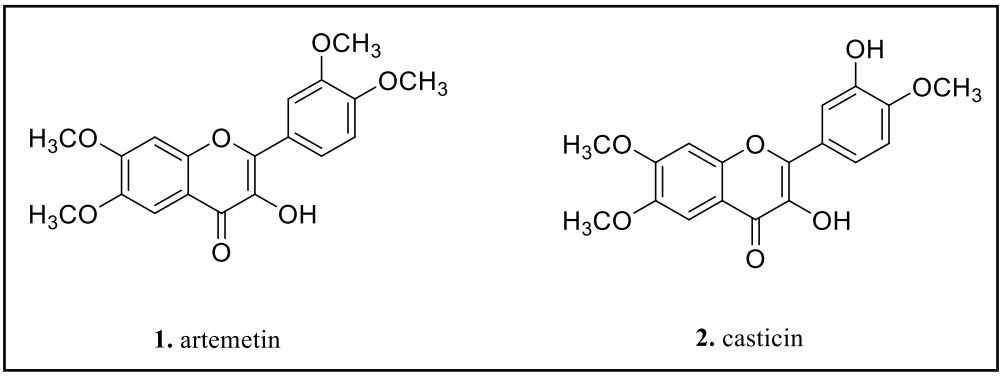

Figure 27. Structures of flavonoids exerting a synergistic activity together with artemisinin.

Concerning trypanosomiasis, treatment with natural products gained an important role in the last decades. Some studies highlighted the promising antitrypanosomal activity of African flora. A review from Ungogo and colleagues, underlined the potential of Nigerian plants for the treatment of protozoal diseases and spotted many active compounds against trypanosomiases derived from flora of the interested areas; terpenes, quinones, flavonols, peptides and glycosides were identified as

efficient antitrypanosomal agents, likely to be studied as new promising lead compounds (Ungogo et al., 2020). Other studies demonstrated the potential of Cameroonian flora and in particular of plants traditionally used as medicinal remedies from local populations. Essential oils (EOs) from *Azadirachta indica* A. Juss., *Aframomum melegueta* K. Schum., *Aframomum daniellii* (Hook) K. Schum., *Clausena anisata* (Willd.) Hook.f., *Dichrostachys cinerea* L. Wight & Arn, *Echinops giganteus* A. Rich., and *Erigeron floribundus* (Kunth) Sch.Bip. were obtained through hydrodistillation and tested against protozoan parasites. The selected plants, widely used to treat several disorders including microbial and parasitic diseases, resulted to be good sources of active compounds against *T. brucei* with a noticeable selectivity, not affecting mammalian cells in *in vitro* tests (Petrelli et al., 2016; Ngahang Kamte et al., 2017). Apiaceae and Asteraceae families revealed to be great sources of antiprotozoal compounds. In a study from Herrmann and colleagues, the main polyacetylene constituting *Carlina acaulis* L., carlina oxide, demonstrated a potent antitrypanosomal and antimicrobial activity accounting for a significantly low EC_{50} value (around 1.0 µg/mL) when compared to the total hexane extract (3.7 µg/mL) (Herrmann et al., 2011). The asteracea *Tithonia diversifolia* (Hemsl) A. Gray. as well, appeared to be a promising source of antitrypanosomal candidates: Sut and colleagues demonstrated that the activity of its methanolic extract was due to the presence of tagitinins and specifically of tagitinin C, which exerted an extraordinary activity, with an EC_{50} value that fell in the nanogram per mL range (4.2 ng/mL) (Sut et al., 2018). Regarding the Apiaceae family, Kamte and colleagues conducted a study on EOs obtained from nine different plants from this family, namely *Siler montanum* Crantz, *Sison amomum* L., *Echinophora spinosa* L., *Kundmannia sicula* (L.) DC., *Crithmum maritimum* L., *Helosciadium nodiflorum* (L.) W.D.J., *Pimpinella anisum* L., *Heracleum sphondylium* L., and *Trachyspermum ammi* (Lindl.) Lem. Results showed that five of the nine tested EOs had significant activity against the parasite with EC_{50} values ranging from 2 to 10 µg/mL (Kamte et al., 2018). A further interesting antitrypanosomal source among the Apiaceae plants, is identifiable in *Smyrnium olusatrum* L. The crop demonstrated a significant antiprotozoal potential with a good safety profile and its main component, isofuranodiene, was identified as the direct responsible of the activity (EC_{50}= 3.0 µg/mL) (Petrelli et al., 2017).

1.3 Aim of the work

Taking into account all the above-mentioned recent studies and the criticalities of current treatments, our research focused on two different approaches. First, we carried out wide-range research that included plants already exploited for their importance in traditional medicine or for other pharmacological and industrial uses. In this regard, we identified *Anthriscus nemorosa* (M.Bieb.) Spreng. and *Cannabis sativa* L., as potential promising sources for antitrypanosomal products. From

these two sources, we obtained both volatile and non-volatile extracts. We then endeavored to isolate the pure compounds and prepared blends to recreate complex mixtures. We aimed to mimic the activity of the total extracts while excluding components that might hinder efficiency.

An attempt of formulation was also performed by preparing nanoemulsions of the essential oil derived from the aerial parts of *A. nemorosa*. The second approach is a synthetic approach, based on a selection of molecules that already showed biological significance but considerably differing from drugs approved for antitrypanosomal use. Hence, the aim was to identify new scaffolds never employed in antiparasitic therapies, in order to avoid resistance phenomena as much as possible. Thus, three series of pyrazolone-base hydrazones were developed and from the most promising candidates metal complexes were synthesized. For the most active molecules, the mechanism of action was investigated through different tests in order to assess cross-resistance, reversibility, and trypanocidal or trypanostatic activity. Additionally, nucleotide metabolism was studied through an indirect HPLC assay, which allowed the identification of a possible enzymatic target.

1.3 References

Abdi, R.D., Agga, G.E., Aregawi, W.G. (2017). A systematic review and meta-analysis of trypanosome prevalence in tsetse flies. BMC Veterinary Research, 13, 100.

Abro, Z., Kassie, M., Muriithi, B., Okal, M., Masiga, D., Wanda, G., Gisèle, O., Samuel, A., Nguertoum, E., Nina, R.A., Mansinsa, P., Adam, Y., Camara, M., Olet, P., Boucader, D., Jamal, S., Issa Garba, A.R., Ajakaiye, J.J., Kinani, J.F., Hassan, M.A., Nonga, H., Daffa, J., Gidudu, A., Chilongo, K. (2021). The potential economic benefits of controlling trypanosomiasis using waterbuck repellent blend in sub-Saharan Africa. Plos one, 16 (7), e0254558.

Akiyoshi, B., Gull, K. (2013). Evolutionary cell biology of chromosome segregation: insights from trypanosomes. Open Biology, 3, 130023-133029.

Angerhofer, C.K., Pezzuto, J.M., Konig, G.M., Wright, A.D., Sticher, O. (1992). Antimalarial activity of sesquiterpenes from the marine sponge *Acanthella klethra.* Journal of Natural Products, 55, 1787–1789.

Babokhov, P., Sanyaolu, A.O., Oyibo, W.A., Fagbenro-Beyioku, A.F., Iremeniam, N.C. (2013). A current analysis of chemotherapy strategies for the treatment of human African trypanosomiasis. Pathogens and Global Health, 107, 242-252.

Bacchi, C.J. (2009). Chemotherapy of Human African Trypanosomiasis. Interdisciplinary Perspective in Infective Diseases, 195040-195045.

Balasegaram, M., Young, H., Chappuis, F., Priotto, G., Raguenaud, M.E., Checchi, F. (2009). Effectiveness of melarsoprol and eflornithine as first-line regimens for gambiense sleeping sickness in nine Medecins Sans Frontieres programmes. Royal Society of Tropical Medicine and Hygiene, 103, 280–290.

Barrett, M.P., Boykin, D.W., Brun, R., Tidwell, R.R. (2007). Human African trypanosomiasis: pharmacological re-engagement with a neglected disease. British Journal of Pharmacology, 152, 1155–71.

Barrett, M.P., Burchmore, R.J., Stich, A., Lazzari, J.O., Frasch, A.C., Cazzulo, J.J., Krishna, S. (2003). The trypanosomiases. The Lancet, 362(9394), 1469-1480.

Bisser, S., N'Siesi, F. X., Lejon, V., Preux, P. M., Van Nieuwenhove, S., Miaka Mia Bilenge, C., Büscher, P. (2007). Equivalence trial of melarsoprol and nifurtimox monotherapy and combination

therapy for the treatment of second-stage *Trypanosoma brucei gambiense* sleeping sickness. The Journal of Infectious Diseases, 195, 322–329.

Bonnet, J., Boudot, C., Courtioux, B. (2015). Overview of the Diagnostic Methods Used in the Field for Human African Trypanosomiasis: What Could Change in the Next Years? BioMed Research International, 2015, 583262.

Borst, P., Fase-Fowler, F., Gibson, W.C. (1987). Kinetoplast DNA of *Trypanosoma evansi*. Molecular and Biochemical Parasitology, 23, 31–38.

Broden, A. (1904). Les infections à trypanosomes au Congo chez l'homme et les animaux (communication préliminaire). Bulletin de la Société Belge d'Études Coloniales, 11,116-139.

Brun, R. (1999) Sleeping sickness in Africa – on the rise again. Karger Gazette 63, 5-7.

Brun, R., Blum, J., Chappuis, F., Burri, C. (2010). Human African trypanosomiasis. Lancet, 375,148–59.

Brun, R., Hecker, H., Lun, Z.-R. (1988). *Trypanosoma evansi* and *T. equiperdum*: Distribution, Biology, Treatment and Phylogenetic Relationship (a Review). Veterinary Parasitology, 79, 95–107.

Brun, R., Lun, Z.R. (1994). Drug sensitivity of Chinese *T. evansi* and *T. equiperdum* isolates. Veterinary Parasitology, 52, 37–46.

Bukachi, S.A., Wandibba, S., Nyamongo, I.K. (2017). The socio-economic burden of human African trypanosomiasis and the coping strategies of households in the South Western Kenya foci. PLoS Neglected Tropical Diseases, 11(10), e0006002.

Büscher, P., Cecchi, G., Jamonneau, V., Priotto, G. (2017). Human African trypanosomiasis. The Lancet ,390, 2397-2409.

Carter, N.S., Fairlamb, A.H. (1993). Arsenical-resistant trypanosomes lack an unusual adenosine transporter. Nature 14, 173-176.

CDC (2019). Life cycle of *Trypanosoma* spp. Available from: http://www.cdc.gov/dpdx/trypanosomiasisAfrican/index.html.

Cecchi, G., Paone, M., Feldmann, U., Vreysen, M.J., Diall, O., Mattioli, R.C. (2014). Assembling a geospatial database of tsetse-transmitted animal trypanosomosis for Africa. Parasites & Vectors, 7(1), 1-10.

Chappuis, F. (2018). Oral fexinidazole for human African trypanosomiasis. The Lancet, 391, 100-102.

Chin, S.W., Uppal, P.K., PremaAlatha, B., Chandrawathani, P., Norazura, A.H., Ramlan M. (2013). Freedom status of dourine (*Trypanosoma equiperdum*) in Malaysia. Malaysian Journal of Veterinary Research, 4(2), 61–64.

Claes, F., Büscher, P., Touratier, L., Goddeeris, B.M. (2005). *Trypanosoma equiperdum*: master of disguise or historical mistake? Trends Parasitology, 21(7), 316–321.

Cox, F. (2004). History of sleeping sickness (African trypanosomiasis). Infectious Disease Clinics of North America, 18, 231-245.

Coyne Jr, P.E. (2001). The eflornithine story. Journal of the American Academy of Dermatology, 45(5), 784-786.

Dagnachew, S., Bezie, M. (2015). Review on *Trypanosoma vivax*. African Journal of Basic & Applied Sciences, 7(1), 41-64.

De Koning, P.H. (2020). The drugs of sleeping sickness: their mechanisms of action and resistance, and a brief history. Tropical Medicine and Infectious Disease, 5, 14.

Deeks, D. E. (2019). Fexinidazole. First Global approval. Spring Nature Switz. 29, 215-220.

Denise, H., Giroud, C., Barrett, M.P., Baltz, T. (1999). Affinity chromatography using trypanocidal arsenical drugs identifies a specific interaction between glycerol-3-phosphate dehydrogenase from *Trypanosoma brucei* and Cymelarsan. European Journal of Biochemistry, 259, 339-346.

Desquesnes, M., Gonzatti, M., Sazmand, A., Thévenon, S., Bossard, G., Boulangé, A., Gimonneau, G., Truc, P., Herder, S., Ravel, S., Sereno, D., Jamonneau, V., Jittapalapong, S., Jacquiet, P., Solano, P., Berthier, D. (2022). A review on the diagnosis of animal trypanosomoses. Parasites & Vectors, 15(1), 1-24.

Desquesnes, M., Holzmuller, P., Lai, D.-H., Dargantes, A., Lun, Z.-R., Jittaplapong, S. (2013). *Trypanosoma evansi* and Surra: A Review and Perspectives on Origin, History, Distribution, Taxonomy, Morphology, Hosts, and Pathogenic Effects. BioMed Research International, 2013, 194176.

DeVisser, M.H., Messina, J.P., Moore, N.J., Lusch, D.P., Maitima, J. (2010). A dynamic species distribution model of *Glossina* subgenus *Morsitans*: The identification of tsetse reservoirs and refugia. Ecosphere, 1 (1), 1-21.

DNDi (2019). https://www.dndi.org/2019/media-centre/press-releases/fexinidazole-sleeping-sickness-approved-democratic-republic-congo/

Dominski, Z., Yang, X., Marzluff, W.F. (2005). The Polyadenylation Factor CPSF-73 Is Involved in Histone-Pre-mRNA Processing. Cell, 123, 37–48.

Donelson, J.E., Gadner, M.J., El-Sayed, N.M. (1999). More surprises from Kinetoplastida. Proceedings of the National Academy of Sciences, 96, 2579-2581.

Eberhardt, A.T., Monje, L.D., Zurvera, D.A., Beldomenico, P.M. (2014). Detection of *Trypanosoma evansi* Infection in Wild Capybaras from Argentina Using Smear Microscopy and Real-Time PCR Assays. Veterinary Parasitology, 202, 226–233.

Elford, B.C., Roberts, M.F., Phillipson, J.D., Wilson, R.J. (1987). Potentiation of the antimalarial activity of qinghaosu by methoxylated flavones. Transactions of the Royal Society of Tropical Medicine and Hygiene, 81, 434–436.

El-On, J., Jacobs, G.P., Weinrauch, L. (1988). Topical chemotherapy of cutaneous leishmaniasis. Parasitology Today, 4, 76–81.

Eperon, G., Balasegaram, M., Potet, J., Mowbray, C., Valverde, O., Chappuis, F. (2014). Treatment options for second-stage gambiense human African trypanosomiasis. Expert Review of Anti-Infective Therapy, 12 (11), 1407–1417.

Fotie, J. (2008). The antiprotozoan potential of flavonoids. Pharmacognosy Reviews, 2(3), 6.

Fournet, A., Barrios, A.A., Munoz, V., Hocquemiller, R., Cave, A., Bruneton, J. (1993a). 2-substituted quinoline alkaloids as potential antileishmanial drugs. Antimicrobial Agents and Chemotherapy, 37, 859–863.

Fournet, A., Hocquemiller, R., Roblot, F., Cave, A., Richomme, P., Bruneton, J. (1993b). Effects of some bisbenzylisoquinoline alkaloids on American Leishmania sp. in BALB/c mice. Phytotherapy Research, 7, 281-284.

Franco, J.R., Simarro, P.P., Diarra, A.; Jannin, J.G. (2014). Epidemiology of human African trypanosomiasis. Clinical Epidemiology, 6, 257-275.

Francois, G., Timperman, G., Elling, W., Assi, L.A., Holenz, J., Bringmann, G. (1997a). Naphthylisoquinoline alkaloids from *Triphyophyllum peltatum*, *Ancistrocladus abbreviatus* and *Ancistrocladus barteri* against *Plasmodium berghei* (Anka strain) *in vivo*. Journal of Ethnopharmacology, 46, 115–120.

Francois, G., Timperman, G., Elling, W., Assi, L.A., Holenz, J., Bringmann, G. (1997b). Naphthylisoquinoline alkaloids against malaria: evaluation of the curative potentials of dioncophylline C and dioncopeltine A against *P. berghei in vivo*. Antimicrobial Agents and Chemotherapy, 41, 2533–2539.

Gamba, D.O., Olet, P.A., Maichomo, M.W., Korir, S.M., Kiteto, I.N. (2021). Role of Kenya Tsetse and Trypanosomiasis Eradication Council (KENTTEC) in Control of African Animal Trypanosomiasis (AAT)/Nagana. In Combating and Controlling Nagana and Tick-Borne Diseases in Livestock, IGI Global, 73-94.

Gashururu, S.R., Maingi, N., Githigia, S.M., Gasana, M.N., Odhiambo, P.O., Getange, D.O., Habimana, R., Cecchi, G., Zhao, W., Gashumba, J., Bargul, J.L., Masiga, D.K. (2021). Occurrence, diversity, and distribution of *Trypanosoma* infections in cattle around the Akagera National Park, Rwanda. PLoS neglected tropical diseases, 15(12), e0009929.

Geiger, A., Cuny, G., Frutos, R. (2005). Two Tsetse Fly Species, *Glossina palpalis gambiensis* and *Glossina morsitans morsitans*, Carry Genetically Distinct Populations of the Secondary Symbiont *Sodalis glossinidius*. Applied and Environmental Microbiology, 71, 8941-8943.

Giordani, F., Morrison, L.J., Rowan T.I.M.G. (2016). The animal trypanosomiases and their chemotherapy: a review. Parasitology, 143, 1862–89.

Gizaw, Y., Megersa, M., Fayera, T. (2017). Dourine: A neglected disease of equids. Tropical Animal Health and Production, 49(5), 887-897.

Goa, K.L., Campoli-Richards, D.M. (1987). Pentamidine isethionate: a review of its antiprotozoal activity, pharmacokinetic properties and therapeutic use in *Pneumocystis carinii* pneumonia. Drugs, 33, 242-258.

Gull, K. (2002). The cell biology of parasitism in *Trypanosoma brucei*: insights and drug targets from genomic approaches? Current pharmaceutical design, 8(4), 241-256.

Gutierrez, C., Desquesnes, M., Touratier, L., Büscher, P. (2010). *Trypanosoma evansi*: Recent Outbreaks in Europe. Veterinary Parasitology, 174, 26–29.

Haag, J., O'hUigin, C., Overath, P. (1998). The molecular phylogeny of trypanosomes: evidence for an early divergence of the Salivaria. Molecular and Biochemical Parasitology, 91, 37-49.

Habila, N., Inuwa, M.H., Aimola, I.A., Udeh, M.U., Haruna, E. (2012). Pathogenic Mechanisms of *Trypanosoma evansi* Infections. Research in Veterinary Science, 93, 13–17.

Headrick, D.R. (2014). Sleeping Sickness Epidemics and Colonial Responses in East and Central Africa, 1900–1940. PLoS Neglected Tropical Diseases, 8(4), e2772.

Herrera, H.M., Alessi, A.C., Marques, L.C., Santana, A.E., Aquino, L.P., Menezes, R.F., Moraes, M.A., Machado, R.Z. (2002). Experimental *Trypanosoma evansi* infection in South American coati (Nasua nasua): hematological, biochemical and histopathological changes. Acta Tropica, 81(3), 203-210.

Herrmann, F., Hamoud, R., Sporer, F., Tahrani, A., Wink, M. (2011). Carlina oxide–a natural polyacetylene from *Carlina acaulis* (Asteraceae) with potent antitrypanosomal and antimicrobial properties. Planta medica, 77(17), 1905-1911.

Hide, G., Tait, A., Maudlin, I., Welburn, S.C. (2007). The origins, dynamics, and generation of *Trypanosoma brucei* rhodesiense epidemics in East Africa. Parasitology Today 12, 50-55.

Jacobs, R.T., Nare, B., Wring, S.A., Orr, M.D., Chen, D., Sligar, J.M., Jenks, M.X., Noe, R.A., Bowling, T.S., Mercer, L.T., Rewerts, C., Gaukel, E., Owens, J., Parham, R., Randolph, R., Beaudet, B., Bacchi, C.J., Yarlett, N., Plattner, J.J., Freund, Y., Ding, C., Akama, T., Zhang, Y.-K., Brun, R., Kaiser, M., Scandale, I., Don, R. (2011). SCYX-7158, an Orally-Active Benzoxaborole for the Treatment of Stage 2 Human African Trypanosomiasis. PLoS Neglected Tropical Diseases, 5, e1151.

Jamabo, M., Mahlalela, M., Edkins, A.L., Boshoff, A. (2023). Tackling sleeping sickness: Current and promising therapeutics and treatment strategies. International Journal of Molecular Sciences, 24(15), 12529.

Jamonneau, V., Ravel, S., Koffi, M., Kaba, D., Zeze, D.G., Ndri, L., Sane, B., Coulibaly, B., Cuny, G., Solano, P. (2004). Mixed infections of trypanosomes in tsetse and pigs and their epidemiological significance in a sleeping sickness focus of Cote d'Ivoire. Parasitology, 129, 693–702.

Kamte, S.L.N., Ranjbarian, F., Cianfaglione, K., Sut, S., Dall'Acqua, S., Bruno, M., Afshar, F.H., Iannarelli, R., Benelli, G., Cappellaccci, L., Hofer, A., Maggi, F., Petrelli, R. (2018). Identification of highly effective antitrypanosomal compounds in essential oils from the Apiaceae family. Ecotoxicology and Environmental Safety, 156, 154-165.

Kapo, N., Goletić, T., Škapur, V., Softić, A., Goletić, Š., Omeragić, J. (2023). Epidemiology of Animal Trypanosomiasis in Trypanosoma—Recent Advances and New Perspectives. El-Ashram, S., Alouffi, A., Mohamed, D., Eds. IntechOpen Limited: London, UK.

Kasozi, K.I., Zirintunda, G., Ssempijja, F., Buyinza, B., Alzahrani, K. J., Matama, K., Nakimbugwe, H.N., Alkazmi, L., Onanyang, D., Bogere, P., Ochieng, J.J., Islam, S., Matovu, W., Nalumenya, D.P., El-Saber Batiha, G., Osuwat, L.O., Abdelhamid, M., Shen, T., Omadang, L., Welburn, S.C. (2021). Epidemiology of trypanosomiasis in wildlife-implications for humans at the wildlife interface in Africa. Frontiers in Veterinary Science, 8, 565.

Kayser, O., Kiderlen, A. F., Croft, S. L. (2003). Natural products as antiparasitic drugs. Parasitology research, 90, S55-S62.

Keating, J., Yukich, J.O., Sutherland, C.S., Woods, G., Tediosi, F. (2015). Human African trypanosomiasis prevention, treatment and control costs: A systematic review. Acta Tropica,150, 4-13.

Kennedy, P.G.E., Rodgers, J. (2019). Clinical and Neuropathogenetic Aspects of Human African Trypanosomiasis. Frontiers in Immunology, 10, 3-7.

Kikwai, C., Ngeiywa, M. (2022). Review on the Socio-Economic Impacts of Trypanosomiasis. Africa Environmental Review Journal, 5(2), 89-100.

Kim, J., Álvarez-Rodríguez, A., Li, Z., Radwanska, M., Magez, S. (2023). Recent Progress in the Detection of Surra, a Neglected Disease Caused by *Trypanosoma evansi* with a One Health Impact in Large Parts of the Tropic and Sub-Tropic World. Microorganisms, 12(1), 44.

Klingbeil, M.M., Motyka, S.A., Englund, P.T. (2002). Multiple mitochondrial DNA polymerases in *Trypanosoma brucei*. Molecular cell, 10(1), 175-186.

Kulohoma, B.W., Wamwenje, S.A., Wangwe, I.I., Masila, N., Mirieri, C.K., Wambua, L. (2020). Prevalence of trypanosomes associated with drug resistance in Shimba Hills, Kwale County, Kenya. BMC research notes, 13 (1), 1-6.

Leigh, O., Emikpe, B., Ogunsola, J.O. (2015). Histopathological changes in some reproductive and endocrine organs of *Trypanosoma brucei* infected West African dwarf goat does. Bulgarian Journal of Veterinary Medicine, 18(1), 31-39.

LiverTox: Clinical and Research Information on Drug Induced Liver Injury (2014). Pentamidine. Bethesda (MD): National Institute of Diabetes and Digestive and Kidney Diseases.

Luckins, A.G. (1988). *Trypanosoma evansi* in Asia. Parasitology Today, 4, 137–142.

Lundkvist, G.B., Kristensson, K., Bentivoglio, M. (2004). Why trypanosomes cause sleeping sickness. Physiology, 19(4), 198-206.

Magez, S., Radwanska, M. (Eds.). (2014). Trypanosomes and trypanosomiasis. Vienna: Springer.

Malvy, D., Chappuis, F. (2011). Sleeping sickness. Clinical Microbiology and Infection, 17(7), 986-995.

Mandel, C.R., Kaneko, S., Zhang, H., Gebauer, D., Vethantham, V., Manley, J.L., Tong, L. (2006). Polyadenylation factor CPSF-73 is the pre-mRNA 3'-end-processing endonuclease. Nature, 444, 953–956.

Matthews, K. R. (2005). The developmental cell biology of Trypanosoma brucei. Journal of cell science, 118(2), 283-290.

Mattioli, R.C., Feldmann, U., Hendrickx, G., Wint, W., Jannin, J., Slingenbergh, J. (2004). Tsetse and trypanosomiasis intervention policies supporting sustainable animal-agricultural development. Journal of Food Agriculture and Environment, 2, 310-314.

Mc Kean, P.G. (2003). Coordination of cell cycle and cytokinesis in *Trypanosoma brucei*. Current Opinion in Microbiology, 6, 600-607.

Mesu, V.K.B.K., Kalonji, W.M., Bardonneau, C., Mordt, O.V., Blesson, S., Simon, F., Delhomme, S., Bernhard, S., Kuziena, W., Lubaki, J.P.F., Vuvu, S.L., Ngima, P.N., Mbembo, H.M., Ilunga, M., Bonama, A.K., Heradi, J.A., Solomo, J.L.L., Mandula, G., Badibabi, L.K., Dama, F.R., Lukula, P.K., Ngolo Tete, D., Lumbala, C., Scherrer, B., Strub-Wourgaft, N., Tarral, A. (2018). Oral fexinidazole

for late-stage African *Trypanosoma brucei gambiense* trypanosomiasis: a pivotal multicentre, randomised, non-inferiority trial. Lancet, 391,144-154.

Meyer, A., Holt, H.R., Selby, R., Guitian, J. (2016). Past and ongoing tsetse and animal trypanosomiasis control operations in five African countries: a systematic review. PLoS neglected Tropical Diseases, 10(12), e0005247.

Midgley, I., Fitzpatrick, K., Taylor, L.M., Houchen, T.L., Henderson, S.J., Wright, S.J., Cybulski, Z.R., John, B.A., McBurney, A., Boykin, D.W., Trendler, K.L. (2007). Pharmacokinetics and metabolism of the prodrugDB289 (2,5-bis[4-(N-methoxyamidino)phenyl]furan monomaleate) in rat and monkey and its conversion to the antiprotozoal/antifungal drug DB75 (2,5-bis(4-guanylphenyl)furan dihydro-chloride). Drug Metabolism & Disposition, 35, 955–967.

Miles M. (2003). American trypanosomiasis (Chagas disease). In: Cook GC, Zumla A, eds. Manson's tropical disease, 21st edn. London: Elsevier Science, 1325–37

Mogk, S., Meiwes, A., Boßelmann, C.M., Wolburg, H. (2014). The lane to the brain: how African trypanosomes invade the CNS. Trends in Parasitology, 30, 470-477.

Munday, J.C., Eze, A.A., Baker, N., Glover, L., Clucas, C., Aguinaga Andrés, D., Natto, M.J., Teka, I.A., McDonald, J., Lee, R.S., Graf, F.E., Ludin, P., Burchmore, R.J.S., Turner, C.R.M., Tait, M., MacLeod, A., Mäser, P., Barrett, M.P., Horn, D., De Koning, H.P. (2014). *Trypanosoma brucei* aquaglyceroporin 2 is a high-affinity transporter for pentamidine and melaminophenyl arsenic drugs and the main genetic determinant of resistance to these drugs. Journal of Antimicrobial Chemotherapy, 69(3), 651-663.

Munday, J.C., Settimo, L., de Koning, H.P. (2015). Transport proteins determine drug sensitivity and resistance in a protozoan parasite, *Trypanosoma brucei*. Frontiers in Pharmacology, 6, 32.

N'Djetchi, M.K., Ilboudo, H., Koffi, M., Kabore´, J., Kabore´, J.W., Kaba, D. Courtin, Bamoro Coulibaly, F., Fauret, P., Kouakou, L., Ravel, S., Deborggraeve, S., Solano, P., De Meeûs, T., Bucheton, B., Jamonneau, V. (2017). The study of trypanosome species circulating in domestic animals in two human African trypanosomiasis foci of Côte d'Ivoire identifies pigs and cattle as potential reservoirs of *Trypanosoma brucei* gambiense. PLoS Neglected Tropical Diseases, 11(10), e0005993.

News medical (2015). DNDi announces successful completion of SCYX-7158 Phase I study for treatment of sleeping sickness.

Ngahang Kamte, S.L., Ranjbarian, F., Campagnaro, G.D., Biapa Nya, P.C., Mbuntcha, H., Woguem, V., Womeni, H.M., Azefack Ta, L., Giordani, C., Barboni, L., Benelli, G., Cappellacci, L., Hofer, A., Petrelli, R., Maggi, F. (2017). *Trypanosoma brucei* inhibition by essential oils from medicinal and aromatic plants traditionally used in Cameroon (*Azadirachta indica*, *Aframomum melegueta*, *Aframomum daniellii*, *Clausena anisata*, *Dichrostachys cinerea* and *Echinops giganteus*). International Journal of Environmental Research and Public Health, 14(7), 737.

Njenga, W. (2007). Factors contributing to school drop out in public secondary schools in Mombasa District, Kenya. Masters Thesis, University of Nairobi.

Nkinin, S.W., Njiokou, F., Penchenier, L., Grebaut, P., Simo, G., Herder, S. (2002). Characterization of *Trypanosoma brucei* sl subspecies by isoenzymes in domestic pigs from the Fontem sleeping sickness focus of Cameroon. Acta tropica, 81(3), 225-232.

Nok, A.J. (2003). Arsenicals (melarsoprol), pentamidine and suramin in the treatment of human African trypanosomiasis. Parasitology Research, 90(1), 71-9.

Nyimba, P.H., Komba, E.V.G., Sugimoto, C., Namangala, B. (2015). Prevalence and species distribution of caprine trypanosomosis in Sinazongwe and Kalomo districts of Zambia. Veterinary Parasitology, 210(3-4), 125-130.

Odiit, M., Kansiime, F., Enyaru, J.C. (1997). Duration of symptoms and case fatality of sleeping sickness caused by *Trypanosoma brucei rhodesiense* in Tororo, Uganda. East Africa Medicine Journal, 74, 792–795.

OIE (2013). Terrestrial Manual. Trypanosomosis (tsetse-transmitted). (Office International des Epizooties (OIE), Paris).

Pal, A., Hall, B.S., Field, M.C. (2002). Evidence for a non-LDL-mediated entry route for the trypanocidal drug suramin in *Trypanosoma brucei*. Molecular and biochemical parasitology, 122(2), 217-221.

Papagni, R., Novara, R., Minardi, M.L., Frallonardo, L., Panico, G.G., Pallara, E., Cotugno, S., Ascoli Bartoli, T., Guido, G., De Vita, E., Ricciardi, A., Totaro, V., Camporeale, M., Segala, F.V., Bavaro, D.F., Patti, G., Brindicci, G., Pellegrino, C., Mariani, M.F., Putoto, G., Sarmati, L., Castellani, C., Saracino, A., Di Gennaro, F., Nicastri, E. (2023). Human African Trypanosomiasis (sleeping sickness): Current knowledge and future challenges. Frontiers in Tropical Diseases, 4, 1087003.

Parsons, M. (2004). Glycosomes: parasites and the divergence of peroxisomal purpose. Molecular microbiology, 53(3), 717-724.

Pérez-Molina, J. A., Molina, I. (2018). Chagas disease. The Lancet, 391(10115), 82-94.

Petrelli, R., Orsomando, G., Sorci, L., Maggi, F., Ranjbarian, F., Biapa Nya, P.C., Petrelli, D., Vitali, L.A., Lupidi, G., Quassinti, L., Bramucci, M., Hofer, A., Cappellacci, L. (2016). Biological activities of the essential oil from *Erigeron floribundus*. Molecules, 21(8), 1065.

Petrelli, R., Ranjbarian, F., Dall'Acqua, S., Papa, F., Iannarelli, R., Kamte, S.L.N., Vittori, S., Benelli, G., Maggi, F., Hofer, A., Cappellacci, L. (2017). An overlooked horticultural crop, *Smyrnium olusatrum*, as a potential source of compounds effective against African trypanosomiasis. Parasitology international, 66(2), 146-151.

Pohlig, G., Bernhard, S.C., Blum, J., Burri, C., Mpanya, A., Lubaki, J.P., Mpoto, A.M., Mununga, B.F., N'tombe, P.M., Manesa Deo, G.K., Mutantu, P.N., Kuikumbi, F.M., Mintwo, A.F., Mununga, A.K., Dala, A., Macharia, S., Bilenge, C.M.M., Ku Mesu, V.K.B., Franco, J.R., Dituvanga, N.D., Tidwell, R.R., Olson, C.A. (2016). Efficacy and Safety of Pafuramidine versus Pentamidine Maleate for Treatment of First Stage Sleeping Sickness in a Randomized, Comparator-Controlled, International Phase 3 Clinical Trial. PLoS Neglected Tropical Diseases, 10(2), e0004363.

Prata A. (2001). Clinical and epidemiological aspects of Chagas disease. Lancet Infection Disease, 1, 92–100.

Priotto, G., Pinoges, L., Fursa, I.B., Burke, B., Nicolay, N., Grillet, G., Hewison, C., Balasegaram, M. (2008). Safety and effectiveness of first line eflornithine for *Trypanosoma brucei gambiense* sleeping sickness in Sudan: cohort study. BMJ, 336, 705-708.

Putt, S.N.H., Shaw, A.P.M. (1982). The socio-economic effects of the control of tsetse transmitted trypanosomiasis in Nigeria. http://www.sciquest.org.nz/

Quintana, J.F., Bueren-Calabuig, J., Zuccotto, F., de Koning H.P., Horn, D., Field, M.C. (2020). Instability of aquaglyceroporin (AQP) 2 contributes to drug resistance in *Trypanosoma brucei*. PLOS Neglected Tropical Disease, 14, e0008458.

Rassi, A. Jr, Rassi, A., Little, W.C. (2000). Chagas heart disease. Clinical Cardiology, 23, 883–89.

Sairafianpour, M., Christensen, J., Staerk, D., Budnik, B.A., Kharazmi, A., Bagherzadeh, K., Jaroszewski, J.W. (2001). Leishmanicidal, antiplasmodial, and cytotoxic activity of novel diterpenoid

1,2 quinones from *Perovskia abrotanoides*: new source of tanshinones. Journal of Natural Products, 64, 1398–1403.

Saleh, M.A., Al-Salahy, M.B., Sanousi, S.A. (2009). Oxidative stress in the blood of camels (Camelus dromedaries) naturally infected with *Trypanosoma evansi*. Veterinary Parasitology, 162(3-4), 192-199

Sanderson, L., Khan, A., Thomas, S. (2007). Distribution of suramin, an antitrypanosomal drug, across the blood–brain and blood– cerebrospinal fluid interfaces in wild-type and P-glycoprotein transporter-deficient mice. Antimicrobial Agents and Chemotherapy, 51(31), 36–46.

Seixas, J. (2005). Investigations on the encephalopathic syndrome during melarsoprol treatment of Human African Trypanosomiasis [PhD thesis]. Lisbon: Instituto de Higiene e Medicina Tropical.

Sekhar, G.N., Watson, C.P., Fidanboylu, M., Sanderson, L., Thomas, S.A. (2014). Delivery of antihuman African trypanosomiasis drugs across the blood-brain and blood-CSF barriers. Advances in Pharmacology, 71, 245–275.

Shaw, A.P.M., Cecchi, G., Wint, G.R.W., Mattioli, R.C., Robinson, T.P. (2014). Mapping the economic benefits to livestock keepers from intervening against bovine trypanosomosis in Eastern Africa. Preventive Veterinary Medicine, 113(2), 197–210.

Shaw, A.P.M., Wint, G.R.W., Cecchi, G., Torr, S.J., Mattioli, R.C., Robinson, T.P. (2015). Mapping the benefit-cost ratios of interventions against bovine trypanosomosis in Eastern Africa. Preventive Veterinary Medicine, 122, 406–416.

Sidney, R., Andrew, McG., James, C., Richard, N. (2013). Dourine – an emerging venereal threat to European horses. AHT /BEVA/DEFrA Equine Quarterly Disease Surveillance report. 6, 7.

Simarro, P.P., Cecchi, G., Franco, J.R., Paone, M., Diarra, A., Ruiz-Postigo, J.A., Fèvre, E.M., Mattioli, R.C., Jannin, J.G. (2012). Estimating and Mapping the Population at Risk of Sleeping Sickness. PLoS Neglected Tropical Diseases, 6, e1859.

Sinha, K.M., Hines, J.C., Downey, N., Ray, D.S. (2004). Mitochondrial DNA ligase in Crithidia fasciculata. Proceedings of the National Academy of Sciences, 101(13), 4361-4366.

Song, J., Baker, N., Rothert, M., Henke, B., Jeacock, L., Horn, D., Beitz, E. (2016). Pentamidine Is Not a Permeant but a Nanomolar Inhibitor of the *Trypanosoma brucei* Aquaglyceroporin-2. PLoS pathogens, 12(2), e1005436.

Sosa Estani, S., Segura, E.L., Ruiz, A.M., Velazquez, E., Porcel, B.M., Yampotis, C. (1998). Efficacy of chemotherapy with benznidazole in children in the indeterminate phase of Chagas disease. American Journal of Tropical Medicine and Hygiene, 59, 526–29.

Stephens, J.W.W., Fantham, H.B. (1910). On the peculiar morphology of a trypanosome from a case of sleeping sickness and the possibility of its being a new species (*T. rhodesiense*). Proceedings of the Royal Society of London, 83, 28-33.

Sternberg, J.M., Gierlinski, M., Bieler, S., Ferguson, M.A. (2014). Evaluation of the diagnostic accuracy of prototype rapid tests for human African trypanosomiasis. PLoS Neglected Tropical Diseases, 8, e3373.

Steverding, D. (2008). The history of African trypanosomiasis. Parasite Vector, 1, 3-11.

Stich, A., Abel, P.M., Krishna, S. (2002). Human African trypanosomiasis. BMJ 325, 203-206.

Sut, S., Dall'Acqua, S., Baldan, V., Kamte, S.L.N., Ranjbarian, F., Nya, P.C.B., Vittori, S., Benelli, G., Maggi, F., Caopellacci, L., Hofer, A., Petrelli, R. (2018). Identification of tagitinin C from *Tithonia diversifolia* as antitrypanosomal compound using bioactivity-guided fractionation. Fitoterapia, 124, 145-151.

Tagboto, S., Townson, S. (2001). Antiparasitic properties of medicinal plants and other naturally occurring products.

Taylor, D.B., Stable Fly (Stomoxys calcitrans, Muscidae) (2022). Encyclopedia of Infection and Immunity, ISBN 9780323903035, 903-913.

Torreele, E., Bourdin Trunz, B., Tweats, D., Kaiser, M., Brun, R., Mazue, G., Bray, M.A., Pecoul, B. (2010). Fexinidazole-a new oral nitroimidazole drug candidate entering clinical development for the treatment of sleeping sickness. PLoS Neglected Tropical Diseases, 4, e923.

Ungogo, M.A., Ebiloma, G.U., Ichoron, N., Igoli, J.O., De Koning, H.P., Balogun, E.O. (2020). A review of the antimalarial, antitrypanosomal, and antileishmanial activities of natural compounds isolated from Nigerian flora. Frontiers in Chemistry, 8, 617448.

Van Nieuwenhove, S., Schechter, P.J., Declercq, J. (1985). Treatment of gambiense sleeping sickness in the Sudan with oral DFMO (DL-alpha-difluoromethylornithine), an inhibitor of ornithine decarboxylase; first field trial. Transactions of the Royal Society of Tropical Medicine and Hygiene, 79(5), 692–698.

Vansterkenburg, E.L., Coppens, I., Wilting, J., Bos, O.J., Fischer, M.J., Janssen, L.H., Opperdoes, F.R. (1993). The uptake of the trypanocidal drug suramin in combination with low-density lipoproteins by *Trypanosoma brucei* and its possible mode of action. Acta tropica, 54(3-4), 237-250.

Vennerstrom, J.L., Lovelace, J.K., Waits, V.B., Hanson, W.L., Klayman, D.L. (1990). Berberine derivatives as antileishmanial drugs. Antimicrobial Agents and Chemotherapy, 34, 918–921.

Vickermann, K. (1976). The diversity of the kinetoplastid flagellates. Biology of the Kinetoplastida. Academic Press London, 11-34.

Vincent, I.M., Creek, D., Watson, D.G., Kamleh, M.A., Woods, D.J., Wong, P.E., Burchmore, R.J.S., Barrett, M.P. (2010). A molecular mechanism for eflornithine resistance in African trypanosomes. PLoS Pathogens, 6, E1001204.

Wall, R.J., Rico, E., Lukac, I., Zuccotto, F., Elg, S., Gilbert, I.H., Freund, Y., Alley, M.R.K., Field, M.C., Wyllie, S., Horn, D. (2018). Clinical and veterinary trypanocidal benzoxaboroles target CPSF3. Proceedings of the National Academy of Sciences USA, 115, 9616–9621.

Wamwiri, F.N., Changasi, R.E. (2016). Tsetse Flies (*Glossina*) as Vectors of Human African Trypanosomiasis: A Review. BioMed Research International, 6201350.

Wang, C.C. (1995). Molecular mechanisms and therapeutic approaches to the treatment of African trypanosomiasis. Annual Review of Pharmacology and Toxicology, 35(11), 93–127.

WHO (2013). Control and surveillance of African trypanosomiasis. World Health Organization Technical Report Series, 984, 1-237.

WHO (2019). WHO interim guidelines for the treatment of gambiense human African trypanosomiasis. Geneva: World Health Organization, Licence: CC BY-NC-SA 3.0 IGO.

WHO (2023a). Trypanosomiasis, human African (sleeping sickness). World Health Organization, fact sheets, 2 May 2023.

WHO (2023b). Stakeholders meet in WHO to review progress towards elimination of human African trypanosomiasis. World Health Organization, departmental news, 8 June 2023.

Wiedemar, N., Graf, F.E., Zwyer, M., Ndomba, E., Renggli, C.K., Cal, M., Schmidt, R.S. Wenzler, T., Mäser, P. (2018). Beyond immune escape: a variant surface glycoprotein causes suramin resistance in *Trypanosoma brucei*. Molecular Microbiology, 107, 57-67.

Wilkinson, S. R., Taylor, M. C., Horn, D., Kelly, J. M., Cheeseman, I. (2008). A mechanism for cross-resistance to nifurtimox and benznidazole in trypanosomes. Proceedings of the National Academy of Sciences, 105, 5022-5027.

William, B.L., Steven, H.S. (2007). Infectious diseases of breeding stallion in: Current Therapy in Large Animal Theriogenology (2nd Ed.), 15–23.

Wilson, W.D., Nguyen, B., Tanious, F.A., Mathis, A., Hall, J.E., Stephens, C.E., Boykin, D.W. (2005). Medications That Target the DNA Minor Groove: Compound Design and Preparation, DNA Interactions, Cellular Distribution and Biological Activity. Current Medicinal Chemistry - Anti-cancer Agents, 5(4), 389-408.

Woodward, R., Gull, K. (1990). Timing of nuclear and kinetoplast DNA replication and early morphological events in the cell cycle of *Trypanosoma brucei*. Journal of cell science, 95(1), 49-57.

Wyllie, S., Foth, B.J., Kelner, A., Sokolova, A.Y., Berriman, M., Fairlamb, A.H. (2016). Nitroheterocyclic drug resistance mechanisms in *Trypanosoma brucei*. Journal of Antimicrobial Chemotherapy, 2015, 625–34.

Zhang, Z.Q., Giroud, C., Baltz, T. (1992). *In vivo* and *in vitro* sensitivity of *T. evansi* and *T. equiperdum* to Diminazene, Suramine, Melcy, Quinapyramine and Isometamidium. Acta Tropica, 50, 101–110.

Ziemann, H. (1905). Beitrag zur Trypanosomenfrage. Zentralblatt für Bakteriologie, Mikrobiologie und Hygiene, 1. Abt Originale, 38, 307-314.

Zoltner, M., Leung, K.F., Alsford, S., Horn, D., Field, M.C. (2015). Modulation of the surface proteome through multiple ubiquitylation pathways in African trypanosomes. PLOS Pathogens, 11, e1005236.

CHAPTER 2

Anthriscus nemorosa

CHAPTER 2 Outline

2.1. Introduction

As previously mentioned, plants from the Apiaceae family have been thoroughly investigated for their promising activity against *T. brucei* (Petrelli et al., 2017; Kamte et al., 2018). Within this family, *Anthriscus nemorosa* (M.Bieb.) Spreng is an aromatic plant, also known by the names of 'gimigimi' or 'peçek' in Turkey (Altundag and Ozturk, 2011) (Fig. 28). *A. nemorosa* grows in European and Asian temperate areas, in countries like Iran, Turkey, Italy and Japan (Nikoli´c, 1973; Nickavar et al., 2009; Tekin et al., 2017). It is an herbaceous perennial plant with erect stems 50-120 cm high, characterized by basal 3-4 pinnate leaves and white flowers in umbellet with bracteoles. The root is fusiform with transverse annulations (Fig. 29). The flowering time goes from April to August and fruits ripen up to September. *A. nemorosa* usually grows in meadows, around forested habitats, or near field areas and close to streams (Tekin et al., 2017). Decoctions are traditionally used as medicinal remedies for various diseases. For instance, its fruits are used for the treatment of gastrointestinal disorders (Altundag and Ozturk, 2011; Bulut et al., 2014), and in case of inflammation and rheumatism (Navchoo and Buth, 1989; Gariola et al., 2014). *A. nemorosa* also finds use in the preparation of herby cheese, called 'otlu peynir', in different areas of Turkey (Karakaya et al. 2019). Plus, ethnobotanical studies revealed its usefulness in improving memory in Alzheimer's disease (Bagci et al., 2016). Several pharmacological activities are attributable to this plant, as the prevention of anxiety and depression (Karakaya et al., 2019; Menemen, 2012). The root EO and the flower ethyl acetate extract demonstrated a significant antioxidant potential (Karakaya et al. 2019). *A. nemorosa* also exerts an antifungal activity, with the hexane extract of its aerial parts being highly efficient against *Candida albicans* (Karimi et al., 2019).

Figure 28. *Anthriscus nemorosa*.

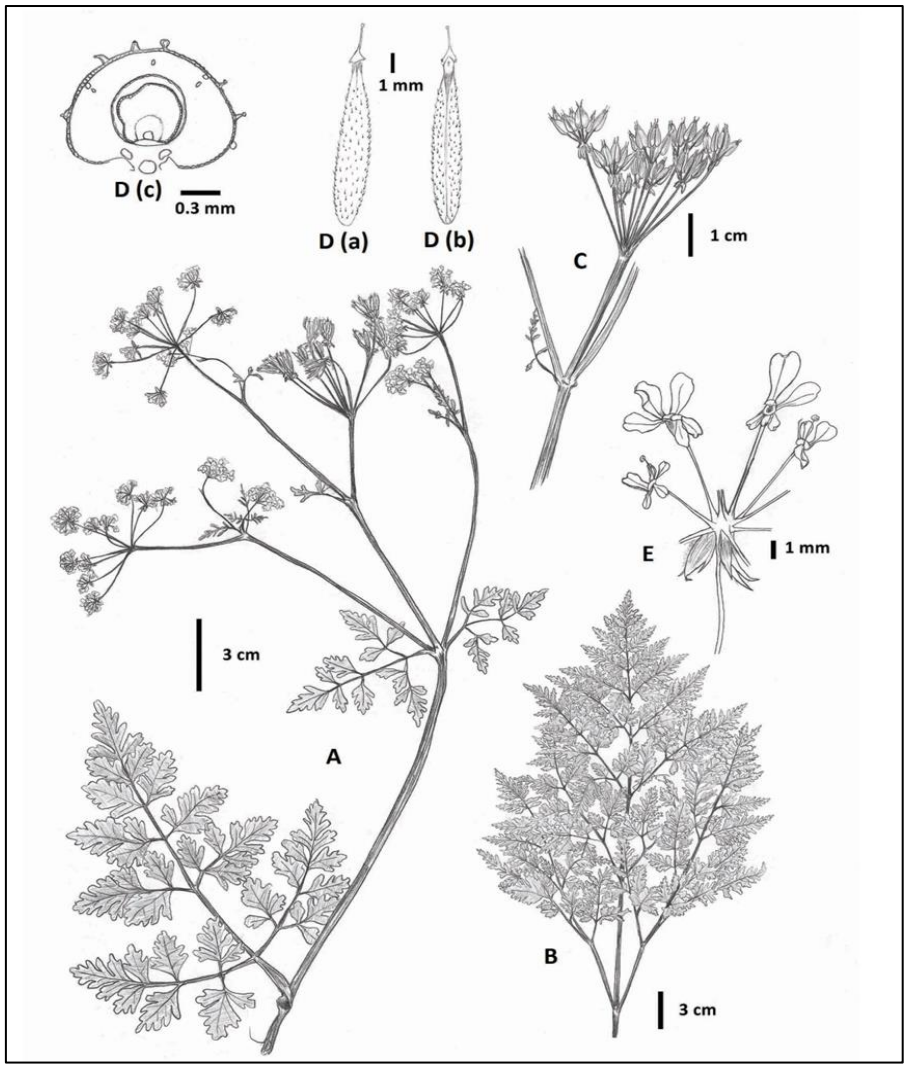

Figure 29. *Anthriscus nemorosa*: A) habit; B) basal leaf; C) fruiting umbel with bracteoles; D a) dorsal view of mericarp; D b) commissural view of mericarp; Dc) cross section of mericarp; E) flowers in umbellet with bracteoles [A) from M.Tekin 1122 (CUFH); B) from M.Tekin 1199 (CUFH); C, Da and Db) from M.Tekin 1144 (CUFH); Dc) from M.Tekin 1249 (CUFH); E) from M. Tekin 1223 (CUFH)].

For the volatile fraction, a few studies are available regarding its antimicrobial, antioxidant, anxiolytic and antidepressant potentials (Pavlovic et al., 2011; Hritcu et al., 2015; Lai et al., 2018). Concerning organic extracts, instead, poor research has been carried out (Forouhandeh et al., 2021).

Since EOs and extracts of some Apiaceae plants represent an attractive alternative approach to fighting protozoan parasites, this study aimed to better define the chemical composition of *A. nemorosa* EOs and extracts and to evaluate their antitrypanosomal activity against *T. brucei*. Being naturally occurring compounds, EOs, and their components are believed to be environmentally safe, user-friendly, and generally not toxic to humans (Karakaya et al., 2019). Unfortunately, these

products can hide unexpected drawbacks; EOs are usually characterized by low stability and water solubility, high volatility, and, as well as for extracts, severe side effects.

In order to overcome these issues, encapsulation in nanoemulsions was used to improve the chemical-physical profile of the EOs and bio-guided assays were performed to select the most promising and safest extracts for human use.

2.2 Essential oils

2.2.1 Results

2.2.1.1 EO composition

EOs from the *A. nemorosa* aerial parts (*A. nemorosa* EO-AP) and roots (*A. nemorosa* EO-R) were obtained by hydrodistillation and their composition is reported in Table 3. A GC-MS analysis was performed on *A. nemorosa* EO-AP and *A. nemorosa* EO-R, affording the identification of thirty-four volatile components, accounting for 98.1% and 98.6% of the total compositions, respectively. Monoterpene hydrocarbons were confirmed to be the predominant class of compounds for both the EOs, but were more abundant in the EOs from the roots (81.5%) than the aerial parts (74.0%). Myrcene resulted to be the most abundant member of this class, reaching percentages of 40.1 and 19.9% of the total chemical composition for *A. nemorosa* EO-AP and *A. nemorosa* EO-R, respectively. β-pinene was present in a similar amount in A. nemorosa EO-R (22.0%), while in A. nemorosa EO-AP its concentration was significantly lower (3.0%). γ-terpinene was detected in comparable concentrations in both the EOs (11.6% and 9.2% in EOs from aerial parts and roots, respectively), whereas (*Z*)-β-ocimene resulted more concentrated in the EO from roots (8.9%) than the aerial parts (4.4%). Considerable levels of sesquiterpene hydrocarbons were also detectable in the two EOs. They accounted for only 1% of the whole composition in the case of the root EO, but they represented the 18.8% of the chemical profile in the aerial part EO, with germacrene D (10.4%), (*E*,*E*)-α-farnesene (4.0%) and δ-cadinene (2.3%) being the most representative constituents. Oxygenated monoterpenes were instead totally absent in both EOs. In contrast, oxygenated sesquiterpenes were detected at 3.0% and 4.4% in the EOs from aerial parts and roots, respectively. Alkanes and other compounds were found in lower amounts in the EOs from the aerial parts and roots (2.3 and 11.2%, respectively), with nonane being the most significant one (1.7% in the EO from aerial parts and 9.5% from the EO from roots).

Table 3. Chemical composition of the EOs obtained from *A. nemorosa* aerial parts and roots.

N°	Component[a]	RI[b]	RI lit.[c]	% *A. nemorosa* EO-AP.	% *A. nemorosa* EO-R	ID[d]
1	*n*-nonane	901	900	1.7	9.5	RI,MS
2	*α*-thujene	921	924	tr[e]	tr	RI,MS
3	*α*-pinene	927	932	0.4	1.7	Std
4	sabinene	964	969	0.4	0.4	Std
5	*β*-pinene	969	974	3.0	22.0	Std
6	myrcene	990	988	40.1	19.9	Std
7	*n*-decane	1001	1000	0.1	0.8	RI,MS
8	*α*-phellandrene	1004	1002		0.2	Std
9	*α*-terpinene	1015	1014	0.1	tr	Std
10	*p*-cymene	1022	1020	2.2	2.8	Std
11	limonene	1024	1024	5.7	11.5	Std
12	*β*-phellandrene	1026	1025	3.0	2.7	Std
13	(*Z*)-*β*-ocimene	1038	1032	4.4	8.9	Std
14	(*E*)-*β*-ocimene	1048	1044	2.8	1.8	Std
15	*γ*-terpinene	1056	1055	11.6	9.2	Std
16	*n*-undecane	1101	1100	0.4	0.9	RI,MS
17	*allo*-ocimene	1129	1128	0.2	0.5	RI,MS
18	*β*-elemene	1384	1389	0.4	tr	RI,MS
19	(*E*)-caryophyllene	1387	1417	0.6	0.1	Std
20	*β*-copaene	1420	1430	0.5		RI,MS
21	(*E*)-*β*-farnesene	1457	1440	0.7		Std
22	germacrene D	1472	1484	10.4		RI,MS
23	1-dodecanol	1476	1469		0.5	RI,MS
24	*epi*-cubebol	1487	1493		0.3	RI,MS
25	(*E*,*E*)-α-farnesene	1508	1505	4.0		RI,MS
26	*δ*-cadinene	1517	1522	2.3	0.9	RI,MS
27	elemol	1543	1534		0.5	RI,MS
28	guaiol	1591	1600		0.8	RI,MS
29	10-*epi*-*γ*-eudesmol	1608	1622		0.5	RI,MS

30	*epi*-*α*-muurolol + *epi*-*α*-cadinol	1633	1640/1638	1.0	0.5	RI,MS
31	*β*-eudesmol	1639	1649	0.2	0.4	RI,MS
32	valerianol	1643	1656	0.1	0.4	RI,MS
33	*α*-cadinol	1646	1652	1.7	0.4	RI,MS
34	bulnesol	1659	1670		0.7	RI,MS
	Oil yield (%, w/w)			0.06	0.08	
	Total identified (%)			98.1	98.6	
	Grouped compounds (%)					
	Monoterpene hydrocarbons			74.0	81.5	
	Oxygenated monoterpenes					
	Sesquiterpenes hydrocarbons			18.8	1.0	
	Oxygenated sesquiterpenes			3.0	4.4	
	Alkanes			2.3	11.2	
	Others				0.5	

[a]Order of elution is from an HP-5MS column (30 m x 0.25 mm, 0.1 µm).

[b]Linear retention index according to Van den Dool and Kratz (1963) [16].

[c]RI taken from ADAMS and/or NIST 17 and FFNSC3 libraries.

[d]Identification method: Std, comparison with the analytical standard; RI, coherence of the calculated RI with those stored in ADAMS, NIST 17, and FFNSC3 libraries. MS, mass spectrum overlapping with those recorded in ADAMS, NIST 17, WILEY 275, and FFNSC3 libraries.

[e]Traces relative % < 0.1.

2.2.1.2 Antitrypanosomal activity

Both *A. nemorosa* EO-AP and *A. nemorosa* EO-R resulted to effectively inhibit *T. brucei* proliferation. However, *A. nemorosa* EO-R demonstrated an EC_{50} value (half maximal effective concentration of a drug) of 2.36 µg/mL, two times higher than the *A. nemorosa* EO-AP EC_{50} (1.17 µg/mL), revealing a milder activity on the parasite. Moreover, the selectivity index (SI) of the root EO was 2.25, two times lower than the one demonstrated by the EO from aerial parts (4.65), assessing its poor safety profile (Table 4 and Fig. 30). Based on these results, the study focused on *A. nemorosa* EO-AP, the most active and selective of the EOs. The main compounds constituting *A. nemorosa* EO-AP, were assayed against *T. brucei* and results are reported in table 4.

Table 4. Antitrypanosomal activity of *A. nemorosa* essential oils and pure compounds. For the pure compounds, their percentages in *A. nemorosa* EO-AP and *A. nemorosa* EO-R are listed just after the names of the compounds.

	EC_{50}		Selectivity Index (SI)
	***T. brucei* (s427)**	**Balb3T3**	
Essential oils	**µg/mL**	**µg/mL**	
A. nemorosa EO-AP	1.17 ± 0.09	5.48 ± 0.61	4.65
A. nemorosa EO-R	2.36 ± 0.09	5.33 ± 0.49	2.25
Pure compounds	**µg/mL (µM)**	**µg/mL (µM)**	
β-pinene (**1**): 3% AP, 22% R	11.4 ± 2.6 (83.7)[c]	>100	>8.77
β-ocimene (**2**): 7,2% AP, 10.7% R	1.1 ± 0.5 (8)[b]	>100	>91
p-cymene (**3**): 2.2% AP, 2.8% R	4.5 ± 1.0 (33)[b]	28 ± 7	6.2
Limonene (**4**): 5.7% AP, 11.5% R	5.6 ± 1.6 (41)[a]	>100	>18
Myrcene (**5**): 40.1% AP, 19.9% R	26.2 ± 0.44 (193)	49.6 ± 0.64	1.9
Farnesene (**6**): 4.7% AP	0.84 ± 0.04 (4.11)	4.09 ± 0.39	4.85
γ-terpinene (**7**): 11.6% AP, 9.2% R	>100	>100	-
Reference drug	**µg/mL (µM)**	**µg/mL (µM)**	
Suramin	0.025 ± 0.001 (0.0147)	> 5	> 262

[a]Data from Petrelli et al., 2016.

[b] Data from Kamte et al., 2018.

[c] Data from Ngahang Kamte et al., 2017.

As noticeable, farnesene and *β*-ocimene (mixture of Z and E isomers), belonging to the chemical group of sesquiterpene hydrocarbons, were identified as the most effective components and demonstrated EC_{50} values comparable to that of the intact oil (0.84 µg/mL and 1.1 µg/mL, respectively). *β*-pinene, *p*-cymene, limonene, myrcene, and *γ*-terpinene were instead less active (EC_{50}

> 4.5 µg/mL). Even if present in a relatively high percentage in the EO, germacrene D was not tested because not commercially available. To resume, the antitrypanosomal activity of the major tested compounds was in the order: farnesene > *β*-ocimene> *p*-cymene > limonene > *β*-pinene > myrcene > *γ*-terpinene.

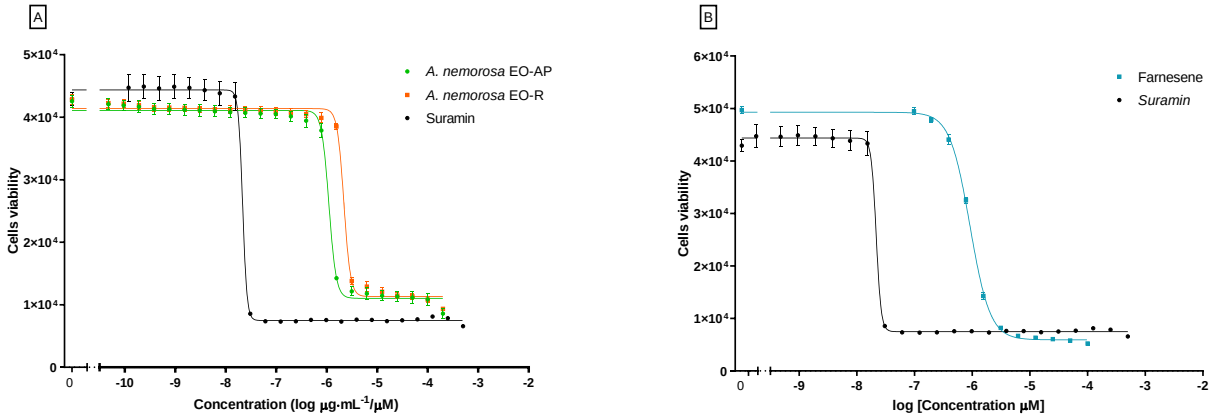

Figure 30. A. Growth inhibition of *T. brucei* treated with *A. nemorosa* EO-AP (green curve) and *A. nemorosa* EO-R (orange curve) with Suramin as control (black curve). B. *T. brucei* growth inhibition with farnesene (light blue curve).

Chemical structures of the bioactive compounds are shown in figure 31, and varied from linear (farnesene, *β*-ocimene, and myrcene) to monocyclic (limonene, *p*-cymene, and *γ*-terpinene) and bicyclic derivatives (*β*-pinene), being characterized by one to four unsaturations.

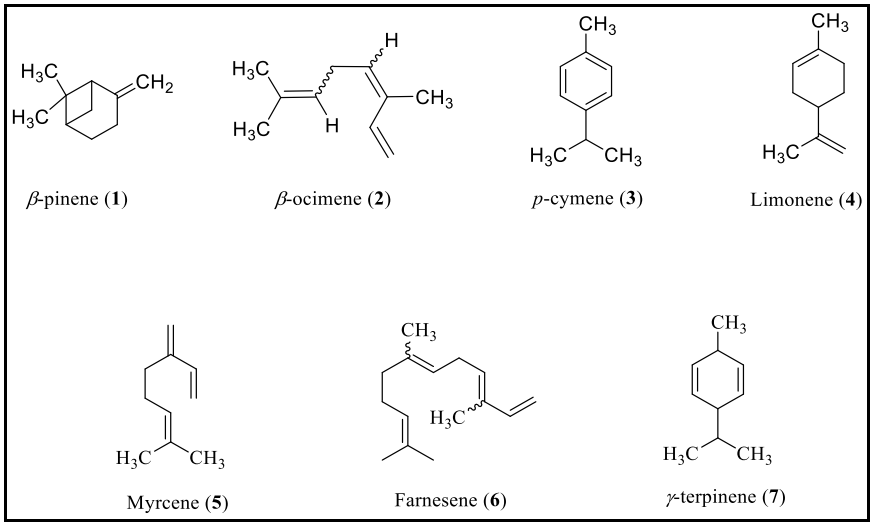

Figure 31. Chemical structures of *β*-pinene (**1**), *β*-ocimene (**2**), *p*-cymene (**3**), limonene (**4**), myrcene (**5**), farnesene (**6**), and *γ*-terpinene (**7**).

2.2.1.3 Artificial mixtures

Because of the best activity of *A. nemorosa* EO-AP with respect to the EO from roots, the first EO was selected to carry out an assay to assess the contribution of the different components to the overall antitrypanosomal activity. In the conducted compound elimination assay, omitted compounds were replaced by acetone. Myrcene appeared to have a protective effect, evident from the enhancement of activity when removed (EC_{50} from 7.25 to 2.25 µg/mL). Limonene, *β*-ocimene, *p*-cymene and farnesene emerged as the major antitrypanosomal constituents of the EO (Table 5). Indeed, if three of these components were removed (Mix 8-11), the EC_{50} value resulted increased, and in a more pronounced way for the simultaneous removal of limonene, *β*-ocimene, and farnesene that produced an enhancement of EC_{50} from 7.25 (Mix 1) to 49.2 µg/mL (Mix 9).

Wadley's formula was then used to evaluate synergistic interactions among the most abundant constituents of the *A. nemorosa* EO-AP. The different components displayed additive, antagonistic, and synergistic relationships. Results suggested several additive interactions among the six studied components of *A. nemorosa* EO-AP (Mix 1, Mix 8-9 and Mix 11). The simultaneous combination of all the considered constituents (Mix 1) gave an EC_{50} value (7.25 µg/mL) 1.7-fold higher than expected (4.09 µg/mL, R = 0.56, additive). More specifically, limonene, *β*-ocimene, *p*-cymene, and farnesene showed synergistic effects with each other (Mix 3-7), synergy prevented by the presence of myrcene (Mix 1). In contrast, there was no negative effect of removing just one of these four active compounds (compare Mix 4-7 with Mix 3), suggesting that the synergy is not dependent on the presence of all four components.

Table 5. Comparative antitrypanosomal activity of six major components of the EO from *Anthriscus nemorosa* aerial parts. Stock solutions were prepared of the complete mixture and different alternative mixtures where one or several components were replaced by DMSO.

	Ratio% w/w							Observed *T.b. brucei* EC_{50} (µg/mL)	Observed Balb3T3 EC_{50} (µg/mL)	Selectivity index (SI)	Expected EC_{50}[a] (µg/mL)		
	Myrcene	*β*-pinene	Limonene	*β*-ocimene	*p*-cymene	Farnesene	Carrier (Acetone)				Wadley[b]	R[c]	S[d]
Mix 1	63.7	4.7	9.1	11.4	3.7	7.4	x	7.25 ± 0.26	28.3 ± 1.06	3.91	4.09	0.56	Add
Mix 2	x	4.7	9.1	11.4	3.7	7.4	63.7	2.25 ± 0.18	9.22 ± 0.67	4.11	4.54	2.01	Syn
Mix 3	x	x	9.1	11.4	3.7	7.4	68.4	1.43 ± 0.16	5.14 ± 0.36	3.63	4.63	3.23	Syn
Mix 4	x	x	x	11.4	3.7	7.4	77.5	1.58 ± 0.14	5.48 ± 0.31	3.47	5.00	3.17	Syn
Mix 5	x	x	9.1	11.4	3.7	x	75.8	1.27 ± 0.02	6.98 ± 0.85	5.46	7.80	6.14	Syn
Mix 6	x	x	9.1	11.4	x	7.4	72.1	1.06 ± 0.04	3.83 ± 0.19	3.62	4.81	4.53	Syn
Mix 7	x	x	9.1	x	3.7	7.4	79.8	1.40 ± 0.11	5.77 ± 0.15	4.11	8.88	6.34	Syn
Mix 8	63.7	4.7	x	x	x	7.4	24.2	15.3 ± 0.33	29.3 ± 3.42	1.91	8.58	0.56	Add
Mix 9	63.7	4.7	x	x	3.7	x	27.9	49.2 ± 3.71	66.8 ± 3.19	1.36	27.28	0.55	Add
Mix 10	63.7	4.7	x	11.4	x	x	20.2	27.1 ± 0.51	25.6 ± 1.21	0.94	7.57	0.28	Ant

Mix 11	63.7	4.7	9.1	x	x	x	22.5	24.3 ± 0.45	60.9 ± 2.87	2.51	22.4	0.92	Add

[a]Expected EC_{50} based on Wadley's calculation model.

[b]Wadley's calculation of expected EC50.

[c] Synergy ratio from Wadley's calculation.

[d] Determination of the interaction of the mixture based on Wadley's determination method: $R > 1.5$, synergistic (Syn) interaction; $1.5 \geq R > 0.5$, additive (Add) interaction; when $R \leq 0.5$, antagonistic interaction.

x = component not included in the Mix

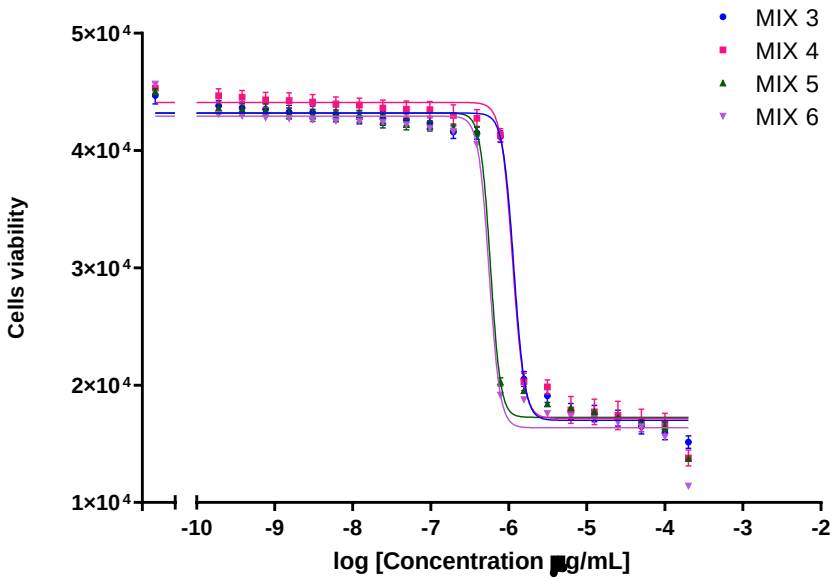

Figure 32. Tests of combinations of EO constituents against *T. brucei*. The different mixes are described in Table 5 and the curves are colored according to the following scheme: Mix 3 (blue curve), Mix 4 (fuchsia curve), Mix 5 (green curve), and Mix 6 (purple curve). Each EC_{50} value represents the mean of three independent experiments with standard errors.

2.2.1.4 Preparation and characterization of A. nemorosa EO-based nanoemulsions

A. nemorosa EO-AP nanoemulsions (NEs) were formulated in order to verify if the EO could be improved in terms of antitrypanosomal potential and safety profile. The surfactant polysorbate 80 at a concentration of 2% (w/w) was used as the stabilizing agent in these nanoemulsions (Table 6). An initial screening to assess the *A. nemorosa* EO-AP total oily phase and the surfactant percentages was carried out to select the final quali-quantitative composition of NEs named NANO A and NANO B (Table 6).

Table 6. Composition of the formulated *A. Nemorosa* EO-based NEs (NANO A and NANO B) and control

Samples	**Composition**
Control	Polysorbate 80 at 2% (w/w) in water
NANO A	2% (w/w) polysorbate 80 + 6% (w/w) *A. nemorosa* EO from aerial parts
NANO B	2% (w/w) polysorbate 80 + 4% (w/w) *A. nemorosa* EO from aerial parts + 2% (w/w) ethyl oleate

The obtained nanoemulsified systems were assessed by the absence of visible oily droplets through optical microscopy. The droplet size distributions of NEs were centered between 140 and 170 nm (mean diameter, Z-average) up to two months from the preparation for NANO A and up to four months for NANO B. At a longer storage time, both NEs showed an increase in the mean droplet diameter, more evident for NANO A than NANO B. Indeed, the mean droplet diameter reached approximately 700 nm for NANO A (after 9 months from the preparation), while it was below 300 nm for NANO B (Figure 33A). Moreover, the polydispersity Index values (PDI) were lower for NANO B than NANO A (Figure 33B). PDI is an indicator (ranging from 0 to 1) of the width of the distribution (a smaller index indicates a monodispersed system) (Sadeghi et al., 2015). Overall, these results highlight the role of ethyl oleate as co-solvent in the formulation, improving the particle size and stability of NEs.

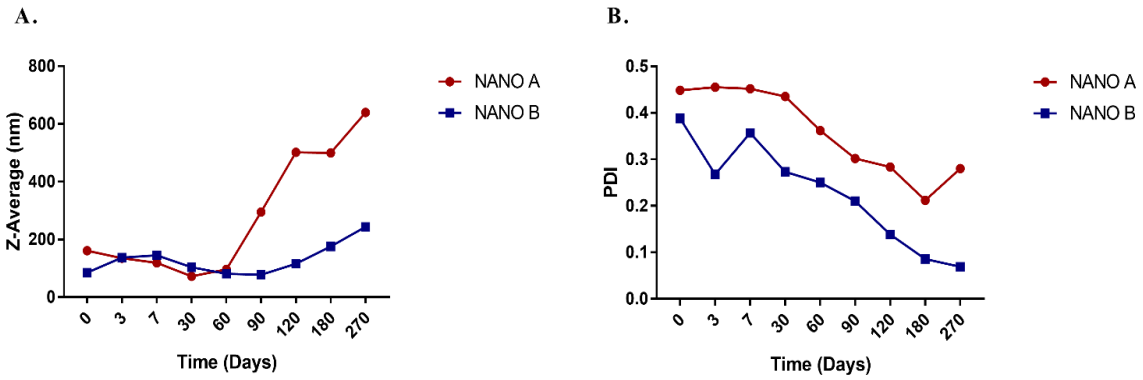

Figure 33. Mean droplet size (A) and polydispersity index (B) of *A. nemorosa* EO-based nanoemulsions at different time points. The mean droplet size is indicated as Z-Average with the diameter in nm.

Both the NEs were then tested to evaluate the influence of the nanoencapsulation on the biological activity of the active ingredients. To determine their *in vitro* antitrypanosomal activity and selectivity, NANO A and NANO B were tested on *T. brucei* s427 and Balb/3T3 cells following the same procedure used for EOs, pure compounds, and artificial mixtures. The activity of NANO A and NANO B resulted much lower than those obtained from pure *A. nemorosa* EO-AP, mainly because the NEs only contain 6% w/w of EO and the major fraction of the weight is constituted by water. For this reason, normalized EC_{50} values by the percentage of EO in the NEs were included (Table 7, in brackets). Even normalized EC_{50} values result higher than the EC_{50} obtained with the EO itself, but NEs are evidently less toxic to mammalian cells (SI > 5). A possible explanation of these results is that the NEs prevent both the effect of the EO on the trypanosomes and on the mammalian cells, but this ameliorating effect seems to

be stronger on mammalian cells, especially with NANO A, resulting in a two times higher SI when compared to the EO itself.

Table 7. Antitrypanosomal activity of *A. nemorosa* EO from aerial parts (EO-AP) and nanoemulsions using NANO A and NANO B.

	EC_{50}		**Selectivity**
	***T. brucei* (s427)**	**Balb3T3**	**Index (SI)**
Nanoemulsions	**µg/mL**	**µg/mL**	
Control	>40000	>40000	
NANO A	167.4 ± 12.8 (normalized 9.89 ± 0.797)	1399 ± 464	8.35
NANO B	322.3 ± 43.5 (normalized 12.7 ± 1.72)	1745 ± 347	5.41

2.2.1.5 Determination of NTP and ADP pools in T. brucei

The effect of *Anthriscus nemorosa* EO-AP and *Anthriscus nemorosa* EO-R on *T. brucei* was investigated through the determination of nucleotide pools of cells grown in culture. Nucleotides were extracted from the parasites and separated by HPLC for quantification. The treatment of trypanosomes with different concentrations of the EOs (0-10 µg/mL) led to a concentration-dependent decrease of all NTP pools (Figure 34A). The four NTPs result equally affected at the lower EO concentration (5 µg/mL), and little deviation is observed at the higher dose. This appears clearer in figure 34B where relative nucleotide pools are plotted as a percentage of the total NTP pool. Relative ADP pools are instead strongly affected by the treatment, suggesting a disturbance of the cellular energy charge (ATP:ADP ratio). Both *Anthriscus nemorosa* EO-AP and *Anthriscus nemorosa* EO-R exerted these effects.

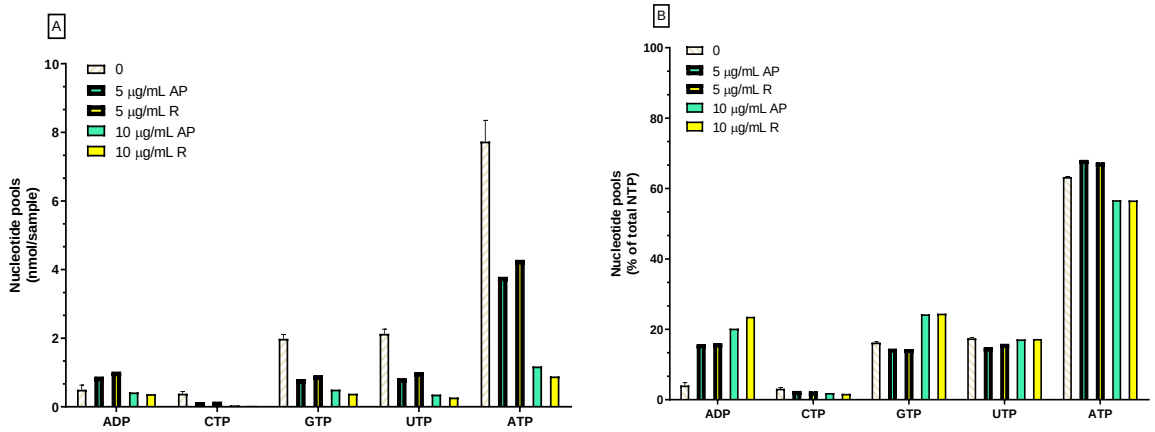

Figure 34. Effect of *A. nemorosa* EOs on *T. brucei* nucleotide pools. A. Levels in nmol per sample of nucleoside triphosphates (NTPs) and ADP when *T. brucei* cells are treated with different concentrations of *A. nemorosa* EO-AP and *A. nemorosa* EO-R; B. Same data as in A, but the nucleotides are replotted as a percentage of the total NTP pool.

2.2.2 Discussion

EOs represent a promising alternative to traditional drugs because of their ability to cross cellular membranes, thanks to their lipophilic nature, and the possibility of interacting with intracellular targets. In this regard, EOs could play pivotal roles against pathogen survival, proliferation, and differentiation (Dhifi et al., 2016). The chemical compositions of the EOs obtained from the aerial parts and roots of a central Italian variety of *A. nemorosa* significantly differ from those previously reported for this species. Karakaya and colleagues found indeed high levels of spathulenol (49.6%) and biclycogermacrene (8.9%), whereas myrcene was practically absent in the aerial parts of a Turkish population (Karakaya et al., 2019). In a study by Nickavar and colleagues, an Iranian population was evaluated and (*E*)-nerolidol (41.7%), *β*-elemene (13%), and *α*-zingiberene (9.9%) were found as the major constituents of the aerial parts of *A. nemorosa* (Nickavar et al., 2009). Instead, (*E*)-caryophyllene (23.6%), caryophyllene oxide (12.3%), *δ*-cadinene (12.1%), and *trans*-pinocarveol (9.8%) were identified as major constituents of aerial parts EO of *A. nemorosa* from another Turkish population (Wagner and Ulrich-Merzenich, 2009). Lastly, Kiliç et al. reported that (*E*)-caryophyllene (15.8%), caryophyllene oxide (14.5%), *δ*-cadinene (13.4%), germacrene D (8.9%) and *trans*-pinocarveol (6.2%) are the most abundant components of aerial parts EO of *A. nemorosa* from Turkey (Kiliç, 2017). Results from the present work compared to the current literature, revealed that

geographic origin, genetics, period of harvesting and environmental conditions, type of processing, and drying could be decisive factors for the nature of the composition of *A. nemorosa* EOs.

This peculiar composition of the EOs certainly had an impact on their antiprotozoal potential. *A. nemorosa* EOs from both aerial parts and roots showed a relevant antitrypanosomal activity with EC_{50} values of 1.17 µg/mL (SI = 4.65) and 2.36 µg/mL (SI = 2.25), respectively (Table 4). Despite the fact that plant EOs frequently exhibit stronger antiparasitic activity with respect to their individual constituents, concerning *A. nemorosa* EOs, the major activity came from two less abundant components, farnesene and *β*-ocimene. When separately tested, they demonstrated comparable or greater antitrypanosomal effects when compared to the natural *A. nemorosa* EO-AP. Farnesene exhibited a lower EC_{50} value (0.85 µg/mL) compared both to the intact oil (1.17 µg/mL) and the best artificial mixture (1.06 µg/mL for Mix 6, Table 4), in which, among the other compounds, farnesene is the most concentrated. Although the intact oil exhibits a lower activity than farnesene, it is interesting to notice that the EC_{50} values are comparable even though the two major antitrypanosomal agents, farnesene and *β*-ocimene, together make up only 11.9% of the total EO. Due to this outcome, synergistic interactions in the EO were investigated.

Additive, synergistic, and antagonistic interactions among constituents of *A. nemorosa* EO-AP were evaluated. Eleven artificial mixtures were prepared, and *in vitro* activities of the blends were compared to EC_{50} values calculated using Wadley's model (expected EC_{50} values). Mix 1 was a blend of all major constituents, mimicking the natural EO but excluding components with no antitrypanosomal activity. The other mixtures were prepared differently, each lacking one or several major constituents being replaced by acetone (Mix 2-11), relying on the natural composition of aerial part EO as indicated by GC-MS. When the six main constituents were present (Mix 1), the observed antitrypanosomal activity was not as high as expected (EC_{50} = 7.25 µg/mL of Mix 1 vs. EC_{50} = 1.17 µg/mL of the intact EO), assessing an additive relationship among the constituents of the mixture (R = 0.56). this suggested that the inactive constituents removed from Mix 1 have some additional synergistic effects on the six components. Indeed, their presence seems necessary to achieve the observed antitrypanosomal efficacy, even if, they don't exert any activity singularly. As shown in Table 5, the activity of *A. nemorosa* EO from aerial parts might be attributed to the presence of its bioactive constituents, limonene, β-

ocimene, *p*-cymene and farnesene (5.7%, 7.2%, 2.2% and 4.7% in the natural EO and 9.1%, 11.4%, 3.7% and 7.4% in the artificial EO, respectively). Mixes 3-7 were prepared mixing these components (Mix 3-7 in Table 5) and they showed strong synergy with R values between 3-6. Considering the concentrations of those four components in the *A. nemorosa* EO-AP (19.8% combined) and their increased activity when combined, the antitrypanosomal activity of the intact oil might be a consequence of their synergistic interaction. Interestingly, this synergy was weakened in the presence of *β*-pinene and completely disappeared in the presence of myrcene. In the EO itself, the antagonistic effects from myrcene and *β*-pinene seem not to be detectable and the EC_{50} value is comparable to Mix 3 where only the synergistic components are present (1.17 µg/mL and 1.43 µg/mL for the EO and Mix 3, respectively).

Artificial mixtures based on EO composition can be successfully used as a multi-target strategy for tackling trypanosomiasis rather than single isolated components. Moreover, investigating the contribution of the various components could help in understanding how to develop more potent antitrypanosomal drugs based on custom blends of monoterpenoids/sesquiterpenoids. Several mechanisms are triggering synergistic interactions. Nonetheless, Wagner and Ulrich-Merzenich indicated four plausible mechanisms: (1) bioavailability effects based on absorption rate and solubility; (2) respective elimination of adverse effects; (3) synergistic multitarget effects and (4) interactions of principal components with resistance mechanisms (Wagner and Ulrich-Merzenich, 2009). One or more of these proposed mechanisms can cause the synergistic interaction detected in the present study. *A. nemorosa* EO-AP is indeed a complex mixture of components that can act differently based on their chemical properties. For example, monoterpenes like limonene, characterized by a cycle bearing an exocyclic methylene group, can react with functional groups of proteins, such as trypanothione synthase, producing cell oxidative damage (Wink, 2008). A different effect is exerted by the aromatic monoterpene *p*-cymene, that, being highly hydrophobic, is easily incorporated into the lipidic membranes, facilitating the penetration of other bioactive components. Its antiprotozoal properties have already been evaluated in a previous study conducted by Monzote and colleagues (Monzote et al., 2012). The acyclic monoterpene hydrocarbon *β*-ocimene, appears instead involved in the plant defense strategies against predators and the first report of its effect against *T. brucei* dates back to 2018 (EC_{50} of 1.1 µg/mL and SI > 91) (Cascone et al., 2015; Kamte et al., 2018). The acyclic olefin (*E*)-*β*-farnesene is produced by several plants as an aphid repellant effective on

various species. Although (*E*)-*β*-farnesene is widespread in plants, this is the first report concerning its antitrypanosomal effectiveness (EC_{50} = 0.84 µg/mL).

In general, EOs exert many biological activities. However, their use is often constrained by several drawbacks such as chemical instability (i.e., polymerization, isomerization, oxidation, and rearrangement), and poor physicochemical properties (e.g., water insolubility, high volatility, and a short half-life) which may end up in a reduction or loss of activity. Nanoemulsions (NEs) of EOs reveal to be interesting tools to overcome these issues, by improving their physicochemical properties and stability. Plus, due to their subcellular size, NEs could enhance tissue penetration and facilitate cellular uptake improving the bioavailability and effectiveness of the active compounds through their solubilization into tiny oily droplets. Previous studies demonstrated the effectiveness of NEs as vehiculating tools for EOs against parasites of medical importance, including *Plasmodium*, *Leishmania*, and *Trypanosoma*. For instance, in a study carried out by Bouyahya and colleauges in 2017, NEs of *Lavandula angustifolia* L. and *Rosmarinus officinalis* L. EOs showed greater antiparasitic effects when compared to the non-emulsified EOs (Bouyahya et al., 2017). In the present study, the NEs resulted in higher EC_{50} values than the ones obtained for the *A. nemorosa* EO-AP. However, the mammalian control cell lines were less sensitive as well, accounting for a slightly better SI. SI against the trypanosomes in comparison to the mammalian cells was higher for NANO A than for the *A. nemorosa* EO-AP (SI = 8.42 for NANO A and 4.65 for the *A. nemorosa* EO-AP).

A potential mechanism of action for *A. nemorosa* EO-AP and *A. nemorosa* EO-R has been hypothesized by measuring NTP and ADP pools through an HPLC analysis. As shown in Figure 4, the treatment of the parasites with the EOs led to a general decrease in the NTP pools and increased relative ADP levels. The increased ADP levels are a sign of disturbances in the energy metabolism, suggesting that the cell is not able to efficiently phosphorylate ADP to ATP. Consequently, other NTP concentrations are enhanced because of their metabolic interdependence through NDP kinase and other enzymes. Indeed, NDP kinase uses NTPs to phosphorylate NDPs. Physiologically, ATP is the most preferable source of phosphate groups since it is the most concentrated in the cell, but other NTPs can also exploited, depending on their abundance. The decrease of other NTP pools is, therefore likely to be a consequence of the disturbed energy metabolism. Another factor that can explain the lowering of nucleotide

levels is that the cells are massively dying, and the number of living cells is, therefore, very low at the end of the incubation period when compared to the untreated cells. An attempt to minimize the influence of this factor was made by keeping the incubation period short. However, with the higher dose of EO, the NTP pools were even more decreased, with no further increase in the ADP pools, indicating that cell death can be a contributing factor also in this short time frame when the EO concentration is high enough. A disturbed energy metabolism is very harmful to the cell, which needs ATP to keep intracellular ion concentrations intact.

2.3 Extracts

2.3.1 Results

2.3.1.1 Extracts production

Aerial parts and roots from *A. nemorosa* were collected, dried and shredded. Two extraction processes were used: digestion with stirring (40 °C for 3 hours), and maceration with ultrasounds (2.40 hours). For both processes, the solvent used was methanol (MeOH). The solvent was separated from the exhausted material through filtration, and it was discolored with activated carbon. After the removal of carbon through further filtration, the methanol was evaporated under pressure using a rotary evaporator to obtain the total extract.

The starting methanolic extracts obtained from both digestion and maceration processes, were subsequently dissolved in water and extracted to produce fractions using solvents at growing polarity, namely hexane, dichloromethane (DCM), ethyl acetate (EtOAc), and *n*-butanol (*n*-BuOH). All the obtained products are reported in the schemes below (Scheme 1 and 2).

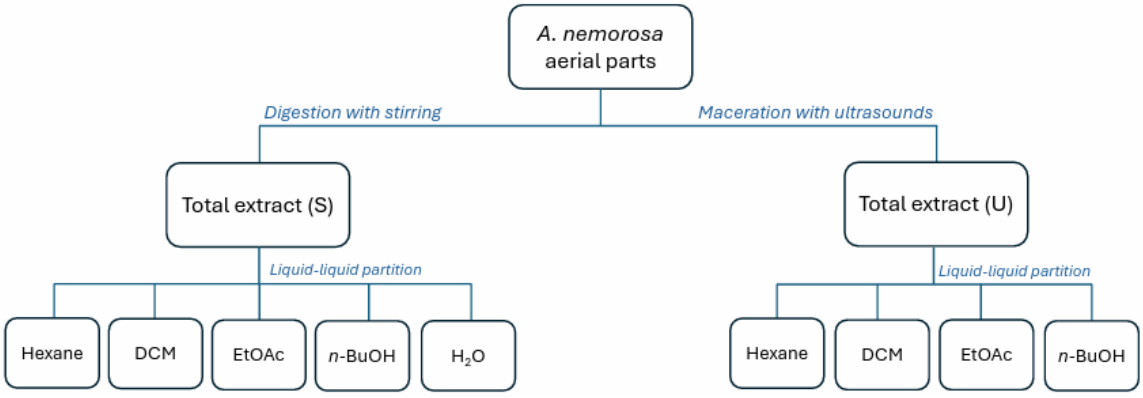

Scheme 1. Extracts and fractions obtained from aerial parts of *A. nemorosa* using solvents at growing polarity (hexane, DCM, EtOAc, and *n*-BuOH). S = digestion with stirring; U = maceration with ultrasounds.

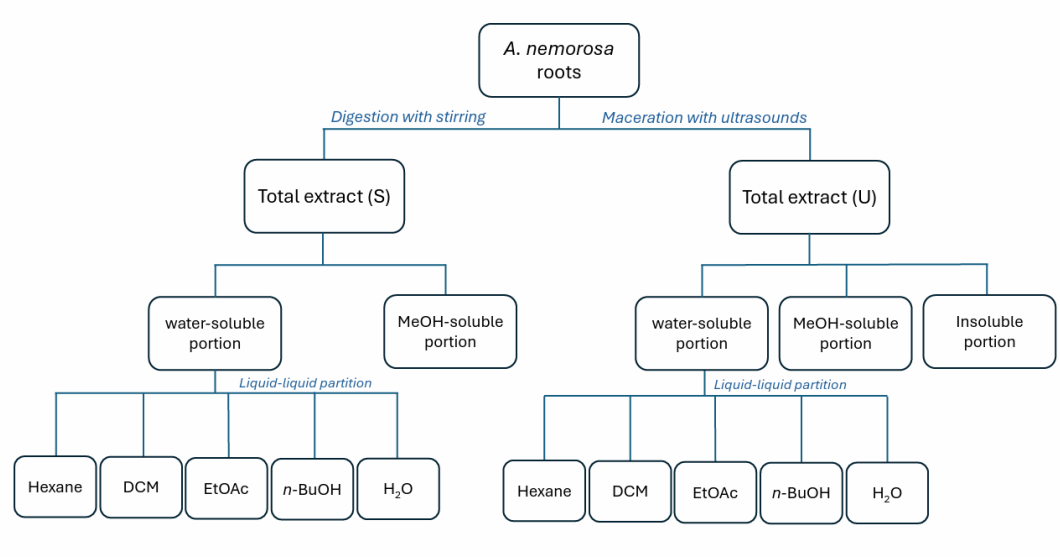

Scheme 2. Extracts and fractions obtained from roots of *A. nemorosa* using solvents at growing polarity (hexane, DCM, EtOAc, and *n*-BuOH). S = digestion with stirring; U = maceration with ultrasounds.

Yields were generally higher for fractions obtained by digestion with stirring than those prepared by maceration with ultrasounds (see Tables S1 and S2 in supporting information). However, all fractions were tested against *T. brucei* to verify if any difference in their activity against the parasite was detectable.

2.3.1.2 In vitro antitrypanosomal activity

Anthriscus nemorosa root and aerial part extracts and all fractions obtained from the liquid-liquid partition were assayed *in vitro* on *T. brucei* bloodstream forms, and their cytotoxicity evaluated against mammalian cells (BALB/3T3 mouse fibroblasts). Results are reported in Table 11. No significant difference in terms of antiprotozoal activity between the two procedures used to obtain the extracts was detected (except for a few fractions); for this reason, the fractions obtained by digestion with stirring, which produced the best yields, were selected for the subsequent analyses.

As noticeable from Table 8, the total methanolic root extract resulted 26 times more active against *T. brucei* than the aerial part extract (EC_{50} = 32.2 and 824 μg/mL, respectively). This preliminary screening determined the total root extract as the most promising candidate. The fractions obtained by its liquid-liquid partition (hexane, DCM, EtOAc, *n*-BuOH, and MeOH fractions) were also tested against *T. brucei* and, when activity was relatively high (EC_{50} < 50 μg/mL), on BALB/3T3 cells. The MeOH fraction was by far the most active fraction, with a

four-fold higher activity than the total methanolic extract against *T. brucei* (EC_{50} = 8.03 and 32.2 μg/mL, respectively). Unfortunately, the selectivity index (SI) for the Root MeOH fraction was 0.02, showing a preferential effect on mammalian cells than on parasites cells and thus, an important cytotoxicity. With the aim to improve SI against *T. brucei*, the MeOH fraction was subjected to a phytochemical characterization and to a bio-guided fractionation in order to produce less cytotoxic sub-fractions.

Table 8. *In vitro* activity of aerial parts, root extracts and fractions from *A. nemorosa*, obtained by digestion with stirring (on the left column) and maceration with ultrasounds (right column), against *T. brucei* and Balb/3T3 cells.

Treatment	EC_{50} (μg/mL)		Selectivity Index (SI)	EC_{50} (μg/mL)		Selectivity Index (SI)
	***T. b. brucei* (s427)**	**Balb/3T3**		***T. b. brucei* (s427)**	**Balb/3T3**	
Aerial part	***Digestion with stirring***			***Maceration with ultrasounds***		
Total methanolic extract	824 ± 8.06	n.d.*	-	1003 ± 9.4	n.d.	-
H_2O fraction	52.3 ± 4.07	n.d.	-	60.1 ± 5.74	n.d.	-
Hexane fraction	17.9 ± 0.62	0.12 ± 0.03	0.007	9.49 ± 0,63	0.002 ± 0.0003	0.0002
DCM fraction	24.9 ± 3.27	0.03 ± 0.002	0.001	64.6 ± 5.23	n.d.	-
EtOAc fraction	62.1 ± 4.22	n.d.	-	535 ± 7.82	n.d.	-
n-BuOH fraction	193 ± 5.23	n.d.	-	936 ± 10.1	n.d.	-
H_2O residual fraction	n.a.[#]	n.d.	-			
Root	***Digestion with stirring***			***Maceration with ultrasounds***		
Total methanolic extract	32.2 ± 2.83	0.12 ± 0.04	0.004	20.2 ± 1.41	0.09 ± 0.005	0.004
H_2O fraction	54.6 ± 3.03	n.d.	-	70.6 ± 4.14	n.d.	-

Hexane fraction	18.7 ± 1.29	0.03 ± 0.004	0.002	14.4 ± 0.68	0.06 ± 0.004	0.004
DCM fraction	17.1 ± 0.83	0.04 ± 0.003	0.002	49.3 ± 2.38	n.d.	-
EtOAc fraction	21.9 ± 1.95	0.23 ± 0.07	0.01	108 ± 3.64	n.d.	-
n-BuOH fraction	587	n.d.	-	557 ± 6.76	n.d.	-
MeOH fraction	8.03 ± 0.33	0.15 ± 0.02	0.02	8.77 ± 0.21	0.007 ± 0.004	0.0008
H_2O residual fraction	n.a.[#]	n.d.	-	n.a.[#]	n.d.	-

* n.d. not determined; [#]n.a. not active

2.3.1.3 Characterization of the Root MeOH fraction by HPLC-MS^n

The HPLC chromatogram of the Root MeOH fraction of *A. nemorosa* is shown in supporting information (Fig. S3). Lignans, phenylpropanoid esters, and flavonoids were identified, accounting for a total of 14 compounds (Figure 35). Identification was performed based on comparison with pure reference compounds using HPLC, molecular weights, and fragment ions by HPLC–MS (Table 9). The main lignans in *A. nemorosa* are podophyllotoxone (**4**) and deoxypodophyllotoxin (**6**) and they were detected through comparison of the retention time of reference compounds by HPLC, the molecular weight (412 and 398, respectively), and the fragment ions. Our data are in agreement with those reported in the literature. Compound **8** was identified as anthriscinol methyl ether, a phenylpropanoid derivative, based on its molecular weight (222), and fragment ions. Fragment ion patterns (191, 151, 120) suggested that compound **9** is *O*-[(*Z*)-2-angeloyloxymethyl-2-butenoyl]-3-methoxy-4,5-methylendioxyamyl alcohol, namely anthriscusin. Anthriscusin is a phenylpropanoid ester derived from anthriscinol and (*Z*)-2-angeloyloxymethyl-2-butenoic acid (compound **14**). Compound **14** has been identified as (*Z*)-2-angeloyloxymethyl-2-butenoic acid, an acyloxycarbocyclic acid, based on its molecular weight (198), and MS fragmentation. Also, chlorogenic acid (**11**) and luteolin-7-*O*-glucoside (**13**) were isolated and identified from the Root MeOH fraction. Chlorogenic acid is a well-known antioxidant with DNA-protecting properties, whereas luteolin-7-*O*-glucoside shows an antioxidant activity comparable to epigallocatechin and epigallocatechin gallate (EGCG).

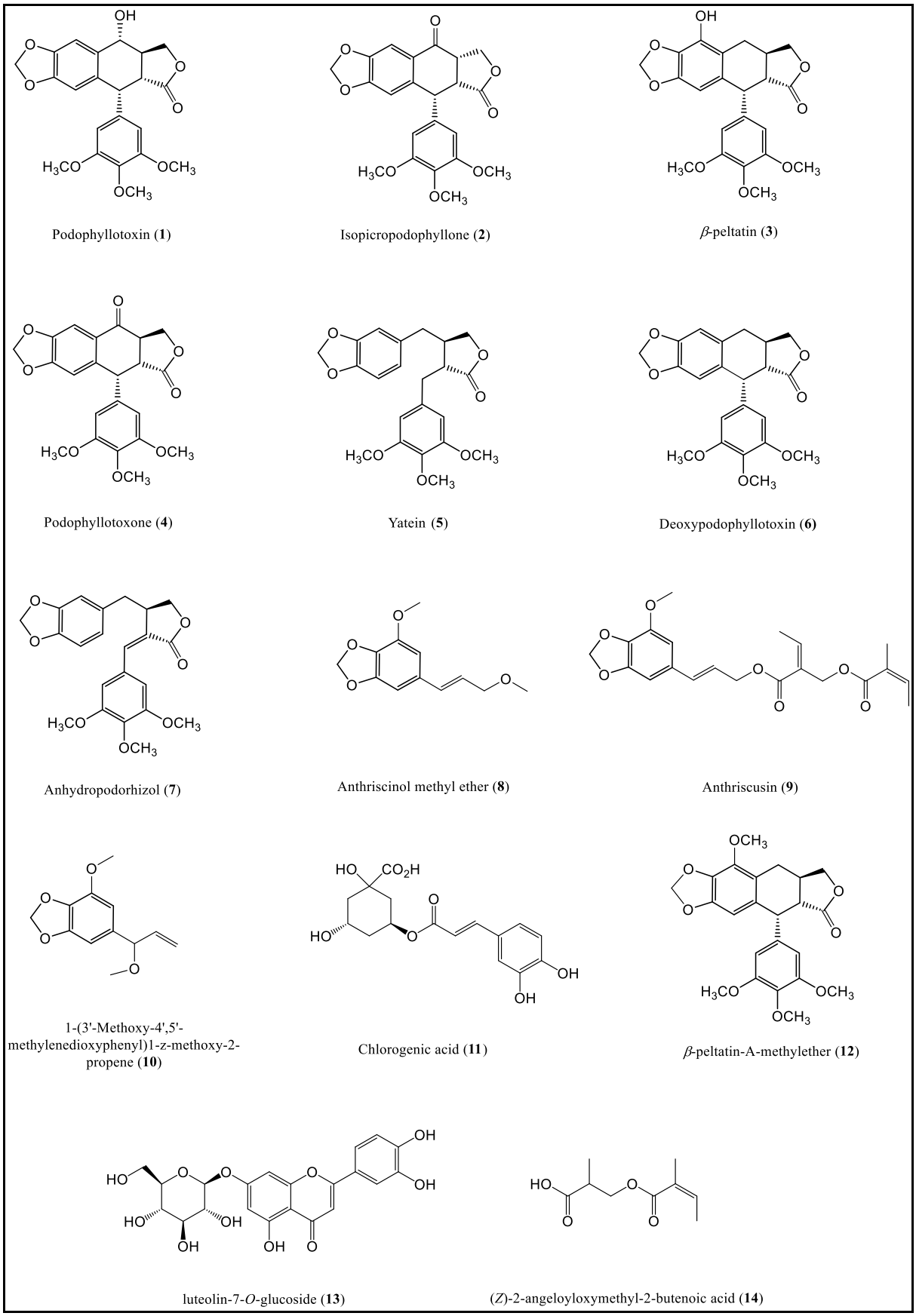

Figure 35. Chemical structures of identified compounds **1-14**.

Table 9. HPLC-MS constituents identified in the Root MeOH fraction of *A. nemorosa*.

Ret. time	Compound	MW	Molecular ions $[M+NH_4]^+$ or $[M+H]^+$	Fragments
8.35	Podophyllotoxin (**1**)	414	432	313, 247, 229. 185
9.74	Isopicropodophyllone (**2**)	412	430	245, 201
10.58	*β*-Peltatin (**3**)	414	432	247, 229, 203, 185
10.81	Podophyllotoxone (**4**)	412	430	245, 201
11.47	Yatein (**5**)	400	418	223, 181
11.77	Deoxypodophyllotoxin (**6**)	398	416	231, 187
12.15	Anhydropodorhizol (**7**)	398	416	231, 135
12.48	Anthriscinol methyl ether (**8**)	222	223	191, 161
12.81	Anthriscusin (**9**)	388	406	191, 151, 120
13.74	1-(3′-Methoxy-4′,5′-methylenedioxyphenyl)1-z-methoxy-2-propene (**10**)	222	229	191, 161
15.25	Chlorogenic acid (**11**)	354	355	191, 179
16.31	β-Peltatin-A-methylether (**12**)	428	446	261, 217
17.45	luteolin-7-*O*-glucoside (**13**)	448	449	285, 240, 198, 133
18.52	(*Z*)-2-Angeloyloxymethyl-2-butenoic acid (**14**)	198	199	181

2.3.1.4 Bio-guided fractionation of the Root MeOH fraction, isolation of its main components, and in vitro evaluation of the antitrypanosomal activity

Root MeOH fraction was subjected to column chromatography over silica gel eluting with mixtures of hexanes-EtOAc of increasing polarity to afford twelve fractions, which were then combined based on their TLC profile into three sub-fractions (named A to C). The composition of each fraction has been determined by HPLC (using the same method described before) and is reported in Table 10.

Table 10. Chemical composition of fractions A-C.

Fractions	Components
Fraction A	Podophyllotoxin (**1**)
	Isopicropodophyllone (**2**)
	β-Peltatin (**3**)
	Podophyllotoxone (**4**)
	Yatein (**5**)
	Deoxypodophyllotoxin (**6**)
Fraction B	Anhydropodorhizol (**7**)
	Anthriscinol methyl ether (**8**)
	Anthriscusin (**9**)
	1-(3′-Methoxy-4′,5′-methylenedioxyphenyl)1-z-methoxy-2-propene (**10**)
Fraction C	Chlorogenic acid (**11**)
	β-Peltatin-A-methylether (**12**)
	luteolin-7-*O*-glucoside (**13**)
	(*Z*)-2-Angeloyloxymethyl-2-butenoic acid (**14**)

As reported in Table 11, sub-fraction B showed the best biological profile against the parasites with almost five-fold higher activity than the MeOH extract (EC_{50} = 1.86 and 8.03 μg/mL, respectively), and an improved selectivity index (SI = 2.61). Instead, the sub-fractions A and C showed an EC_{50} against *T. brucei* cells comparable to that of the MeOH fraction (EC_{50} = 12.9 and 7.53 vs 8.03 μg/mL, respectively), and a remarkable toxicity towards mammalian cells.

Table 11. Inhibitory effects of sub-fractions, pure compounds, and suramin against *T. brucei* and Balb/3T3 cells.

Treatment	EC_{50} (μg/mL)		Selectivity Index (SI)
	***T. brucei* (s427)**	**Balb/3T3**	
Sub-fractions from MeOH fraction			
Sub-fraction A	12.9 ± 1.45	0.06 ± 0.03	0.005
Sub-fraction B	1.86 ± 0.14	4.83 ± 0.16	2.61
Sub-fraction C	7.53 ± 0.14	1.07 ± 0.13	0.14
Pure compounds			
Anthriscusin	10.4 ± 1.65	20.9 ± 1.22	2.01
Podophyllotoxin	33.2 ± 3.28	0.005 ± 0.0001	0.0002
Deoxypodophyllotoxin	45 ± 4.68	0.009 ± 0.0001	0.0002
Reference drug			
Suramin	0.0191 ± 0.002	>100	>100

Thus, sub-fraction B was subjected to repeated chromatographic separations to afford the pure compound anthriscusin (**9**), which has been characterized based on its NMR and MS spectroscopic data, and comparison with data reported in the literature (Table 12). In the same way, sub-fraction A was subjected to repeated chromatographic separations to afford the two lignans, podophyllotoxin (**1**) and deoxypodophyllotoxin (**6**). Unfortunately, it was not possible to isolate any other pure compound from sub-fraction C. Isolated podophyllotoxin (**1**), deoxypodophyllotoxin (**6**), and anthriscusin (**9**) were also tested against *T. brucei*, and BALB/3T3 cells and suramin has been used as the reference drug (Table 14).

Table 12. ^{1}H (400 MHz) NMR spectral data of Anthriscusin (**9**) in $CDCl_3$

Position	**d_H, mult. (*J* in Hz)**
1	6.57 d (11.6)
2	5.78 dt (11.6, 6.6)
3	4.96 dd (6.6, 1.4)
1’	-
2'	6.45 (br s)
3'	-
4'	-
5'	-
6’	6.46 (br s)
-OC*H*$_2$O-	6.00 s
-OC*H*$_3$	3.92 s
1"	-
2"	-
3’’	6.49 q (7.2)
4’’	2.13 d (7.2)
5"	4.85 s
1'"	-
2"’	-
3’’’	6.08 qd (7.2, 1.4)
4’’’	1.97 dq (7.2, 1.4)
5’’’	1.89 p (1.4)

2.3.2 Discussion

Anthriscus nemorosa extracts are, unfortunately understudied. For organic extracts of this plant, only antioxidant potential and preliminary anticancer activity were assessed. Ethyl acetate extracts from roots of *A. nemorosa* seem indeed to exert antioxidant activity by inhibiting acetylcholinesterase, whereas *n*-hexane extracts from aerial parts exhibit *in vitro* cytotoxic activity on breast cancer cell lines (Karakaya et al., 2019; Forouhandeh et al., 2021). Few studies report pharmacological potential for other species of the Anthriscus family. Aqueous extracts from *Anthriscus sylvestris* (L.) Hoffm. leaves revealed their role as anti-inflammatory agents, demonstrating effectiveness in chondroprotection and in the treatment of lung inflammation (Lee et al., 2018a; Lee et al., 2018b; Kim et al, 2019). Extracts derived from aerial parts and roots of *Anthriscus cerefolium* (L.) Hoffm. showed scavenger effects on DPPH and hydroxyl radicals, confirming their value as antioxidant agents (Fejes et al., 2000). As far as is known, the present study is the first report on the antiprotozoal activity of *A. nemorosa* extracts.

Extracts from aerial parts and roots were prepared using two different procedures in order to select the most performing technique in terms of yield and biological activity. Comparing the two processes, digestion with stirring at 40°C for 2.4 h provided higher yields and a slightly enhanced antiparasitic activity. Indeed, the aforementioned parameters allowed us to obtain extracts from aerial parts and roots that accounted for 14.95% and 8.41%, respectively of the starting amounts of material processed. Maceration with ultrasounds instead, produced lower amounts of extracts; the process gave a yield of 10.64% for the aerial parts and of 7.19% for the roots. Even the liquid-liquid partition of the extracts obtained through digestion produced higher amounts of organic fractions (hexane, DCM, EtOAc and *n*-BuOH fractions), whereas the maceration extract gave a higher amount in residual-water fraction, suggesting that the first extraction process gave a product with a more various composition, richer in different polarity compounds.

The extract obtained through digestion and the relative fractions obtained by liquid-liquid partition were selected for subsequent analyses, since they also demonstrated a slightly better activity against *T. brucei*. In general, as noticeable from table 11, both the starting extract and the derived fractions showed lower or comparable EC_{50} values with respect to the maceration extract and fractions. Unfortunately, from the results of the cytotoxicity tests, they all appear to preferentially act on mammalian cells, assessing their non-selectivity for *T. brucei*. To overcome this issue and enhance the selectivity index, the fraction that demonstrated the most potent antitrypanosomal effect, namely

the methanolic fraction from the root extract (Root MeOH fraction), was selected for further investigations.

The fraction was analyzed through HPLC-DAD-MS and 14 compounds were identified. Among these, the phenylpropanoid ester anthriscusin (isolated for the first time in 1978 by Kozawa and colleagues from *A. sylvestris*) and two cytotoxic renowned lignans, namely podophyllotoxin and deoxypodophyllotoxin. This was not surprising, since Fejes and colleagues previously highlighted the massive presence of these two lignans in the aqueous extracts of *A. cerefolium* roots (Fejes et al., 2003). The two compounds were suggested as the components likely to be responsible for the strong activity on mammalian cells. This hypothesis was confirmed by the *in vitro* tests performed for sub-fractions (A-C) and isolated compounds, obtained by silica-gel chromatography of the Root MeOH fraction. The starting fraction was indeed sub-fractionated using gradient-based hexane/ethyl acetate mixtures in several rounds.

Sub-fractions A and B were further purified to afford podophyllotoxin and deoxypodophyllotoxin from the first and the phenylpropanoid ester anthriscusin from the second one. As expected, both sub-fraction A and the two lignans isolated from it, revealed a strong cytotoxicity. Fraction B, instead, showed the best biological profile against the parasites with almost five-fold higher activity than the Root MeOH fraction (EC_{50} = 1.86 and 8.03 μg/mL, respectively), and an improved SI (2.61). Anthriscusin exhibited relatively strong activity against *T. brucei* cells (EC_{50} = 10.4 μg/mL) and did not significantly affect the mammalian cells (SI = 2.1). However, it is worth pointing out that sub-fraction B demonstrated a lower EC_{50} (1.86 μg/mL) than pure anthriscusin. The observed antitrypanosomal activity might be a consequence of a synergistic interaction between anthriscusin and different components present in sub-fraction B (i.e., anhydropodorhizol and/or anthriscinol methyl ether). This kind of synergistic phenomenon is very common in extracts characterized by wide chemical compositions like that of *A. nemorosa*. To the best of our knowledge, this study provides the first report on anthriscusin as a potential antiprotozoal agent.

2.4 Conclusion

To the best of our knowledge, this is the first report on the antiprotozoal activity of *A. nemorosa* derived products. The overall results of this study have indeed highlighted the potential of *A. nemorosa* EOs and extracts as relevant sources of bioactive substances and paved the way toward the opportunity to develop new prototypes for future antitrypanosomal drug development. The sesquiterpene farnesene stood out as a promising drug candidate among the main constituents of the EO from aerial parts of *A. nemorosa*. Moreover, the *in vitro* tests on *T. brucei* of artificial mixtures

assessed the synergistic and additive properties of the most abundant compounds present in the EO. Limonene, *β*-ocimene, *p*-cymene, and farnesene seemed to behave synergistically when simultaneously present, whereas myrcene exhibited a protective effect. An attempt to improve the physicochemical characteristics of this promising EO from *A. nemorosa* was made through the preparation of nanoemulsions, resulting in an increased safety profile. Finally, the EOs mechanism of action was investigated. A significant decrease in NTP pools and a concomitant increase in ADP detected through HPLC analysis suggested a strong affection of *T. brucei* energy metabolism. However, further studies are needed to understand the more exact mode of action and the possible molecular targets related to the antitrypanosomal activity of *A. nemorosa* EOs.

Concerning extracts, the root extract appeared to be the most interesting for its pronounced activity with respect to the aerial parts extract, pushing the research to deepen and improve both the efficacy and the selectivity index. A first bio-guided fractionation of the root extract was performed with solvents at different polarities and the methanolic fraction was selected to be further sub-fractioned. From the sub-fractions it was possible to isolate three main components (podophyllotoxin, deoxypodophyllotoxin, and anthriscusin), and their antitrypanosomal activity was evaluated *in vitro*. The results revealed that the two lignans are the responsible compounds for the cytotoxic activity on mammalian cells, while anthriscusin exerts a mild antiprotozoal activity that is enhanced when administered together with anhydropodorhizol and/or anthriscinol methyl ether (components of the starting sub-fraction B from which anthriscusin was isolated). The synergistic relationships among the constituents of sub-fraction B need to be deepened with future investigations.

2.5 Materials and Methods

2.5.1 Plant material

Aerial parts and roots of a wild population of *A. nemorosa* growing in Camerino, central Italy (620 m a.s.l., N 43°1'3.78''; E 13°06'9.68'') were collected in May 2019 and April 2021. A voucher specimen was authenticated by one of the authors (F.M.) and deposited in the Herbarium Universitatis Camerinensis (CAME, included in the online edition of Index Herbariorum c/o School of Biosciences and Veterinary Medicine, University of Camerino, Italy) under the code CAME#29276; it was also archived in the anArchive system for Botanical Data (http://anarchive.it).

2.5.2 Chemicals

Pure constituents of the EOs were purchased from Sigma-Aldrich [β-pinene (99%), farnesene (a mixture of isomers), limonene (97%), ocimene (a mixture of α and β isomers), *p*-cymene (99%), γ-terpinene (97%), St Louis, MO, USA], and Merck (myrcene; Darmstadt, Germany).

2.5.3 Hydrodistillation

Hydrodistillation (HD) was performed on dried samples of aerial parts and roots of *A. nemorosa*. In both cases, we used 2.5 kg of plant material soaked in a 20 L glass flask filled with 12 L of water, heated by a mantle system Falc MA (Falc Instruments, Treviglio, Italy) for 5 h. The EOs were recovered by a glass Clevenger-type apparatus and stored at 4°C before chemical characterization and biological evaluation. The EO yield was calculated on a dry-weight basis.

2.5.4 GC-MS analysis

The chemical composition of *A. nemorosa* EOs was analyzed through an Agilent 6890N GC-MS system coupled to a 5973N single quadrupole detector mass spectrometer. The separation was provided by an HP-5MS capillary column (5% phenylmethylpolysiloxane, 30 m x 0.25 mm i.d., 0.1 µm f.t., Agilent, Santa Clara, CA, USA). The temperature program was as follows: 60 °C for 5 min, then 4 °C min-1 up to 220 °C, finally 11 °C min-1 to 280 °C, maintained for 15 min, for a total run time of 65 min. The temperature of the injector and detector was 280 °C. Helium (He) was the carrier gas, with a flow rate of 1 mL min-1 and a 1:50 split ratio. The chromatograms were acquired in full scan in the range 29.0–400.0 uma, using electron-impact (EI, 70 eV) mode. Dilution 1:100 of essential oils in n-hexane was injected (2 µL) into the GC-MS system. The MSD ChemStation (Agilent, Version G1701DA D.01.00) and the NIST Mass Spectral Search Program were employed for the data analysis. Identifying the principal compounds was achieved by the correspondence of retention

indices and mass spectra to those of ADAMS, NIST 17, FFNSC2, and WILEY 275 libraries. Furthermore, the analytical standards available in the laboratory (Sigma-Aldrich, Milan, Italy) were used for further confirmation. The relative peak area percentages were obtained by area normalization without using correction factors (Quassinti et al., 2013).

2.5.5 T. brucei and mammalian cell culture

T. brucei s427 bloodstream forms (subspecies *T. b. brucei*) and mammalian Balb/3T3 fibroblasts (ATCC no CCL-163) were harvested as reported in Ngahang Kamte, et al., 2017. *T. brucei* cells were cultured in HMI-9 medium supplemented with 5% (v/v) heat inactivated fetal bovine serum (FBS) and 10 mL/L of 100x penicillin-streptomycin (Gibco, Billings, MT, USA) at a temperature of 37° C with 5% CO_2.

Mammalian fibroblasts were cultured in Dulbecco's modified Eagle's medium (Sigma-Aldrich, St Louis, MO, USA) supplemented with 10% (v/v) heat-inactivated fetal bovine serum, L-glutamine (0.584 g/L) and 10 mL/L of 100x penicillin-streptomycin (Gibco, Billings, MT, USA) with the same temperature and CO_2 conditions as the parasites.

2.5.6 Growth inhibition assay on T. brucei and Balb/3T3 cells

All the compounds that were tested were dissolved in dimethyl sulfoxide (DMSO). The final DMSO concentration in each well was less than 1% in all experiments and has no effect on the trypanosomes in this concentration range. They were serially diluted in 96-wells microtiter plates with growth medium to obtain a range of concentrations from 2×10^{-5} µg/mL to 200 µg/mL (100 µL/well). In each well 100 µL of *T. brucei* or mammalian fibroblasts cell culture were added to have 20,000 and 2000 cells per well respectively. The plates were incubated for 48 h at 37° C with 5% CO_2, treated with 20 µL of 0.5 mM resazurine (Sigma-Aldrich, St Louis, MO, USA) and treated for 24 h at the incubation conditions. Subsequently, the surviving cells were quantified by fluorescence (540 nm excitation and 590 nm emission) with an Infinite M200 microplate reader (Tecan Group, Ltd. Männedorf, Switzerland). Data were analyzed using the GraphPad Prism 5.04 software to obtain EC_{50} values by fitting the data to a log inhibitor vs. response curve (variable slope, four parameters) and calculating the selectivity index (SI) from the comparison of *T.brucei* and Balb/3T3 EC_{50} values.

2.5.7 Comparative activities

To evaluate individual constituents' contribution to overall activity, a compound-elimination assay was conducted as previously described by Miresmailli (Miresmailli et al., 2006). A series of artificial EOs were prepared using the constituents in their natural proportions, either as the full mixture or with one, two, or three constituents omitted. Each artificial EO had the same amounts in weight of individual compounds as in the complete EO, with the amounts of missing compounds replaced by DMSO.

2.5.8 Synergistic interactions among four major constituents

To evaluate potential synergies between the six major constituents (farnesene, β-ocimene, *p*-cymene, limonene, β-pinene, myrcene), mixtures were prepared following the actual constituent ratio based on chemical analysis of the EO. These artificial oils were applied to T. brucei or mammalian cell culture, and their EC_{50} values were calculated after 48 h. To determine the mixtures' relationships, we used a statistical model, named Wadley's model (Don-Pedro, 1996), to compare expected and observed EC_{50} values. Based on Wadley's calculation, the expected EC_{50} values (assuming additive interaction) were determined from the equation:

$$E = \frac{a + b + c \ldots . + n}{\frac{a}{\mathrm{EC}_{50(a)}} + \frac{b}{\mathrm{EC}_{50(b)}} + \frac{c}{\mathrm{EC}_{50(c)}} \ldots + \frac{n}{\mathrm{EC}_{50(n)}}}$$

where a is the proportion of compound A in the mixture, and 〖 EC 〗_(50 (a)) is the EC50 of compound A. The interaction between the observed and theoretical EC50 values was compared as:

$$R = \frac{expected\ E\mathrm{C}_{50}}{observed\ \mathrm{EC}_{50}}$$

The relationship between the constituents of the mixture was defined as either synergistic (when $R > 1.5$), additive ($1.5 \geq R > 0.5$), or antagonistic ($R \leq 0.5$) based on this model.

2.5.9 Preparation of A. nemorosa EO-based nanoemulsions

For the preparation of NANO A, *A. nemorosa* EO (from aerial parts) was added dropwise to a Polysorbate 80 aqueous solution under high-speed stirring (Ultraturrax T25 basic, IKA® Werke GmbH & Co.KG, Staufen, Germany) for 5 min at 9500 rpm to form an emulsion with final concentrations of 6% (w/w) EO and 2% (w/w) polysorbate. The obtained emulsion was then homogenised by using a French Pressure Cell Press (American Instrument Company, AMINCO, MY,

USA) for four cycles at the pressure of 130 MPa. NANO B was formulated in a similar way but a 1:2 (w/w) mixture of ethyl oleate and EO was used in the first step instead of the pure EO.

2.5.10 Nanoemulsion characterization

The formation of nanoemulsions was assessed by polarizing optical microscope (MT9000, Meiji Techno Co Ltd., Chikumazawa, Miyoshi machi, Iruma-gun, Saitama 354-0043, Japan) equipped with a 3 megapixel CMOS camera (Invenio 3S, DeltaPix, Denmark). Particle size measurements were performed through the dynamic light scattering (DLS) technique using a Zetasizer nanoS (Malvern Instruments, Worcestershire, UK) equipped with a backscattered light detector working at 173°. The analysis was performed at 25°C at different time points: 0 day, 3 days, 7 days, 1 month, 2 months, 3 months, 4 months, 6 months and 9 months (Kavallieratos et al., 2021).

2.5.11 Determination of NTP and ADP Pools in T. brucei

Blood-stream forms of T. b. brucei (strain s427) were maintained at 37° C and 5% CO_2 in Hirumi's modified Iscove's Medium (HMI)-9 medium lacking thymidine and Serum Plus but containing 10% fetal bovine serum. The omission of thymidine does not affect the growth of the parasites (Hofer et al., 1998). Trypanosomes (50 mL, 10^6 cells/mL), harvested in late logarithmic phase, were chilled on ice for 5 min before being collected and centrifuged at × g for 5 min at 4°C. Subsequently, the liquid was decanted and the pellet resuspended in the remaing liquid in the tube by tapping the bottom of the tube. The resuspended slurry was transferred to an Eppendorf tube, and centrifuged at 16000 × g for 1 min at 4°C. The supernatant was discarded and the collected trypanosomes were disintegrated by pipetting them up and down in 500 µL of ice-cold 0.6 M trichloroacetic acid containing 15 mM $MgCl_2$. The resultant solution was centrifuged at 16000 × g for 1 min at 4°C, and the supernatant was extracted with 720 µl chloroform (78% v/v)-trioctylamine (22% v/v). Each sample was purified by an OASIS WAX cartridge as described previously (Ranjbarian et al., 2021) and the collected solution was evaporated to dryness in a Speedvac (Thermo Fisher Scientific Savant, USA) and dissolved in 200 µL of water. This fraction was analyzed by HPLC using the Fast Protocol (Ranjbarian et al., 2021) to quantify ADP and NTPs with a 150 x 3 mm C18-WP HPLC column (ChromaNik Technologies Inc., Osaka, Japan). The mobile phase was a ternary mixture of 43% solution A (23 g/L KH2PO4 pH 5.6 in 5.8% acetonitrile); 37% solution B (5.8% acetonitrile) and 20% solution C (3.52 g/L tetrabutylammonium bromide in 5.8% acetonitrile) and the column temperature was 30°C. The nucleotides were quantified by measuring areas and comparing them to the areas of a 1 µM standard nucleotide mixture.

2.5.12 Extracts from aerial parts of A. nemorosa

14 Kg of flowers and leaves of *A. nemorosa* were dried at 50 °C for 24 hours (Essiccatori a flusso orizzontale Domus B10, Potenza 550 W, Tauro essiccatori) and shredded (Molino trita piante Albrigi s.r.l.) using a 2 mm sieve. After drying, weight was reduced to 2.05 Kg, with a loss of 84,95 % in water. The extracts were prepared using two different procedures.

Digestion with stirring

The digestion of 1 Kg of aerial parts was performed through stirring at 40 °C for 3 hours, using 7.5 L of methanol (MeOH) as solvent. The extract was filtered, 100 g of carbon were added to the filtrate to remove chlorophyll (under stirring, overnight, at room temperature) and then removed through celite filtration. MeOH was concentrated under vacuum with a rotary evaporator (Rotavapor R-100, Buchi Labortechnik). The total extract amount was 149.50 g. Part of the total extract (80 g) was solubilized in 500 ml of water and liquid-liquid partitions with solvents at growing polarity was performed (330 ml of solvent x 3 extractions): hexane, dichloromethane (DCM), ethyl acetate (EtOAc), and *n*-butanol (*n*-BuOH). The aqueous fraction was freeze-dried, while the other fractions were treated with anhydrous sodium sulfate, filtered, and reduced under pressure.

Maceration with ultrasounds

The maceration of 195 g of aerial parts was performed through ultrasounds bath (AU-220 ARGO LAB MOD.) for 2.40 hours, using 2.7 L of methanol. The extract was filtered and treated with 40 g of carbon (under stirring, overnight, at room temperature), and then removed through celite filtration. MeOH was concentrated under vacuum and from the total extract amount (20.745 g) 14.745 g were solubilized in 60 ml of water to perform liquid-liquid partitions with the same solvents and modalities used for the extracts obtained from digestion. Yields for the extracts from both processes are shown in supporting information (Table S1).

2.5.13 Extracts from roots of A. nemorosa

8.5 Kg of *A. nemorosa*'s roots were collected, dried, and shredded with the same methods of the aerial parts. After drying, weight was reduced to 1.9 Kg, with a water loss of 77,42 %. The extracts were prepared following the same two procedures used for aerial parts.

Digestion with stirring

The digestion of 851 g of roots was performed through stirring at 40 °C for 3 hours, using 3.5 L of methanol. The extract was filtered, the solvent evaporated, and the total extract was concentrated under vacuum yielding 71.55 g of extract.

500 mL of water were added to 62.53 g of the total extract, but only a part of it was dissolved, while the water-insoluble part was dissolved in 500 mL of methanol. The water-soluble portion was subjected to liquid-liquid partition with solvents at growing polarity (330 ml of solvent x 3 extractions): hexane, dichloromethane (DCM), ethyl acetate (EtOAc), and *n*-butanol (*n*-BuOH). The aqueous fractions (the initial and residual fractions) were freeze-dried, while the other fractions were treated with anhydrous sodium sulfate, filtered and concentrated under vacuum. The water-insoluble portion, already solubilized in MeOH, was treated with anhydrous sodium sulfate, filtered, and concentrated under vacuum.

Maceration with ultrasounds

The maceration of 200 g of roots was performed through ultrasounds bath for 2.40 hours, using 1.5 L of methanol. The extract was filtered, and the total extract was concentrated under vacuum yielding 14.385 g. From 10 g of the total extract, 3 portions were obtained: a water-soluble portion that was solubilized with 85 mL and subjected to the liquid-liquid partition as previously described; a water-insoluble portion solubilized in 85 mL of methanol, filtered, and concentrated under vacuum; a totally insoluble portion that was concentrated under vacuum. Yields for extracts from *A. nemorosa* roots are reported in supporting information (Table S2).

2.5.14 HPLC-DAD-MS^n analysis of Root MeOH fraction and sub-fractions A-C

An Agilent 1260 chromatograph with an autosampler and a diode array detector (DAD), interfaced with a Varian MS 500 ion trap mass spectrometer, was employed to quantify lignans, phenylpropanoid esters, flavonoids, and related structures in MeOH fraction and sub-fractions A-C. Chromatographic separation was achieved on Agilent Eclipse XDB C18 (3.0 m x 150 mm x 3.5 μm). The detection wavelength was in the λ range of 200-400 nm. Mobile phase A [H2O: ACN (95:5)] and B [ACN:H2O(95:5)], both in 0.1% formic acid and 2 mM ammonium formate. The injection volume was 5 μL with a flow rate of 1 mL/min using a gradient program of 30 min consisting of 1 min of B 30%, followed by a linear gradient until 15 min B 90%, at 20 min B 90%, at 25 min B 30% and at 30 min B 30%. The ionization was performed by electrospray in the positive mode, which resulted in the formation of $(M+H)^+$ and/or $(M+NH_4)^+$ adduct ions. The source temperature was set

to 450 °C. The MS parameters were the following: spray chamber temperature, 45°C; needle voltage, 4700 V; capillary voltage, 85 V; RF loading, 80%; nebulizing gas pressure, 25 psi (nitrogen); drying gas pressure, 15 psi. Chromatograms were acquired in the turbo data depending on the scanning (TDDS) mode.

2.5.15 Bio-guided fractionation of Root MeOH fraction and isolation of its main components

The most active MeOH fraction (20 g) was subjected to column chromatography over silica gel (63-200 μm, 9 x 40 cm) eluting with mixtures of hexanes-EtOAc of increasing polarity (100:0 to o:100, 1L each one) to afford twelve fractions, which were combined based on their TLC profile into three sub-fractions (named A to C). The composition of each fraction has been determined by HPLC using the method described in the HPLC section. The sub-fraction A (7.5 g) was subjected to further silica gel flash chromatography (15–40 μm, 6.5 × 30 cm) using mixtures of hexane-diethyl ether of increasing polarity (100:0 to 0:100) to afford pure podophyllotoxin and deoxypodophyllotoxin as white needles. The two lignans were identified based on their spectral data (^{1}H and ^{13}C NMR) and by comparison with those reported in the literature for the same compounds. The sub-fraction B (6.5 g) was purified by silica gel column chromatography (15–40 μm, 1 × 30 cm) using hexanes-DCM mixtures of increasing polarity (0–100%) to yield pure anthriscusin, as a white powder. The phenylpropanoid ester anthriscusin was identified based on its spectral data (^{1}H and ^{13}C NMR) and by comparison with the data reported in the literature for the same compound. Finally, the sub-fraction C (6 g) was subjected to several rounds of silica gel column chromatography, but not possible to get any pure compounds.

2.5.16 NMR analysis of podophyllotoxin (1), deoxypodophyllotoxin (6), and anthriscusin (9)

NMR analysis was performed on a Bruker Ultrashield Plus 400MHz spectrometer equipped with a 5-mm CPTCI cryo-probe (^{1}H-^{13}C/^{15}N/2H+Z-gradients) operating at 303 K. The structure identification of the purified compounds was based on a selection of ^{1}H and ^{13}C NMR spectra based on complexity or quantity of the sample. The proton and carbon chemical shifts were referenced to the internal reference TMS (proton δ = 0.00 ppm; carbon, δ = 0.00 ppm). The data were processed using Topspin 2.1 pl5 and analysed with Mnova 6.2.1. The ^{1}H NMR and ^{13}C NMR profiles of podophyllotoxin (**1**), deoxypodophyllotoxin (**6**), and anthriscusin (**9**) matched with those described in the literature and are reported below.

Podophyllotoxin (1)

Appearance: white needles

^{1}H NMR ($CDCl_3$) δ: 6.67 (s, 1H, H-6), 6.52 (s, 1H, H-3), 6.35 (s, 2H, H-2', 6'), 5.95 (d, *J* = 12.0 Hz, 2H, -OCH_2O-), 4.60 (s, 1H, H-7'), 4.46 (s, 1H, H-9a), 3.92 (s, 1H, H-9b), 3.81 (s, 3H, 4'-OCH_3), 3.75 (s, 6H, 3',5'-OCH_3), 3.08 (d, *J* = 12.0 Hz, 1H, H-7b), 2.77 (m, 1H, H-7a), 2.74 (m, 2H, H-8, 8').

^{13}CNMR ($CDCl_3$) δ: 175.1 (C-9'), 152.7 (C-3',5'), 147.2 (C-5), 146.9 (C-4), 137.2 (C-4'), 136.5 (C-1'), 130.8 (C-1), 128.5 (C-2), 110.7 (C-3), 108.7 (C-6), 108.4 (C-2',6'), 101.4 (-OCH_2O-), 72.3 (C-9), 61.0 (4'-OCH_3), 56.4 (3',5'-OCH_3), 47.7 (C-8'), 43.9 (C-7'), 33.3 (C-7), 32.9 (C-8).

Deoxypodophyllotoxin (6)

Appearance: white needles

^{1}H NMR ($CDCl_3$) δ: 7.02 (s, 1H, H-6), 6.43 (s, 2H, H-2', 6'), 6.36 (s, 1H, H-3), 5.93 (d, *J* = 18.0 Hz, 2H, -OCH_2O-), 4.49 (dd, *J* = 3.6, 7.2 Hz, 1H, H-7'), 4.48 (s, 1H, H-9a), 3.83 (s, 3H, 4'-OCH_3), 3.80 (s, 6H, 3',5'-OCH_3), 3.21 (dd, *J* = 9.0 Hz ,5.4 Hz, 1H, H-7b), 2.74 (m, 2H, H-8,8'). 2.18 (d, *J* = 7.8 Hz, 1H, H-7a).

^{13}C NMR ($CDCl_3$) δ: 178.0 (C-9'), 153.8 (C-3', 5'), 147.6 (C-4), 147.3 (C-5), 139.5 (C-1'), 137.3 (C-4'), 132.2 (C-1), 130.8 (C-2), 109.5 (C-3), 105.8 (C-2', 6'), 105.6 (C-6), 101.4 (-OCH_2O-), 70.0 (C-9), 69.7 (C-7), 61.1 (4'- OCH_3), 56.4 (3',5'-OCH_3), 45.6 (C-8'), 44.2 (C-7'), 42.9 (C-8).

Anthriscusin (9)

Appearance: white powder

^{1}H NMR ($CDCl_3$) δ: 6.62 (d, 1H, *J* = 1.3 Hz, 6'-H), 6.55 (d, 1H, *J* = 1.3 Hz, H-2'), 6.57 (d, 1H, *J* = 15.8 Hz, H-1), 6.16 (dt, *J* = 15.8, 6.5 Hz, 1H, H-2), 4.82 (dd, *J* = 6.5, 1.0 Hz, 2H, H-3), 6.48 (q, *J* = 7.2 Hz, 1H, H-3"), 6.06 (qd, *J* = 7.2, 1.5 Hz, 1H, H-3"'), 3.92 (s, 3H, -OCH_3), 2.14 (d, *J* =7.2 Hz, 3H, H-4"), 1.96 (dq, *J* = 7.2, 1.5 Hz, 3H, H-4"'), 1.87 (p, *J* = 1.5, 3H, H-5"'), 5.99 (s, 2H, -OCH_2O-), 4.86 (br s, 2H, H-5").

^{13}C NMR ($CDCl_3$) δ: 167.6 (C-1"'), 165.8 (C-"), 149.1 (C-5'), 143.7 (C-3"), 143.6 (C-3'), 138.2 (C-3"'), 135.3 (C-4'), 134.1 (C-1), 131.2 (C-1'), 127.8 (C-2"), 127.7 (C-2"'), 121.8 (C-2), 106.9 (C-2'), 101.6 (-OCH_2O-), 100.2(C-6'), 65.2 (C-5"), 64.9 (C-3), 56.6 (-OCH3), 20.6 (C-5"'), 15.9(C-4"), 15.8 (C-4"').

2.6 References

Adams, R.P. (2007). Identification of Essential Oil Components by Gas Chromatography/ Mass Spectrometry, Allured Publishing Corporation, Carol Stream, Illinois.

Altundag, E., Ozturk, M. (2011). Ethnomedicinal studies on the plant resources of east Anatolia, Turkey. Procedia - Social and Behavioral Sciences, 19, 756–777.

Bagci, E., Aydin, E., Ungureanu, E., Hritcu, L. (2016). Anthriscus nemorosa essential oil inhalation prevents memory impairment, anxiety and depression in scopolamine-treated rats. Biomedicine & Pharmacotherapy, 84, 1313-1320.

Bouyahya, A., Et-Touys, A., Bakri, Y., Talbaui, A., Fellah, H., Abrini, J., Dakka, N. (2017). Chemical composition of *Mentha pulegium* and *Rosmarinus officinalis* essential oils and their antileishmanial, antibacterial and antioxidant activities. Microbial pathogenesis, 111, 41-49.

Bulut, G., Tuzlacı, E., Doğan, A., Şenkardeş, İ., Doğan, A., Şenkardeş, İ. (2014). An ethnopharmacological review on the Turkish Apiaceae species. Journal of Faculty of Pharmacy of Istanbul University, 44(2), 163-179.

Cascone, P., Iodice, L., Maffei, M.E., Bossi, S., Arimura, G.I., Guerrieri, E. (2015). Tobacco overexpressing β-ocimene induces direct and indirect responses against aphids in receiver tomato plants. Journal of plant physiology, 173, 28-32.

Dhifi, W., Bellili, S., Jazi, S., Bahloul, N., Mnif, W. (2016). Essential oils' chemical characterization and investigation of some biological activities: A critical review. Medicines, 3(4), 25.

Don-Pedro, K.N. (1996). Investigation of single and joint fumigant insecticidal action of citrus peel oil components. Pest Science, 46, 79–84.

Fejes, S., Blázovics, A., Lugasi, A., Lemberkovics, É., Petri, G., Kéry, Á. (2000). *In vitro* antioxidant activity of *Anthriscus cerefolium* L. (Hoffm.) extracts. Journal of ethnopharmacology, 69(3), 259-265.

Fejes, S., Lemberkovics, É., Balázs, A., Apáti, P., Kristó, T.S., Szöke, E., Kery, A., Blázovics, A. (2001). Antioxidant activity of different compounds from *Anthriscus cerefolium* L. (Hoffm.). In International Conference on Medicinal and Aromatic Plants (Part II) 597, 191-198.

FFNSC, 2, (2012). Flavors and Fragrances of Natural and Synthetic Compounds, Mass Spectral Database, Shimadzu Corps, Kyoto.

Forouhandeh, H., Zarchini, M., Safarzadeh, E., Molavi, O., Asgharian, P., Tarhriz, V. (2021). Evaluation of the Cytotoxic Activity of *Anthriscus nemorosa* on Breast Cancer Cells. Journal of Contemporary Medical Sciences, 7(4).

Gairola, S., Sharma, J., Bedi, Y.S. (2014). A cross-cultural analysis of Jammu, Kashmir and Ladakh (India) medicinal plant use. Journal of Ethnopharmacology, 155, 925–986.

Hofer, A., Ekanem, J.T., Thelander, L. (1998). Allosteric regulation of *Trypanosoma brucei* ribonucleotide reductase studied *in vitro* and *in vivo*. Journal of Biological Chemistry, 273(51), 34098-34104.

Hritcu, L., Akbaba, E.A., Bağcı, E. (2015). *Anthriscus nemorosa* essential oil exhibits anxiolytic and antidepressant like effects and improves memory on amnesia induced rats.

Kamte, S.L.N., Ranjbarian, F., Cianfaglione, K., Sut, S., Dall'Acqua, S., Bruno, M., Afshar, F.H., Iannarelli, R., Benelli, G., Cappellacci, L., Hofer, A., Maggi, F., Petrelli, R. (2018). Identification of highly effective antitrypanosomal compounds in essential oils from the Apiaceae family. Ecotoxicology and Environmental Safety, 156, 154-165.

Karakaya, S., Yılmaz, S.V., Koca, M., Demirci, B., Sytar, O.K. (2019). S. A. N. A. Screening of non-alkaloid acetylcholinesterase inhibitors from extracts and essential oils of *Anthriscus nemorosa* (M. Bieb.) Spreng.(Apiaceae). South African Journal of Botany, 125, 261-269.

Karimi, S., Farzaneh, F., Asnaashari, S., Parina, P., Sarvari, Y., Hazrati, S. (2019). Phytochemical Analysis and Anti-microbial Activity of Some Important Medicinal Plants from North-west of Iran. Iranian Journal of Pharmaceutical Research, 18, 1871.

Kavallieratos, N. G., Skourti, A., Nika, E. P., Ntalaka, C. T., Boukouvala, M. C., Bonacucina, G., Cespi, M., Petrelli, R., Cappellacci, L., Maggi, F., Benelli, G., Canale, A. (2021). Isofuranodiene-based nanoemulsion: larvicidal and adulticidal activity against tenebrionid beetles attacking stored wheat. Journal of Stored Products Research, 93, 101859.

Kiliç, Ö. (2017). Essential oil composition of aerial parts of two Anthriscus Pers. species from Turkey. Journal of Essential Oil Bearing Plants, 20(2), 591-596.

Kim, S.B., Lee, A.Y., Chun, J.M., Lee, A.R., Kim, H.S., Seo, Y.S., Moon, B.C., Kwon, B.I. (2019). *Anthriscus sylvestris* root extract reduces allergic lung inflammation by regulating interferon regulatory factor 4-mediated Th2 cell activation. Journal of ethnopharmacology, 232, 165-175.

Kozawa, M., Morita, N., Hata, K. (1978). Structure of anthriscusin, a new phenylpropanoid ester from the roots of *Anthriscus sylvestris* Hoffm. Chemical and Pharmaceutical Bulletin, 26(4), 1337-1338.

Lai, P., Rao, H., Gao, Y. (2018). Chemical composition, cytotoxic, antimicrobial and antioxidant activities of essential oil from *Anthriscus caucalis* M. Bieb grown in China. Records of Natural Products, 12(3), 290-294.

Lee, S.A., Moon, S.M., Han, S.H., Hwang, E.J., Hong, J.H., Park, B.R., Choi, M.S., Ahn, H., Kim, J.S., Kim, H.J., Chun, H.S., Kim, D.K., Kim, C.S. (2018a). *In vivo* and *in vitro* anti-inflammatory effects of aqueous extract of *Anthriscus sylvestris* leaves. Journal of medicinal food, 21(6), 585-595.

Lee, S.A., Moon, S.M., Han, S.H., Hwang, E.J., Park, B.R., Kim, J.S., Kim, D.K., Kim, C.S. (2018b). Chondroprotective effects of aqueous extract of *Anthriscus sylvestris* leaves on osteoarthritis *in vitro* and *in vivo* through MAPKs and NF-κB signaling inhibition. Biomedicine & Pharmacotherapy, 103, 1202-1211.

Menemen, Y. (2012). Anthriscus Pers. In: Güner, A., Aslan, S., Ekim, T., Vural,M., Babaç, M.T. (Eds.), Türkiye Bitkileri Listesi (Damarlı Bitkiler). Nezahat Gökyiğit Botanic Garden Publications, İstanbul, Turkey, 62–64.

Miresmailli, S., Bradbury, R., Isman, M.B. (2006). Comparative toxicity of *Rosmarinus officinalis* L. essential oil and blends of its major constituents against *Tetranychus urticae* Koch (Acari: Tetranychidae) on two different host plants. Pest Management Science: formerly Pesticide Science, 62(4), 366-371.

Monzote, L., Alarcón, O., Setzer, W. N. (2012). Antiprotozoal activity of essential oils. Agriculturae Conspectus Scientificus, 77(4), 167-175.

Navchoo, I.A., Buth, G.M. (1989). Medicinal system of Ladakh, India. Journal of Ethnopharmacology, 26, 137–146.

Ngahang Kamte, S.L., Ranjbarian, F., Campagnaro, G.D., Biapa Nya, P.C., Mbuntcha, H., Woguem, V., Womeni, H.M., Azefack Tapondjou, L., Giordani, C., Barboni, L., Benelli, G., Cappellacci, L.,

Hofer, A., Petrelli, R., Maggi, F. (2017). *Trypanosoma brucei* inhibition by essential oils from medicinal aromatic plants traditionally used in Cameroon (*Azadirachta indica*, Aframomum melegueta, *Aframomum daniellii*, *Clausena anisata*, *Dichrostachys cinerea* and *Echinops giganteus*). International Journal of Environmental Research and Public Health, 14, 737.

Nickavar, B., Mojab, F., Mojahedi, A. (2009). Composition of the essential oil from Anthriscus nemorosa. Chemistry of Natural Compounds, 45, 443-444.

Nikoli´c, V. (1973). *Anthriscus Pers*. In Flora SR Srbije; Josifovi´c, M., Ed.; Srpska Akademija Nauka i Umetnosti: Beograd, Serbia, 5, 334–338.

NIST, (2008). Mass Spectral Library (NIST/EPA/NIH), Gaithersburg, USA, National Institute of Standards and Technology,.

Pavlović, M., Petrović, S., Milenković, M., Couladis, M., Tzakou, O., Niketić, M. (2011). Chemical composition and antimicrobial activity of *Anthriscus nemorosa* root essential oil. Natural product communications, 6(2), 1934578X1100600229.

Petrelli, R., Orsomando, G., Sorci, L., Maggi, F., Ranjbarian, F., Biapa Nya, P.C., Petrelli, D., Vitali, L.A., Lupidi, G., Quassinti, L., Bramucci, M., Hofer, A., Cappellacci, L. (2016). Biological Activities of the Essential Oil from *Erigeron floribundus*. Molecules, 21, 1065–1079.

Petrelli, R., Ranjbarian, F., Dall'Acqua, S., Papa, F., Iannarelli, R., Kamte, S.L.N., Vittori, S., Benelli, G., Maggi, F., Hofer, A., Cappellacci, L. (2017). An overlooked horticultural crop, *Smyrnium olusatrum*, as a potential source of compounds effective against African trypanosomiasis. Parasitology international, 66(2), 146-151.

Quassinti, L., Bramucci, M., Lupidi, G., Barboni, L., Ricciutelli, M., Sagratini, G., Papa, F., Caprioli, G., Petrelli, D., Vitali, L.A., Vittori, S., Maggi, F. (2013). *In vitro* biological activity of essential oils and isolated furanosesquiterpenes from the neglected vegetable *Smyrnium olusatrum* L. (Apiaceae). Food chemistry, 138(2-3), 808-813.

Ranjbarian, F., Sharma, S., Falappa, G., Taruschio, W., Chabes, A., Hofer, A. (2022). Isocratic HPLC analysis for the simultaneous determination of dNTPs, rNTPs and ADP in biological samples. Nucleic Acids Research, 50(3), e18-e18.

Sadeghi, R., Etemad, S.G., Keshavarzi, E., Haghshenasfard, M. (2015). Investigation of alumina nanofluid stability by UV–vis spectrum. Microfluidics and Nanofluidics, 18, 1023–1030.

Tekin, M., Civelek, Ş.E.M.S.E.T.T.İ.N. (2017). A taxonomic revision of the genus Anthriscus (Apiaceae) in Turkey. Phytotaxa, 302(1), 001-026.

Wagner, H., Ulrich-Merzenich, G. (2009). Synergy research: approaching a new generation of phytopharmaceuticals. Phytomedicine, 16(2-3), 97-110.

Wink, M. (2008). Evolutionary advantage and molecular modes of action of multi-component mixtures used in phytomedicine. Current drug metabolism, 9(10), 996-1009.

2.7 Supporting information

Table S1. liquid-liquid partition extracts yields (% w/w) for *A. nemorosa* aerial parts.

Aerial parts extract	Digestion stirring yield	Maceration ultrasound yield
Hexane	0.26 %	0.32 %
DCM	2.50 %	0.19 %
EtOAc	1.41 %	0.38 %
n-BuOH	6.52 %	2.45 %
Residual H_2O	87.94 %	79.48 %

Table S2. liquid-liquid partition extracts yields (% w/w) for *A. nemorosa* roots.

Roots extract	Digestion stirring yield	Maceration ultrasound yield
Hexane	0.68 %	0.35 %
DCM	1.74 %	0.36 %
EtOAc	1.66 %	0.05 %
n-BuOH	3.48 %	2.39 %
Residual H_2O-soluble portion	53.09 %	65.90 %
MeOH-soluble portion	26.43 %	26.62 %
Insoluble portion	-	2.37 %

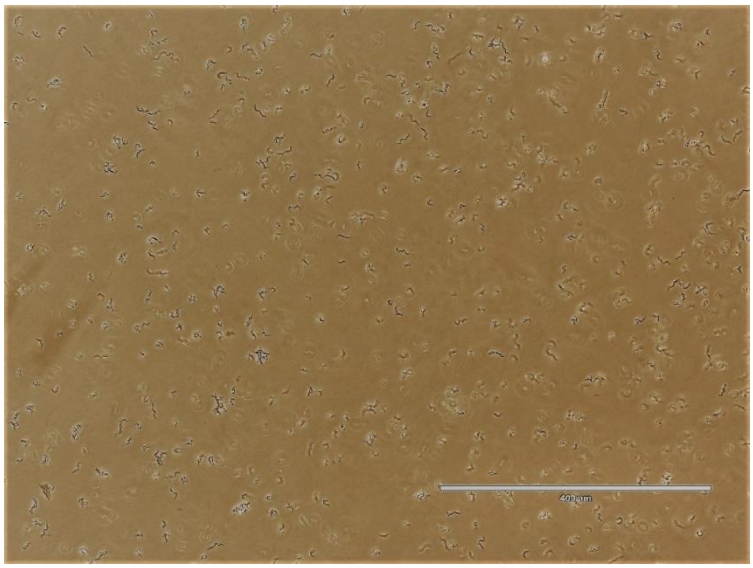

Figure S1. *T. brucei* s427 on an optical microscope.

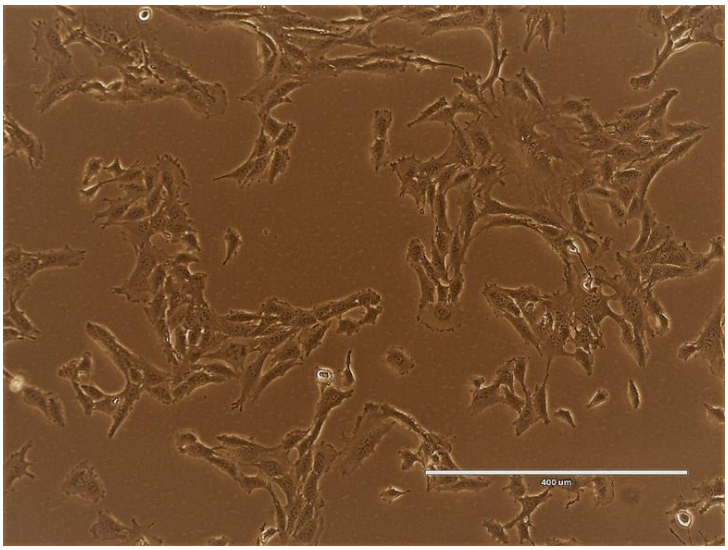

Figure S2. Balb/3T3 on an optical microscope.

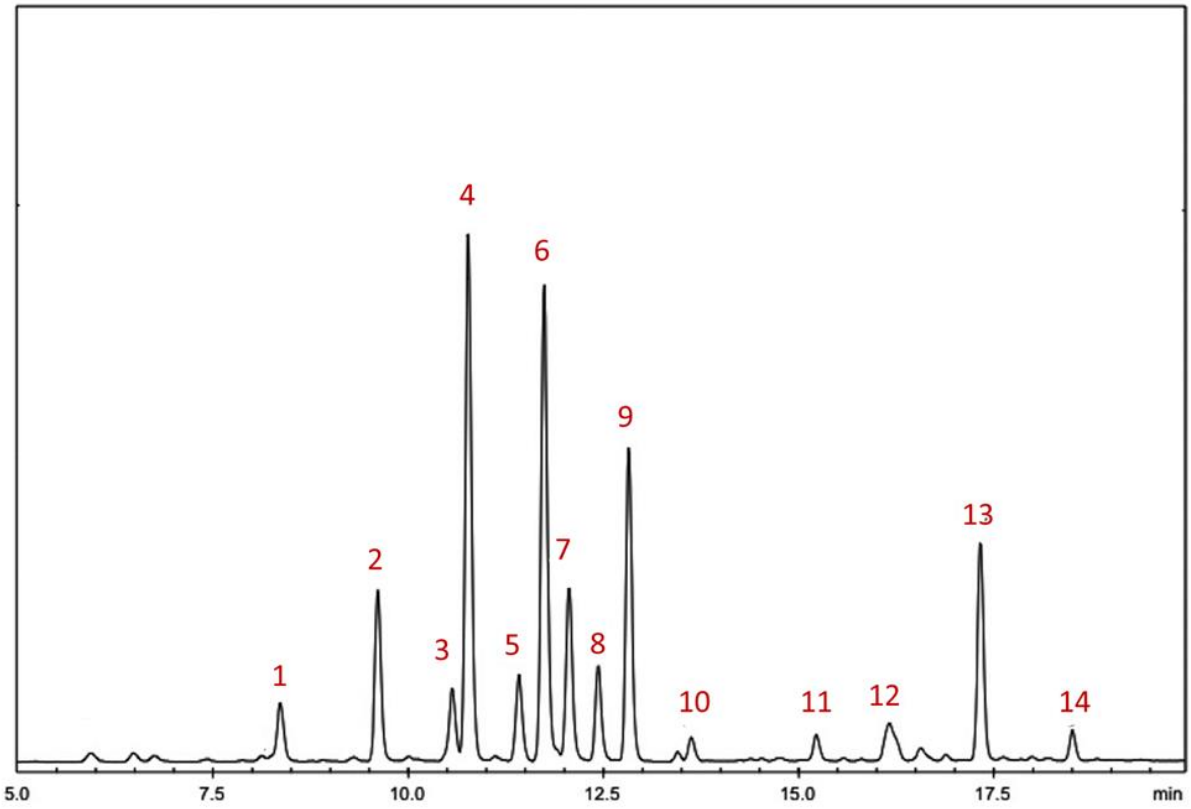

Figure S3. HPLC chromatogram of Root MeOH fraction of *A. nemorosa*.

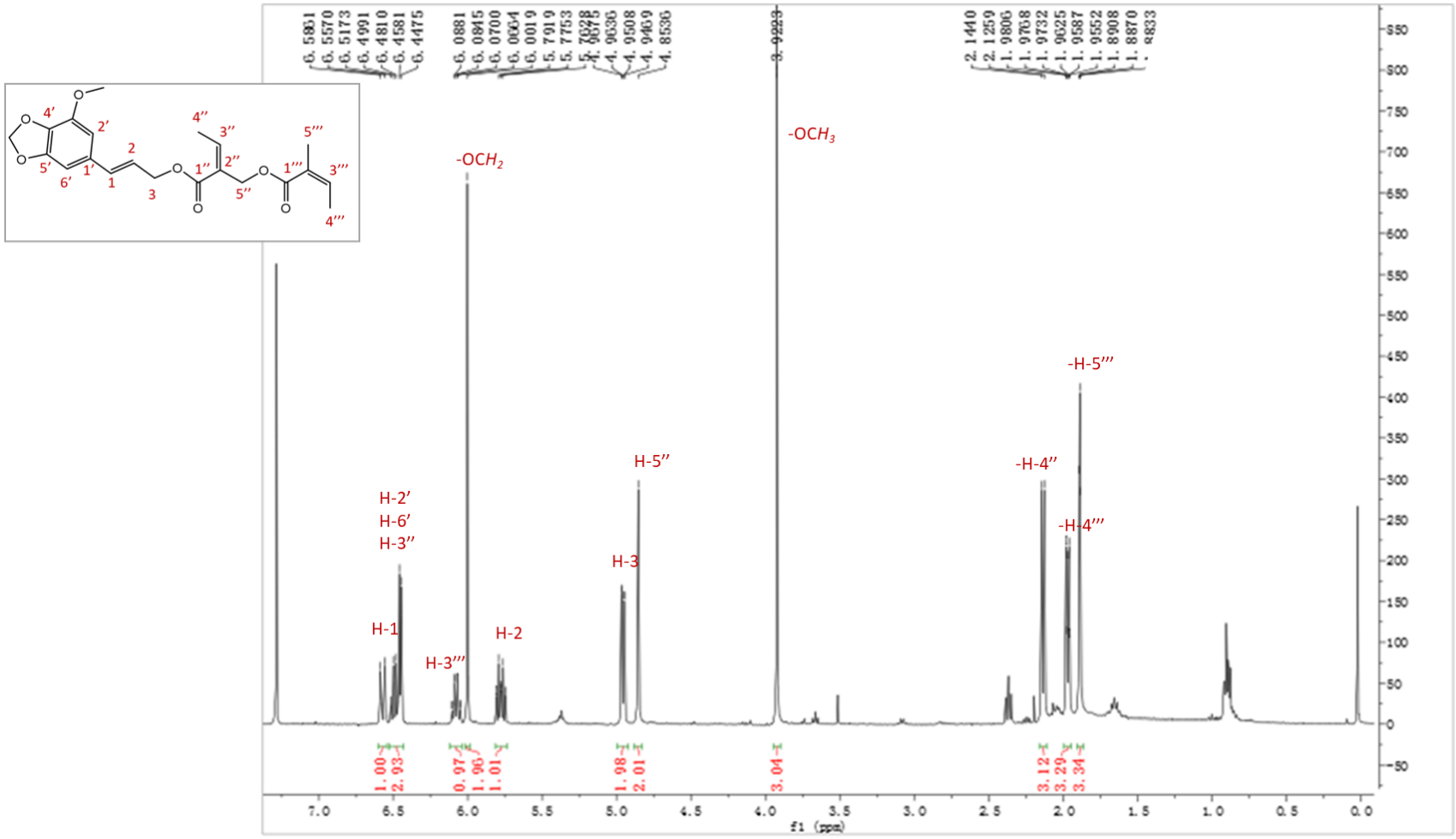

Figure S4. ^{1}H-NMR spectrum of anthriscusin **(9)**.

CHAPTER 3

Cannabis sativa

CHAPTER 3 Outline

3.1 Introduction

The number of species and subspecies in the *Cannabis* genus has long been controversial, since it is really a highly variable species in terms of not just botany, but also chemical constituents and genetics. In Table 13 the current accepted botanical nomenclature for *Cannabis sativa* L. is reported. However, classification of *C. sativa* is commonly based not only on the botanical approach but also on the one related to the secondary metabolites, dividing the species into different chemotypes. Specifically, the ratio of absolute concentrations of the 2 main cannabinoids found in Cannabis, Δ^9-tetrahydrocannabinol (Δ^9 -THC) and cannabidiol (CBD), is used for the aforementioned second method of classification.

Table 13. Botanical taxonomy of *Cannabis sativa* L.

Category	Botanical nomenclature
Kingdom	Plantae – Plants
Subkingdom	Tracheobionta – Vascular plants
Superdivision	Spermatophyta – Seed plants
Division	Magnoliophyta – Flowering plants
Class	Magnoliopsida - Dicotyledons
Subclass	Hamamelididae
Order	Urticales
Family	Cannabaceae
Genus	*Cannabis*
Species	*Cannabis sativa* L.

As far as the classification related to the secondary metabolites is concerned, three main chemotypes are distinguished according to the ratio of THC (the psychotropic chemical compound)/CBD concentration, as shown in Table 14.

Thus, all the cannabis plants with high levels of THC, that are devoid of CBD and mainly used for narcotic uses or medical purposes, are characteristic of Chemotype I. Instead, all the cannabis specimens with an intermediate and similar concentration of the two main cannabinoids are typical of Chemotype II, whereas hemp can be considered cannabis of the Chemotype III, since it is characterised by high CBD levels, compared to the THC content.

Table 14. Cannabis sativa chemotypes based on THC/CBD concentration ratio.

Chemotypes	Cannabinoids content
I	THC > CBD
II	THC = CBD
III	THC < CBD
IV	CBG

Regarding the botanical description, *C. sativa* is an annual plant, characterised by rough erect and branched stems from 80 cm to 6 m variously high (Fig. 36). They are formed by a woody interior, and an outer green bark, constituted by fibres held together by pectin. Roots are fibrous and adventitious and can reach a depth of up to 200-250 cm in suitable, loose soils. Green leaves are mainly opposite, petiolate, and pubescent, with their characteristic palmate shape that is formed by three to nine lanceolate, acuminate, and serrated segments. In nature, hemp is a predominantly dioecious species, meaning that female and male inflorescences can be found just separately in distinct plants, that are thus divided in "female plants" and "male plants", accordingly. Concerning inflorescences, they are gathered in groups of 2-6 at the axils of bracts forming short spikes. Once they reach maturity, they release pollen, and the male plant, at the end of its cycle, dies (Thomas and ElSohly, 2016).

Figure 36. *Cannabis sativa* inflorescences (Everweed company).

Cannabis sativa can adapt to different climates and habitats, unless in extreme conditions, and, therefore, can be cultivated in different climatic conditions and soil (Farag and Kayser, 2017). Indeed, it is a widespread species in nature, thriving from hot sea level to the temperate and alpine foothills of the Himalayas, from where it has probably spread over the last 10,000 years (Merlin, 2003).

Cannabis sativa is one of the first plants cultivated and used by man for centuries, thus having a large number of various industrial applications (Ranalli and Venturi, 2004). According to its uses, Cannabis can be divided into two distinct groups: marijuana and industrial hemp. The first one characterized by a significant amount of the psychotropic compound THC, being employed for its recreational purposes and potential medicinal value, especially for the treatment of a wide range of diseases, such as inflammatory conditions, enteric infections or for pain relief (Doyle and Spence, 1995); whereas, industrial hemp finds use in many fields such as green building and engineering, textile fibres and paper production, foods and beverages, dietary supplements, alternative proteins, pharmaceuticals, cosmetics, and EO-based pesticides (Pilla, 2011; McPartland and Sheikh, 2018; Benelli et al., 2018; Pavlovic et al., 2019; Crini et al., 2020; Tabari et al., 2020).

Behind the unique pharmacological and toxicological properties of *C. sativa* lies its phytocomplex nature (Elsohly and Elsohly, 2007). More than 500 compounds have been identified and isolated from this plant, and among these, more than 100 are phytocannabinoids (Thomas and ElSohly, 2016). The other non-cannabinoids constituents are terpenoids, flavonoids, alkaloids, phytosterols, phenol fatty acids, hydrocarbons, and carbohydrates. Furthermore, simple alcohols, acids, esters, lactones, aldehydes, and ketones have been identified (Ramirez, 2016). In particular, all the cannabinoids and other secondary metabolites, such as terpenes and terpenoids, present in the form of EOs, are biosynthesized in the epidermal glands or glandular hairs called trichomes (Fig. 37). Indeed, those structures present in the leaves and inflorescences produce a kind of resin inside a secretory cavity, giving their glandular head a spherical shape (Bertoli et al., 2010).

Figure 37. *Cannabis sativa* trichomes under the microscope (Medical Cannabis Network).

Due to the variety of bioactive compounds present in the plant, biological activities cannot be traced back to a single constituent since many of them can contribute together to the so called "entourage effect", a proposed mechanism explaining the synergistic action among cannabis compounds to modulate the overall effects of the plant (Russo, 2011; Sanchez-Ramos, 2015). Recently Kakudidi and colleagues reported that hemp had been used in traditional medicine in Africa for centuries, since its introduction by Arab traders from India, and they suggested the possible use of leaves and inflorescences as well to treat over 20 ailments, including protozoal infections (Kakudidi et al., 2022). In addition, Menghini and colleagues highlighted the potential of EOs from industrial hemp inflorescences as protective agents in an *in vivo* model of tissue wound induced by *Leishmania tropica*. the causative agent of *Leishmaniasis recidivans,* a form of cutaneous leishmaniasis (Menghini et al., 2021).

However, despite several studies underlined the hemp's therapeutic potential as an antimicrobial, anti-inflammatory, and anticancer agent (Nissen et al., 2010; Zengin et al., 2018; Ferrante et al., 2019; Ingallina et al., 2020; Orlando et al., 2020; Di Giacomo et al., 2021) and the possible application of its EOs as a novel insecticide with low ecological impact on the environment (Regnault-Roger et al., 2012), few works have dealt with its antiprotozoal activity.

Based on these considerations, this study focused on deepening the knowledge about the antitrypanosomal activity of *Cannabis sativa*, paying particular attention to EOs and hydrophilic extracts derived from different plant chemotypes.

3.2 Essential oils (EOs)

3.2.1 EOs from CBD varieties

Twelve were the analyzed cultivars in this study, eight of which were CBD-rich varieties, namely Fresh Mountain, Lemon Conti Kush, Venom OG, Gorilla Glue, Amnesia cookies, 24K, White Shark, and Pablito, while the remaining four were CBG-rich (CBG 4, CBG 14, CBG 18, and CBG 32). Samples were kindly provided by Everweed company. The EOs yields of the hemp varieties obtained from hydrodistillation varied between 0.485 and 1.814% for the 8 studied varieties that were characterized by higher CBD content, as shown in Figure 38, while the percentages were included between 0.229 and 0.61% for the other four CBG varieties (Figure 39); yields resulted considerably high in both cases if compared to those obtained for the EOs from the industrial hemp varieties included in the European catalog (Pieracci et al., 2021).

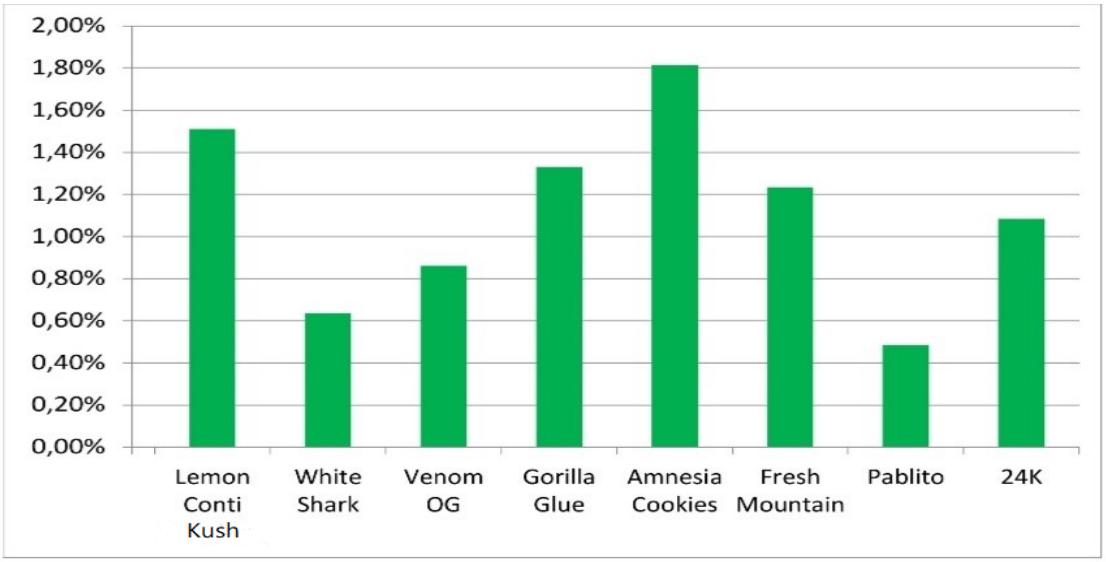

Figure 38. Histogram of the yields obtained for the EOs of the studied 8 CBD-rich varieties.

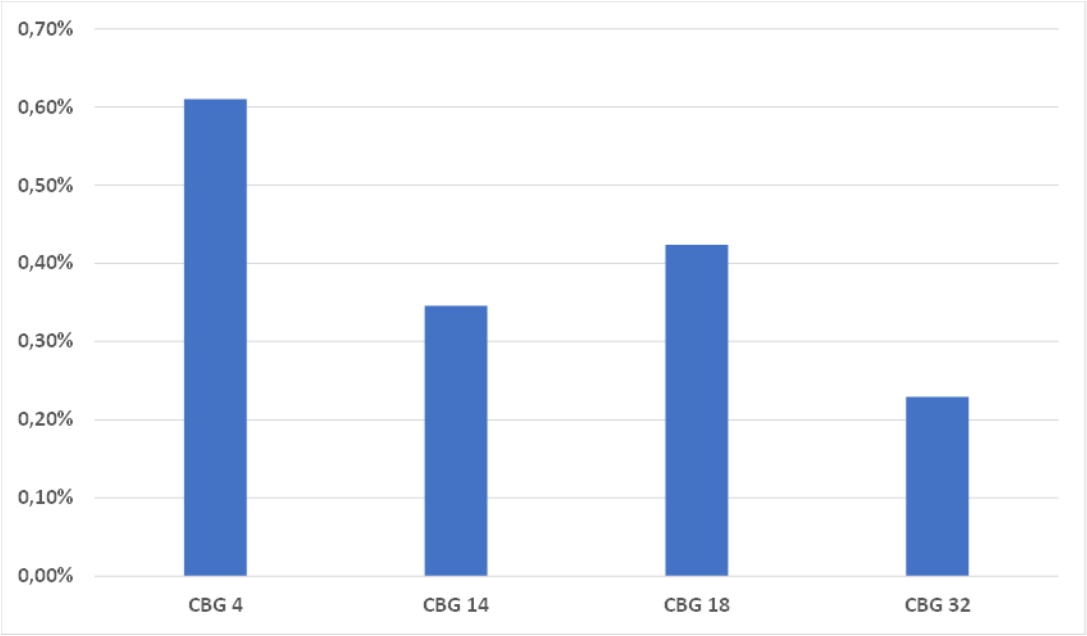

Figure 39. Histogram of the yields obtained for the EOs of the 4 CBG-rich varieties.

EOs composition was subsequently investigated through a GC-MS analysis that demonstrated high amounts of monoterpenes and sesquiterpenes among the CBD varieties. Table 15 shows the percentages of the constituents, with respect to the total identified.

1) In Amnesia Cookies 98.4% of the components were identified and the results showed high levels of myrcene (27.1%), *α*-pinene (24.6%) and (*E*)-caryophyllene (15.6%).
2) In Fresh Mountain the levels of myrcene (26.0%) and of (*E*)-caryophyllene (16.0%) were particularly high (Figure 46), extremely high values compared to the percentages of the other components that were identified. The total identification was 98.13%.
3) In Gorilla Glue (Figure 45) 96.1% of the components were identified. The main ones were (*E*)-caryophyllene (17.6%) and seline-3,7(11)-diene (15.3%).
4) Results in Lemon Conti Kush show a very high concentration of terpinolene (30.2%), the highest found among all the EOs. The identification of the constituents in Lemon Conti Kush was 96.5%.
5) For the Pablito variety, the total identification percentage was 96.1%; in particular, (*E*)-caryophyllene (15.5%), myrcene (10.7%), *α*-pinene (9.0%), guaiol (8.8%) and *α*-bisabolol (8.6%) predominate.
6) In the Venom OG an identification percentage of 96.63% was obtained; in particular, two compounds predominate, *α*-pinene (23.3%) and (*E*)-caryophyllene (17.1%).

7) The identification rate for the White Shark was 97.5%; this variety is rich in myrcene (21.5%), terpinolene (11.8%), (*E*)-caryophyllene (11.4%), *α*-pinene (11.3%) and limonene (10.2%).
8) 95.4% of compounds have been identified in the 24K variety, instead. (*E*)-caryophyllene and 10-*epi*-*γ*-eudesmol were the components that showed the highest values, respectively 19.9% and 10.2%.

In general, the EOs of many of the CBD varieties studied were found to be particularly rich in sesquiterpenes (Figure 40).

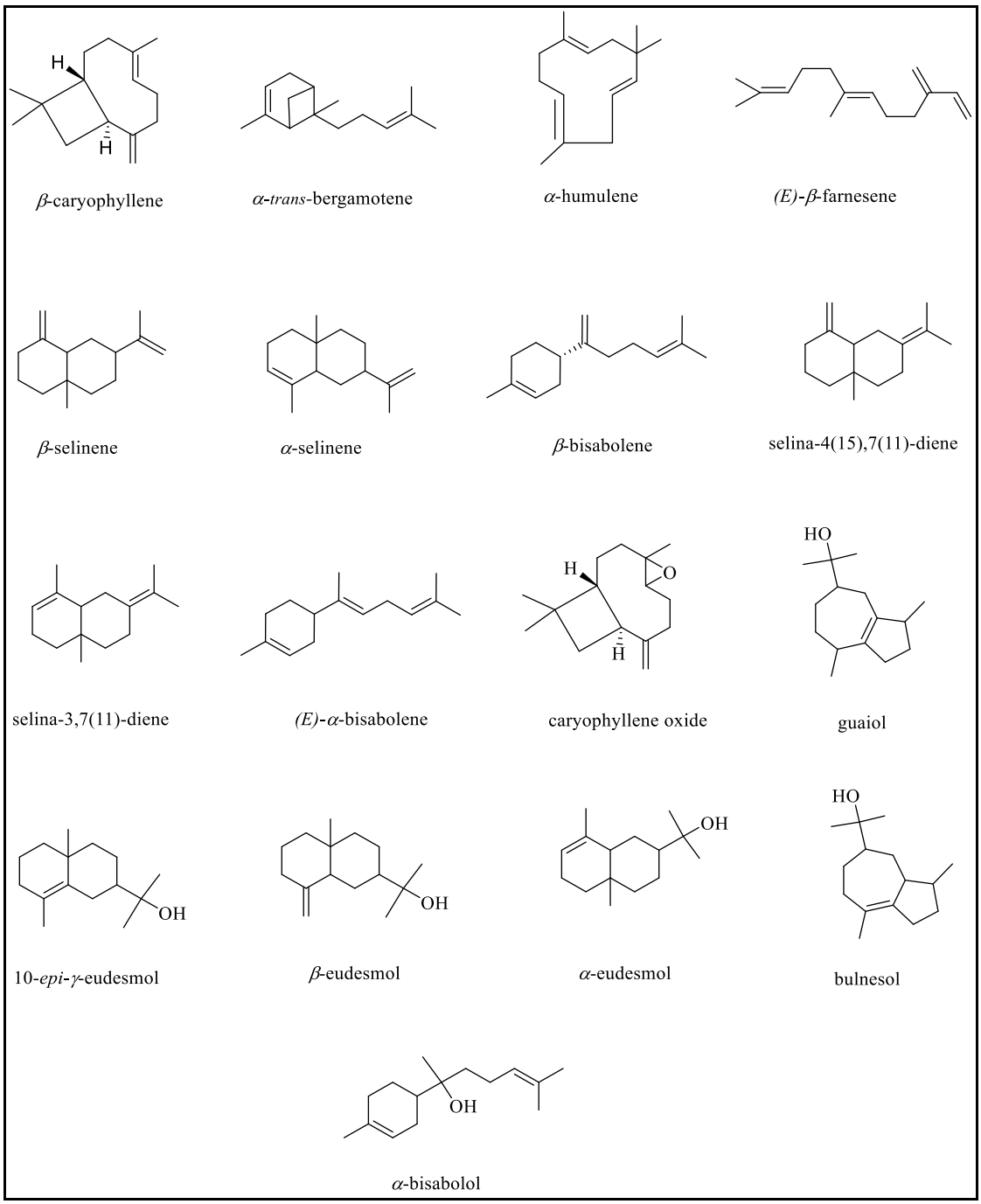

Figure 40. Chemical structures of the main sesquiterpenes found in the EOs of CBD varieties.

Table 15. Results obtained from the GC-MS analysis of the EOs of the 8 investigated CBD varieties

				Varieties								
				Pablito	White Shark	Gorilla Glue	24K	Fresh Mountain	Venom OG	Lemon Conti Kush	Amnesia Cookies	
N	**Compound[a]**	**RI[b] exp.**	**RI[c] lit.**	**%**								**ID[d]**
1	heptanal	901	901	0.9	0.3	0.2	0.2	0.2	0.3	0.6	tr[e]	RI,MS
2	*α*-tujene	926	924		0.1		0.2			tr	tr	RI,MS
3	*α*-pinene	932	933	9.0	11.3	0.7	0.2	11.0	23.3	12.5	24.6	Std
4	camphene	947	946	0.1	0.3	0.1	0.2	0.2	0.4	0.2	0.3	Std
5	*β*-pinene	975	974	3.0	4.2	0.7	0.2	4.0	5.0	4.8	8.2	Std
6	myrcene	990	988	10.7	21.5	6.6	0.2	26.0	9.7	14.9	27.1	Std
7	*α*-phellandrene	1004	1002	tr	0.5			tr	tr	tr	tr	Std
8	*δ*-3-carene	1009	1008		0.4					tr		Std
9	*α*-terpinene	1016	1014	tr	0.4		0.1	tr	tr	tr	tr	Std
10	limonene	1027	1024	2.7	10.2	6.8	4.6	3.9	3.9	2.8	1.8	Std
11	1,8-cineole	1030	1026	0.1	tr		1.5		tr		0.2	Std
12	(*Z*)-*β*-ocimene	1038	1032		tr				tr			Std
13	(*E*)-*β*-ocimene	1048	1044	tr	tr					tr		Std
14	*γ*-terpinene	1058	1054	tr	0.3	tr	0.3		tr	0.1	tr	Std
15	terpinolene	1087	1086	0.3	11.8	0.3	0.4	0.2	0.1	1.0	0.1	RI,MS

16	linalool	1099	1095	0.2	1.0	0.9	2.9	0.1	1.0	0.4	tr	Std
17	*endo*-fenchol	1112	1114	0.2	0.8	1.7	1.0	0.8	0.7	0.6	tr	RI,MS
18	*trans*-pinene hydrate	1120	1119	0.1	0.5	1.1	0.6	0.5	0.4	0.4	tr	RI,MS
19	borneol	1164	1165	0.1	0.2	0.4	0.3	0.2	0.3	0.2	tr	Std
20	*α*-terpineol	1189	1186	0.3	1.0	1.4	1.3	0.6	0.7	0.4	0.1	Std
21	hexyl isobutanoate	1192	1191			0.1			tr	0.3		RI,MS
22	sativene	1393	1390			0.1		tr		0.1		RI,MS
23	*α-cis*-bergamotene	1416	1411		0.1	0.1	0.2	tr	0.1	0.1		RI,MS
24	*(E)*- caryophyllene	1420	1417	15.5	11.4	17.6	19.9	16.0	17.1	10.7	15.3	Std
25	*α-trans*-bergamotene	1436	1432	0.2	1.0	1.3	1.4	0.4	0.7	0.9	0.1	RI,MS
26	*α*-guaiene	1439	1439			tr		2.8				RI,MS
27	*α*-humulene	1455	1452	6.5	3.0	4.7	6.3	4.7	4.9	4.1	7.6	Std
28	(*E*)-*β*-farnesene	1457	1454	0.1	1.1	1.2	1.5	0.2	0.6	0.8	tr	Std
29	*allo*-aromadendrene	1462	1458	0.1		tr	0.2	tr	tr	0.2	tr	RI,MS
30	*γ*-muurolene	1478	1478			0.1		0.1		0.1		RI,MS
31	*γ*-curcumene	1480	1481			0.1	tr					RI,MS
32	*β*-selinene	1487	1489	0.8	0.2	0.2		0.6	0.1	0.5	1.3	RI,MS
33	valencene	1494	1496	0.2		0.4			0.1		0.1	RI,MS
34	*α*-selinene	1496	1498	0.7	0.2	0.5	0.1	0.8	0.1	0.8	1.1	RI,MS
35	*β*-dihydro-agarofuran	1501	1503	0.1	tr	0.1	0.1		0.1	tr	tr	RI,MS

36	*α*-bulnesene	1507	1509	0.1				6.3				RI,MS
37	*β*-bisabolene	1509	1505	0.7	0.1	1.4	1.9	1.1	0.1	1.6	0.1	RI,MS
38	*β*-curcumene	1512	1514		0.1	0.2	0.2		tr	0.1		RI,MS
39	sesquicineole	1515	1515	tr	0.1	0.1	0.5	0.1	0.2	0.3		RI,MS
40	zonarene	1522	1528	0.1	tr	0.9		0.3				RI,MS
41	selina-4(15),7(11)-diene	1536	1544	0.3	0.1	7.1		3.5	0.1	5.0	0.1	RI,MS
42	selina-3,7(11)-diene	1543	1538	1.7	0.3	12.5	1.8	7.8	0.3	8.7	0.7	RI,MS
43	caryophyllene oxide	1584	1582	0.8	0.2	0.2	0.5	0.6	1.0	0.4	0.1	Std
44	guaiol	1598	1600	7.5	3.0	5.8	9.7	tr	5.9	3.3	2.1	RI,MS
45	eudesmol-5-*epi*-7-*epi*-*α*	1606	1607	0.4	0.1	0.2	0.4		0.2	0.1	tr	RI,MS
46	10-*epi*-*γ*-eudesmol	1621	1622	7.6	4.1	7.0	10.2	tr	6.5	4.6	3.0	RI,MS
47	*γ*-eudesmol	1633	1630	1.7	0.5	0.8	1.5		1.0	0.5	0.3	RI,MS
48	*β*-eudesmol	1651	1649	3.1	1.3	1.8	3.4	tr	2.3	1.1	0.7	RI,MS
49	*α*-eudesmol	1654	1652	4.3	2.0	2.8	4.7	0.2	3.2	1.7	1.1	RI,MS
50	eudesmol-7-*epi*-*α*	1659	1658	0.8	0.3	0.5	0.9		0.6	0.3	0.1	RI,MS
51	bulnesol	1668	1670	6.0	2.6	4.4	7.2		3.9	2.7	1.7	RI,MS
52	*α*-bisabolol	1684	1685	8.6	0.2	2.7	8.4	4.3	0.5	5.2	tr	Std
53	eudesm-7(11)-4-ol	1697	1700	tr	tr	0.1		tr	tr	0.3		RI,MS
54	cannabidiol	2427	2430	0.2	0.6	0.2	0.4	0.5	1.0	0.5	0.1	Std
55	cannabichromene	2434	2440	tr	tr	tr	tr	tr	tr	tr	tr	RI,MS

Compound classes								
Monoterpene hydrocarbons	25.93	61.09	16.30	6.7	45.89	42.82	36.70	62.31
Oxygenated monoterpene hydrocarbons	0.97	3.08	4.41	6.6	1.71	2.74	1.62	0.31
Sesquiterpene hydrocarbons	27.08	17.72	48.41	33.45	44.60	24.20	33.70	26.49
Oxygenated sesquiterpenes hydrocarbons	40.92	14.45	26.50	47.47	5.22	25.43	20.51	9.14
Cannabinoids	0.22	0.66	0.21	0.39	0.50	1.06	0.50	0.17
Other	0.95	0.32	0.30	0.18	0.21	0.38	0.97	tr
Total identified (%)	96.07	97.32	96.13	95.42	98.13	96.63	93.80	98.42

[a] Order of elution of components from an HP-5MS column.

[b] Linear retention index according to Van den Dool and Kratz (1963).

[c] RI taken from the ADAMS and/or NIST 17 and FFNSC2 libraries.

[d] Identification methods: Std, comparison with analytical standards;

RI, consistency of the calculated RI with those reported in the ADAMS, NIST 17 and FFNSC2 libraries; MS, mass spectrum superimposed with those reported in the ADAMS, NIST 17 and FFNSC2 libraries.

and tr: traces, relative% <0.1.

3.2.2 EOs from CBG varieties

CBG varieties proved to be characterized by high amounts of monoterpenes and sesquiterpenes as well (Figure 41). The detailed profiles are described below.

1) In CBG 4 97.3% of the components were identified and the results showed quite high levels of *β*-myrcene (25.7%) and *β*-caryophyllene (9.9%).
2) The levels of *β*-myrcene and *β*-caryophyllene were particularly high also in CBG 14 (23.7% and 17.9%, respectively), along with a quite abundant percentage of *α*-pinene (11.3%), as well. The total identification was 97.7%.
3) In CBG 18, 96.8% of the components were identified. Among all the four EOs from CBG varieties, CBG 18 showed the highest percentage of *β*-myrcene (34.9%), *α*-pinene (13.9 %) and D-limonene (7.2%) as well resulted in relatively high concentrations.
4) The highest value of *β*-caryophyllene concentration (19.6%) was found in CBG 32. The results showed, again, quite high concentrations of *β*-myrcene (11.8%) together with *α*-bisabolol (9.8%) and *α*-humulene (8.0%) (Figure 49).

EOs obtained from CBG varieties were found to be particularly rich in monoterpenes (from 47.1% of monoterpene hydrocarbons in CBG 4 to 60.0% in CBG 18) rather than sesquiterpenes, except for CBG 32, characterized by the highest value of sesquiterpene hydrocarbons (52.6%) and the lowest one for the monoterpene hydrocarbons (17.1%), among these 4 EOs (Table 16).

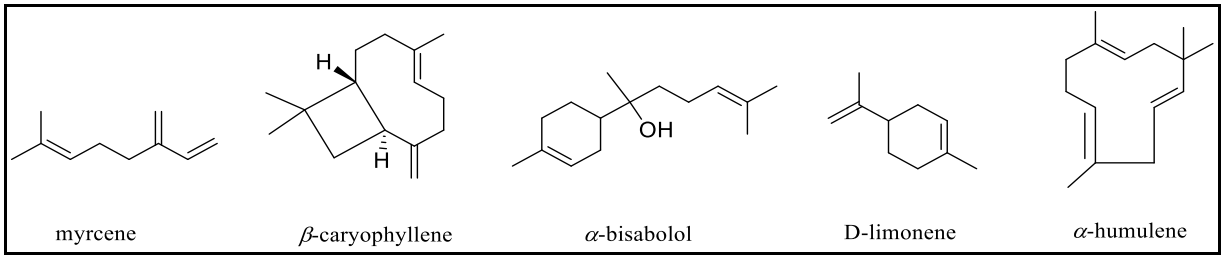

Figure 41. Main monoterpenes and sesquiterpenes detected in EOs from CBG-rich varieties.

Table 16. Results obtained from the GC-MS analysis of the EOs of the 4 investigated CBG varieties.

	Compound	RT	RI-exp	RI-lit	CBG 4	CBG 14	CBG 18	CBG 32
1	heptanal	5.55	902	901	0.50	0.94	1.14	1.05
2	*α*-pinene	6.64	932	932	6.58	11.28	13.93	0.38
3	camphene	7.15	947	946	0.12	0.30	0.41	0.05
4	*β*-pinene	8.16	975	974	2.02	1.82	2.59	0.36
5	*β*-myrcene	8.73	991	988	25.65	23.73	34.94	11.77
6	*α*-phellandrene	9.20	1004	1002	0.38	0.40	0.15	0.03
7	*α*-terpinene	9.67	1016	1014	0.42	0.38	0.16	n.f.
8	D-limonene	10.13	1028	1024	3.74	3.14	7.15	4.26
9	1,8-cineole	10.21	1030	1026	0.90	2.17	2.02	n.f.
10	*β*-trans-ocimene	10.93	1049	1044	1.79	1.75	n.f.	n.f.
11	*γ*-terpinene	11.30	1058	1154	0.44	0.48	0.29	0.01
12	terpinolene	12.44	1088	1086	5.91	5.09	0.33	0.28
13	linalool	12.90	1100	1098	0.82	0.31	0.37	0.27
14	nonanal	13.09	1105	1100	0.21	0.67	0.47	0.84
15	endo-fenchol	13.37	1112	1114	0.22	0.25	0.91	0.84
16	(*E*)-pinene hydrate	13.67	1120	1119	0.12	0.14	0.30	0.38
17	borneol	15.34	1165	1165	0.08	0.11	0.26	0.15

18	terpinen-4-ol	15.78	1176	1174	0.34	0.29	0.14	0.01
19	*α*-terpineol	16.29	1190	1186	0.36	0.49	0.70	0.30
20	hexyl butyrate	16.41	1193	1191	0.48	0.08	0.42	0.37
21	*α*-(*Z*)-bergamotene	24.02	1416	1411	0.12	0.21	0.20	0.39
22	*β*-caryophyllene	24.14	1420	1417	9.91	17.94	4.23	19.58
23	*α*-(*E*)-bergamotene	24.66	1437	1432	1.74	2.54	2.36	3.78
24	*α*-humulene	25.21	1454	1452	3.14	6.05	1.28	8.02
25	*β*-(*Z*)-farnesene	25.33	1458	1453	2.40	2.63	2.58	4.44
26	9-*epi*-(*E*)-caryophyllene	25.44	1462	1464	0.37	0.13	0.25	0.74
27	*γ*-curcumene	26.04	1481	1481	0.11	0.19	0.14	0.47
28	*β*-selinene	26.14	1484	1489	0.49	0.81	0.13	0.89
29	valencene	26.46	1494	1496	0.10	0.14	n.f.	0.28
30	*α*-selinene	26.51	1496	1498	0.67	0.89	0.28	1.62
31	*β*-bisabolene	26.92	1509	1505	2.77	0.86	0.55	3.23
32	*β*-curcumene	27.02	1513	1514	0.44	0.30	0.40	0.73
33	sesquicineole	27.19	1519	1515	0.33	0.07	0.06	0.33
34	7-*epi*-*α*-selinene	27.27	1521	1520	0.21	0.61	0.22	0.86
35	*β*-sesquiphellandrene	27.37	1525	1521	0.31	0.18	0.17	0.56
36	selina-4(15),7(11)-diene	27.70	1536	1544	2.12	0.45	0.10	0.84

37	*β*-maaliene	27.79	1539	n.found	1.13	1.65	0.31	2.43
38	selina-3,7(11)-diene	27.90	1543	1545	5.01	0.74	0.22	1.07
39	(*E*)-*α*-bisabolene	27.93	1544	n.found	n.f.	0.92	n.f.	2.66
40	caryophyllene oxide	29.11	1584	1582	1.48	1.80	0.33	3.14
41	guaiol	29.54	1599	1600	1.34	0.23	3.43	0.44
42	humulene epoxide II	29.87	1611	1608	0.53	0.56	0.18	1.14
43	*γ*-eudesmol	30.16	1621	1630	2.47	1.60	4.38	3.32
44	*β*-eudesmol	31.01	1651	1649	0.71	0.26	2.08	0.61
45	*α*-eudesmol	31.09	1654	1652	1.04	0.41	3.01	1.10
46	bulnesol	31.50	1669	1670	0.91	0.05	2.49	0.08
47	*α*-bisabolol	31.94	1685	1685	5.52	0.91	0.06	9.82
48	eudesm-7(11)-en-4-ol	32.28	1697	1700	0.22	0.34	0.01	1.04
49	cannabidiol	48.14	2429		0.48	0.28	0.47	0.83
50	cannabichromene	48.23	2437		0.04	0.02	0.03	0.04
51	cannabigerol	49.79	2587		0.08	0.09	0.21	0.50
	Compound classes							
	Monoterpene hydrocarbons				47.05	48.37	59.95	17.14
	Oxygenated monoterpene hydrocarbons				2.83	3.75	4.7	1.96
	Sesquiterpene hydrocarbons				31.04	37.24	13.42	52.6

Oxygenated sesquiterpenes hydrocarbons	14.55	6.24	16.04	20.56
Cannabinoids	0.6	0.39	0.71	1.37
Other	1.19	1.69	2.02	2.25
Total identified	97.25	97.71	96.84	96.35

3.2.3 In vitro antitrypanosomal activity

The twelve commercial varieties of *C. sativa* L. essential oils were assayed *in vitro* on *T. brucei* bloodstream forms, as well as against mammalian cells (BALB/3T3 mouse fibroblasts), as a counter-screen for toxicity, and the results are reported in Table 17.

EOs from the 8 high-CBD varieties (named Fresh Mountain, Lemon Conti Kush, Venom OG, Gorilla Glue, Amnesia Cookies, 24K, White Shark, and Pablito) showed a preferential effect on mammalian cells than on parasites cells, with low selectivity indices (SI) ranging from 0.42 to 0.66. On the other hand, EOs from the 4 high-CBG chemovars (named CBG4, CBG14, CBG18, and CBG32) were more selective against *T. brucei* than mammalian cells, with SI ranging from 1.11 to 2.09. As reported in Table 5, CBG18 chemovar resulted to be the most active essential oil, with almost a four-fold higher activity against S427 than the best high-CBD chemovar Venom OG (EC_{50} = 9.14 and 24.4 μg/mL, respectively).

Pure cannabinoids were also tested on the parasite. The 3 commercially available cannabidiol (CBD), cannabigerol (CBG), and cannabichromene (CBC) were assayed both on *T. brucei* and mammalian fibroblasts. As shown in table 17, CBG emerged three times more active than CBD against the parasite (EC_{50} = 3.25 and 9.25 μg/mL, respectively). Furthermore, the selective index for CBG was 7.45, showing a preferential effect on target cells compared with CBD (4.4). Surprisingly, CBC resulted to be less active and selective than the other two cannabinoids assayed.

Table 17. Antitrypanosomal activity of 12 commercial varieties of *Cannabis sativa* L. EOs and pure cannabinoids.

	EC_{50}		**Selectivity Index (SI)**
	***T. b. brucei* (s427)**	**Balb3T3**	
Essential oils	**μg/mL**	**μg/mL**	
Fresh Mountain	34.42 ± 2.64	15.31 ± 0.61	0.44
Lemon Conti Kush	25.82 ± 1.09	11.22 ± 0.49	0.45
Venom OG	24.43 ± 1.11	14.75 ± 0.61	0.61
Gorilla Glue	25.41 ± 1.17	10.22 ± 0.49	0.41
Amnesia cookies	30.72 ± 2.45	20.39 ± 0.61	0.66
24K	24.98 ± 1.73	10.38 ± 0.49	0.42

White Shark	27.21 ± 1.43	10.51 ± 0.61	0.37
Pablito	26.09 ± 1.03	12.13 ± 0.49	0.46
CBG 4	21.09 ± 1.75	23.53 ± 1.49	1.11
CBG 14	14.39 ± 0.88	16.15 ± 0.91	1.12
CBG 18	9.14 ± 0.21	19.13 ± 0.49	2.09
CBG 32	19.27 ± 1.11	28.43 ± 1.32	1.47
Cannabinoids	**µM**	**µM**	
CBD	9.25 ± 0.26	41.33 ± 1.06	4.46
CBG	3.25 ± 0.18	24.22 ± 0.67	7.45
CBC	22.43 ± 0.16	51.27 ± 0.36	2.28
Reference drug	**µM**	**µM**	
Suramin	0.025 ± 0.001	> 5	> 200

3.3 Hydrophilic extracts (HEs)

3.3.1 HEs production and antitrypanosomal activity

Hydrophilic extracts (HEs) were prepared through lyophilization of the residual water from the hydrodistillation process. Yields are reported in supporting information.

As reported in Table 18, the antiprotozoal potential of HEs has been evaluated through *in vitro* tests against s427 cells and their selectivity assessed through assays on fibroblast cells. The HE from Gorilla Glue chemovar showed the best biological profile against the parasites with almost three-fold higher activity than HE from Fresh Mountain chemovar (EC_{50} = 15.38 and 41.88 µg/mL, respectively) and an improved selectivity index (SI = 4.43 and 1.26, respectively, Figure 50). The other HEs showed a weak EC_{50} against s427 cells, and for this reason, the toxicity towards mammalian cells has not been calculated.

Table 18. Antitrypanosomal activity of 12 commercial varieties of *Cannabis sativa* L. HEs.

	EC_{50}		Selectivity Index (SI)
	***T. b. brucei* (S427)**	**Balb3T3**	
Hydrophilic extracts (HE)	**µg/mL**	**µg/mL**	
Fresh Mountain	41.88 ± 1.64	52.73 ± 1.91	1.26
Lemon Conti Kush	95.05 ± 2.11	-	-
Venom OG	66.61 ± 1.34	-	-
Gorilla Glue	15.38 ± 0.22	68.22 ± 2.55	4.43
Amnesia cookies	54.32 ± 2.11	-	-
24K	64.85 ± 1.92	-	-
White Shark	166.6 ± 5.22	-	-
Pablito	164.1 ± 6.33	-	-
CBG 4	123.1 ± 3.11	-	-
CBG 14	143.1 ± 2.35	-	-
CBG 18	96.12 ± 1.35	-	-
CBG 32	175.1 ± 6.35	-	-
Reference drug	**µM**	**µM**	
Suramin	0.025 ± 0.001	> 5	> 200

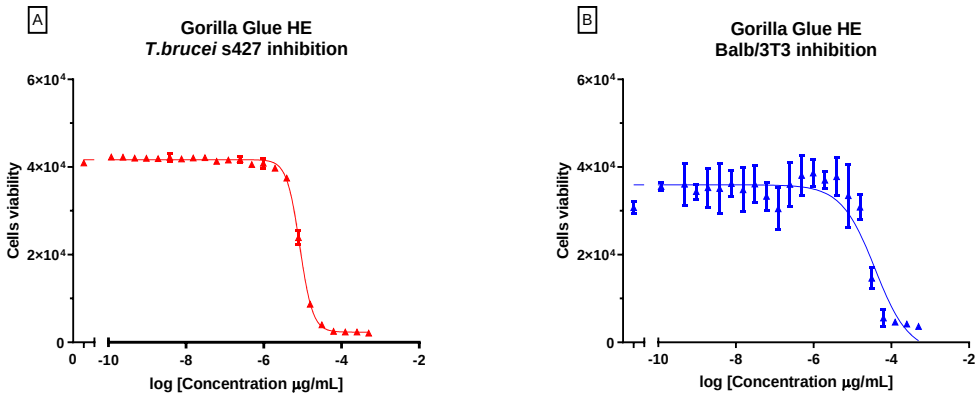

Figure 42. Growth inhibition of *T. b. brucei* s427 (A) and Balb/3T3 cells (B) induced by Gorilla Glue HE.

3.3.2 Characterization of HEs by HPLC-DAD-MS^n

The HE derived from Gorilla Glue residual water resulted to be the most active against *T. brucei* cells (15.38 μg/mL, Table 18) among the other HEs, and has been subjected to extensive chemical characterization and purification of its main flavonoids. The HPLC-DAD-MS^n analysis of flavones allowed us to identify 11 compounds, i.e., luteolin, apigenin, quercetin glycosides, and the hemp-specific flavonoids cannflavin A and B. Furthermore, the flavonoids cannabisin A and B were also identified and quantified, as reported in Table 19.

The 11 flavonoids were identified based on a comparison with pure reference compounds using HPLC, molecular weights, and fragment ions by HPLC–MS. Data were in agreement with those reported in the literature. The main flavonoids identified were luteolin-C-hexoside-O-rutinoside (2.51 mg/g), apigenin-hexoside-glucuronide (0.79 mg/g), rutin (0.75 mg/g), and cannflavin A (0.62 mg/g). As expected, cannabinoids were present in negligible amounts due to their poor water solubility.

Table 19. HPLC-DAD-MS^n characterization of flavonoids in HEs.

Compound	Content in Gorilla Glue HE (mg/g)
cannabisin A	0.33
cannabisin B	0.30
luteolin-C-hexoside-O-rutinoside	2.51
rutin	0.75
luteolin-hexoside-hexoside	0.21
vitexin 2"-O-glucoside	0.40
apigenin-hexoside-glucuronide	0.79
luteolin 7-glucuronide	0.29
apigenin 7-glucuronide	0.31
cannflavin B	0.12
cannflavin A	0.62

3.3.3 Bio-guided fractionation of Gorilla Glue HE

Gorilla Glue HE, being the most active among HEs, was subjected to column chromatography over silica gel eluting with mixtures of hexanes-EtOAc of increasing polarity to afford twelve fractions, which were combined based on their TLC profile into four fractions (named A to D). The composition of each fraction has been determined by HPLC (using the same method described before) and has been reported in Table 20. As reported in Table 21, fraction D showed an improved biological profile against the parasites if compared with the Gorilla Glue HE (EC_{50} = 11.14 and 15.38 μg/mL, respectively) and a slightly improved selectivity index (SI = 5.33 and 4.3, respectively).

Table 20. Chemical composition of fractions A-D.

Fractions	**Components**
Fraction A	Cannabisin A Cannabisin B Undefined minor components
Fraction B	Rutin Vitexin 2″-O-glucoside, Luteolin-hexoside-hexoside, Luteolin-C-hexoside-O-rutinoside
Fraction C	Apigenin-hexoside-glucuronide Luteolin 7-glucuronide Apigenin 7-glucuronide
Fraction D	Cannflavin A Cannflavin B

Table 21. Antitrypanosomal activity of fractions from Gorilla Glue HE and pure compounds flavonoids.

	EC_{50}		Selectivity Index (SI)
	***T. b. brucei* (S427)**	**Balb3T3**	
Fractions from Gorilla Glue HE	**µg/mL**	**µg/mL**	
Fraction A	176.6 ± 4.33	-	-
Fraction B	na[a]	-	-
Fraction C	na	-	-
Fraction D	11.14 ± 0.31	60.38 ± 1.97	5.33
Reference drug	**µM**	**µM**	
Suramin	0.025 ± 0.001	> 5	> 200

[a] na = not active, EC_{50} > 200 mg/mL

3.3.4 Isolation of Cannflavin A

The good activity of Fraction D pushed towards the phytochemical investigation of the fraction in order to isolate their constituting compounds. Thus, fraction D was processed through preparative HPLC to afford a cannflavin B enriched fraction and pure cannflavin A as white needles. NMR and MS spectroscopic data and comparison with data reported in the literature confirmed their identity.

Cannflavin A was further characterized by ^{1}H and ^{13}C NMR. The ^{1}H NMR spectra of cannflavin A exhibited three peaks of area 3H in the region between 1.5 and 2.0 ppm and 2 peaks of area 1H in the region between 5.0 and 5.5 ppm, consistent with three methyl groups and two vinylic protons, respectively, suggesting the presence of a geranyl group.

The complete ^{1}H and ^{13}C-NMR assignments are shown in Table 22.

Table 22. ^{1}H and ^{13}C NMR assignments for cannflavin A.

Position	Cannflavin A	
	δ_H	δ_C
2	-	164.6
3	6.55	103.1
4	-	182.4
5	-	158.4
6	-	112.5
7	-	161.9
8	6.42	92.9
9	-	156.3
10	-	104.2
1’	-	123.4
2’	7.40	109.3
3’	-	147.0
4’	-	149.9
5’	6.86	115.5
6’	7.42	120.0
1’’	3.25	20.85
2’’	5.16	122.2
3’’	-	133.8
4’’	1.89	39.4
5’’	1.98	26.2
6’’	4.98	124.2
7’’	-	130.6
8’’	1.47	24.3
9’’	1.53	16.4
10’’	1.70	15.0
O-CH_3	3.89	55.1

COSY, TOCSY, and HMBC spectra also demonstrated peak patterns that were consistent with a geranyl group for cannflavin A as reported by Choi and colleagues (Choi et al., 2004). Initial NMR assignments for cannflavin A were performed using the COSY, TOCSY, and HSQC spectra to assign all proton resonances as well as those of proton-bearing carbons and an HMBC experiment was then used to complete the carbon assignments (Spectra in supporting information). HMBC correlations were observed from both the 5-OH hydroxyl proton and the 1" proton on the geranyl group to the same carbon resonance (shown as bold arrows in Fig. 43). The 5-OH hydroxy proton is too far away from the carbon at position 8 for an HMBC correlation to be observed, and the geranylation was supposed to be at the 6 position.

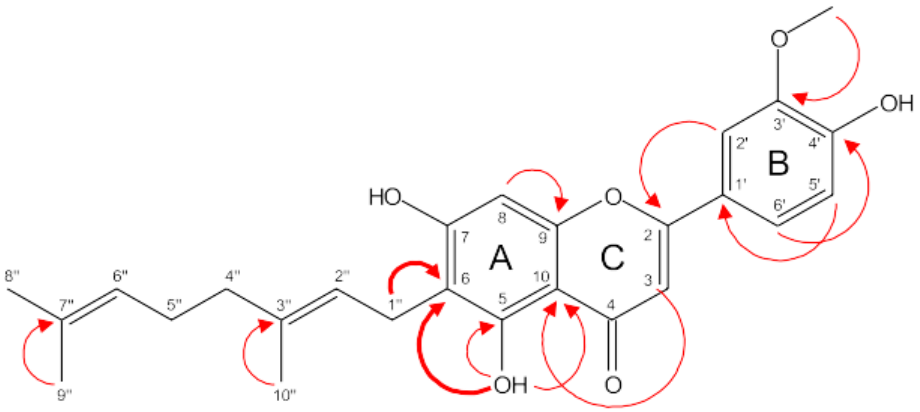

Figure 43. Key HMBC correlations for cannflavin A. Bold arrows indicate correlations that were observed from both the 5- OH hydroxyl proton and the 1" proton on the geranyl group to the same carbon resonance.

Isolated cannflavin A, and the enriched cannflavin B fraction were also tested against s427, and BALB/3T3 cells. Suramin has been used as the reference drug (Table 23).

The results showed that cannflavin A exhibited strong activity against s427 cells (EC_{50} = 1.81 µg/mL) and did not significantly affect the mammalian cells (SI = 14.4, Figure 44). Usually, a compound that showed a selectivity index >2 is considered selective against *T. brucei* cells and may represent a good starting point for developing new antiprotozoal drugs. Instead, cannflavin B enriched fraction had a higher EC_{50} (12.06 µg/mL) than cannflavin A (EC_{50} = 1.81 µg/mL).

Table 23. Antitrypanosomal activity of isolated compounds.

	EC_{50}		Selectivity Index (SI)
	***T. b. brucei* (s427)**	**Balb3T3**	
Flavonoids	**µg/mL or µM**	**µg/mL or µM**	**SI**
Cannflavin A	1.81 ± 0.05	26.08 ± 0.85	14.4
Cannflavin B enriched fraction	12.06 ± 0.14	28.33 ± 0.89	2.35
Reference drug	**µM**	**µM**	
Suramin	0.025 ± 0.001	> 5	> 200

*na = not active

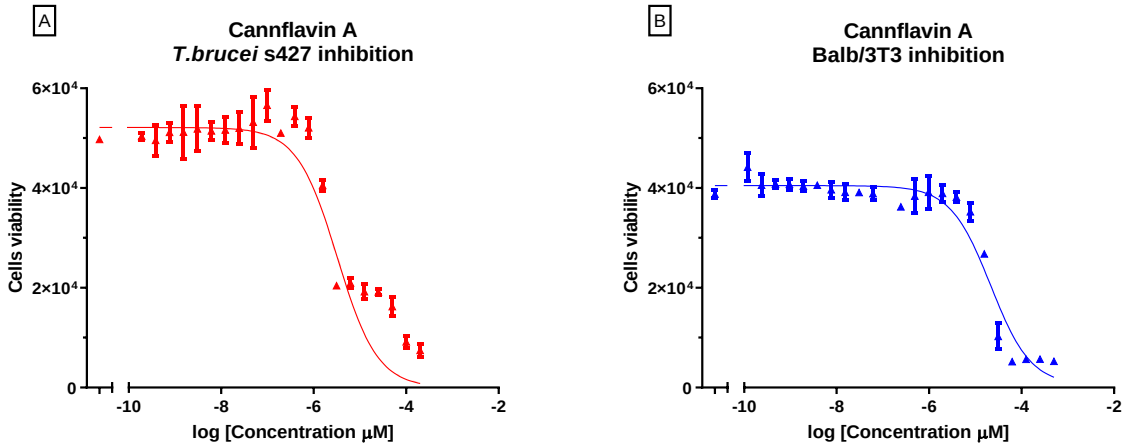

Figure 44. Growth inhibition of *T. brucei* s427 (A) and Balb/3T3 (B) cells induced by Cannflavin A.

3.4 Discussion

Cannabis sativa has been widely studied for its numerous and various biological activities. In particular, EOs have played an important role in pharmacological research due to their varied composition. EOs are indeed characterized by a great variability, which depends on the evaluated chemovars, cultivation conditions, and processing procedures. Besides composition, the amount of EO collectible is also influenced by several factors, e.g., genetics, plant biomass status, environmental and climatic conditions, post harvesting, drying, etc. In the present study, the yields of the EOs ranged from 0.23% w/w in CBG32 to 1.81% w/w in Amnesia Cookies. The yields were considerably high when compared to the maximum yield value for hemp EO

found in the literature, corresponding to 0.60%, and to the yields for EOs from the certified European hemp varieties (Fiorini et al., 2019; Abdollahi et al., 2020; Rossi et al., 2020). The enhanced yields for the studied varieties are probably attributable to using only non-pollinated female inflorescences for the hydrodistillation process. Indeed, it has been proved that pollinated flowers of *C. sativa* produce half the amount of EO with respect to non-pollinated flowers (Meier and Mediavilla, 1998). Also stress conditions can influence the secretion of EOs e.g., climate and temperature changes, as well as harvesting, processing, and storage (Pate, 1994). Regarding the composition of the EOs, the volatile profiles of the 12 varieties considerably differ among each other overall, with respect to their original monoecious varieties. This can be due to differences in the extraction method and plant material status. For instance, the EOs from 24K and Gorilla Glue chemovars were characterized by mainly sesquiterpenes and in particular by (*E*)-caryophyllene; the EO from Carmagnola, the variety from which 24K and Gorilla Glue derived, is instead mainly constituted by monoterpenes when fresh inflorescences are steam-distilled, whereas a higher sesquiterpene content is detected when hydrodistillation of dry inflorescences is carried out (Nissen et al., 2010; Pieracci et al., 2021). The same trend was observed for Pablito EO, for which sesquiterpenes represented the most abundant components differently from its original variety Santhica 70, whose EO presents a high percentage of monoterpenes, and especially myrcene (Iseppi et al., 2019). On the contrary, EOs from Lemon Conti Kush, Fresh Mountain, and Amnesia Cookies showed a high content of monoterpenes consistently with what is reported for the variety from which they originate, the Kompolti variety (Palmieri et al., 2021). In general, peculiar sesquiterpenes such as 10-*epi*-γ-eudesmol and guaiol in 24 K, selina-3,7(11)-diene and selina-4(15),7(11)-diene in Gorilla Glue, and α-bisabolol in Pablito, were detected in significant amounts. These sesquiterpenes were not frequent in hemp EOs from other studies, e.g., selina-3,7(11)-diene and α-bisabolol were found in low amounts in Carmagnola EO studied by Bertoli et al. (2010) whereas none of them were detected in the Kompolti EO from Novak and colleagues (Novak et al., 2001). Concerning EOs obtained from CBG rich varieties, their composition seems to be characterized by mainly monoterpenes. Specifically, α-pinene, β-myrcene, and D-limonene resulted as the most abundant components of the EOs. CBG32 EO represented an exception, being characterized by a volatile profile more similar to that obtained for EOs derived from CBD rich cultivars. Indeed, CBG32 EO accounted for 52.6% of sesquiterpenes hydrocarbons and 20.56% of oxygenated sesquiterpenes, whereas the monoterpenic fraction only reached the 19.1%. Both CBD and CBG rich cultivars derived EOs were tested *in vitro* on *T. brucei* and their antitirypanosomal potential was evaluated. Generally, EOs from CBD rich varieties

demonstrated a mild activity on trypanosomes but resulted more toxic on mammalian cells, thus suggesting they are not employable for therapeutic purposes. On the contrary, EOs from CBG rich cultivars showed an enhanced activity on the parasite when compared to the abovementioned EOs, and an ameliorated safety profile, with selectivity indices over 2.

Pure cannabinoid activities were also analyzed. Cannabinoids and cannabinoid-rich organic extracts already proved to have a role in the inhibition of *T. cruzi* and *T. evansi* invasion, respectively (Croxford et al., 2005; Abdelrahman et al., 2012). Testing them on *T. brucei*, CBD and CBG showed EC_{50} values of 9.25 And 3.25 µM, respectively. CBC resulted less active with a higher EC_{50} (22.43 µM). CBG appeared as the safest among cannabinoids with a SI of 7.45 when compared to SI of CBD and CBC (4.45 and 2.28, respectively). The more pronounced activity of EOs derived from CBG-rich varieties could be related to the activity of pure CBG against the parasite. However, the amount of cannabinoids detected in EOs is not sufficient to identify CBG as the agent responsible for the antitrypanosomal activity of the intact EO.

Hydrophilic extracts (HE) were prepared by lyophilizing the residual water from hydrodistillation. The most promising extract in terms of antitrypanosomal activity (Gorilla Glue HE) was then evaluated in its composition in order to identify the responsible agents for this effect. Notably, *C. sativa* is characterized by a variety of hydrosoluble phenolic compounds, e.g. flavonoids, phenolic acids, phenol amides, and lignanamides. For this reason, it was hypothesized that these compounds could have an impact on the activity of the HE against *T. brucei*. Gorilla Glue HE was found to be rich in flavonoids and specifically in luteolin-C-hexoside-O-rutinoside, rutin, apigenin-hexoside-glucuronide, and cannflavin A (amounts > 0.5 mg/g of HE). Fractionation of the HE and subsequent *in vitro* evaluation of their activity, proved that the fraction D, rich in cannflavins, presented an interesting antitrypanosomal potential (EC_{50} value of 11.14 µg/mL). This finding pushed the research to test the isolated components of the fraction: cannflavin A was successfully isolated, whereas for cannflavin B an enriched fraction was obtained. Both the products were tested, assessing the more potent antiprotozoal efficacy of cannflavin A with respect both to the cannflavin B enriched fraction and to fraction D. Cannflavin A was isolated for the first time in 1985 by Barrett and colleagues (Barrett et al., 1985) and was identified as a flavonoid characteristic of *C. sativa*. Over the last years, many biological activities were attributed to this flavonoid, such as anti-inflammatory, neuroprotective, anticancer, and antiviral activities (Barrett et al., 1986; Werz et al., 2014; Lowe et al., 2016; Akhtar et al., 2019; Eggers et al., 2019; Lowe et al., 2020; Rasool et al., 2020a; Rasool et al., 2020b). In general, *C. sativa* flavonoids and derived products have been poorly

studied for their antiprotozoal potential. Radwan and colleagues (2008) proved that non-cannabinoid components from *C. sativa*, including cannflavins, displayed antileishmanial activity and Nok and colleagues (1994) reported the *in vitro* efficacy of an ether seed extract of *C. sativa* against *T. brucei* (Nok et al., 1994; Radwan et al., 2008). However, to the best of our knowledge, this is the first report of cannflavin A as an antitrypanosomal agent.

3.5 Conclusion

Although *C. sativa* is characterized by a wide range of phytochemicals, much attention has been primarily given to the two phytocannabinoids, Δ^9-tetrahydrocannabinol (THC) and cannabidiol (CBD), due to their distinctive activities in humans. These bioactivities can be further enhanced through the interaction of THC and CBD with other phytocannabinoids or non-phytocannabinoid chemicals, such as terpenes and flavonoids, a phenomenon that is termed the entourage effect. Flavonoids therapeutics potential in *C. sativa* and the entourage effect are currently understudied.

Firstly, this work sheds light on the valorization of different products from the hydrodistillation of hemp varieties, namely, essential oils (EOs) and hydrophilic extracts (HEs), which proved to be worthy of exploitation in industrial and health applications.

Then, although preliminary, our results confirmed the usefulness of *C. sativa* as an effective herbal remedy for the treatment of protozoan infectious diseases and highlighted the opportunity to use the flavonoid cannflavin A as an inspiring lead compound for designing future antitrypanosomal drugs. Further studies are needed, in particular, to increase the knowledge about the mode of action and the possible molecular targets related to the antitrypanosomal activity of cannflavin A. Studying different derivatives as well as strictly related prenylated flavonoids can be a good starting point to explore structure-activity relationships. Synthetic or semisynthetic flavonoid derivatives can be produced to follow a rational approach for developing more active antitrypanosomal drug candidates.

3.6 Materials and methods

3.6.1 Plant material

The 12 varieties of *C. sativa* studied were provided by EverWeed CBD company (Sibillini National Park, Amandola (FM), Conti district), and obtained by crossbreeding. 24K and Gorilla Glue belong to Carmagnola variety (male inflorescences) crossed with an undeclared variety; Amnesia Cookies, Fresh Mountain, and Lemon Conti Kush come from a basic Kompolti variety (male inflorescences) crossed with an undeclared variety; Pablito derives basically from Santhica 70 variety crossed with an undeclared variety whereas Venom OG and White Shark were obtained by replanting the seeds of the 24K variety. Concerning CBG-rich varieties, CBG 4, 14, 18 and 32 were obtained by crossbreeding selected Pablito plants. Full genetics crosses were not disclosed because of a future patent application possibility.

Plants were cultivated in appropriate and controlled conditions, without the use of pesticides, herbicides, and chemical fertilizers and with a sustainable, integrated agriculture. Specifically, initially, 18 hours of light were needed, to ensure that the plant remained in the vegetative stage, then agamic reproduction with the cuttings occurred. The latter were subsequently cut and placed in a hydroponic greenhouse where they were allowed to root. Once born, the plant was transferred to the ground and covered with large, black mulching sheets, so that they could reflect the sunlight. It was then made to grow up to about 60 cm in height, thanks to the aid of nets. Drip irrigation (or also known as micro-irrigation) was used. Nutrition was also very scrupulously regulated in order to keep low THC levels, and the NPK macronutrients used affect the growth and development of the plant, noting how nitrogen affects the THC content in the plant, in particular.

The harvesting took place when the hairs of the plant were 80-90% amber in colour from September until the second week of October. The branches were cut individually and then subjected to the action of a machine that eliminated the larger surface leaves. The plants were then hung from wires in a dark and airy room and fans along with dehumidifiers were used to avoid, above all, the formation of mold and to eliminate any residual moisture. Flowers were divided from the branches and they were again deprived of any smaller residual leaves. Lastly, the obtained hemp was closed in hermetic containers of a dark colour to protect the product from the light.

3.6.2 Hydrodistillation

Hydrodistillation (HD) was performed on dried samples of aerial parts of the 12 *C. sativa* cultivars. For all the samples, 200 g of plant material soaked in 6 L of distilled water heated by a mantle system Falc MA (Falc Instruments, Treviglio, Italy) for 5 h. The EOs were recovered by a glass Clevenger-type apparatus and stored at 4°C before chemical characterization and biological evaluation. The EOs yields were calculated on a dry-weight basis and reported in supporting information.

3.6.3 GC-MS analysis

The chemical composition of *C. sativa* EOs was analyzed through an Agilent 6890N GC-MS system coupled to a 5973N single quadrupole detector mass spectrometer. The separation was provided by an HP-5MS capillary column (5% phenylmethylpolysiloxane, 30 m x 0.25 mm i.d., 0.1 µm f.t., Agilent, Santa Clara, CA, USA). The temperature program was as follows: 60 °C for 5 min, then 4 °C min-1 up to 220 °C, finally 11 °C min-1 to 280 °C, maintained for 15 min, for a total run time of 65 min. The temperature of the injector and detector was 280 °C. Helium (He) was the carrier gas, with a flow rate of 1 mL min-1 and a 1:50 split ratio. The chromatograms were acquired in full scan in the range 29.0–400.0 uma, using electron-impact (EI, 70 eV) mode. Dilution 1:100 of essential oils in n-hexane was injected (2 µL) into the GC-MS system. The MSD ChemStation (Agilent, Version G1701DA D.01.00) and the NIST Mass Spectral Search Program were employed for the data analysis. Identifying the principal compounds was achieved by the correspondence of retention indices and mass spectra to those of ADAMS, NIST 17, FFNSC2, and WILEY 275 libraries. Furthermore, the analytical standards available in the laboratory (Sigma-Aldrich, Milan, Italy) were used for further confirmation. The relative peak area percentages were obtained by area normalization without using correction factors (Quassinti et al., 2013).

3.6.4 Lyophilization of HD residual water

The frozen residual water after EO distillation was freeze-dried at − 54 °C and 0.05mbar, through a BUCHI Lyovapor™ L-200 freeze-dryer (Büchi Labortechnik AG, Flawil, Switzerland). The hydrophilic extracts (HE) were ground in a mortar and the resulting powders were maintained at 4 °C for subsequent analyses. Yields are reported in table S2 in supporting information.

3.6.5 HPLC-DAD-MS^n analysis

An Agilent 1260 chromatograph with an autosampler and a diode array detector (DAD), interfaced with a Varian MS 500 ion trap mass spectrometer, was employed to quantify flavonoids in the Gorilla Glue HE. For the analysis of flavonoids and minor compounds, the column was an Agilent Eclipse XDB C18 (3.0 m × 150 mm × 3.5 μm), and the mobile phase was represented by a mixture of 1% formic acid in water (A) and acetonitrile (B). At the beginning, the gradient was 95% A, and in 30 min reached 100% B, with a flow rate of 0.4 mL/min. Data were collected by DAD in the λ range of 200–400 nm. The mass spectrometer was provided with an electrospray ion (ESI) source, which was employed in negative ion mode. The MS parameters were the following: spray chamber temperature, 45 °C; needle voltage, 4700 V; capillary voltage, 85 V; RF loading, 80%; nebulizing gas pressure, 25 psi (nitrogen); drying gas pressure, 15 psi; drying gas temperature, 300 °C. Spectra were acquired in the 50–1000 *m/z* range. Chromatograms were acquired from the turbo data depending on the scanning (TDDS) mode, allowing the generation of fragmentation spectra for the most intense ionic species. For the analysis of cannabinoids, an Agilent XDB (4.6 m × 250 mm × 5.0 μm) was used as the stationary phase. The gradient of elution was performed using water 1% formic acid (A) acetonitrile (B) and methanol (C). The gradient started with 30% A and 70% B, and in 20 min arrived at 70% B and 30% C; in 23 minutes it reached 100% C and stayed isocratic up to 33 minutes. Data were detected with DAD in the λ range of 200–400 nm. ESI-MS spectra were collected in positive ion mode for the neutral cannabinoids, and in negative ion mode for the acidic forms. Compounds were identified based on *m/z* values and retention times, and by comparison with authentic standards. For quantitative purposes, standard solutions in concentration from 0.1 to 100 μg/mL were set up to develop the calibration curves. For this purpose, rutin and quercetin-3-O-glucoside were selected for phenols content determination. For the analyses, the sample was finely ground and about 200 mg were weighed and extracted with 25 mL of MeOH/H_2O 70:30. The extract was sonicated in an ultrasound bath for 15 min and centrifuged, and then the supernatant was taken and inserted into HPLC vials.

3.6.6 Gorilla Glue HE fractionation

Gorilla Glue HE (30 g) was subsequently subjected to column chromatography over silica gel (63-200 mm, 9 x 40 cm) eluting with mixtures of hexanes-EtOAc of increasing polarity (100:0 to 0:100) to afford twelve fractions, which were combined based on their TLC profile into four fractions (named A to D). The composition of each fraction has been determined by HPLC

using the method described in the HPLC-DAD-MS^n analysis section. Fraction yields are reported as % of the total Gorilla Glue HE (Table S3 in supporting information).

3.6.7 Cannflavin A isolation

Fraction D (1 g) was purified through preparative HPLC to afford pure cannflavin A as a crystalline solid (16 mg) and an enriched cannflavin B fraction (29 mg). An Agilent 1260 chromatograph with an autosampler and a diode array detector (DAD) was used. Fraction D was purified in several rounds (injection volume 100 µL) with an Agilent ZORBAX SB-C18 column (4.6 x 50/21.2 x 150) at a flow rate of 10 mL/min and a pump pressure of 250 barr. The gradient of elution was performed using water 1% formic acid (A) and methanol (B). The gradient started with 50% A and 50% B; in 30 minutes it reached 100% B and stayed isocratic up to 45 minutes. Data were detected with DAD at a wavelength of 350 nm. For the analyses, the fraction was dissolved in 0.75 mL of methanol with the help of sonication in an ultrasound bath for 10 minutes.

The two flavonoids were identified on the basis of their spectral data (UV-Vis for cannflavin B and ^{1}H and ^{13}C NMR for cannflavin A) and by comparison with those reported in the literature for the same compounds.

3.6.8 NMR analysis of Cannflavin A

NMR analyses were performed on a Bruker Ultrashield Plus 500MHz spectrometer equipped with a 5-mm CPTCI cryo-probe (^{1}H-^{13}C/^{15}N/2H+Z-gradients) operating at 303 K. The structure identification of the purified compounds was based on a selection of ^{1}H and ^{13}C NMR spectra based on complexity or quantity of the sample. The proton and carbon chemical shifts were referenced to the internal reference TMS (proton d = 0.00 ppm; carbon, d = 0.00 ppm). Data were processed using Topspin 2.1 pl5 and analyzed with Mnova 6.2.1. The ^{1}H NMR and ^{13}C NMR profile of cannflavin A matched with that described in the literature and is reported below. Peak assignments for cannflavin A were determined using standard 2D pulse sequences (HSQC and HMBC). The HMBC was collected with 768 increments in the indirect dimension; all other experiments were collected with 256 indirect increments. The HMBC coupling constant was set to 10 Hz. All spectra are reported in supporting information.

Cannflavin A: ^{1}H NMR (DMSO) δ: 6.55 (s, 1H, H-3), 6.42 (s, 1H, H-8), 7.40 (s, 1H, H-2′), 6.86 (d, *J* = 8.3 Hz, 1H, H-5), 7.42 (d, *J* = 8.3 Hz, 1H, H-6′), 3.25 (d, *J* = 7.1 Hz, 2H, H-1″), 5.16 (dt, *J* = 1.1, 7.2 Hz, 1H, H-2″), 1.89 (t, *J* = 7.1 Hz, 2H,H-4″), 1.98 (m, 2H, H-5″), 4.98 (t, *J* = 7.1 Hz, 1H, H-6″), 1.47 (s, 3H, H-8″), 1.53 (s, 3H, H-9), 1.70 (s, 3H, H-10″), 3.89 (s, 3H, O-CH_3).

^{13}C NMR (DMSO) δ: 164.6 (C-2), 103.1 (C-3), 182.4 (C-4), 158.4 (C-5), 112.5 (C-6), 161.9 (C-7), 92.9 (C-8), 156.3 (C-9), 104.2 (C- 10), 123.4 (C-1′), 109.3 (C-2′), 147.0 (C-3′), 149.9 (C-4′), 115.5 (C-5′), 120.0 (C-6′), 20.85 (C-1"), 122.2 (C-2"), 133.8 (C-3"), 39.4 (C-4"), 26.2 (C-5"), 124.2 (C-6"), 130.6 (C-7"), 24.3 (C-8"), 16.4 (C-9"), 15.0 (C-10"), 55.1 (O-CH_3).

3.6.9 T. brucei and Balb/3T3 cell culture

T. brucei s427 bloodstream forms (subspecies *T. b. brucei*) and mammalian Balb/3T3 fibroblasts (ATCC no CCL-163) were harvested as reported in Ngahang Kamte, et al., 2017. *T. brucei* cells were cultured in HMI-9 medium supplemented with 5% (v/v) heat inactivated fetal bovine serum (FBS) and 10 mL/L of 100x penicillin-streptomycin (Gibco, Billings, MT, USA) at a temperature of 37° C with 5% CO_2.

Mammalian fibroblasts were cultured in Dulbecco's modified Eagle's medium (Sigma-Aldrich, St Louis, MO, USA) supplemented with 10% (v/v) heat-inactivated fetal bovine serum, L-glutamine (0.584 g/L) and 10 mL/L of 100x penicillin-streptomycin (Gibco, Billings, MT, USA) with the same temperature and CO_2 conditions as the parasites.

3.6.10 Growth inhibition assay

All the compounds that were tested were dissolved in dimethyl sulfoxide (DMSO). The final DMSO concentration in each well was less than 1% in all experiments and has no effect on the trypanosomes in this concentration range. They were serially diluted in 96-wells microtiter plates with growth medium to obtain a range of concentrations from 2×10-5 µg/mL to 200 µg/mL (100 µL/well). In each well 100 µL of *T. brucei* or mammalian fibroblasts cell culture were added to have 20,000 and 2000 cells per well respectively. The plates were incubated for 48 h at 37° C with 5% CO_2, treated with 20 µL of 0.5 mM resazurine (Sigma-Aldrich, St Louis, MO, USA) and treated for 24 h at the incubation conditions. Subsequently, the surviving cells were quantified by fluorescence (540 nm excitation and 590 nm emission) with an Infinite M200 microplate reader (Tecan Group, Ltd. Männedorf, Switzerland). Data were analyzed using the GraphPad Prism 8 software to obtain EC_{50} values by fitting the data to a log inhibitor vs response curve (variable slope, four parameters) and calculating the selectivity index (SI) from the comparison of *T. brucei* and Balb/3T3 EC_{50} values.

3.7 References

Abdelrahman, S.H., Mousa, I.M., Khojali, S.M.E., Ismail, A.A. (2012). Trypanocidal effect of *Cannabis sativa* on experimental camel trypansomosis.

Abdollahi, M., Sefidkon, F., Calagari, M., Mousavi, A., Mahomoodally, M.F. (2020). A comparative study of seed yield and oil composition of four cultivars of Hemp (*Cannabis sativa* L.) grown from three regions in northern Iran. Industrial Crops and Products, 152, 112397.

Akhtar, A., Hussain, W., Rasool, N.J.U.S. (2019). Probing the pharmacological binding properties, and reactivity of selective phytochemicals as potential HIV-1 protease inhibitors. Universal Sciences, 24, 441–464.

Barrett, M., Scutt, A., Evans, F. (1986). Cannflavin A and B, prenylated flavones from *Cannabis sativa* L. Experientia, 42, 452–453.

Benelli, G., Pavela, R., Lupidi, G., Nabissi, M., Petrelli, R., Ngahang Kamte, S.L., Cappellacci, L., Fiorini, D., Sut, S., Dall'Acqua, S., et al. (2018). The crop-residue of fiber hemp cv. Futura 75: From a waste product to a source of botanical insecticides. Environmental science and pollution research international, 25, 10515–10525.

Bertoli, A., Tozzi, S., Pistelli, L. and Angelini, L.G. (2010). Fibre hemp inflorescences: From crop residues to essential oil production, Industrial Crops and Products, 32, 3, 329– 337.

Bertoli, A., Tozzi, S., Pistelli, L., Angelini, L.G. (2010). Fibre hemp inflorescences: From crop-residues to essential oil production. Industrial Crops and Products, 32, 329–337.

Crini, G., Lichtfouse, E., Chanet, G., Morin-Crini, N. (2020). Applications of hemp in textiles, paper industry, insulation and building materials, horticulture, animal nutrition, food and beverages, nutraceuticals, cosmetics and hygiene, medicine, agrochemistry, energy production and environment: A review. Environmental Chemistry Letters, 18, 1451-1476.

Croxford, J.L., Wang, K., Miller, S.D., Engman, D.M., Tyler, K.M. (2005). Effects of cannabinoid treatment on Chagas disease pathogenesis: balancing inhibition of parasite invasion and immunosuppression. Cellular microbiology, 7(11), 1592-1602.

Di Giacomo, V., Recinella, L., Chiavaroli, A., Orlando, G., Cataldi, A., Rapino, M., Di Valerio, V., Politi, M., Antolini, M.D., Acquaviva, A., Bacchin, F., Di Mascio, M., Leone, S., Brunetti, L., Menghini, L., Carradori, S., Zengin, G., Ak, G., Ferrante, C. (2021). Metabolomic Profile

and Antioxidant/Anti-Inflammatory Effects of Industrial Hemp Water Extract in Fibroblasts, Keratinocytes and Isolated Mouse Skin Specimens. Antioxidants, 10, 44.

Doyle, E., Spence, A. A. (1995). Cannabis as a medicine? British Journal of Anaesthesia, 74, 4, 359–361.

Eggers, C., Fujitani, M., Kato, R., Smid, S. (2019). Novel cannabis flavonoid, cannflavin A displays both a hormetic and neuroprotective profile against amyloid b mediated neurotoxicity in PC12 cells: Comparison with geranylated flavonoids, mimulone and diplacone. Biochemical Pharmacology, 169, 113609.

Elsohly, H.N., Elsohly, M.A. (2007). Marijuana smoke condensate, Marijuana and the cannabinoids, 67–96.

Farag S., Kayser O. (2017). The Cannabis Plant: Botanical Aspects.

Ferrante, C., Recinella, L., Ronci, M., Menghini, L., Brunetti, L., Chiavaroli, A., Leone, S., Di Iorio, L., Carradori, S., Tirillini, B., Angelini, P., Covino, S., Venanzoni, R., Orlando, G. (2019). Multiple pharmacognostic characterization on hemp commercial cultivars: Focus on inflorescence water extract activity. Food Chemistry and Toxicology, 125, 452–461.

Fiorini, D., Molle, A., Nabissi, M., Santini, G., Benelli, G., Maggi, F. (2019). Valorizing industrial hemp (*Cannabis sativa* L.) by-products: Cannabidiol enrichment in the inflorescence essential oil optimizing sample pre-treatment prior to distillation. Industrial Crops and Products, 128, 581–589.

Ingallina, C., Sobolev, A.P., Circi, S., Spano, M., Fraschetti, C., Filippi, A., Di Sotto, A., Di Giacomo, S., Mazzoccanti, G., Gasparrini, F., Quaglio, D, Campiglia, E., Carradori, S., Locatelli, M., Vinci, G., Rapa, M., Ciano, S., Giusti, A.M., Botta, B., Ghirga, F., Capitani, D., Mannina, L. (2020). *Cannabis sativa* L. Inflorescences from Monoecious Cultivars Grown in Central Italy: An Untargeted Chemical Characterization from Early Flowering to Ripening, Molecules, 25, 1908.

Iseppi, R., Brighenti, V., Licata, M., Lambertini, A., Sabia, C., Messi, P., Pellati, F., Benvenuti, S. (2019). Chemical Characterization and Evaluation of the Antibacterial Activity of Essential Oils from Fibre-Type *Cannabis sativa* L. (Hemp). Molecules, 24, 2302.

Izzo, L., Castaldo, L., Narváez, A., Graziani, G., Gaspari, A., Rodríguez-Carrasco, Y., Ritieni, A. (2020). Analysis of phenolic compounds in commercial *Cannabis sativa* L. inflorescences using UHPLC-Q-Orbitrap HRMS. Molecules, 25, 3, 631.

Kakudidi, E., Tugume, P., Asiimwe, S., Anywar, G. (2022). Traditional and Modern Health Uses of *Cannabis sativa* L. in Africa and Its Phytochemical and Pharmacological Profile, Cannabis/Marijuana for Healthcare, 189.

Lowe, H., Toyang, N.J. (2016). Therapeutic agents containing cannabis flavonoid derivatives targeting kinases, sirtuins and oncogenic agents for the treatment of cancers. U.S. Patent WO2016178713A1.

Lowe, H.I., Toyang, N.J., (2020). Flavocure Biotech, Llc. Therapeutic agents containing cannabis flavonoid derivatives for the prevention and treatment of neurodegenerative disorders. U.S. Patent, 10, 751, 320.

McPartland, J.M., Sheikh, Z. (2018). A review of *Cannabis sativa*-based insecticides, Miticides, and repellents. Journal of Entomology and Zoology Studies, 6, 1288-1299.

Meier, C., Mediavilla, V. (1998). Factors influencing the yield and the quality of hemp (*Cannabis sativa* L.) essential oil. Journal of the International Hemp Association, 5, 16–20.

Menghini, L., Ferrante, C., Carradori, S., D'Antonio, M., Orlando, G., Cairone, F., Cesa, S., Filippi, A., Fraschetti, C., Zengin, G., Ak, G., Tacchini, M., Iqbal, K. (2021). Chemical and Bioinformatics Analyses of the Anti-Leishmanial and Anti-Oxidant Activities of Hemp Essential Oil. Biomolecules, 11, 272.

Merlin, M.D. (2003). Archaeological Evidence for the Tradition of Psychoactive Plant Use in the Old World, Economic Botanics 57, 3, 295–323.

Ngahang Kamte, S.L., Ranjbarian, F., Campagnaro, G.D., Biapa Nya, P.C., Mbuntcha, H., Woguem, V., Womeni, H.M., Azefack Tapondjou, L., Giordani, C., Barboni, L., Benelli, G., Cappellacci, L., Hofer, A., Petrelli, R., Maggi, F. (2017). *Trypanosoma brucei* inhibition by essential oils from medicinal aromatic plants traditionally used in Cameroon (*Azadirachta indica*, Aframomum melegueta, *Aframomum daniellii*, *Clausena anisata*, *Dichrostachys cinerea* and *Echinops giganteus*). International Journal of Environmental Research and Public Health, 14, 737.

Nissen, L., Zatta, A., Stefanini, I., Grandi, S., Sgorbati, B., Biavati, B., Monti, A. (2010). Characterization and antimicrobial activity of essential oils of industrial hemp varieties (*Cannabis sativa* L.). Fitoterapia, 81, 413–419.

Nissen, L., Zatta, A., Stefanini, I., Grandi, S., Sgorbati, B., Biavati, B., Monti, A. (2010). Characterization and antimicrobial activity of essential oils of industrial hemp varieties (*Cannabis sativa* L.). Fitoterapia, 81, 413–419.

Novak, J., Zitterl-Eglseer, K., Deans, S.G., Franz, C.M. (2001). Essential oils of different cultivars of *Cannabis sativa* L. and their antimi crobial activity. Flavour and Fragrance Journal, 16, 259–262.

O'Croinin, C., Le, T.S., Doschak, M., Löbenberg, R., Davies, N.M. (2023). A validated method for detection of cannflavins in hemp extracts. Journal of Pharmaceutical and Biomedical Analysis, 235, 115631.

Orlando, G., Recinella, L., Chiavaroli, A., Brunetti, L., Leone, S., Carradori, S., Di Simone, S., Ciferri, M.C., Zengin, G., Ak, G., Abdullah, H., Cordisco, E., Sortino, M., Svetaz, L., Politi, M., Angelini, P., Covino, S., Venanzoni, R., Cesa, S., Menghini, L., Ferrante, C. (2020). Water Extract from Inflorescences of Industrial Hemp Futura 75 Variety as a Source of Anti-Inflammatory, Anti-Proliferative and Antimycotic Agents: Results from *In Silico*, *In Vitro* and *Ex Vivo* Studies. Antioxidants, 9, 437.

Palmieri, S., Maggio, F., Pellegrini, M., Ricci, A., Serio, A., Paparella, A., Lo Sterzo, C. (2021). Effect of the Distillation Time on the Chemical Composition, Antioxidant Potential and Antimicrobial Activity of Essential Oils from Different *Cannabis sativa* L. Cultivars. Molecules, 26, 4770.

Pate, D.W. (1994). Chemical ecology of Cannabis. Journal of the International Hemp Association, 2, 32–37.

Pavlovic, R., Panseri, S., Giupponi, L., Leoni, V., Citti, C., Cattaneo, C., Cavalletto, M., Giorgi, A. (2019). Phytochemical and ecological analysis of two varieties of hemp (*Cannabis sativa* L.) grown in a mountain environment of Italian Alps. Frontiers in Plant Science, 10, 1265.

Pellati, F., Brighenti, V., Sperlea, J., Marchetti, L., Bertelli, D. Benvenuti, S. (2018). New methods for the comprehensive analysis of bioactive compounds in *Cannabis sativa* L.(hemp). Molecules, 23(10), 2639.

Pieracci, Y., Ascrizzi, R., Terreni, V., Pistelli, L., Flamini, G., Bassolino, L., Fulvio, F., Montanari, M., Paris, R. (2021). Essential Oil of *Cannabis sativa* L: Comparison of Yield and Chemical Composition of 11 Hemp Genotypes. Molecules, 26, 13, 4080.

Pieracci, Y., Ascrizzi, R., Terreni, V., Pistelli, L., Flamini, G., Bassolino, L., Fulvio, F., Montanari, M., Paris, R. (2021). Essential Oil of *Cannabis sativa* L: Comparison of Yield and Chemical Composition of 11 Hemp Genotypes. Molecules, 26, 4080.

Pilla, S. (2011). Engineering applications of bioplastics and biocomposites-An overview. Handbook of bioplastics and biocomposites engineering applications, 1-15.

Quassinti, L., Bramucci, M., Lupidi, G., Barboni, L., Ricciutelli, M., Sagratini, G., Papa, F., Caprioli, G., Petrelli, D., Vitali, L.A., Vittori, S., Maggi, F. (2013). *In vitro* biological activity of essential oils and isolated furanosesquiterpenes from the neglected vegetable *Smyrnium olusatrum* L. (Apiaceae). Food Chemistry, 138, 808–813.

Radwan, M.M., ElSohly, M.A., Slade, D., Ahmed, S.A., Wilson, L., El-Alfy, A.T., Khan, I.A., Ross, S.A. (2008). Non-cannabinoid constituents from a high potency *Cannabis sativa* variety. Phytochemistry, 69, 14, 2627-2633.

Ramirez, M.R. (2016). Potential Health Benefits of Cannabis Extracts: A Review, *International* Journal of Chemical and Biomedical Science, 2, 1, 1–8.

Ranalli, P., Venturi, G. (2004). Hemp as a raw material for industrial applications. Euphytica, 140(1), 1-6.

Rasool, N., Akhtar, A., Hussain, W. (2020a). Insights into the inhibitory potential of selective phytochemicals against Mpro of 2019-nCoV: A computer-aided study. Structural Chemistry, 31, 1777–1783.

Rasool, N., Majeed, A., Riaz, F., Hussain, W. (2020b). Identification of novel inhibitory candidates against two major Flavivirus pathogens via CADD protocols: *In silico* analysis of phytochemical binding, reactivity, and pharmacokinetics against NS5 from ZIKV and DENV. Structural Chemistry, 31, 2189–2204.

Regnault-Roger, C., Vincent, C., Arnason, J.T. (2012). Essential oils in insect control: Low-risk products in a high-stakes world. Annual Review of Entomology, 57, 405–424.

Rossi, P., Cappelli, A., Marinelli, O., Valzano, M., Pavoni, L., Bonacucina, G., Petrelli, R., Pompei, P., Mazzara, E., Ricci, I., Maggi, F., Nabissi, M. (2020). Mosquitocidal and anti-inflammatory properties of the essential oils obtained from monoecious, male, and female inflorescences of hemp (*Cannabis sativa* L.) and their encapsulation in nanoemulsions. Molecules, 25, 3451.

Russo, E.B. (2011). Taming THC: potential cannabis synergy and phytocannabinoid-terpenoid entourage effects, British Journal of Pharmacology, 163, 7, 1344–64.

Sanchez-Ramos, J. (2015). The entourage effect of the phytocannabinoids, Annals of Neurology, 77, 6, 1083.

Tabari, M.A., Khodashenas, A., Jafari, M., Petrelli, R., Cappellacci, L., Nabissi, M., Maggi, F., Pavela, R., Youssefi, M.R. (2020). Acaricidal properties of hemp (*Cannabis sativa* L.) essential oil against *Dermanyssus gallinae* and *Hyalomma dromedarii*. Industrial crops and products, 147, 112238.

Thomas, B., ElSohly, M. (2016). The Botany of *Cannabis sativa* L. In, 1–26.

Werz, O., Seegers, J., Schaible, A.M., Weinigel, C., Barz, D., Koeberle, A., Allegrone, G., Pollastro, F., Zampieri, L., Grassi, G., Appendino, G. (2014). Cannflavins from hemp sprouts, a novel cannabinoid-free hemp food product, target microsomal prostaglandin E2 synthase-1 and 5-lipoxygenase. PharmaNutrition, 2, 53–60.

Zengin, G., Menghini, L., Di Sotto, A., Mancinelli, R., Sisto, F., Carradori, S., Cesa, S., Fraschetti, C., Filippi, A., Angiolella, L., Locatelli, M., Mannina, L., Ingallina, C., Puca, V., D'Antonio, M., Grande, R. (2018). Chromatographic Analyses, *In Vitro* Biological Activities and Cytotoxicity of *Cannabis sativa* L. Essential Oil: A Multidisciplinary Study, Molecules, 23, 3266.

3.8 Supporting information

Table S1 EOs yields for the 12 analyzed *C. sativa* cultivars.

Cultivar	EO yield % w/w
Fresh Mountain	1.23
Lemon Conti Kush	1.03
Venom OG	0.86
Gorilla Glue	1.33
Amnesia cookies	1.81
24K	1.08
White Shark	0.64
Pablito	0.49
CBG 4	0.61
CBG 14	0.35
CBG 18	0.42
CBG 32	0.23

Table S2 HEs yields for the 12 *C. sativa* cultivars.

Cultivar	HE yield % w/w
Fresh Mountain	0.91
Lemon Conti Kush	0.74
Venom OG	0.53
Gorilla Glue	1.62
Amnesia cookies	1.39
24K	0.86
White Shark	1.19
Pablito	1.33
CBG 4	0.98
CBG 14	1.22
CBG 18	0.87
CBG 32	1.01

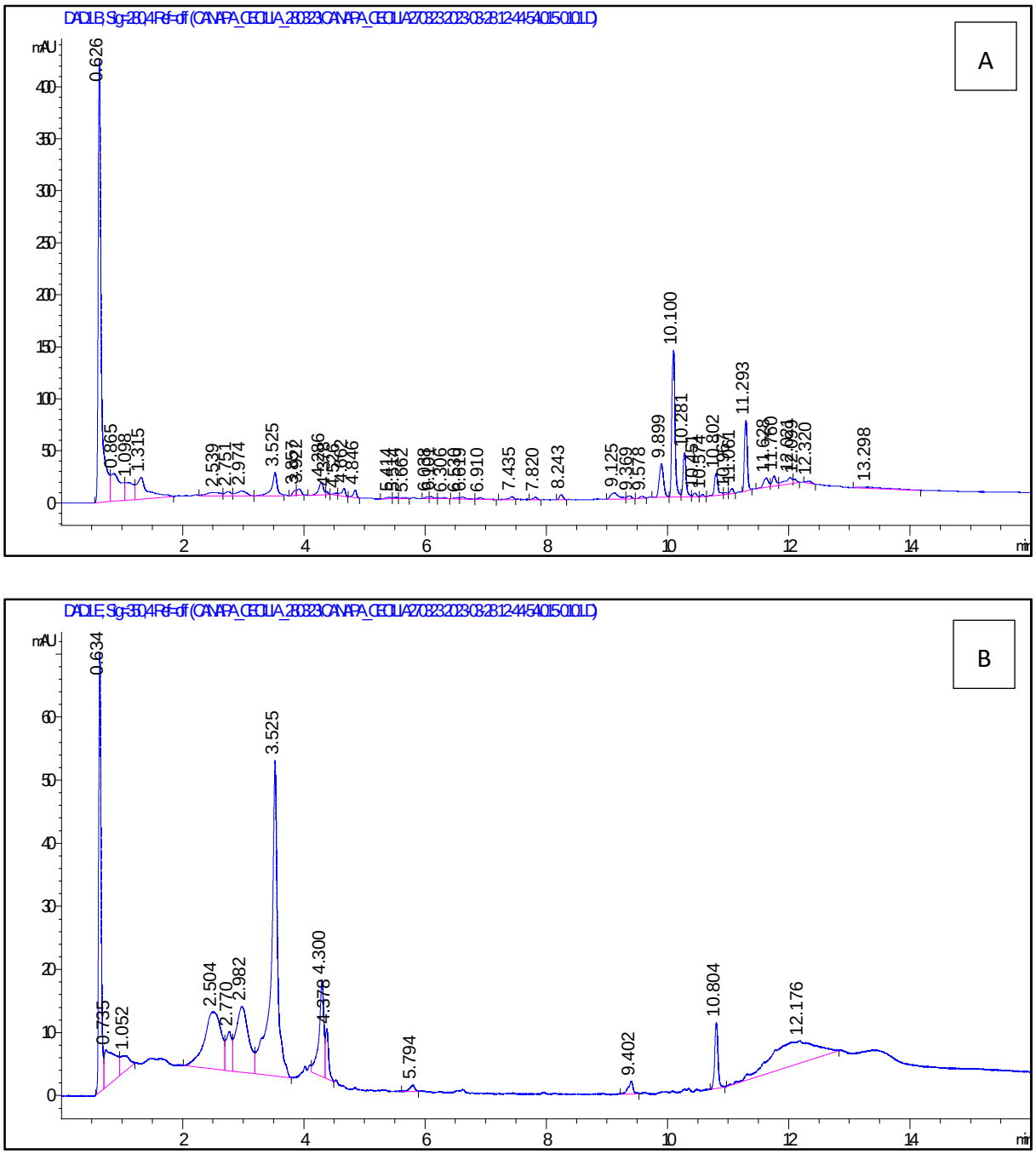

Figure S1. HPLC-DAD chromatograms for Gorilla Glue HE at A) 280 nm and B) 350 nm wavelength.

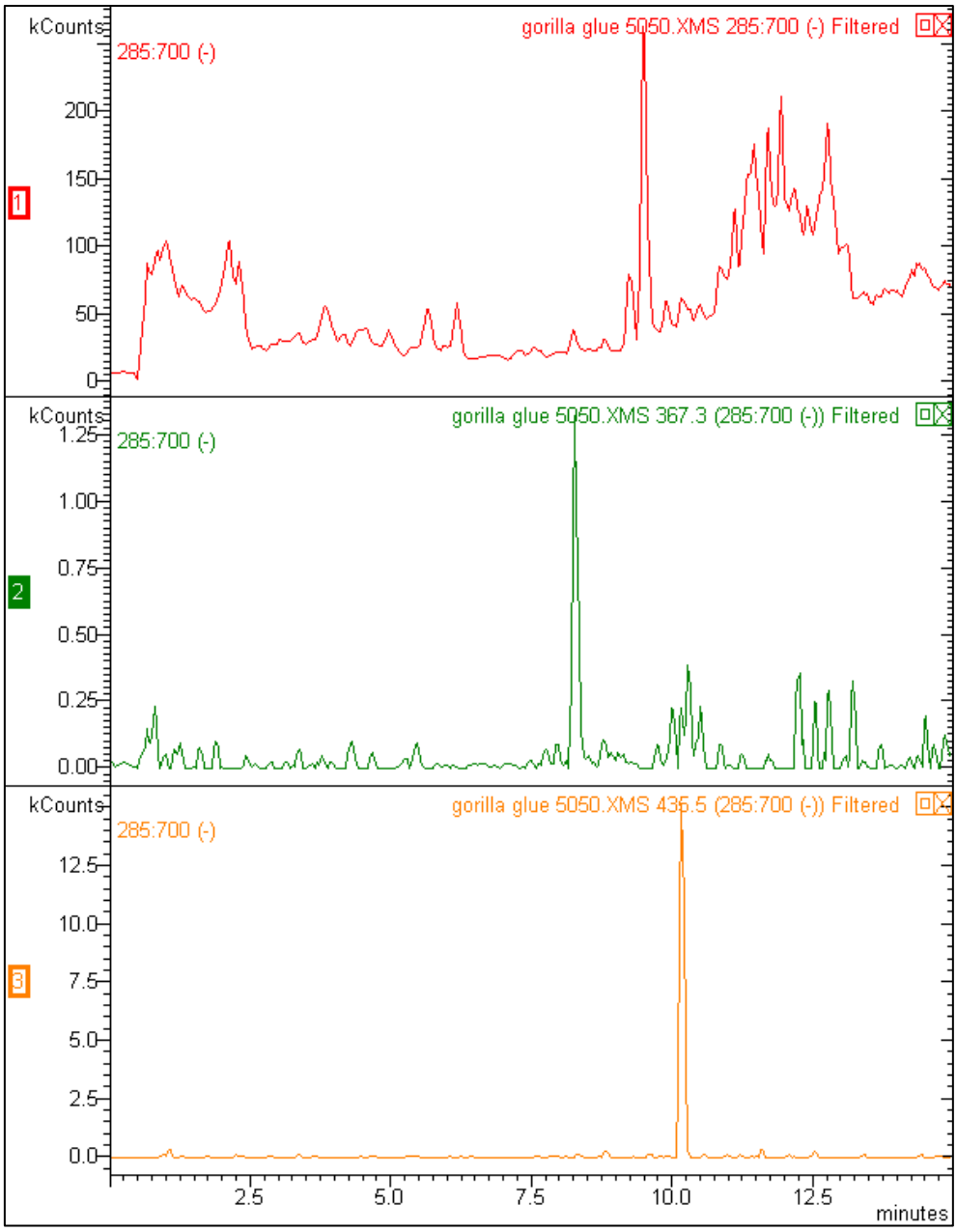

Figure S2. MS-spectra in negative ion mode (M-1) for Gorilla Glue HE (1). Peaks for Cannflavin B (2) and Cannflavin A (3) are visible.

Table S3. Gorilla Glue HE fractionation yields.

Fraction	Yields
Fraction A	25.0 %
Fraction B	21.67 %
Fraction C	20.0 %
Fraction D	3 %

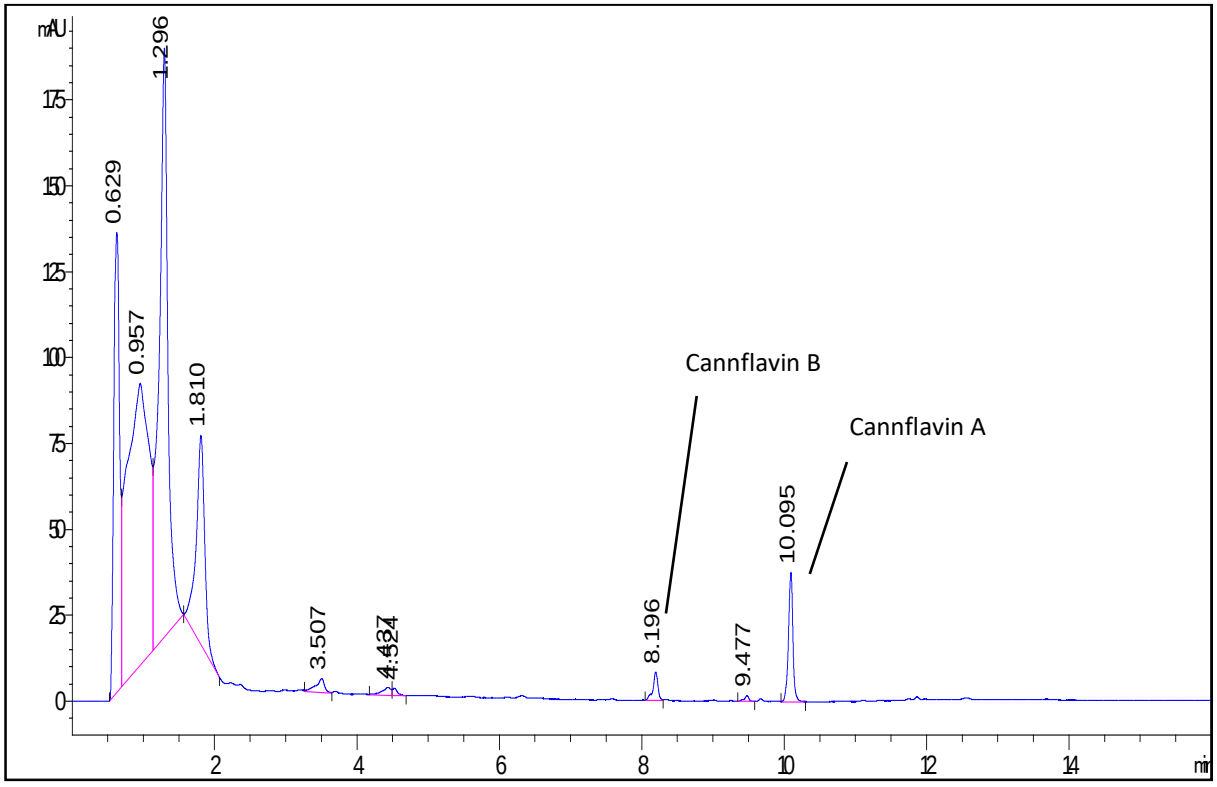

Figure S2. HPLC-DAD Chromatogram of Cannflavins rich fraction D (350 nm wavelength).

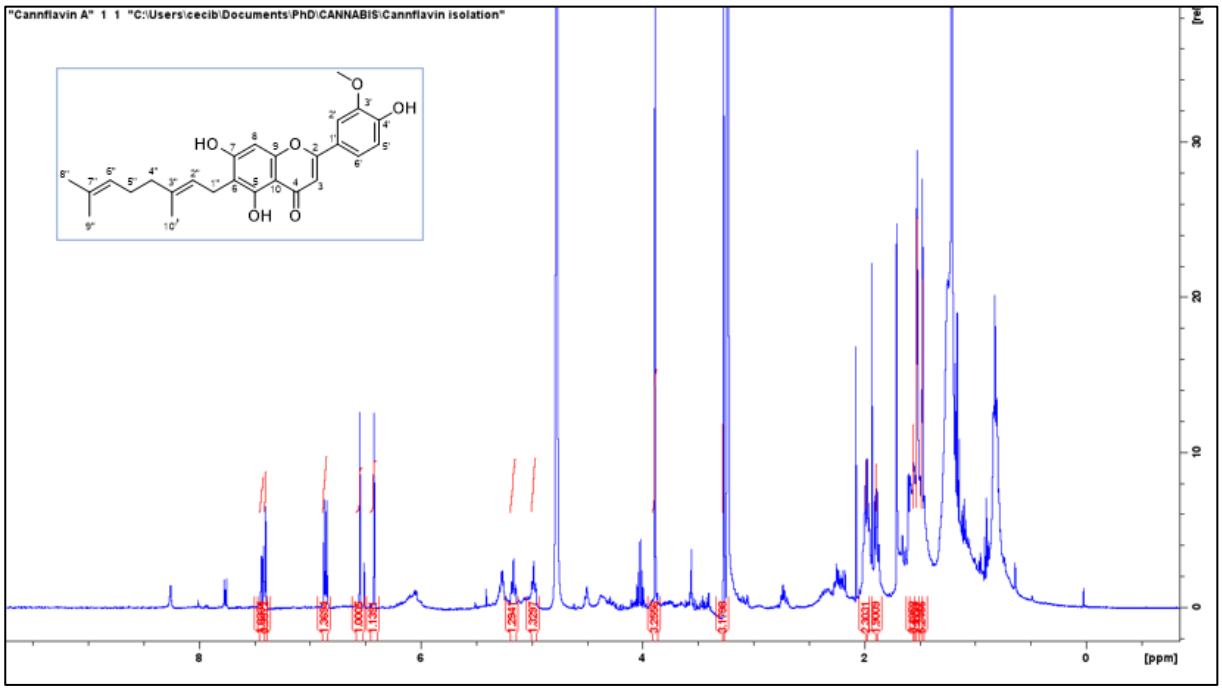

Figure S3. ^{1}H NMR for Cannflavin A.

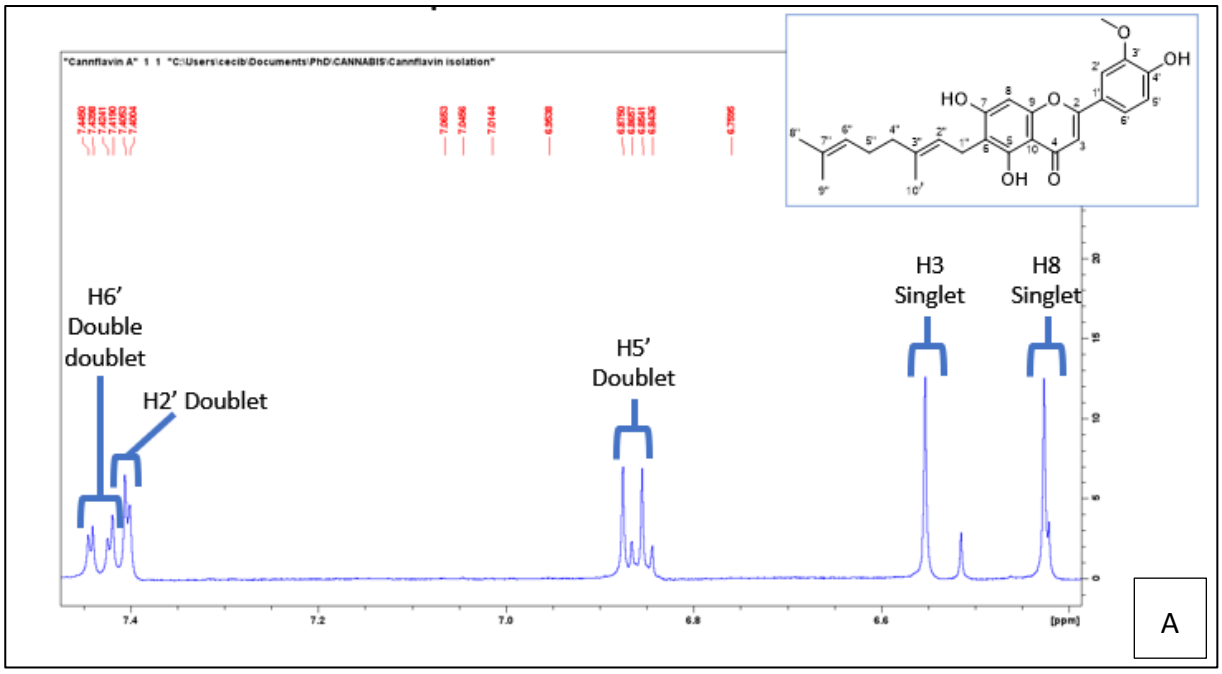
H6'
Double
doublet
H2' Doublet
H5'
Doublet
H3
Singlet
H8
Singlet
A

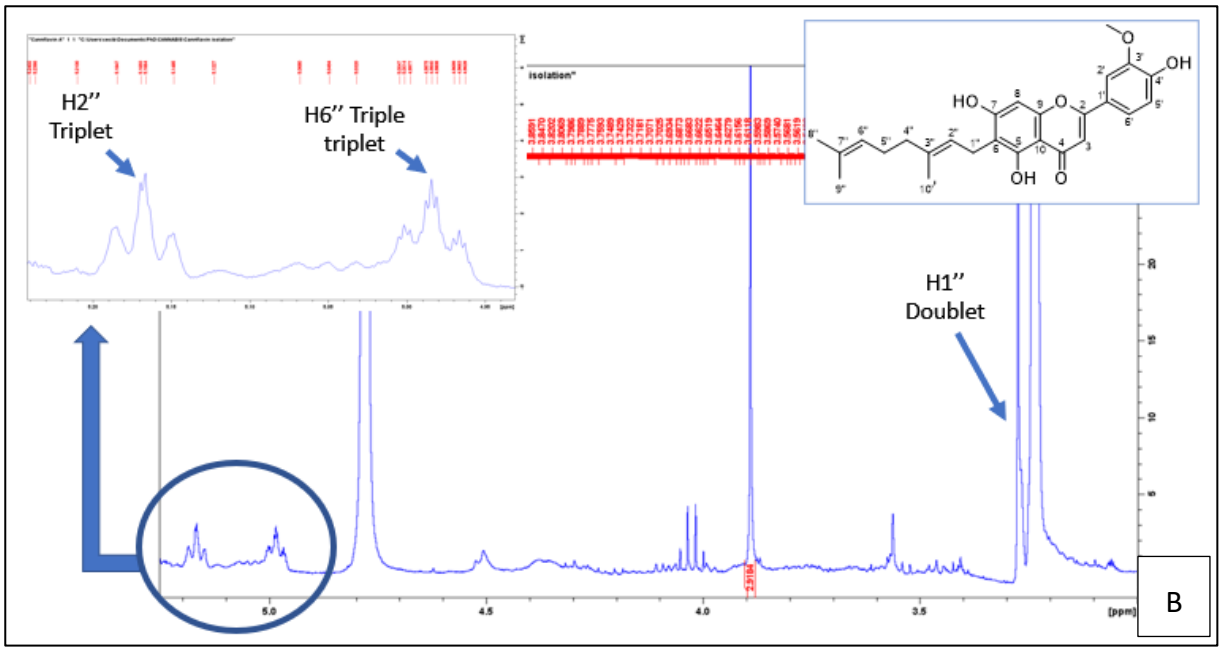
H2''
Triplet
H6'' Triple
triplet
H1''
Doublet
B

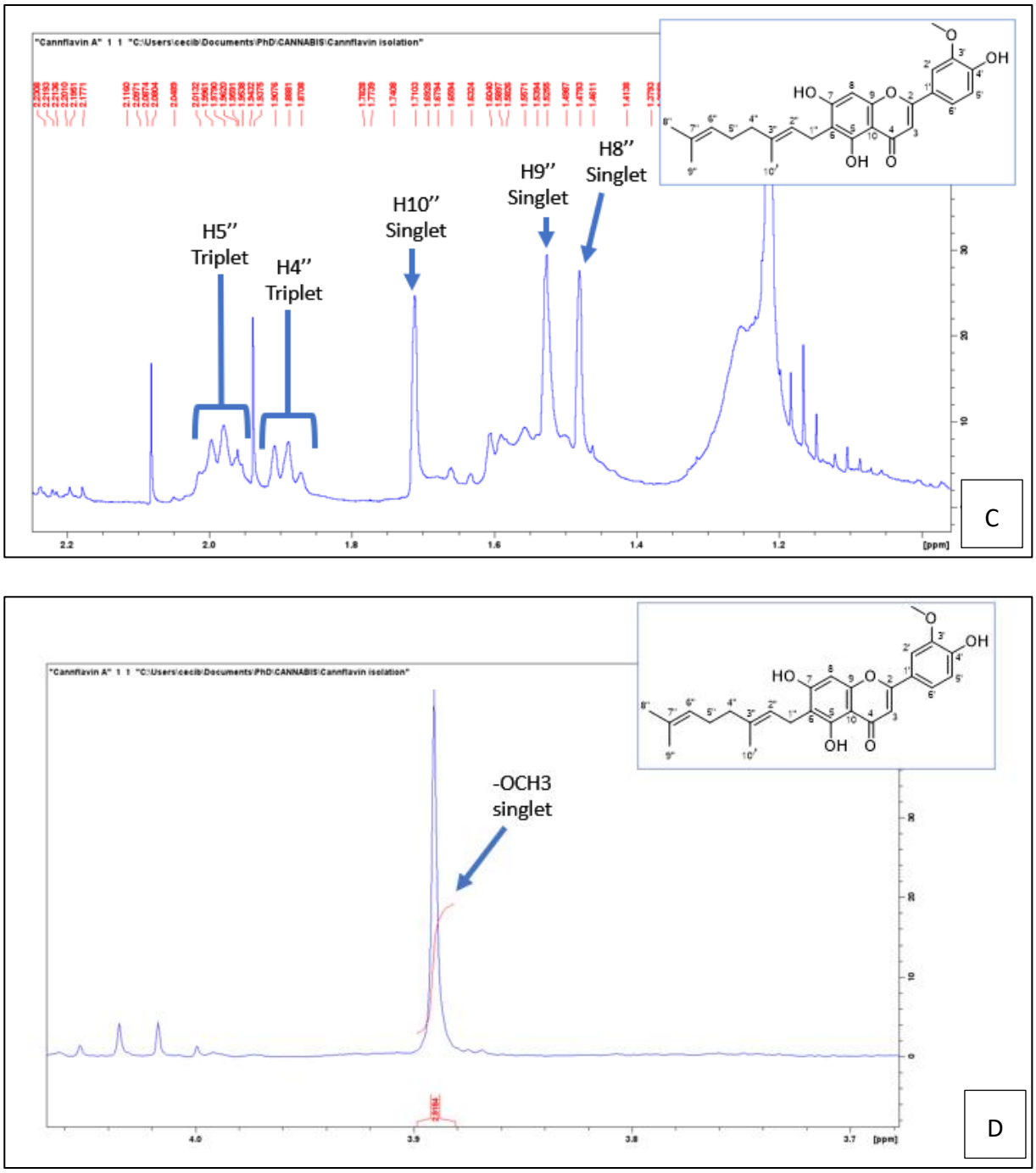

Figure S4. H assignments for Cannflavin A. A) assignments for H3, H8, H2', H5', and H6'; B) assignments for H1'', H2'', and H6''; C) assignments for H4'', H5'', H8'', H9'', and H10''; D) assignment for -OCH_3 singlet.

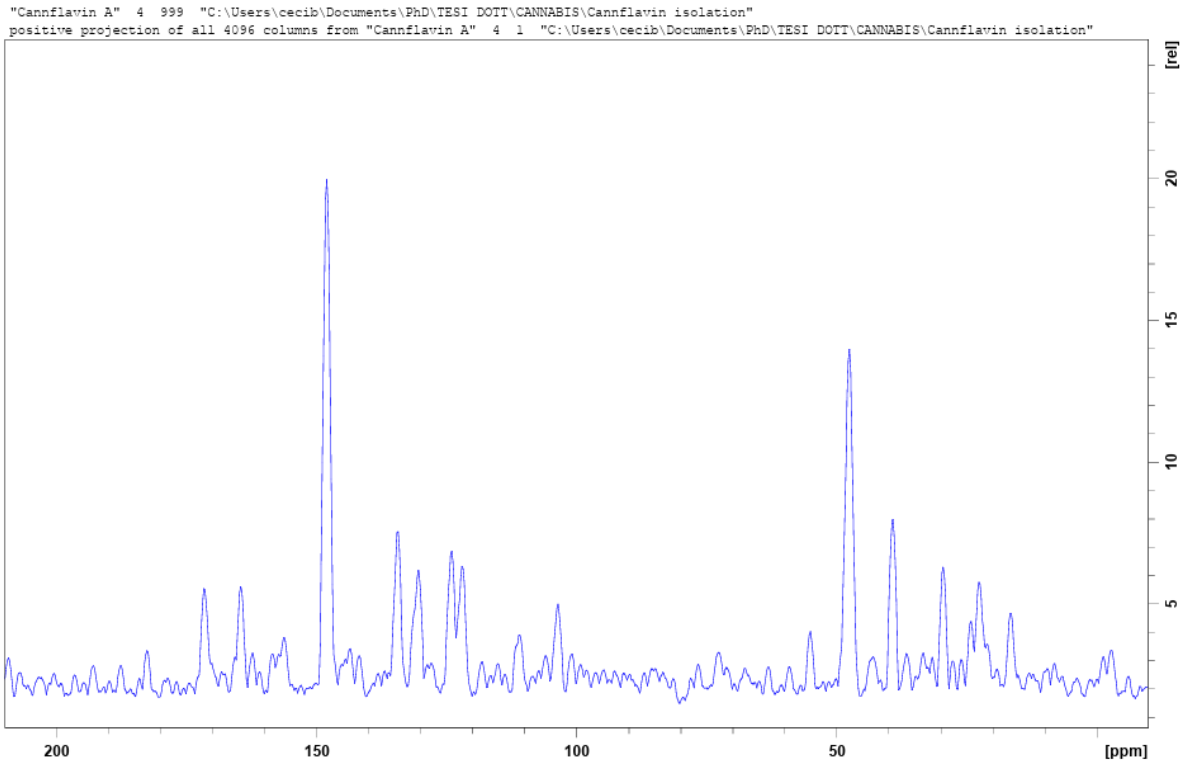

Figure S5. ^{13}C NMR for Cannflavin A.

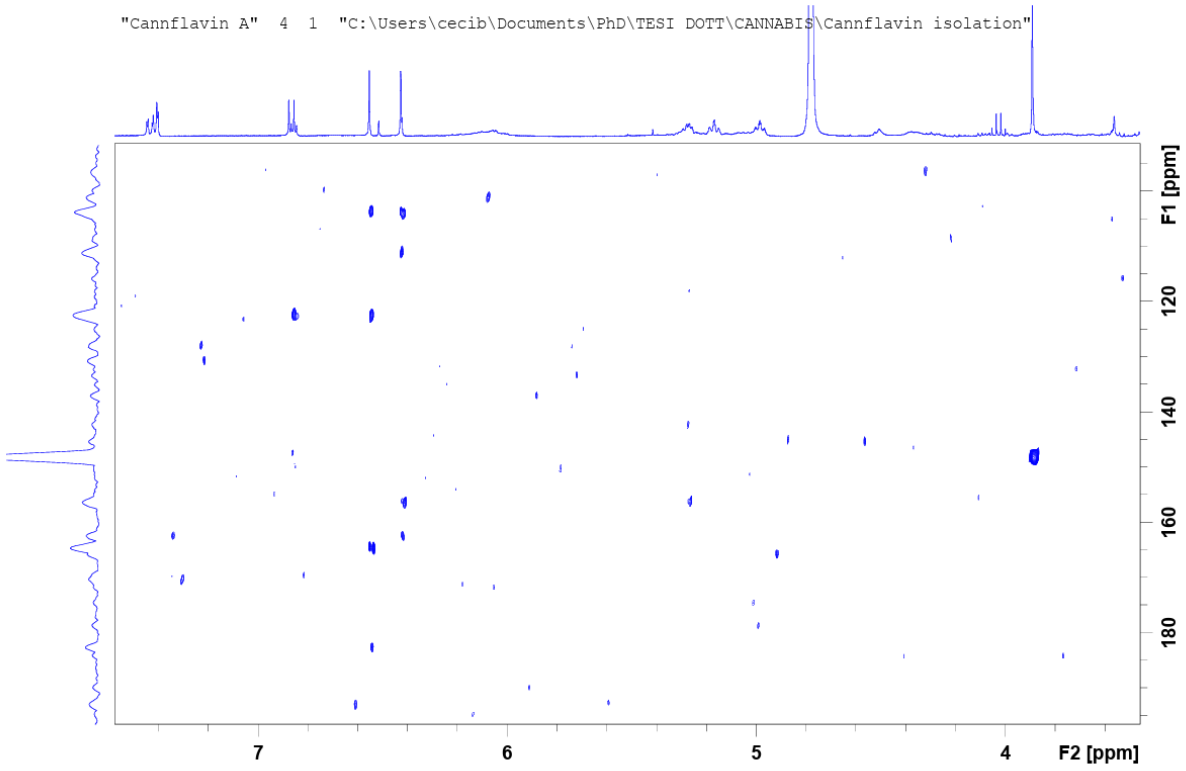

Figure S6. HMBC spectrum for Cannflavin A.

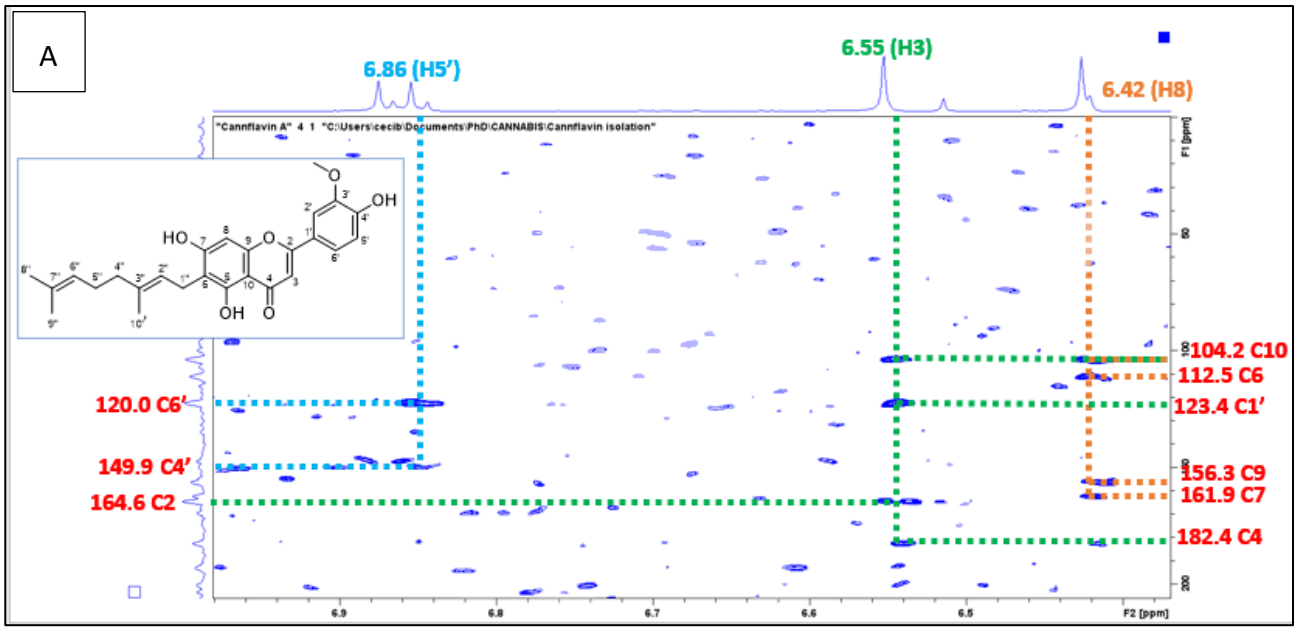
A
6.86 (H5')
6.55 (H3)
6.42 (H8)
104.2 C10
112.5 C6
120.0 C6'
123.4 C1'
149.9 C4'
156.3 C9
164.6 C2
161.9 C7
182.4 C4
F2 [ppm]

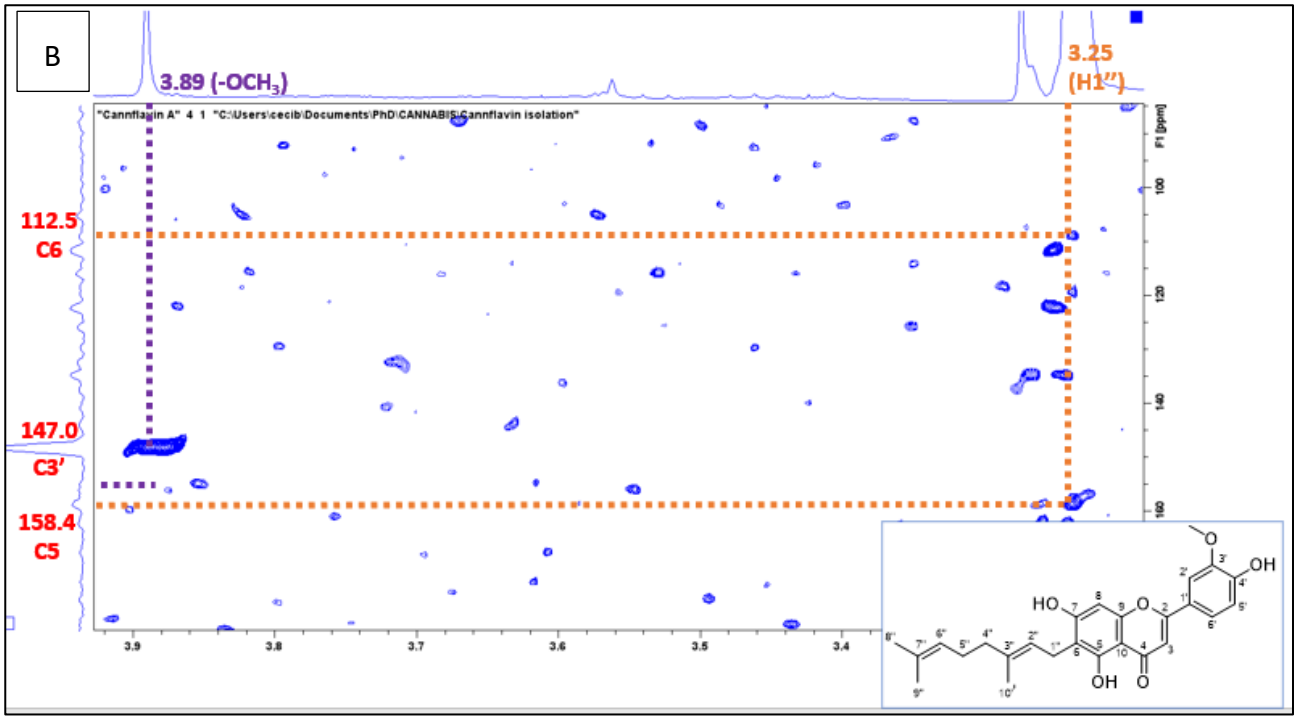
B
3.89 (-OCH3)
3.25
(H1'')
112.5
C6
147.0
C3'
158.4
C5

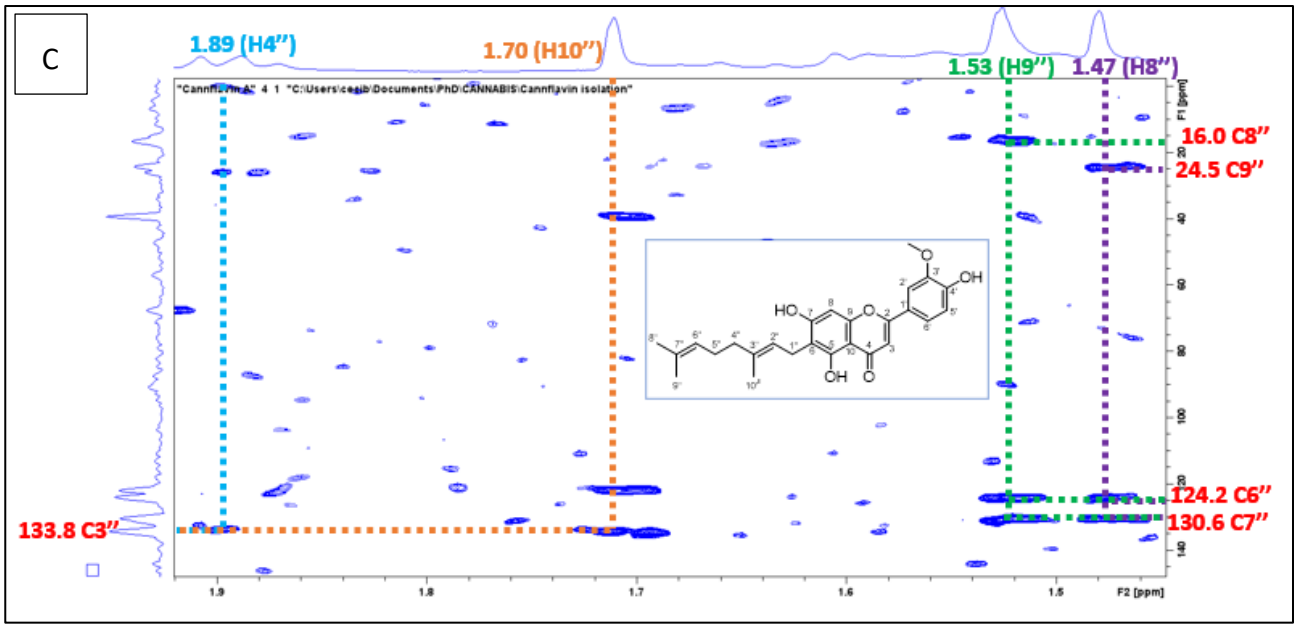

Figure S7. Carbon-hydrogen correlations in HMBC spectrum highlighted in A), B), and C).

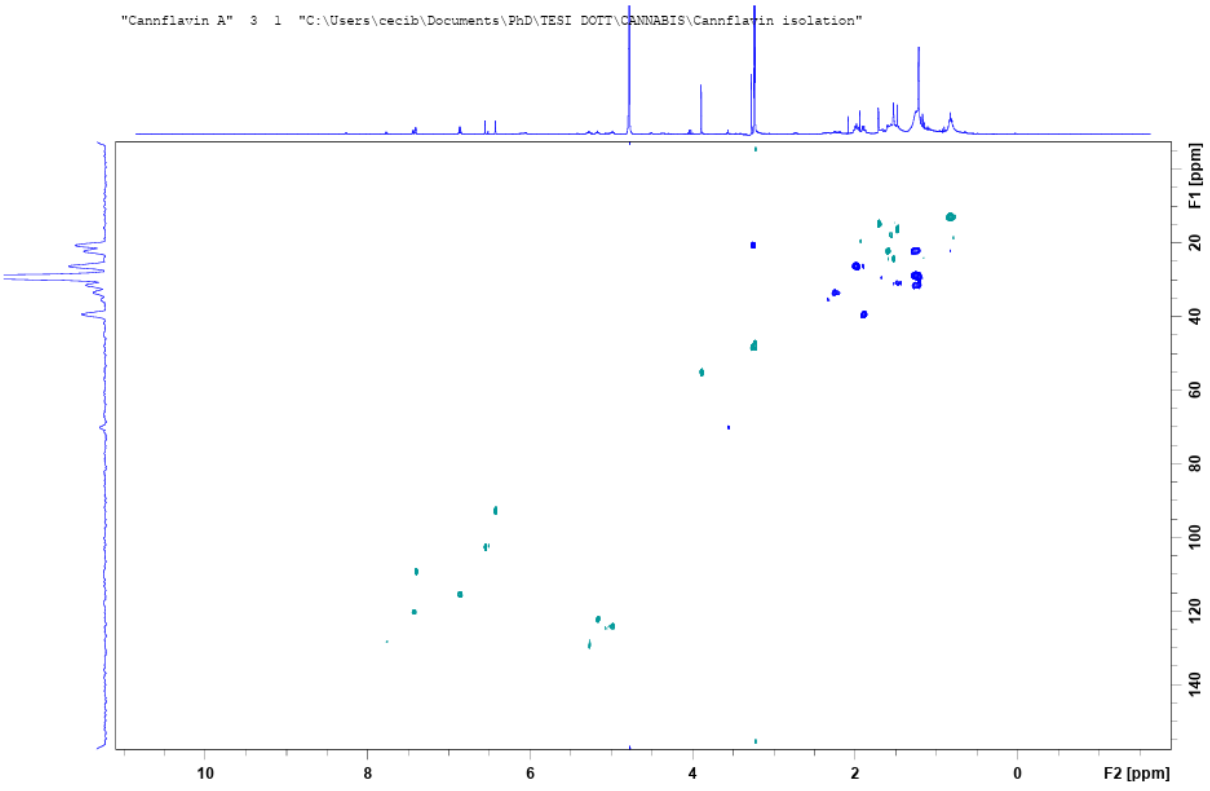

Figure S8. HSQC spectrum for Cannflavin A.

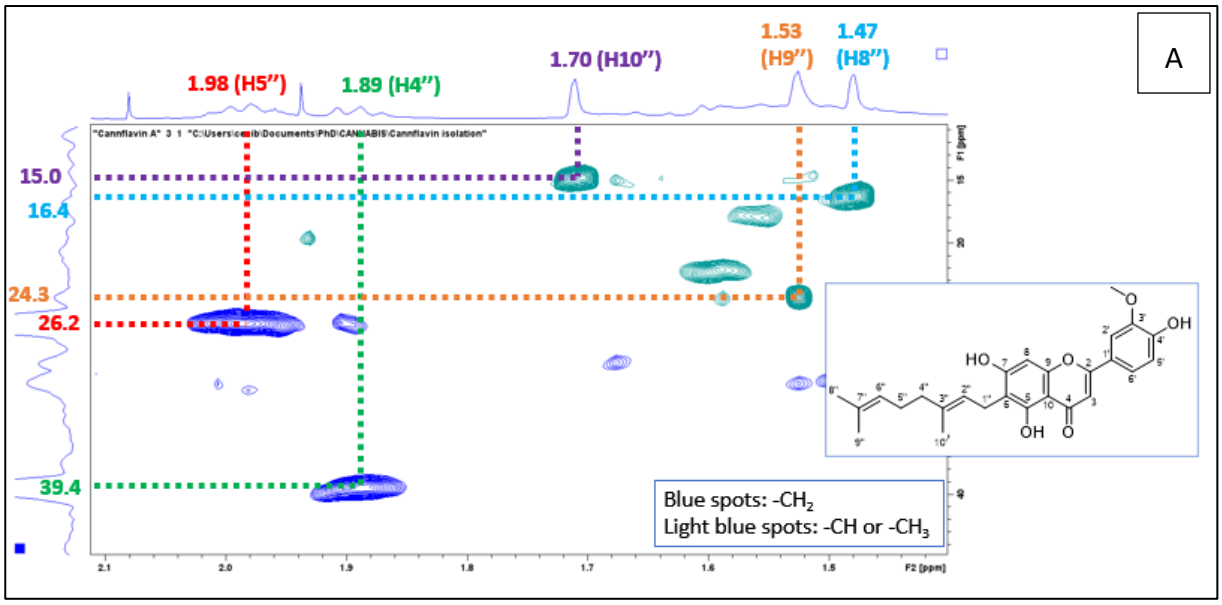
A
1.98 (H5'')
1.89 (H4'')
1.70 (H10'')
1.53 (H9'')
1.47 (H8'')
15.0
16.4
24.3
26.2
39.4
Blue spots: -CH2
Light blue spots: -CH or -CH3
F2 [ppm]

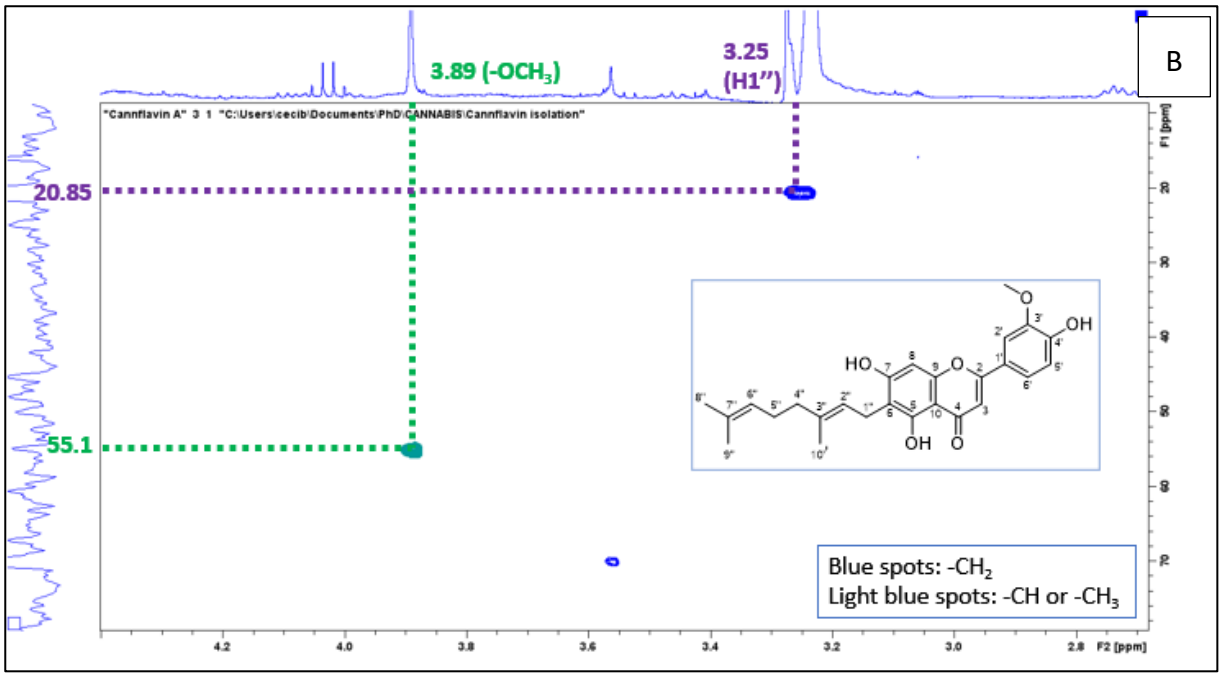
B
3.89 (-OCH3)
3.25 (H1'')
20.85
55.1
Blue spots: -CH2
Light blue spots: -CH or -CH3
F2 [ppm]

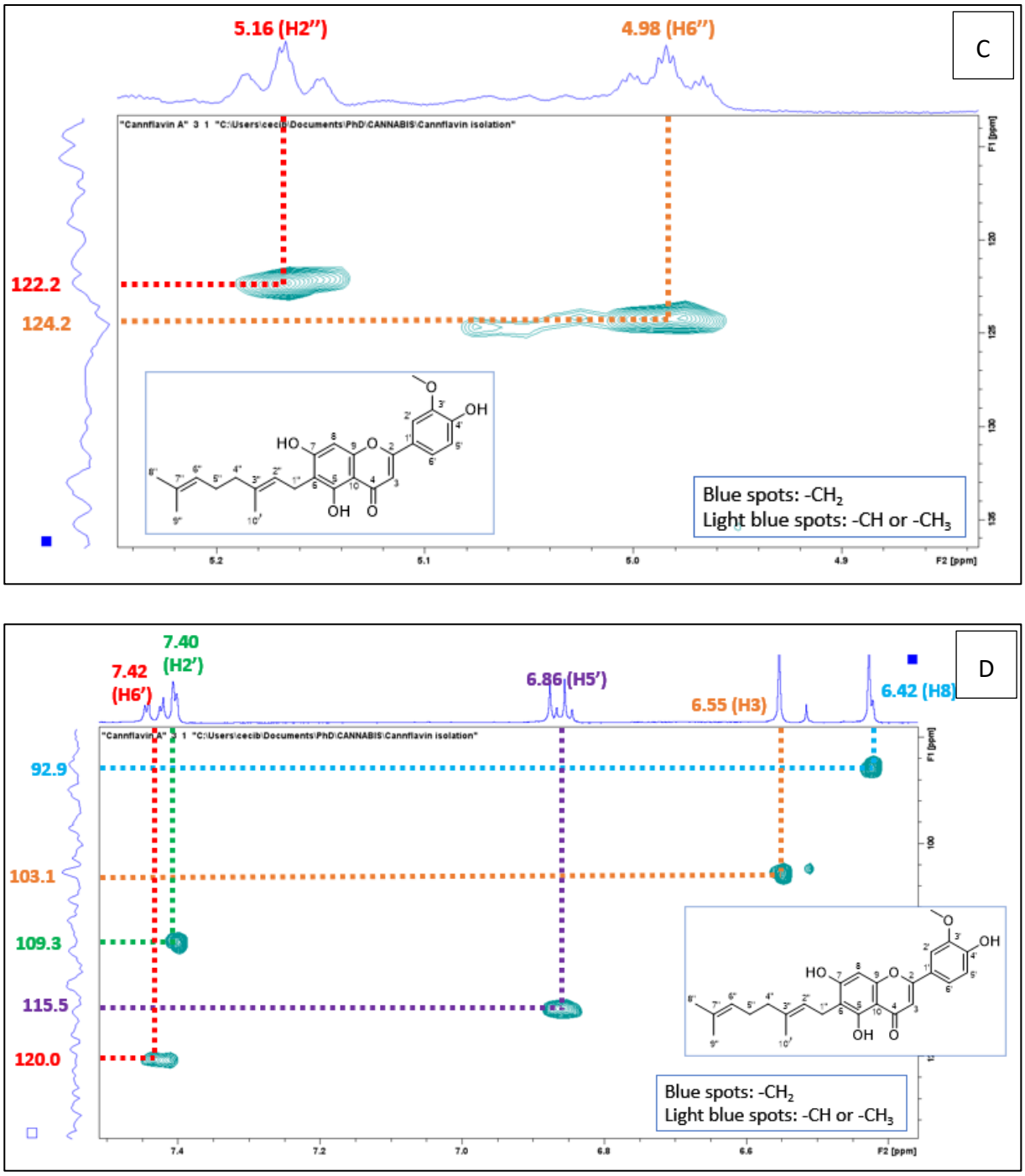

Figure S9. Carbon-hydrogen correlations in HSQC spectrum highlighted in A), B), C) and D).

CHAPTER 4

Pyrazolone-based hydrazones and derived metal complexes

CHAPTER 4 Outline

4.1 Introduction

Both hydrazones and their derived metal complexes have been widely studied in the last decades, showing many pharmacological activities, such as antibacterial, fungicidal, analgesic and anti-inflammatory, cardioprotective, anticancer, and antiparasitic behaviors (Verma et al., 2014). Moreover, their antiprotozoal potential has been demonstrated by many studies. Some hydrazone-based compounds resulted effective against *Plasmodium falciparum* (Acharya et al., 2008; Fattorusso et al., 2008), whereas a class of nitrofuran hydrazones and other derivatives were found to exert activity against *T. cruzi* (dos Santos et al., 2009; Gerpe et al., 2009; Caputto et al., 2011).

The combination of hydrazones with pyrazolones can produce potent biological molecules due to the association of their strong pharmacological effects. Indeed, the pyrazolone moiety is also characterized by a variety of biological properties, including antitumor, antioxidant, anti-inflammatory, antimicrobial, and antihyperglycemic activities (Zhao et al., 2020). From previous studies of our research group, a series of Zn(II) complexes with acylpyrazolones demonstrated antiproliferative activity against human breast cancer cells, and multitarget anticancer activity was assessed for pyrazolone-based hydrazones and their ruthenium(II) complexes (Pettinari et al., 2018; Marchetti et al., 2019; Cuccioloni et al., 2020). Furthermore, some Cu(II) and Zn(II) complexes with acylpyrazolones and acylhydrazone-5-pyrazolones were recently reported and found to display *in vitro* antimalarial activity (Shaikh et al., 2019; Shaikh et al., 2020; Shaikh et al., 2021).

Based on these findings, three series of pyrazolone-based hydrazones (PbH**1**-**36**) have been synthetized and screened against *T. brucei* and HFF cells. The two most active analogs (PbH**26** and PbH**27**) were selected as ligands for the synthesis of their corresponding Zn(II) and Cu(II) complexes (**C1**-**4**). The most active and selective metal complexes containing a Zn(II) center (**C1** and **C2**) were further investigated together with their ligands to identify the mechanism of action and the possible target, trying to exclude cross resistances, and to understand which cellular processes are altered by the action of the potential drugs.

4.2 Results

4.2.1 Synthesis of the three series of pyrazolone-based hydrazones

PbH **1**-**36** were synthesized starting from three precursors: one for the phenyl series (PP), one for the thiophene series (TP), and one for the benzyl series (BP). As previously reported, the three precursors were obtained through a three-steps reaction (Scheme 3) (Marchetti et al., 2015). Ethyl acetoacetate (**1**) and phenyl hydrazine (**2**) were combined in methanol and in the presence of acetic acid as a

catalyst to give 3-methyl-1-phenylpyrazolin-5-(4H)-one (**3**). The deprotonation of the pyrazolone ring in position 4 by calcium hydroxide in dry pyridine promoted the acylation at that position with the proper acyl chloride.

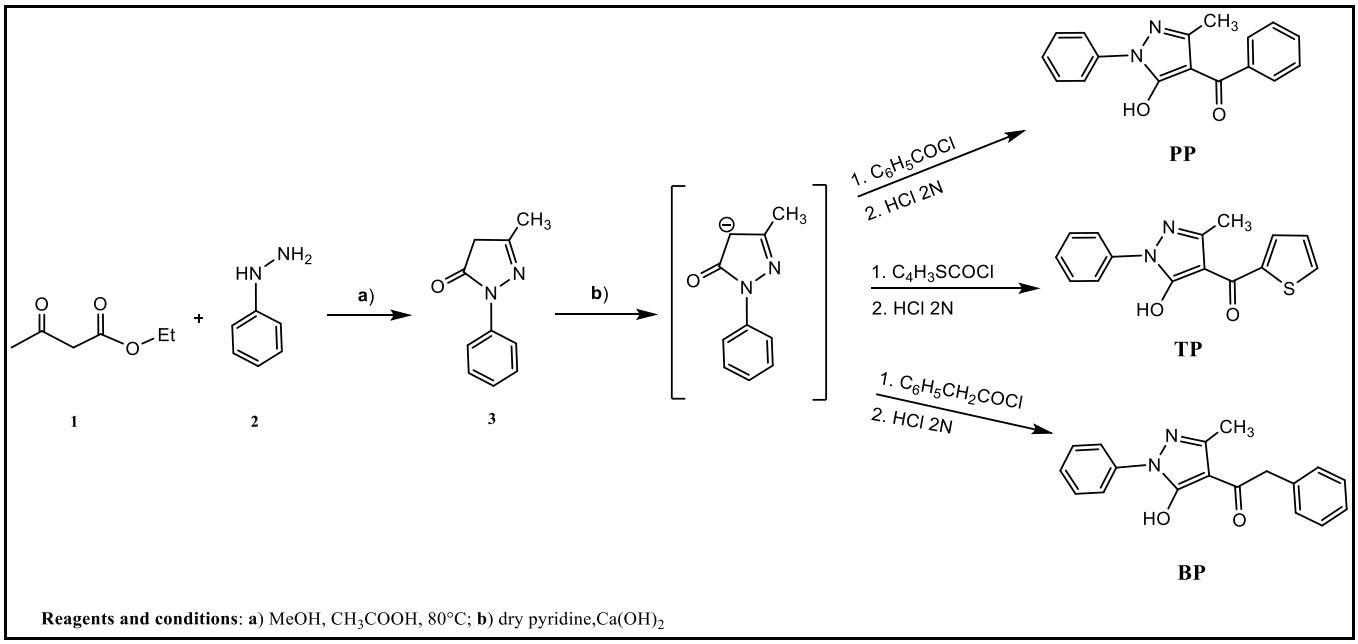

Scheme 3. Three steps reaction scheme for PbH precursors (PP, TP, and BP).

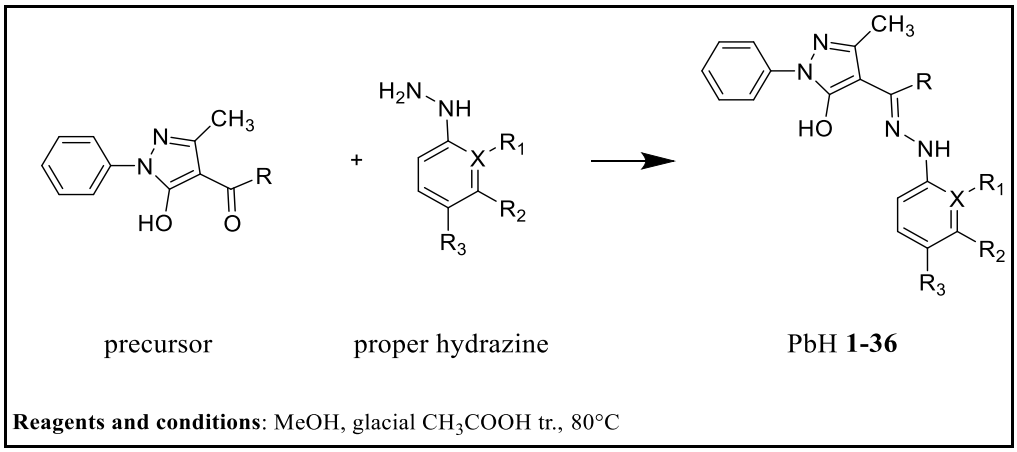

Scheme 4. General reaction scheme for PbH **1-36**.

The resulting precursors were treated with the proper hydrazine in equimolar amounts and in methanol using glacial acetic acid in traces to afford the final products, namely PbH **1-36** (Scheme 4) (Marchetti et al., 2019). Structures are reported in Tables 24, 25, and 26.

Table 24. Chemical structures for PbH **1-12**.

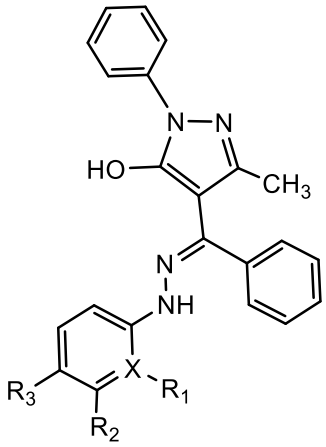

Compounds	X	R_1	R_2	R_3
PbH01	CH	-	H	H
PbH02	N	-	H	H
PbH03	CH	-	H	CF_3
PbH04	CH	-	H	CN
PbH05	CH	-	H	COOH
PbH06	CH	-	H	OCH_3
PbH07	CH	-	H	NO_2
PbH08	CH	-	NO_2	H
PbH09	C	NO_2	H	NO_2
PbH10	CH	-	H	F
PbH11	CH	-	H	Cl
PbH12	CH	H	H	Br

Table 25. Chemical structures for PbH **13-24**.

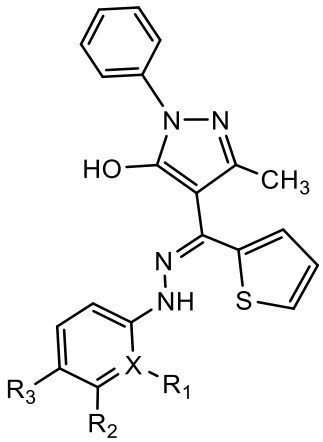

Compounds	X	R_1	R_2	R_3
PbH13	CH	-	H	H
PbH14	N	-	H	H
PbH15	CH	-	H	CF_3
PbH16	CH	-	H	CN
PbH17	CH	-	H	COOH
PbH18	CH	-	H	OCH_3
PbH19	CH	-	H	NO_2
PbH20	CH	-	NO_2	H
PbH21	C	NO_2	H	NO_2
PbH22	CH	-	H	F
PbH23	CH	-	H	Cl
PbH24	CH	-	H	Br

Table 26. Chemical structures for PbH **25-36**.

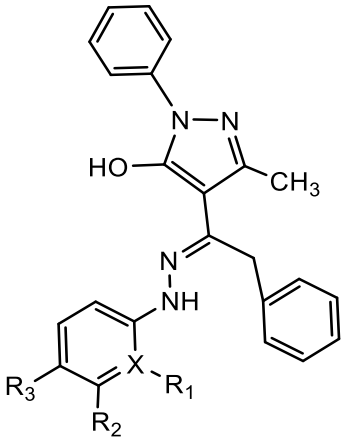

Compounds	X	R_1	R_2	R_3
PbH25	CH	-	H	H
PbH26	N	-	H	H
PbH27	CH	-	H	CF_3
PbH28	CH	-	H	CN
PbH29	CH	-	H	COOH
PbH30	CH	-	H	OCH_3
PbH31	CH	-	H	NO_2
PbH32	CH	-	NO_2	H
PbH33	C	NO_2	H	NO_2
PbH34	CH	-	H	F
PbH35	CH	-	H	Cl
PbH36	CH	-	H	Br

PbH **1-36** are air-stable in the solid-state and soluble in most organic solvents. They have been characterized through ^{1}H and ^{13}C NMR and ESI-MS analyses.

4.2.2 Cytotoxicity studies

All 36 synthesized compounds were assayed *in vitro* against *T. brucei*. Results are shown in Table 27. In general, the thiophene series appears to be ineffective against the parasite, exhibiting EC_{50} values over 10 µM, whereas the phenyl series demonstrates good activity (EC_{50} < 10 µM). However, the two most active compounds are derivatives of the benzyl precursor, namely PbH**26** and PbH**27**, accounting for EC_{50} values of 0.565 and 0.295 µM, respectively. All analogs with relevant antitrypanosomal efficacy (EC_{50} values < 50 µM) were tested against human foreskin fibroblasts (HFF) to evaluate their toxicity on humans. Safety profiles were generally acceptable, although some analogs from the thiophene series showed surprisingly low SI (PbH**15** and PbH**18**), suggesting they lack selectivity towards the parasite.

Table 27. Activity of pyrazolone-based hydrazones PbH **1-36** against *T. b. brucei* s427 and HFF cells.

Compounds	EC_{50} *T. b. brucei* s427	EC_{50} HFF	Selectivity Index (SI)
Phenyl series	**µM**	**µM**	
PbH01	42.17 ± 10.4	98.2 ± 17.34	2.32
PbH02	5.12 ± 0.357	>200	>39.06
PbH03	7.42 ± 0,195	>200	>29.95
PbH04	7.68 ± 0.622	>200	>26.04
PbH05	>100	-	-
PbH06	6.64 ± 0.382	>200	>30.12
PbH07	62.38 ± 3.25	-	-
PbH08	3.05 ± 0.24	>200	>65.57
PbH09	>100	-	-
PbH10	7.18 ± 0.177	>200	>27.86
PbH11	5.34 ± 0.194	>200	>37.45
PbH12	4.70 ±0.682	>200	>42.55
Thiophene series	**µM**	**µM**	
PbH13	51.18 ± 12.34	-	-
PbH14	27.26 ± 1.34	>200	7.34
PbH15	28.57 ± 3.39	54.97 ± 9.94	1.92
PbH16	27.14 ± 4.26	>200	>7.37
PbH17	>100	-	-
PbH18	20.49 ± 1.98	9.12 ± 3.93	0.45
PbH19	> 100	-	-
PbH20	18.14 ± 2.83	> 200	>11.02

PbH21	>100	-	-
PbH22	17.45 ± 3.29	>200	>11.46
PbH23	14.85 ± 1.22	97.73 ± 10.5	6.58
PbH24	25.33 ± 3.16	92.34 ± 7.33	3.65
Benzyl series	**µM**	**µM**	
PbH25	16.61 ± 0.88	>200	>12.04
PbH26	0.565 ± 0.04	84.17 ± 0.12	>100
PbH27	0.295 ± 0.01	>200	>100
PbH28	65.10 ± 6.28	-	-
PbH29	>100	-	-
PbH30	>100	-	-
PbH31	>100	-	-
PbH32	28.61 ± 1.73	>200	>6.99
PbH33	>100	-	-
PbH34	>100	-	-
PbH35	40.08 ± 2.46	>200	>4.99
PbH36	34.05 ± 3.53	>200	>5.87
Reference drug	**nM**	**µM**	
Pentamidine	2.83 ± 0.53	>200	>100

4.2.3 Synthesis of the metal complexes

The two most active and selective compounds coming from the benzyl series (PbH**26** and PbH**27**) were selected as ligands for synthesizing four metal complexes. The basic anionic forms of PbH**26** coordinate Zn(II) and Cu(II) in a chelating κ-O,N,N tridentate fashion affording complexes [Zn(PbH26)$_2$] (**C1**) and [Cu(PbH26)$_2$] (**C3**), respectively (Scheme 5). Whereas, the anionic form of PbH**27** coordinates Zn(II) and Cu(II) atom in a chelating κ-N,O bidentate fashion affording complexes [Zn(PbH27)$_2$(MeOH)$_2$] (**C2**), and [Cu(PbH27)$_2$] (**C4**) (Scheme 5).

The structures of **C2** and **C4**, with the two N,O-chelating ligands in anti-configuration, have been proposed on the basis of analogous Zn(II) and Cu(II) complexes previously reported in the literature with other non-symmetrical pyrazolone-based hydrazones (Marchetti et al., 2019). Complexes **C1−4** are air-stable in the solid-state and are soluble in most organic solvents, but not in alcohols and water.

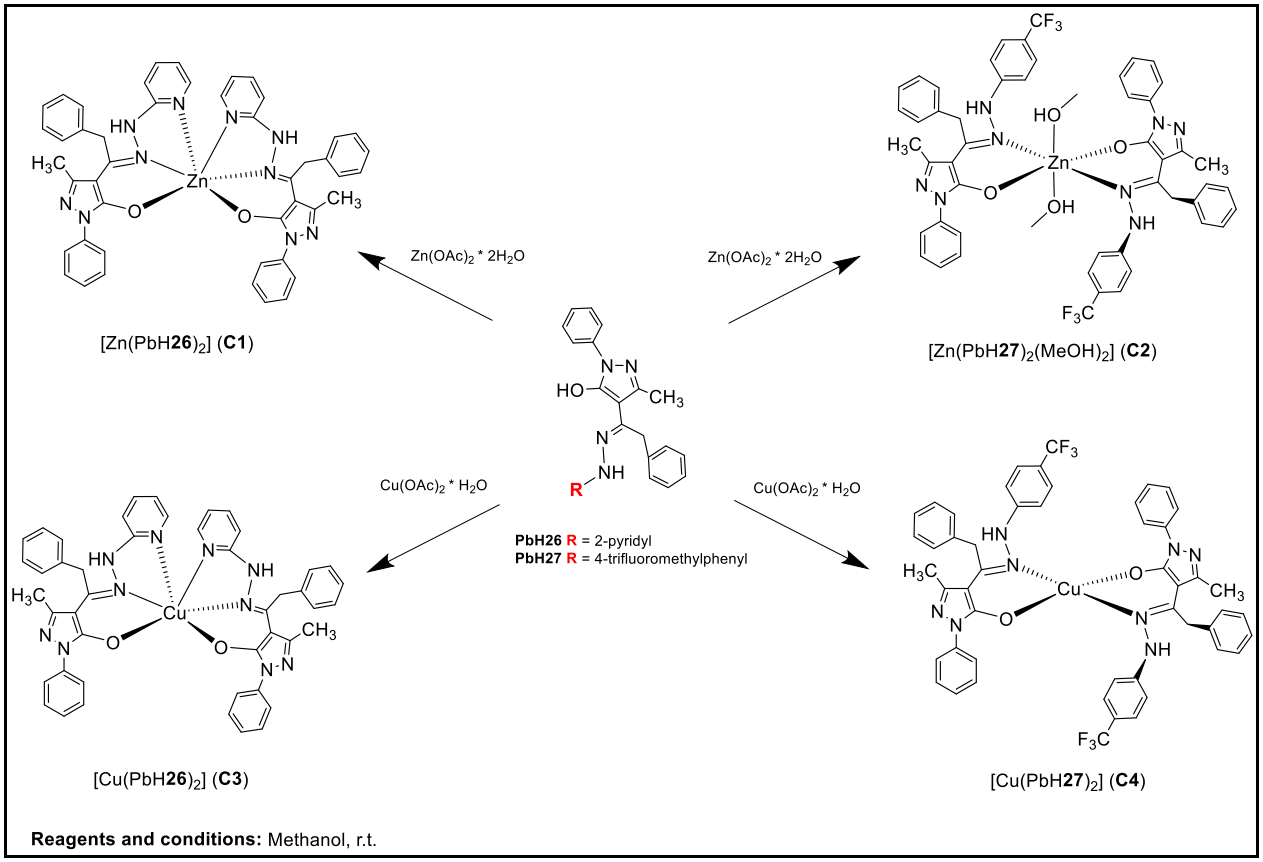

Scheme 5. Synthetic procedures to complexes **C1-4**.

The ^{1}H and ^{13}C NMR spectra in $CDCl_3$ of Zn(II) complexes **C1** and **C2** are in accordance with the expected structures containing the N,N,O-dichelating (**C1**) and N,O-chelating (**C2**) ligands, confirming the existence of complexes in solution with the ligands signals downfield shifted with respect to the corresponding signals in the free ligands spectrum.

Positive ESI-MS spectra recorded in acetonitrile display a similar pattern for all complexes **C1-4**, with main peaks being due to $[M(PbHx)_2]^+$, or to $[M(PbHx)_2 + Na]^+$, and also to clusters $[M_2(PbHx)_3]^+$. Spectra are reported in supporting information.

When the synthesis of complex **C4** is performed at room temperature, leaving the reaction mixture under stirring for 24 h, the red precipitate, corresponding to **C4**, slowly converts to a dark green color. This green precipitate was investigated spectroscopically and with single crystal X-ray analysis confirming the degradation of the coordinated PbH**27** ligand to acylpyrazolones, by loss of (4-(trifluoromethyl)phenyl)hydrazine. The new complex is indicated as $[Cu(PP)_2]$ (**C5**) (Scheme 6).

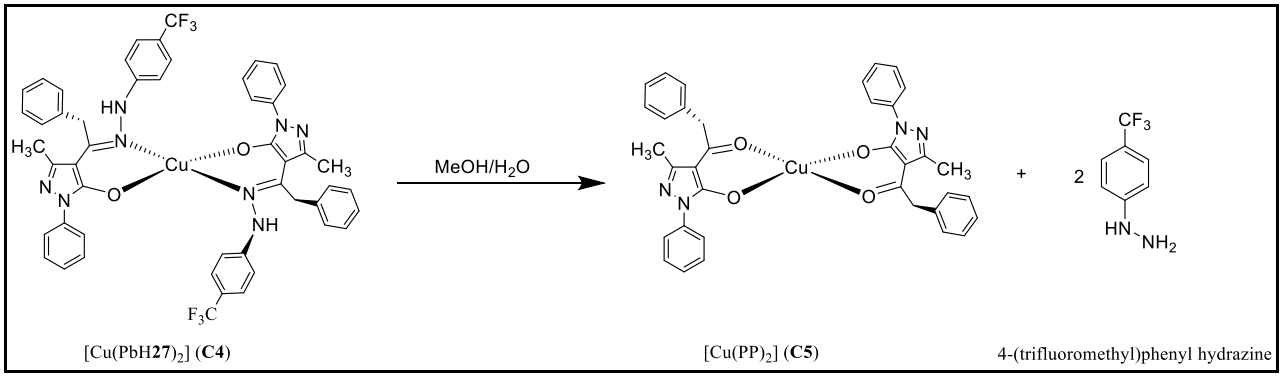

Scheme 6. Decomposition pathway of **C4** to **C5**.

4.2.4 In vitro antitrypanosomal activity of metal complexes

C1-4 were subsequently assayed against *T. brucei* and HFF cells, and results are reported in Table 28. The two Zn(II) complexes (**C1** and **C2)** displayed considerable activity, below 1 µM, and enhanced with respect to their original ligands. Specifically, **C1** and **C2** exerted an effect 3-fold higher when compared to PbH**26** and PbH**27**, respectively. On the other hand, Cu(II) complexes **C3** and **C4** demonstrated EC_{50} values of 12.76 and 4.369 µM, respectively, showing a considerably milder activity with respect to ligands. Moreover, **C3** and **C4** resulted active on HFF cells, exhibiting a certain cytotoxicity (SI of 1.34 and 7.55). Instead, **C1** and **C2** appeared inactive towards HFF cells, displaying a good safety profile with SI over 100.

Table 28. *In vitro* activity of complexes **C1-4**.

	EC_{50} *T.b.* s427 (µM)	**EC_{50} HFF (µM)**	**Selectivity Index (SI)**
Complexes			
[Zn(PbH26)$_2$] (C1)	0.169 ± 0.01	>200	>100
[Zn(PbH27)$_2$(MeOH)$_2$] (C2)	0.084 ± 0.14	>200	>100
[Cu(PbH26)$_2$] (C3)	12.76 ± 4.06	17.16 ± 3.45	1.34
[Cu(PbH27)$_2$] (C4)	4.369 ± 0.38	32.98 ± 0.35	7.55
Reference drug			
Pentamidine	0.010 ± 0.001	>200	>100

4.2.5 Crystallography

Taking into account the promising activity of PbH**27** and its derived Zn(II) metal complex **C2**, a crystallography study was conducted for both of them. Figures 45 and 46 show the X-ray single crystal molecular structure of PbH**27** and complex **C2**, with an atomic numbering scheme. Table 29 reports selected angles and bond distances for both compounds. Detailed data and refinements are shown in supporting information, Table S1.

In the solid crystalline state, PbH**27** was found in the N-H, C=O tautomeric form (tautomer II), in a triclinic crystal system. Its overall structure is not planar, with a peculiar orientation of the hydrazone fragment (C-N-N-C torsion angle of 149.5(2)°). Intramolecular hydrogen bond between the N-H and the C=O carbonyl group is observed [N(1)---O(1) and N(1)-H(1a) ∠O(1) of 2.670(3) and 2.706(2) Å].

The X-ray crystal structure analysis of **C2** confirmed its neutral nature and, therefore the general formula [Zn(PbH**27**)$_2$(MeOH)$_2$]. Indeed, **C2** co-crystallized with two methanol molecules in the asymmetric unit (Figure 46). The zinc ion, located on the symmetry inversion center, is hexa-coordinated with two N,O bis-chelated PbH**27** ligands and two oxygen atoms belonging to methanol

molecules. The oxygen and nitrogen atoms of the chelated PbH**27** lie in the same plane and bond distances at the zinc ion. Most of the intermolecular interactions are attributable to methanol molecules, both coordinated and co-crystallized (Figure 47).

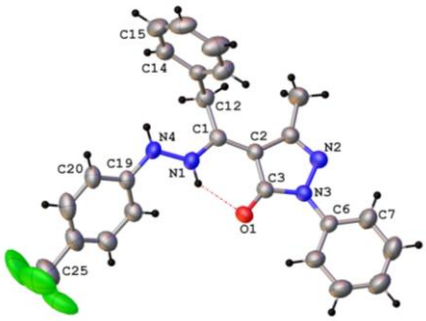

Figure 45. Ortep view of the asymmetric unit content of PbH**27** with atomic numbering scheme and intramolecular N-H---O hydrogen bond (ellipsoids at the 40% level).

Table 29. Selected bond distances (Å) and angles (°) in ligand PbH27, and complex C2.

Bond	**PbH27**	**Bond**	**C2**
N(1)-N(4)	1.401(3)	M-O(1)	2.008(2)
N(1)-C(1)	1.335(3)	Zn-N(1)	2.100(3)
C(1)-C(2)	1.401(3)	Zn-$O(2)_{solv}$	2.223(2)
C(2)-C(3)	1.438(3)	N(1)-N(4)	1.420(4)
C(2)-C(4)	1.451(3)	N(1)-C(1)	1.302(4)
C(3)-N(3)	1.390(3)	C(1)-C(2)	1.435(4)
C(3)-O(1)	1.264(3)	C(2)-C(3)	1.417(4)
N(2)-N(3)	1.412(3)	C(2)-C(4)	1.425(4)
N(2)-C(4)	1.309(3)	C(3)-N(3)	1.359(4)
N(3)-C(6)	1.416(3)	C(3)-O(1)	1.281(4)
		O(1)-Zn-N(1)	87.9(1)
		O(1)-Zn-O(2)	85.7(1)
		O(1)-Zn-$N(1)^{i}$	92.1(1)
		N(1)-Zn-$O(2)^{i}$	89.0(1)
		i = -x+2,-y,-z+2 ;	
		ii = -x,-y+2,-z+2	

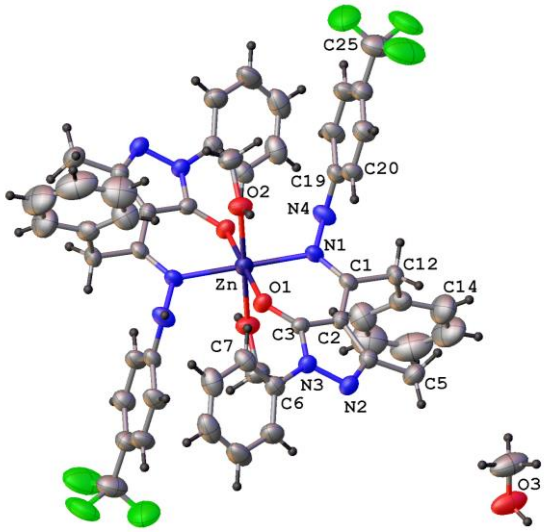

Figure 46. Ortep view of the asymmetric unit content of $[Zn(PbH27)_2(MeOH)_2]$ (**C2**) with atomic numbering scheme (ellipsoids at the 40% level).

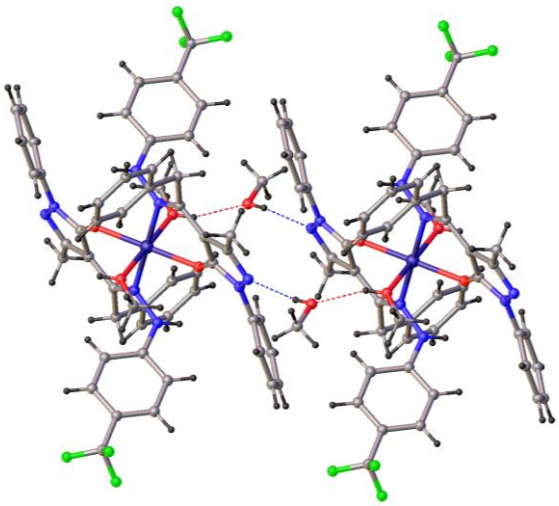

Figure 47. Crystal packing view of **C2** showing the N–H···O and O–H···O hydrogen bonds involving both coordinated and lattice methanol molecules.

In particular, the co-crystallized methanol molecules act as both hydrogen bond donors and acceptors, with the formation of O-H---N and O-H---O interactions with the nitrogen atom N(3) of the pyrazole ring and the hydrogen atom of the coordinated methanol molecule [$O(3)\cdots N(2)^{i}$ 2.828(4) Å, O(3)-H(3) ∠N(2) 161°, i = -x+1, -y+1, -z+2; $O(2)\cdots O(3)^{ii}$ 2.698(4) Å, O(2)-H(2) ∠O(3) 157°, ii = x, y-1, z].

4.2.6 Theoretical DFT analysis

Density functional theory (DFT) at the B3LYP/6-311G** level of theory was used to analyze tautomers I and II of PbH**27** (Figure 48). Small energy differences between them were detected (see

Table S2). Tautomer I appears to be the predominant species in the solution, consistent with experimental NMR data. Indeed, computed ^{1}H and ^{13}C NMR spectra for tautomer I of PbH**27** are comparable with the experimental data, whereas for tautomer II the match results are less precise (see Figure S1). Instead, the solid-state favors tautomer II species. The proposed structural parameters of tautomer II coincide with X-ray data (see Figure S2). Specifically, the experimental C=O bond distance of 1.264(3) Å is well reproduced by calculations (1.241 Å for II versus 1.327 Å for tautomer I).

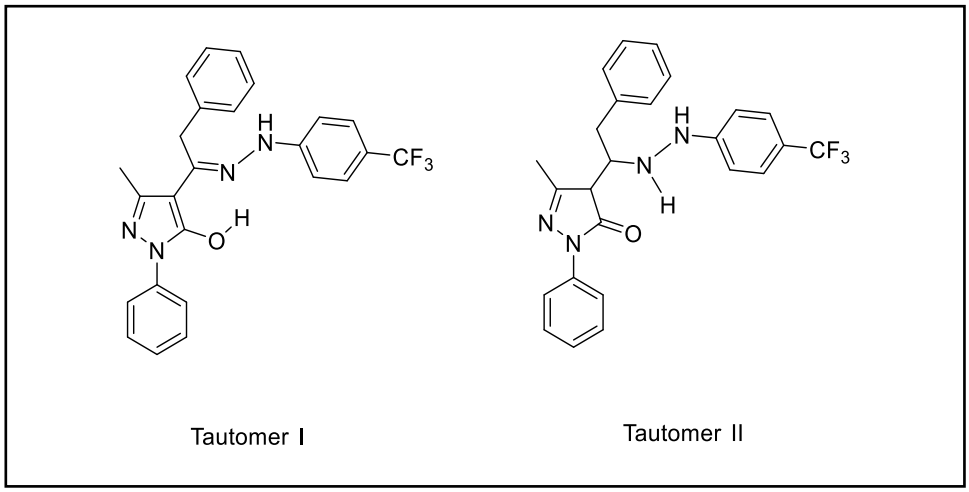

Figure 48. Tautomeric forms for PbH**27**.

In order to understand the coordination potential of PbH**27** in Zn(II) complex **C2**, the electronic conformation of the anion [PbH**27**]$^{-}$ was studied. The bonding localization of [PbH**27**]$^{-}$ is in accordance with the deprotonation of tautomer II, exhibiting a shorter C=O bond (1.232Å) than the C−N bond (1.303 Å). Evidently, these distances change upon coordination with the zinc ion. HOMO−2 and HOMO−3 are the two MOs involved in the coordination to the metal atom for PbH**27**, with a minor contribution of HOMO−9. In these MOs lone pairs of the N and O donor atoms take part in the in-phase and out-of-phase contributions of the σ type, which make the M−O and M−N bonds possible.

These MOs were compared with those obtained from the single-point calculation of the PbH**27** ligand with the geometry found in the optimization of **C2**. In this case, the in-phase and out-of-phase combinations are clearly detected in HOMO−1and HOMO−3.

Complex **C2** was also analyzed by DFT. Figure 49 shows the optimized structure of the complex. The combination of methods and basis sets gave a good match of the calculated and experimental structural parameters, providing a precise structural description of **C2** (Table S3).

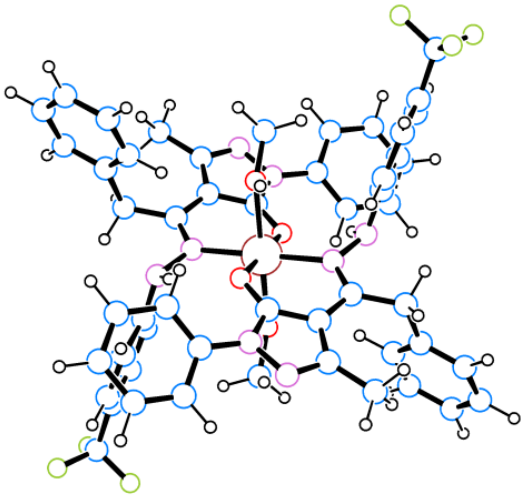

Figure 49. Optimized structure of complex **C2**.

The PbH**27** ligand exhibits delocalized C-O and C-N bonds (1.279 and 1.315 Å, respectively) in agreement with experimental values, and the two six membered metallacycles [Zn(PbH**27**)] show an envelope conformation with an angle between the ligand and molecular planes of 30.3º (experimental 30.9º). The proposed optimized structure of **C2** also gives a calculated NMR that matches well with experimental ^{1}H and ^{13}C NMR spectra (R2 value of 0.9971 in the correlation shown in Figure S3). To rationalize the observed trans disposition of methanol molecules in **C2**, we optimized the hypothetic complex [Zn(PbH**27**)$_2$] without these solvent ligands. The resulting structure is square planar, which is unexpected for a four-coordinated d^{10} complex. This fact suggests that the adoption of such a geometry is mainly due to steric reasons. This is confirmed by optimizing the related complex [Zn(PbH**27***)$_2$], where the PbH**27*** ligand is like PbH**27**, but the *p*-trifluoromethylphenyl substituent is replaced by a methyl group. Optimized [Zn(PbH**27***)$_2$] is tetrahedral and is 5.8 kcal/mol (ΔG) more stable than the square planar structure. Consequently, the presence of the *p*-trifluoromethylphenyl group in PbH**27** causes enough steric pressure to impede the adoption of the expected d10-tetrahedral arrangement of [Zn(PbH**27**)$_2$], explaining the trans-(MeOH)$_2$ geometrical configuration observed in **C2**.

4.2.7 Mechanism of action investigation

Due to the good activity of several compounds coming from the three pyrazolone-based hydrazone series and the two zinc complexes derived from PbH**26** and PbH**27**, the most active molecules were considered to deepen the study of their mode of action. The aim was to elucidate which processes and mechanisms are involved in the antiprotozoal effect of the drug candidates, studying the type of cellular inhibition displayed and trying to identify one or more targets inside the parasite.

4.2.7.1 Cross resistance assessment

Cross resistance among current chemotherapies is a phenomenon that unfortunately occurs when resistances to drugs arise. Thus, new potential antitrypanosomal drugs need to be tested for cross resistance in order to assess that, at least, they are not cross-resistant with diamidine and arsenic based treatment currently employed (i.e., pentamidine, diminazene, and melarsoprol). Moreover, it is preferable to also assess the efficacy of the new drug candidates on animal strains of *Trypanosoma*; indeed, veterinary pathologies are becoming a great economic and social issue in the African continent, and the development of a unique therapy (both for humans and animals) is desirable. Exactly for these reasons, the most promising analogs from the three synthesized series (compounds characterized by EC_{50} values below 10 μM) were selected and tested against: a multi-drug resistant laboratory strain of *T. b. brucei*, resistant to the diamidines and melaminophenyl arsenicals (*T. b.* B48); a specific suramin resistant *T. b. brucei* strain (*T. b.* SUR10) and two animal trypanosomiasis strains, namely *T. evansi* and *T. equiperdum*. All assays were carried out in three independent experiments for each compound with positive controls, i.e., pentamidine, diminazene, and suramin; negative controls were included using drug-free incubations. The obtained fluorescence intensities were analyzed using the GraphPad Prism 8 software, and data were plotted by non-linear regression to a sigmoid curve with variable slopes, to determine EC_{50}. From the results, it appears evident that there is very little difference among wild type (WT), B48, and SUR10 *T. brucei* strains activity. Resistance factors (RF), obtained by the ratio between the activity of a compound on the resistant strain and its activity on the WT, were calculated. Generally, an RF widely superior to 1 indicates cross-resistance, whereas an RF below 1 means an enhanced sensitivity of the resistant strain to the compound tested. Calculated RFs for the synthesized products are almost all close to 1 (or at least not close to the RF values calculated for positive controls), meaning that they potentially act on the parasite without involving any current drug uptake mechanisms. Moreover, also the RFs related to *T. evansi* and *T. equiperdum* are all not distant from the unity, suggesting that the drugs are effective on these two animal trypanosomiasis species and on the WT with comparable potency (Table 30).

Table 30. Cross resistance evaluation of the most active PbH analogs**, C1**, **C2**, and **C4**.

	Trypanosoma cell lines tested									
	T. b. brucei s427		*T. b.* B48		*T. b.* SUR10		*T. evansi*		*T. equiperdum*	
	EC_{50} (µM)	**SI**	**EC_{50} (µM)**	**RF***	**EC_{50} (µM)**	**RF**	**EC_{50} (µM)**	**RF**	**EC_{50} (µM)**	**RF**
PbH02	5.12 ± 0.36	*39.09*	5.90 ± 0.30	1.15	9.39 ± 0.64	1.84	4.86 ± 0.08	0.95	14.18 ± 1.36	2.77
PbH03	7.42 ± 0.20	*26.95*	8.30 ± 0.05	1.12	9.39 ± 0.64	1.26	15.11 ± 0.16	2.04	1.45 ± 0.27	0.20
PbH04	7.68 ± 0.62	*26.03*	6.28 ± 0.41	0.82	4.79 ± 0.25	0.62	11.97 ± 0.91	1.56	9.90 ± 1.67	1.29
PbH06	6.64 ± 0.38	*30.11*	5.85 ± 0.28	0.88	4.14 ± 0.37	0.62	6.00 ± 0.36	0.90	5.79 ± 0.53	0.87
PbH08	3.05 ± 0.24	*65.57*	6.28 ± 0.15	2.06	4.51 ± 0.06	1.48	9.85 ± 0.20	3.23	1.13 ± 0.01	0.37
PbH10	7.18 ± 0.18	*27.85*	6.30 ± 0.40	0.88	4.78 ± 0.19	0.67	8.58 ± 1.00	1.19	5.26 ± 0.53	0.73
PbH11	5.34 ± 0.19	*37.43*	5.26 ± 0.14	0.98	3.81 ± 0.89	0.71	4.80 ± 0.42	0.90	3.72 ± 0.51	0.70
PbH12	4.70 ± 0.68	*42.56*	3.94 ± 0.49	0.84	3.84 ± 0.54	0.82	4.53 ± 0.09	0.96	4.07 ± 0.54	0.87
PbH26	0.565 ± 0.04	*>100*	0.664 ± 0.004	1.18	0.385 ± 0.03	0.68	0.287 ± 0.03	0.51	0.443 ± 0.02	0.78
PbH27	0.295 ± 0.01	*>100*	0.561 ± 0.12	1.90	0.304 ± 0.08	1.03	0.872 ± 0.20	2.96	0.067 ± 0.01	0.23
C1	0.169 ± 0.01	*>100*	0.267 ± 0.02	1.58	0.246 ± 0.22	1.46	0.129 ± 0.28	0.76	0.312 ± 0.05	1.85
C2	0.084 ± 0.14	*>100*	0.105 ± 0.09	1.25	0.132 ± 0.08	1.57	0.071 ± 0.45	0.85	0.111 ± 0.08	1.32
C4	4.369 ± 0.38	*7.59*	3.83 ± 0.08	0.88	5.619 ± 0.08	1.29	1.964 ± 0.20	0.45	2.138 ± 0.01	0.49
Reference drug										
Pentamidine	0.010 ± 0.001	*>100*	0.425 ± 0.09	44.10	-	-	0.007 ± 0.001	0.7	0.103 ± 0.01	11.40
Diminazene	0.062 ± 0.02	*>100*	2.986 ± 0.20	48.16	-	-	-	-	-	-
Suramin	0.009 ± 0.002	*>100*	-	-	0.190 ± 0.017	21.12	-	-	-	-

*Resistance factor (RF) = ratio between EC_{50} on the resistant strain and EC_{50} on the WT. RF>>1 cross-resistance; RF=1, no cross resistance; RF<<1, sensitivity for resistant strain.

4.2.7.2 Effect of different concentrations of test compounds following long and limited exposures

The most promising compounds (PbH**26**, PbH**27**, **C1,** and **C2**) were selected for the evaluation of their activity on the parasites at long exposures (up to 32 h). All of them were tested at three concentrations (2 x EC_{50}, 5 x EC_{50}, and 10 x EC_{50}), and treated *T. brucei* growth was evaluated compared to a drug-free control. As visible from graphs (Fig. 50), PbH**27** and its zinc derivative **C2** seem to cause 100% mortality within 16 hours at the higher concentrations (5 x EC_{50} and 10 x EC_{50}) and can thus be defined as trypanocidal at those concentrations. On the contrary, after treatment with PbH**26** and **C1**, cells do not die in a brief time frame (at least not within 24 h), but their growth appears to be stopped at almost all concentrations tested, suggesting the trypanostatic nature of these two drugs.

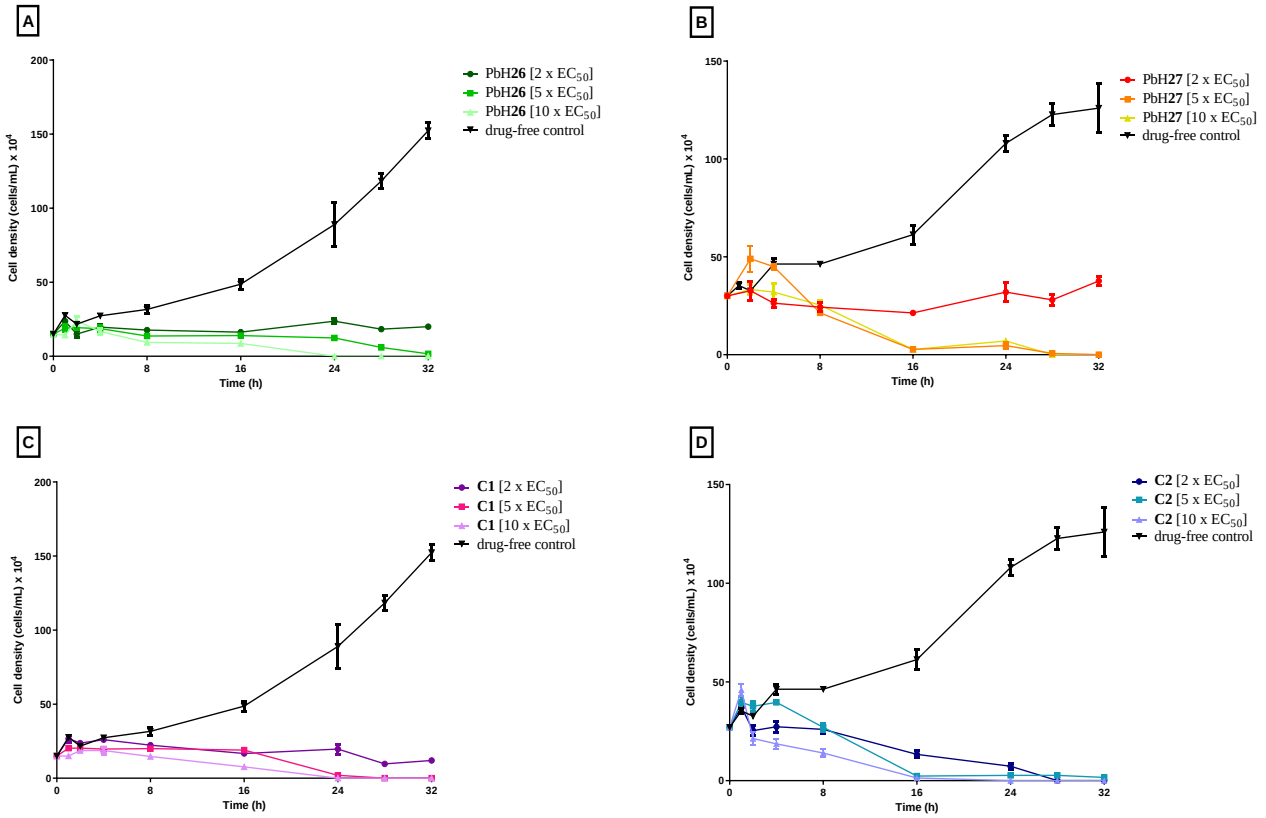

Figure 50 Growth curves of *T. brucei* WT s427 grown in the continuous presence of PbH**26**, PbH**27**, **C1,** and **C2** (A, B, C, and D, respectively) at indicated concentrations (2 x EC_{50}, 5 x EC_{50}, and 10 x EC_{50}), or untreated (drug-free control).

The effect on trypanosome (s427 WT) proliferation was also studied after a limited duration exposure of the cells to PbH**27**, the most active test compound.

The initial density was set at 2 × 10^5 cells/mL, the cells were treated with the appropriate test compound concentration (2 x EC_{50}) except for the drug-free control. The cultures were incubated at

37 ºC and 5% CO_2 and monitored for a period of 24 hours. Once this time has passed, a sample of cells treated with PbH**27** were centrifuged, washed and re-seeded (2×10^5 cells/mL) with fresh media. Subsequently, living cells were counted at each time point up to 72 h. The counting was performed in triplicate and the average values obtained were plotted against time using GraphPad prism 8 software. From the results, it appears evident that the growth pattern with limited exposures to PbH**27** is significantly different from the one of long-term exposure (Fig. 51, orange line). The result shows that the growth patterns of cells with limited exposure were different from those with long-time exposure to PbH**27** (Fig. 51, red line). Indeed, after the washing and re-seeding of cells after 24 h treatment, parasites start growing again, suggesting that the effect of the drug on trypanosomes is reversible.

Thus, PbH**27** appears to be rapidly trypanocidal in the continuous presence of the two higher concentrations; following the wash after 24 h, the effect seems to vanish, meaning that the drug doesn't act through an irreversible mode of action.

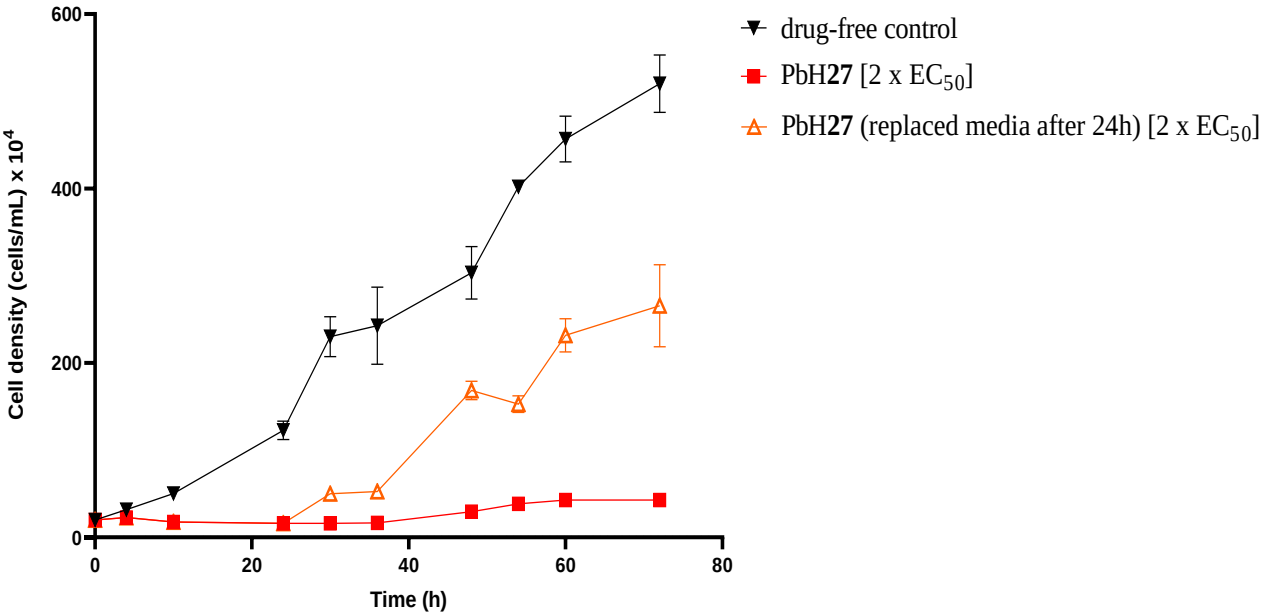

Figure 51. Growth curve showing the effect of PbH**27** (2 x EC_{50} concentration) on trypanosome proliferation after a limited exposure (24 hours) up to 72 hours.

4.2.7.3 Cell cycle determination

The effect of PbH**27** on cell cycle progression was evaluated through the measurement of DNA content on a 24-hour basis. To achieve this aim, Fluorescence Activated Cell Sorting Technology (FACS) was used in BSF *T. b. brucei* s427 WT. Cell density was initially adjusted to 1×10^7 cells/mL

with and without test compound and, at each time point, 1 mL of sample was taken into microfuge tubes and centrifuged at 1620 × g for 10 min at 4 °C, washed in PBS containing 5 mM EDTA and re-suspended, then fixed by treating it with 1 mL of 70% methanol and 30% PBS/EDTA. The sample was then left at 4 °C overnight in the dark, and the samples were subsequently washed once with 1 mL PBS/EDTA, re-suspended in 1 mL PBS/EDTA containing 10 µg/mL propidium iodide (PI) and incubated at 37 °C in 5% CO_2 atmosphere for 45 minutes. Samples were analyzed by a Becton Dickinson FACSCalibur using the FL2-Area detector and CellQuest software. Data obtained were analyzed using flowJo software (Flowjo LLC, Ashland, OR, USA; histograms in supporting information, Fig. S4) and elaborated with GraphPad prism 8 software. From Figure 52 it is noticeable that the cell cycle of parasites treated with PbH**27** is subjected to a stop in the G1-G2 turnover, causing an accumulation of cells in G1 phase already after 6 hours from the first exposure and a consequent proportional lower percentage of G2-phase cells.

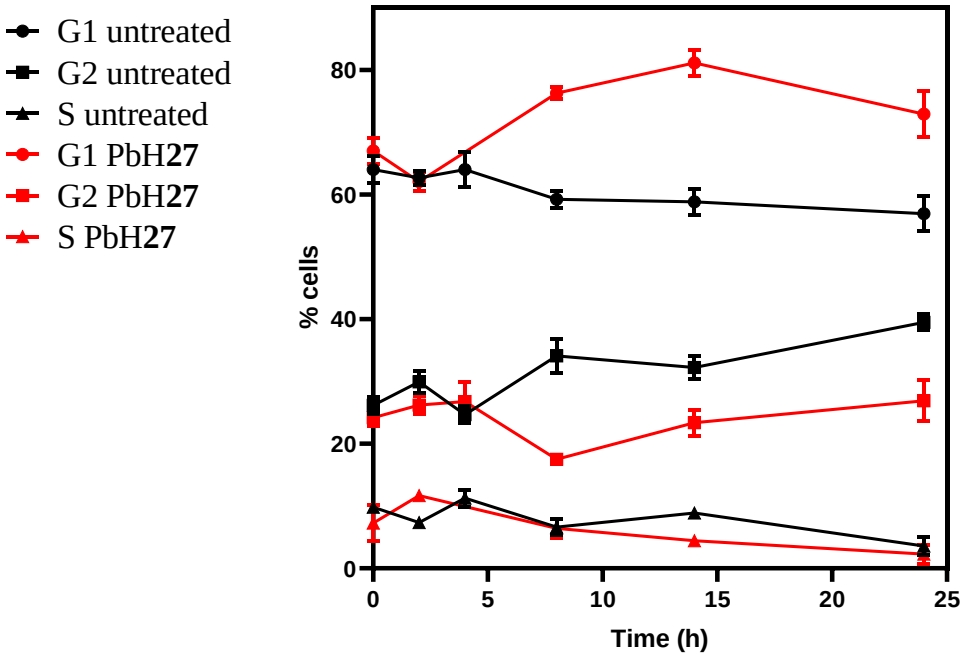

Figure 52. Percentage of cells at various cell division stages in populations treated or not treated with 2 x EC_{50} PbH**27**. The percentages are the average of two independent determinations and SEM, obtained using flow cytometry after cell permeabilization and staining with propidium iodide.

4.2.7.4 Fluorescence microscopy

Because of the results obtained from the flow cytometry, an understanding of cell cycle events after treatment with PbH**27** may help in interpreting the mode of action of the anti-parasite compound. Fluorescence microscopy is an interesting tool to accomplish this purpose. Cells were stained with

4′,6-diamidino-2-phenylindole (DAPI), and Mitotracker RED (MT) and incubated with PbH**27** at 2 x EC_{50} concentration. Cells were visualized under a fluorescent microscope at various time points within the incubation period, and results were presented as a percentage of 200 cells, and scores for DNA configuration were given as 1N1K, 1N2K, and 2N2K, where N is nucleus; and K is kinetoplast (Fig. 53).

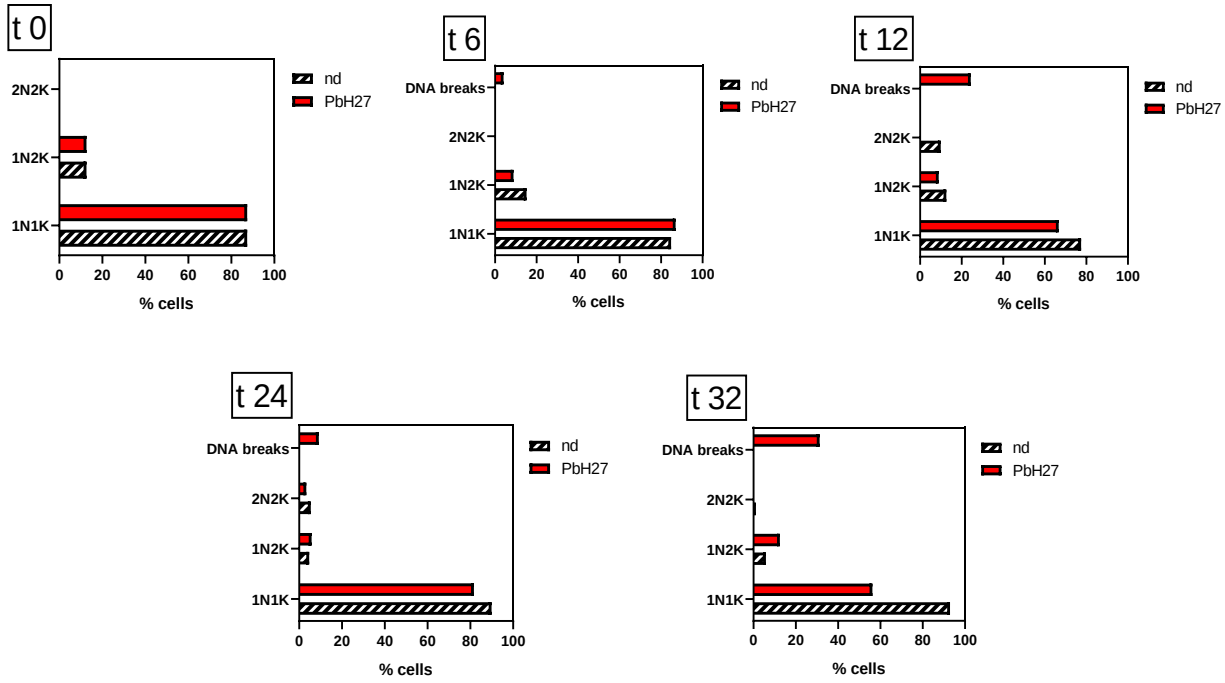

Figure 53. Cell cycle determination in *T. brucei* s427 WT using DAPI. Fixed cells prepared on slides were visualized under a fluorescence microscope at different time points up to 32 hours of incubation with and without PbH**27**. Values were expressed as a percentage of 200 counted cells. N = nuclear DNA; K = kinetoplast DNA.

Fluorescence microscopic examination of DNA configuration revealed cell cycle defects already after 8 hours of incubation with PbH**27**, and in a more pronounced manner after 12 hours. DNA synthesis seems not to be accomplished and DNA abnormalities appear with a concomitant decrease in cells in all stages of the cell division process (Table 31). DNA looks fragmented whereas the mitochondrion seems not to be affected at all, suggesting that PbH**27** doesn't alter its membrane and it is not involved in the drug's mechanism of action.

Table 31. DNA contents and mitochondrial examination of treated and untreated (drug-free) cells. Images of *T. brucei* s427 wild type showing DNA breaks following 8 hours of incubation with or without PbH**27** (2 x EC_{50}), taken with the aid of a fluorescent microscope.

N = nuclear DNA; K = kinetoplast DNA; DAPI = 4',6-diamidino-2-phenylindole; MT = Mitotracker RED

	DAPI	**MT**
1N1K drug-free	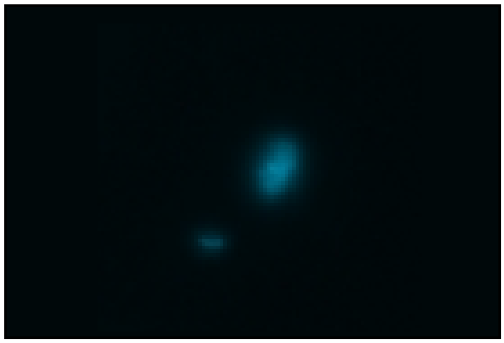	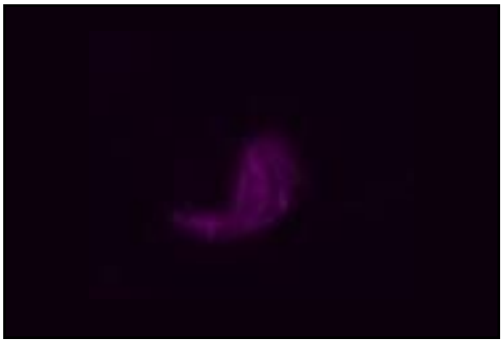
1N2K drug-free	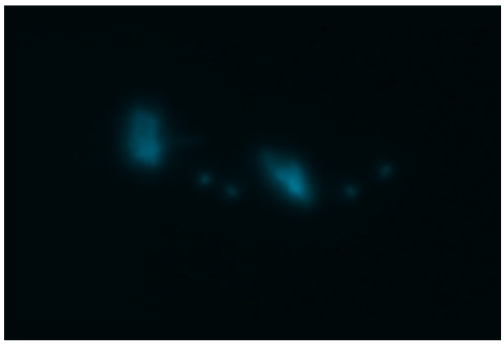	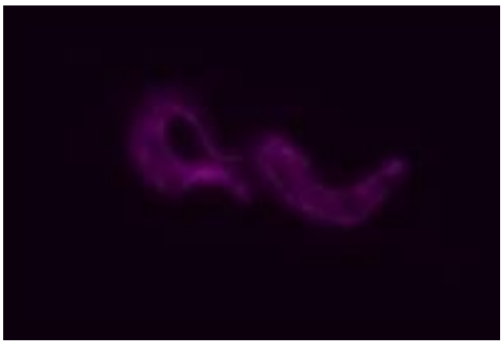
2N2K drug-free	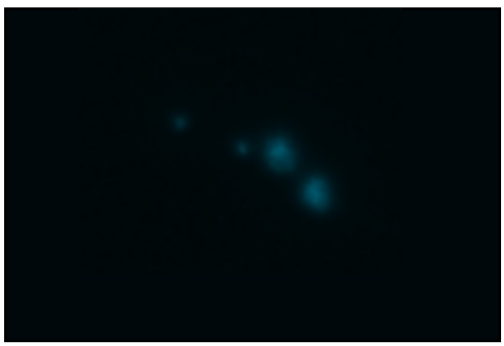	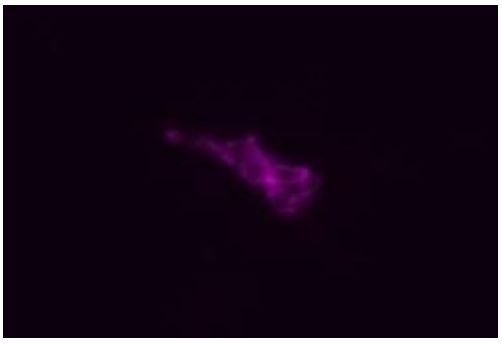
DNA breakages PbH27 treated cells (already after 8 h)	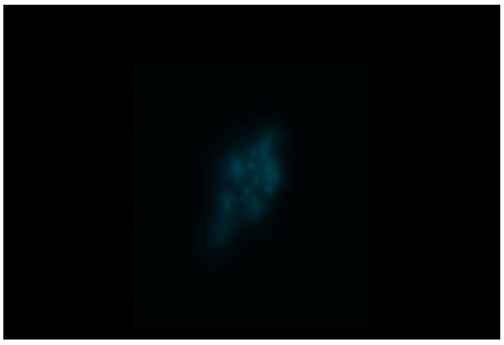	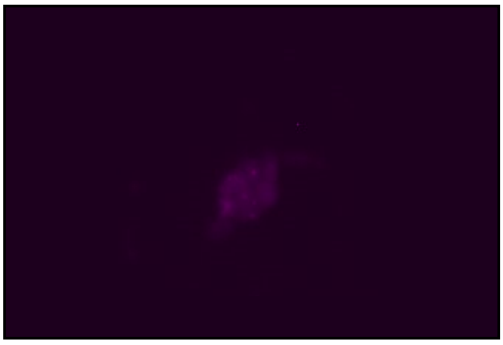

4.2.7.5 Determination of di- and triphosphate nucleotide (NDPs and NTPs) pools by HPLC

Nucleotide triphosphates (NTP), deoxynucleotide triphosphates (dNTP), and adenosine diphosphate (ADP) pools of parasites treated with PbH**27** and its Zn(II) complex **C2** were measured by HPLC and compared to the pools of untreated *T. brucei* cells. The method from Ranjbarian et al. (2021) was adopted. The cell density of a 50 mL culture was adjusted to 1 x 10^6 logarithmically growing cells/mL, and drugs were added to reach a 5 µM concentration. After incubation of 1 h, NTPs, dNTPs, NDPs, and dNDPs were extracted with trichloroacetic acid, and quantification was performed using HPLC.

Changes in di- and triphosphate nucleotide pools were detected between treated and non-treated trypanosomes (chromatograms in supporting information, Fig. S5). The first noticeable difference lies in the levels of cytosine triphosphate (CTP) and deoxycytosine triphosphate (dCTP). Despite the fact that CTP and dCTP levels are low even in *T. brucei* cells in normal conditions (almost 2% of the total NTP pool), pools appeared much lower in parasites treated with PbH**27** and especially with the Zn-complex **C2** (Fig. 54, A). CTP levels in cells treated with the ligand PbH**27** were 4-fold reduced with respect to non-treated CTP pools, whereas **C2** caused a more profound decrease, with CTP accounting for 6% of the CTP pool of the control group. For other NTPs or ADP, no obvious effect was observed (Fig. 54, B).

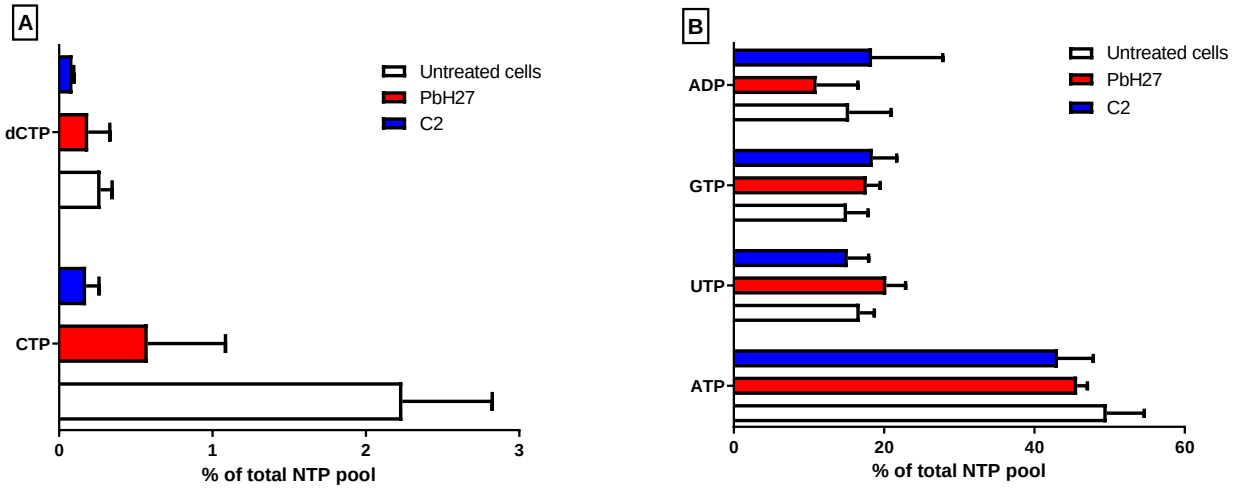

Figure 54. A) Differences in CTP and dCTP pools in non-treated cells and cells treated with PbH**27** and **C2** (both of them at a concentration of 5 µM for 1 h). B) Differences in NTP pools in non-treated cells and cells treated with PbH**27** and **C2** (both of them at a concentration of 5 µM for 1 h).

Concerning deoxynucleotides, treatment with the two drugs caused an enhancement of all dNTPs and in a more pronounced way, for **C2**. Percentages of dATP, dGTP, and dTTP of the total dNTP pool of both treated and untreated cells are reported in fig. 55.

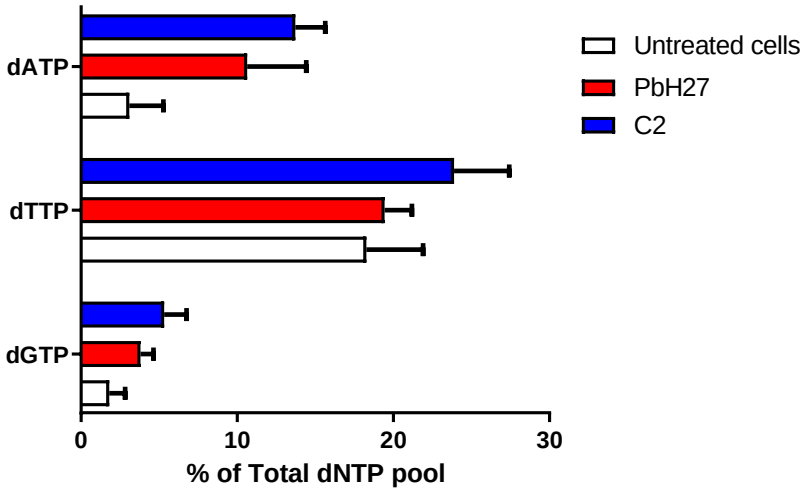

Figure 55. Increased deoxynucleotide pools in cells treated with 5 μM PbH**27** and **C2** for 1 h (compared to deoxynucleotide pools in non-treated control cells).

4.3 Discussion

Pyrazolone-based hydrazones represent a biologically interesting class of compounds, due to the pharmacological properties of both the pyrazolone and hydrazone constituting moieties (Verma et al., 2014; Zhao et al., 2020). In the present study, three series of analogs were synthesized, and their antitrypanosomal potential was assessed. The three series differed for the substituent in C12 position, namely phenyl, thiophenyl, and benzyl groups for PP, TP, and BP series, respectively, and for the groups present in the aromatic ring with direct binding to the hydrazone moiety (Fig. 56).

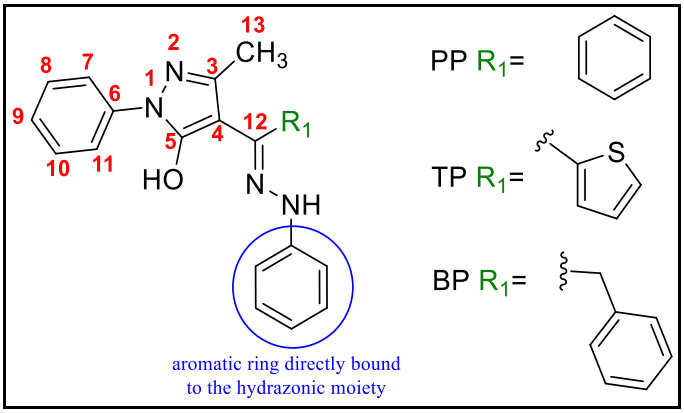

Figure 56. General structure scheme for pyrazolone-based hydrazones PbH**1-36**.

Different substituents confer different biological activities. Indeed, although pyrazolone and hydrazone groups are present for all the analogs tested, antitrypanosomal activity varies considerably based on the substitutions carried out. TP and BP series generally appeared very mildly active when

compared to the PP series; indeed, EC_{50} values of the analogs are mainly over 10 µM, whereas in the PP series, 8 of the 12 constituting compounds displayed good *in vitro* efficacy (EC_{50} < 10 µM). However, substituents of the aromatic ring bound to the hydrazone function also exert a strong influence on the antiprotozoal potential (Fig. 57). For instance, PbH**26** and PbH**27**, belonging to the BP series, emerged as the two most active analogs (EC_{50} values of 0.565 and 0.295 µM, respectively), although no other compound from the same series displayed a significant effect on *T. brucei*. The aromatic ring bound to the hydrazone moiety of PbH**26** is a pyridine, whereas the one for PbH**27** is substituted with a trifluoromethyl group in *para* position.

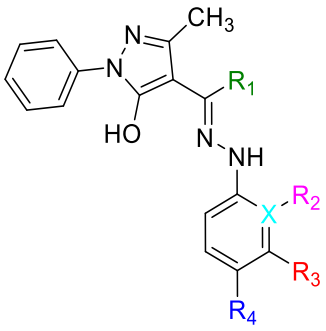

PbH**1-12**: $R_1 = C_6H_5$
PbH**13-24**: $R_1 = C_4H_3S$
PbH**25-36**: $R_1 = CH_2C_6H_5$

PbH**02**, PbH**14**, PbH**26:** X = N
All the others: X = -CH

PbH**09,** PbH**21**, PbH**33**: $R_2 = -NO_2$
All the others: R_2 = H

PbH**08**, PbH**20**, PbH**32**: $R_3 = -NO_2$
All the others: R_3 = H

PbH**03**, PbH**15**, PbH**27**: $R_4 = -CF_3$
PbH**04**, PbH**16**, PbH**28**: R_4 = -CN
PbH**05**, PbH**17**, PbH**29**: R_4 = -COOH
PbH**06**, PbH**18**, PbH**30**: $R_4 = -OCH_3$
PbH**07**, PbH**19**, PbH**31**: $R_4 = -NO_2$
PbH**09**, PbH**21**, PbH**33**: $R_4 = -NO_2$
PbH**10**, PbH**22**, PbH**34**: R_4 = -F
PbH**11**, PbH**23**, PbH**35**: R_4 = -Cl
PbH**12**, PbH**24**, PbH**36**: R_4 = -Br
All the others: R_4 = H

Figure 57. Substitutions on the aromatic ring directly bound to thew hydrazone function.

Specifically, antitrypanosomal activity seems to be positively or negatively influenced by specific substituents on that aromatic ring. The absence of substituents notably lowers the efficacy on *T. brucei*, as demonstrated by the high EC_{50} values for PbH**01** and PbH**13**, and, in a less pronounced manner, for PbH**25** (EC_{50} of 42.17 and 51.18 µM for PbH**01** and PbH**13**, respectively; EC_{50} of 16.61 for PbH**25**). The addition of an acid function in *para* position, instead, causes total loss of antiparasitic potency, as noticeable for PbH**05**, PbH**17**, and PbH**29**, which resulted totally inactive. For the PP series, generally, substitution with an electron-withdrawing group in *para* position generally intensifies the compounds' efficacy on *T. brucei*. PbH**03**, PbH**04**, and PbH**06**, which are *para*-substituted with electron-withdrawing groups, are characterized by EC_{50} values below 10 µM, as well as PbH**10**, PbH**11**, and PbH**12**, which present a halogen in *para* position. Halogen-substituted analogs show decreasing activity as the halogen electronegativity increases; fluoro-substituted PbH**10** is less active than the chloro-substituted PbH**11**, which in turn is less effective than PbH**12**, bromine-substituted.

PbH**07** represents an exception, being practically inactive on the parasites although carrying a nitro group in *para* position of the aromatic ring of interest. Indeed, antitrypanosomal activity variation linked to nitro substitutions is peculiar for all the three series considered. Substitution in *para* and in *para* and *orto* positions diminishes antiparasitic efficacy (PbH**07**, and PbH**09** from PP series, PbH**19**, and PbH**21** from TP series, and PbH**31**, and PbH**33** from BP series exhibited EC_{50} values > 50 µM). Interestingly, substitution in *meta* position with a nitro group produces three active analogs: PbH**08**, being the most potent of the PP series with an EC_{50} value of 3.05 µM, PbH**20** and PbH**32** from TP and BP series, respectively, showing mild antitrypanosomal profile, which results enhanced when compared to the other nitro analogs (EC_{50} values of 18.14 µM for PbH**20** and 28.61 µM for PbH**32**). This great difference underlines the pivotal role of the position of substituents on the aromatic ring bound to the hydrazonic function for the pharmacological activity.

As already mentioned, despite PP series being the only one generally displaying significant activity, the two most potent compounds came from BP series. Due to the already proved antiprotozoal efficacy of Zn(II) and Cu(II) complexes (Chohan et al., 2014; Portes et al., 2016; Rice et al., 2016; Reddy et al., 2017), PbH**26** and PbH**27** were chosen to be ligands for the synthesis of four Zn(II) and Cu(II) complexes that were subsequently tested against *T. brucei*. The complexes were synthesized by combining ligands with zinc acetate and copper acetate, respectively, to give **C1-4**. Complexes were assayed *in vitro,* and two of them displayed significant activity, specifically the two Zn(II) complexes, namely **C1** and **C2**, exhibiting EC_{50} values of 0.169 and 0.084 µM, respectively. Although both demonstrated an activity 3-fold enhanced with respect to their ligands, **C2** proved to be 2-fold more active than **C1**, and for this reason, it was considered for subsequent studies along with its precursor, PbH**27**.

X-ray crystallography studies on PbH**27** and **C2** were carried out to afford a complete characterization of the two active compounds. From this analysis, it was possible to notice that PbH**27** crystallizes in the triclinic space group in the tautomeric form N-H,N-H,C=O, differently from monoclinic complexes previously reported from the zwitterionic form (Marchetti et al., 2005). The bond distance detected for C(3)-O(1) (1.264(3)) was consistent with C=O distances already found for similar pyrazolone-based hydrazones (Zhang et al., 2013). Moreover, N(1)-C(1) and N(2)-C(4) show values of bond distances and angles very similar to C=N double bond. In general, PbH**27** is not planar and is characterized by a C-N-N-C torsion angle of 149.5(2), conferring a peculiar orientation to the hydrazone moiety. From the crystal also, typical intramolecular hydrogen bonds are visible, specifically between the N-H and C=O groups ([N(1)···O(1) and N(1)−H(1a)∠O(1) of 2.670(3) and 139(3)°, respectively). For **C2**, the neutral complex nature was confirmed by the analysis. Oxygen

and nitrogen atoms of both chelated PbH**27** ligands lie in the same plane; plus, Zn-O and Zn-N distances resulted comparable to those measured for similar complexes (Marchetti et al., 2005). Interestingly, **C2** co-crystallizes with a methanol molecule in the asymmetric unit. The Zn-O bonds with the oxygen from the methanol molecule appear elongated when compared to the other Zn-O bonds. Moreover, methanol molecules are responsible for most of the intermolecular interactions of the complex and behave as both hydrogen bond donors and acceptors.

DFT analysis allowed instead to calculate the electronic structures of PbH**27** and **C2**. Density functional theory is a technique that allows to hypothesize the conformation of a molecule and its arrangement in the space by considering its electron density regardless of the orbitals involved in the bonding system (Adams, 2001). From this analysis, tautomer I was found to be the predominant species for PbH**27** in solution; however, in the solid state the observed species was tautomer II. For the study of **C2** electronic conformation, the anionic form of its ligand PbH**27** was studied. The bonding localization of PbH**27**$^-$ was found to be consistent to the deprotonation of tautomer II, with C=O bond shorter than the C-N bond (1.232Å vs 1.303 Å). Finally, the trans disposition of the two methanol molecules bonded to the Zn ion was investigated. The hypothetical **C2** complex missing the two solvent molecules was optimized, as [Zn(PbH**27**)$_2$]. The structure revealed to be unexpectedly square planar; indeed, this conformation is atypical for a d^{10} complex, suggesting that this geometry is adopted to overcome steric issues. A further confirmation was provided by the optimization of [Zn(PbH**27***)$_2$], being PbH**27*** substituted with a methyl group instead of the trifluoromethyl group in *para* position. [Zn(PbH**27***)$_2$] appears tetrahedral and far more stable than the square planar complex. The trifluoromethyl group evidently creates steric hindrance, explaining the adoption of the square planar structure and, therefore, the trans-(MeOH)$_2$ geometrical configuration observed in **C2**.

A better understanding of the mechanisms involved in the antiprotozoal activity of the most effective pyrazolone-based hydrazones was required. For this reason, the first check was for excluding cross resistances. Unfortunately, the resistance phenomenon occurred for most of the currently available drugs used for the treatment of trypanosomiasis. Indeed, being discovered and commercialized decades ago, they became obsolete, and the parasite had the chance to develop mechanisms to evade their action, making them inefficient. Testing compounds on laboratory-developed resistant strains allowed to exclude cross-resistance with pentamidine, diminazene, and suramin, confirming they don't exploit the same processes implemented by the commercial drugs. All compounds showed activity on the multi-resistant strain *T. brucei* B48 and on suramin resistant strain *T. brucei* SUR10 that were comparable with the activity on the wild type *T. brucei*. This was evident from the resistance factors (RFs) ranging from 0.62 to 2.06. RFs are obtained from the ratio between the activity on the

resistant strain and that on the WT strain. If RF results widely superior to 1, the activity of the compound is dramatically lowered in the resistant strain when compared to the effect on the WT, meaning the drug exploits mechanisms for which the parasite already demonstrated resistance. On the other hand, when the RF is below 1, an enhanced sensitivity of the resistant strain to the compound tested is noticeable. Finally, when the RFs are close to the unity (as per the present case), compounds considered potentially act on the parasite without involving any of the current drugs uptake mechanisms and they can be defined not cross-resistant. Cross-resistance was also evaluated for the drugs on animal trypanosomiasis strains, i.e., *T. evansi* and *T. equiperdum*. Being both the veterinary and the human pathology a huge social and economic issue for the African continent, a unique therapy is desirable. Results demonstrate that the compounds from the three pyrazolone-based hydrazone series can be employed even for the treatment of *T. evansi* and *T. equiperdum* infections, exhibiting RFs relatively close to 1.

Due to the sub-micromolar efficacy of PbH**26**, PbH**27**, **C1** and **C2**, the study proceeded focusing on these compounds. First, their activity on *T. brucei* at long exposures was monitored in order to assess their trypanocidal or trypanostatic behavior. PbH**26** and its derived Zn(II) complex **C1** demonstrated a very similar trypanostatic behavior, causing a stop in the growth of cells at both 2 x EC_{50} and 5 x EC_{50}; on the contrary, PbH**27** and **C2** exhibited a trypanocidal effect at both the higher concentrations tested (5 x EC_{50} and 10 x EC_{50}).

Although **C2** appeared to be more active, PbH**27** was considered for mode of action analyses. Indeed PbH**27** is more easily affordable and, presumably, the mechanism by which it exerts antitrypanosomal activity is not different from that of its Zn(II) derivative, **C2**.

PbH**27** was therefore tested at a limited exposure timeframe to evaluate the reversibility of the drug action on the parasite. Some drugs like diamidines act very slowly, but only need a short time to exert their effect (from 1 to 3 hours); even when the exposure to the drug ceases, trypanosomes keep dying, meaning the effect displayed in the very first phases of the exposure is irreversible (Barrett et al., 2007). This peculiarity of diamidines might be helpful in reducing potential toxic effects associated with keeping compounds at peak circulation levels for long timeframes. Unfortunately, from the test performed in the present work, it was evident that PbH**27** acts with a reversible mechanism. Indeed, after a treatment of 24 hours at a concentration of 2 times the EC_{50}, when the cells are no longer exposed to the drug, they start growing again. Evidently, PbH**27** is not kept inside the cell and continuous contact with the parasite is needed for the exhibition of the activity. Thus, to be effective,

the drug needs to remain in circulation for a longer time, or, alternatively, to be administered at higher doses.

In the recent research, many antitrypanosomal classes of compounds revealed to have an influence on the cell cycle, causing alterations or arrest at different stages (Franco, 2020; Cuevas-hernandez et al., 2020, Rodriguez-hernandez et al., 2020; Cuevas-hernandez et al., 2021). To verify if the effective pyrazolone-based hydrazones could cause alterations of the cell cycle, PbH**27** was subjected to flow cytometry. Flow cytometry is a technology that rapidly analyzes single cells as they flow past single or multiple lasers (McKinnon, 2018). In this analysis, cells are stained with a fluorescent DNA dye, namely propidium iodide (PI) which quantitatively binds DNA. DNA amount changes based on the cell cycle phase in which the cell is, and therefore, measuring the fluorescent emission from the cells allows to understand in which stage cells are. Single time-point measurements can show the percentage of G1 cells, S phase cells, and G2 or M phase cells. Since cell cycle phase distribution patterns have been shown to change based on pathological states, flow cytometry was performed on PbH**27** treated cells to verify the correlation of its activity to DNA disturbances. Results showed that PbH**27** generated a stop in the G1-G2 turnover, and cells accumulated in G1 phase already after 6 hours from the first exposure. As a consequence, G2-phase cells appear enhanced. Presumably, the drug interferes in some way with the cell cycle at the very first stage, causing an imbalance in the amounts of parasitic cells in different stages when compared to the untreated ones. However, the increase in the amount of G1 phase cells is not dramatic, thus suggesting that the arrest of the cell cycle is not the primary mechanism of inhibition.

Fluorescence microscopy was then performed to give a visual witness of the cell cycle disturbance. DNA configuration assessment revealed abnormalities in the DNA already after 8 h from the first exposure, with a concomitant decrease in cells in all stages of the cell division process. Damaged DNA appeared irregularly fragmented, making subsequent replication impossible. As expected, the mitochondrion was not involved in the activity of PbH**27**. Indeed, from images captured with Zeiss microscope, it appeared intact, meaning no imbalance in membrane potential is detectable.

Finally, both PbH**27** and **C2** were considered for their nucleotide pools. The attention was focused on the peculiar nucleotide metabolism of *T. brucei*: the parasite is indeed unable to synthesize purines that are therefore recovered from the host, and, to produce pyrimidines, it only relies on a unique *de novo* pathway for the cytidine triphosphate synthesis (CTP) (Hammond and Gutteridge, 1982; Marr and Muller, 1995). CTP synthesis is catalyzed by CTP synthetase (CTPS), on which the parasites depend completely for the production of the nucleotide triphosphate, and therefore represents a key

trypanosome target (Hofer et al., 2001). Cells were treated with PbH**27** and **C2,** and nucleotides and deoxynucleotides were quantified in treated and untreated samples. Results showed that CTP and dCTP amounts are considerably lowered by the treatments; all the other deoxynucleotide pools are enhanced instead. This behavior allowed to assume that the target of the pyrazolone-based hydrazone and its Zn(II) complex could be CTPS. Indeed, as already mentioned, CTPS physiologically catalyzes CTP synthesis from UTP, being the only way to produce CTP in the parasitic cell; the inhibition of this enzyme causes a lowering in CTP amount that subsequently leads to a reduction in dCTP pools; because of low levels of dCTP, DNA synthesis doesn't take place, resulting in a consequent accumulation of all the other deoxynucleotides. The impossibility of synthesizing DNA from DNA polymerase eventually leads to cells death. It was interesting to notice that this effect was observed in both PbH**27** and **C2** treated cells, but in a more pronounced manner for the Zn(II) complex. This finding suggested that there might be a difference in the transport or in the absorption of the drug inside the parasitic cell; possibly, the cation eases the penetration of the drug across the membranes, leading to an enhanced DNA inhibition effect. However, further studies are certainly needed to confirm this hypothesis.

4.4 Conclusion

Research on trypanosomiasis is an ongoing endeavor, marked by the discovery and development of effective drugs. However, numerous challenges persist, including the emergence of drug resistance, the onset of veterinary pathologies, and difficulties related to compliance and administration.

Our study, although preliminary, shed light on a new class of promising compounds in the fight against trypanosomiasis. PbH**26** and PbH**27** emerged as the two most promising antitrypanosomal candidates, along with their Zn(II) complexes **C1** and **C2**. Particularly, PbH**27** and **C2** were studied for their better *in vitro* activity (EC_{50} of 0.295 and 0.084 µM, respectively), trying to investigate and reveal the molecular mechanisms occurring in the parasitic cell. They were found to be safe on mammalian cells, not cross-resistant, and trypanocidal at 5 x EC_{50} and 10 x EC_{50}. Moreover, cells treated with PbH**27** and **C2** were subjected to investigation of DNA disturbances through flow cytometry, and fluorescence microscopy. Analyses revealed an impossibility in carrying DNA synthesis out, with a stop of the cell cycle in G1 phase, and the formation of broken DNA agglomerates. Through an NTP and NDP quantification by HPLC it has been possible to hypothesize that the cause of the alteration of DNA synthesis operated by PbH**27** and, in a more pronounced manner, by **C2**, could be due to the inhibition of CTPS, a pivotal enzyme in the parasitic deoxynucleotide production. The enhanced activity of **C2** on nucleotides with respect to that of

PbH**27** can be explained by the presence of the metal cationic function, which could ease the transport of the molecule inside the cell and facilitate the exhibition of the effect. Further studies on the mechanism of action are needed to confirm these hypotheses.

4.5 Material and methods

All reagents and solvents were purchased from Sigma-Aldrich Chemical Co, were analytical grade and were used as received. Thin layer chromatography (TLC) was run on silica gel 60 F254 plates. Analogs (PbH**1-36**), and **C1** and **C2** were characterized by ^{1}H NMR, ^{13}C NMR, and ESI-MS. For **C3** and **C4** ^{1}H-NMR and ^{13}C-NMR analysis was not possible, and IR and UV-Vis analyses were performed. Precursors and intermediates were characterized only by ^{1}H NMR and ESI-MS analyses.

^{1}H-NMR and ^{13}C-NMR spectra were recorded a 500 Bruker Ascend (500 MHz for ^{1}H and 125 MHz for ^{13}C) instrument operating at room temperature. The chemical shift values are expressed in δ values (ppm) and coupling constants (*J*) are in Hertz; tetramethylsilane (TMS) was used as an internal standard. Proton chemical data are reported as follows: chemical shift, multiplicity (s = singlet, d = doublet, dd = doublet of doublets, pd = pseudo doublet, t = triplet, dt = doublet of triplets, pt = pseudo triplet, q = quartet, dq = doublet of quartets, pq = pseudo quartet, m = multiplet, br s = broad singlet) coupling constant(s), integration. The presence of all exchangeable protons was confirmed by the addition of D_2O. ^{1}H-NMR and ^{13}C-NMR spectra were assigned with the aid of {^{1}H-^{1}H} COSY, {^{1}H-^{13}C} HSQC and {^{1}H-^{13}C} HMBC NMR techniques. Indirect ^{15}N NMR chemical shifts were assigned based on the {^{1}H–^{15}N}-HSQC and {^{1}H–^{15}N}-HMBC NMR techniques. Mass spectra were recorded on an HP 1100 series instrument. Measurements were performed in the positive or negative ion mode as indicated (+ or -), using atmospheric pressure electrospray ionization (API-ESI). Elemental analyses (C, H, and N) were determined on ThermoFisher Scientific FLASH 2000 CHNS analyzer and are within 0.4% of theoretical values.

4.5.1 Synthesis of the three series of pyrazolone-based hydrazones

*3-methyl-1-phenylpyrazolin-5-(4H)-one (**3**)*

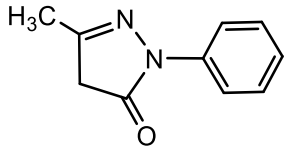

Ethyl acetoacetate (**1**) (3.07 g, 23.6 mmol) and phenyl hydrazine (**2**) (14 mL, 12.72 g, 0.117 mmol) were combined in methanol, and a catalytic amount of acetic acid was added dropwise. Reaction mixture was

heated to reflux and left stirring for 2 hours. A solid white-pink precipitate formed and was washed with 100 mL of diethyl ether. The suspension was filtered, and the solid crystallized with hot methanol, affording a white crystalline powder (3.9 g, 95% yield).

^{1}H NMR ($CDCl_3$) δ: 2.19 (s, 3H), 3.42 (s, 2H), 7.19-7.16 (t, *J* = 7.6 Hz, 1H), 7.41-7.37 (t, *J* = 5.6 Hz, 2H), 7.87-7.85 (d, *J* = 6.6 Hz, 2H).

ESI-MS (−) CH_3OH (m/z, relative intensity %): 175.11 [100].

1-(5-hydroxy-3-methyl-1-phenyl-1H-pyrazol-4-yl)-2-phenylmethan-1-one (PP), 1-(5-hydroxy-3-methyl-1-phenyl-1H-pyrazol-4-yl)-2-benzylmethan-1-one (BP) and 1-(5-hydroxy-3-methyl-1-phenyl-1H-pyrazol-4-yl)-2-tiophenylmethan-1-one (TP)

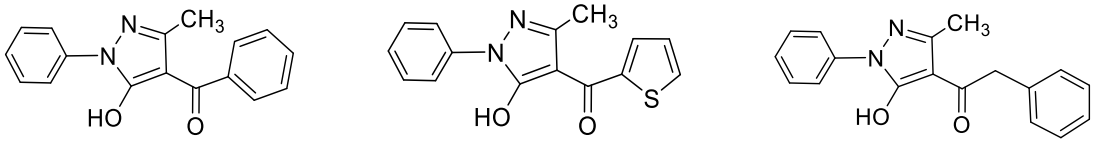

PP TP BP

3-methyl-1-phenylpyrazolin-5-(4H)-one (**3**) was dissolved in 60 mL of dry pyridine and put in ice. Calcium hydroxide (12.5 g, 167 mmol) was added. Subsequently proper acyl chloride was added dropwise. Acyl chlorides used were benzoyl chloride for PP (12.51g, 89 mmol); thiophen-2-carbonyl chloride for TP (13.04g, 89 mmol) and phenylacetyl chloride for BP (13.75g, 89 mmol). The reaction mixtures were kept in ice and stirred for 24 hours. 300 mL of HCl 2N were added, and the precipitates that were obtained were rinsed with water. Products were obtained as light brown, red-brown, and brown powders (for PP, TP and BP, respectively) soluble in alcohols, acetone, acet onitrile, DMSO, and chlorinated solvents. Yields for PP, TP and BP were 57% (14.12g), 64% (16.20 g) and 78% (20.29 g), respectively.

PP:

^{1}H NMR ($CDCl_3$) δ: 2.11 (s, 3H), 7.24 - 7.37 (m, 1H), 7.41 - 7.58 (m, 4H), 7.51 - 7.64 (m, 1H), 7.67 - 7.73 (m, 2H), 7.85 - 7.94 (m, 2H), 11.2 (br s, OH).

ESI-MS (−) CH_3OH (m/z, relative intensity %): 278.3 [100].

TP:

^{1}H-NMR ($CDCl_3$) δ: 2.43 (s, 3H), 7.17 (d, *J* = 8.4 Hz, 1H), 7.29 (t, *J* = 8.2 Hz, 1H), 7.47 (t, *J* = 7.6 Hz, 2H), 7.72 (t, *J* = 8.6 Hz, 1H), 7.74 (d, *J* = 8.6 Hz, 1H), 7.84 (d, *J* = 8.6 Hz, 2H), 12.1 (br s, OH).

ESI-MS (−) CH_3OH (m/z, relative intensity %): 283.3 [100].

BP:

^{1}H NMR ($CDCl_3$) δ: 2.53 (s, 3H), 4.09 (s, 2H) 7.12–7.48 (m, 4H), 7.82 (d, *J* = 8.6 Hz, 6H) 10.6, (br s, OH).

ESI-MS (−) CH_3OH (m/z, relative intensity %): 291.3 [100].

*General procedure for the synthesis of PbH **1-36***

The pyrazolone-based hydrazones were synthesized following the method previously reported (Marchetti et al., 2015). A mixture of the appropriate precursor (1.0 equiv) and the appropriate hydrazine (1.0 equiv) in methanol (10 mL) containing 5−10 drops of glacial acetic acid was heated to 80 °C, and the reaction was monitored by TLC ($CHCl_3$/MeOH 96:4 v/v). Precipitates slowly formed from the hot solutions, and after completion, the reaction mixtures were placed at 4°C overnight. The obtained precipitates were filtered, redissolved in ethanol (10 mL), and recrystallized from slow evaporation of the solutions, to give variously colored solids which were collected by filtration and dried to constant weight.

Phenyl series

*2-((5-hydroxo-3-methyl-1-phenyl-1H-pyrazol-4-yl)(phenyl)methylene)-1-phenylhydrazine) (PbH**01**)*

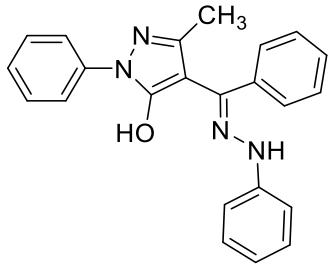

PP (1 g, 3.59 mmol) and phenylhydrazine (350 µL, 3.56 mmol, d = 1.099 g/mL) were combined in methanol (50 mL) as described in the general procedure. PbH**01** was afforded as a yellow solid with a yield of 1.158 g (89%).

Anal. Calc. for $C_{23}H_{20}N_4O$; C, 74.98; H, 5.47; N, 15.21%; found: C, 75.34; H, 5.75; N, 15.67%.

^{1}H NMR ($CDCl_3$) δ: 1.52 (s, 3H), 6.83 (t, *J* = 7.3 Hz, 1H), 6.96 (s, 1H), 7.17 (t, *J* = 7.4 Hz, 2H), 7.42 (m, 5H), 7.68 (t, *J* = 7.5 Hz, 2H), 7.73 (t, *J* = 7.2 Hz, 1H), 7.80 (t, *J* = 7.6 Hz, 1H), 8.05 (d, *J* = 7.7 Hz, 2H), 12.62 (br s, OH).

^{13}C NMR ($CDCl_3$) δ: 26.8 (s, CH_3), 122.5, 126.2, 128.8, 129.2, 129.3, 131.0, 132.9, 137.5 (C of C_6H_5(C=N) and C_6H_5(N)), 113.9, 122.4, 129.5, 143.0 (C of C_6H_5(NH)), 104.0 (s, C3), 151.3 (s, C4), 160.5 (s, C5), 155.6 (s, C=N).

ESI-MS (−) CH_3OH (m/z, relative intensity %): 368.4 [100].

*2-((5-hydroxo-3-methyl-1-phenyl-1H-pyrazol-4-yl)(phenyl)methylene)-1-(2-pyridin)hydrazine) (PbH**02**)*

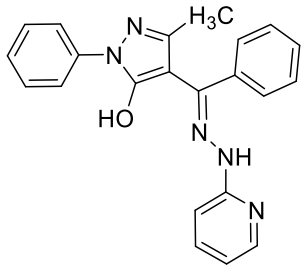

PbH**02** was afforded by the reaction of PP (385 mg, 1.387 mmol) and pyridine hydrazine (150 mg, 1.374 mmol) at conditions described in the general procedure. The final product appeared as a brown-yellow solid with a yield of 0.333 g (65%).

Anal. Calc. for $C_{22}H_{19}N_5O$; C, 71.53; H, 5.18; N, 18.96%; found: C, 72.35; H, 5.33; N, 19.44%.

^{1}H NMR ($CDCl_3$) δ: 1.52 (s, 3H), 6.64 (d, *J* = 6.9 Hz, 1H), 6.73 (t, *J* = 6.6 Hz, 1H), 7.47 (t, *J* = 8.0 Hz, 1H), 7.50 (m, 2H), 7.52 (m, 2H), 7.54 (m, 2H), 7.55 (t, *J* = 7.5 Hz, 1H), 7.81 (d, *J* = 8.3 Hz, 2H), 7.91 (d, *J* = 5.9 Hz, 2H), 8.04 (d, *J* = 6.9 Hz, 1H), 12.17 (br s, OH).

^{13}C NMR ($CDCl_3$) δ: 26.8 (s, CH_3), 122.5, 126.2, 128.8, 129.2, 129.3, 131.0, 132.9, 137.5 (C of C_6H_5(C=N) and C_6H_5(N)), 108.9, 117.9, 138.3, 148.1, 153.0 (C of C_5H_4N(NH)), 104.0 (s, C3), 151.3 (s, C4), 159.3 (s, C5), 155.6 (s, C=N).

ESI-MS (−) CH_3OH (m/z, relative intensity %): 369.4 [100].

*2-((5-hydroxo-3-methyl-1-phenyl-1H-pyrazol-4-yl)(phenyl)methylene)-1-(trifluormeth-4-yl)phenylhydrazine) (PbH**03**)*

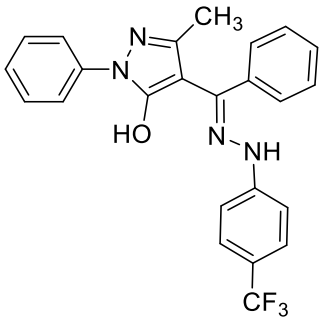

The same reaction was performed to obtain PbH**03** using 700 mg of PP (2.515 mmol) and 438 mg of 4-(trifluoromethyl)phenylhydrazine (2.49 mmol) in methanol (50 mL). The product precipitated as a yellow-brown powder (yield: 0.620 g, 57%).

Anal. Calc. for $C_{24}H_{19}N_4OF_3$; C, 66.05; H, 4.39; N, 12.84%; found: C, 65.61; H, 4.31; N, 13.08%.

^{1}H NMR ($CDCl_3$) δ: 1.87 (s, 3H), 6.28 (d, *J* = 8.3 Hz, 1H), 7.55 (m, 8H), 7.72 (d, *J* = 7.8 Hz, 2H), 7.79 (d, *J* = 8.1 Hz, 2H), 8.00 (d, *J* = 8.1 Hz, 1H), 8.86 (s, 1H), 11.91 (br s, OH).

^{13}C NMR ($CDCl_3$) δ: 26.8 (s, CH_3), 122.5, 126.2, 128.8, 129.2, 129.3, 131.0, 132.9, 137.5 (C of C_6H_5(C=N) and C_6H_5(N)), 116.6, 120.3, 124.2, 126.5, 148.1 (C of C_5H_4N(NH)), 124.1 (s, CF_3), 104.0 (s, C3), 151.3 (s, C4), 159.3 (s, C5), 155.6 (s, C=N).

ESI-MS (−) CH_3OH (m/z, relative intensity %): 436.4 [100].

*2-((5-hydroxo-3-methyl-1-phenyl-1H-pyrazol-4-yl)(phenyl)methylene)-1-(4-cyano)phenylhydrazine) (PbH**04**)*

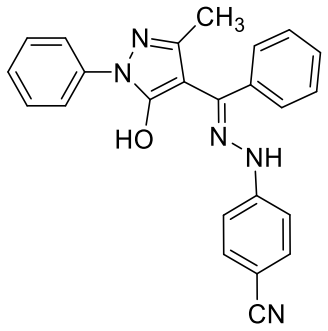

PP (250 mg, 0.898 mmol) and cyanophenylhydrazine (151 mg, 0.890 mmol) were combined in 15 mL of methanol as described in the general procedure, to give PbH**04** as a yellow solid (0.088 g, 25% yield).

Anal. Calc. for $C_{24}H_{19}N_5O$; C, 73.27; H, 4.87; N, 17.80%; found: C, 73.57; H, 5.11; N, 17.56%.

^{1}H NMR ($CDCl_3$) δ: 1.37 (s, 3H), 6.58 (s, 2H), 7.15 (s, 2H), 7.18 (t, *J* = 7.4 Hz, 1H), 7.34 (m, 6H), 7.66 (t, *J* = 7.4 Hz, 1H), 7.95 (d, *J* = 8.6 Hz, 3H), 12.40 (br s, OH).

^{13}C NMR ($CDCl_3$) δ: 26.8 (s, CH_3), 122.5, 126.2, 128.8, 129.2, 129.3, 131.0, 132.9, 137.5 (C of C_6H_5(C=N) and C_6H_5(N)), 102.6, 117.2, 119.1, 147.4 (C of C_5H_4N(NH)), 118.6 (C≡N), 104.0 (s, C3), 151.3 (s, C4), 159.3 (s, C5), 155.6 (s, C=N).

ESI-MS (−) CH_3OH (m/z, relative intensity %): 393.5 [100].

*2-((5-hydroxo-3-methyl-1-phenyl-1H-pyrazol-4-yl)(phenyl)methylene)-1-hydrazinil)benzoic acid (PbH**05**)*

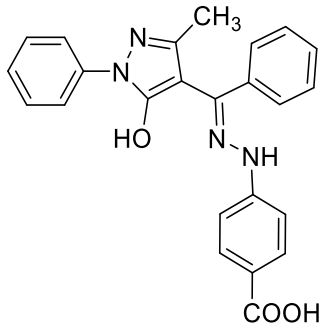

PP (400 mg, 1.437 mmol) and 4-(hydrazine)benzoic acid (216 mg, 1.419 mmol) were combined in methanol (17 mL) as described in the general procedure. PbH**05** was obtained as a white solid with a yield of 0.456 g (78%).

Anal. Calc. for $C_{24}H_{20}N_4O_3$; C, 69.89; H, 4.89; N, 13.58%; found: C, 70.44; H, 4.29; N, 13.67%.

^{1}H NMR ($CDCl_3$) δ: 1.41 (s, 3H), 6.74 (d, *J* = 8.7 Hz, 2H), 7.18 (t, *J* = 14.6 Hz, 1H), 7.38 (t, *J* = 15.5 Hz, 2H), 7.48 (m, 4H), 7.81 (m, 3H), 8.01 (d, *J* = 7.8 Hz, 2H), 8.90 (s, 1H), 11.95 (br s, COOH) 12.42 (br s, OH).

^{13}C NMR ($CDCl_3$) δ: 26.8 (s, CH_3), 122.5, 126.2, 128.8, 129.2, 129.3, 131.0, 132.9, 137.5 (C of C_6H_5(C=N) and C_6H_5(N)), 115.6, 120.2, 131.3, 148.2 (C of C_6H_5(NH)), 104.0 (s, C3), 151.3 (s, C4), 159.3 (s, C5), 155.6 (s, C=N), 169.3 (COOH).

ESI-MS (−) CH_3OH (m/z, relative intensity %): 412.5 [100].

*2-((5-hydroxo-3-methyl-1-phenyl-1H-pyrazol-4-yl)(phenyl)methylene)-1-(4-methoxy)phenylhydrazine) (PbH**06**)*

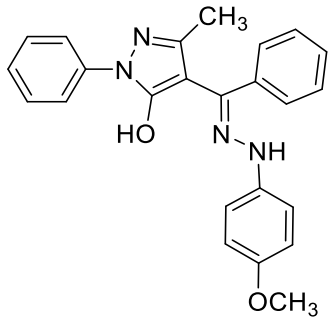

PbH**06** was afforded by the reaction of PP (250 mg, 0.899 mmol) and 4-(methoxy)phenyl hydrazine (155 mg, 0.887 mmol) at conditions described in the general procedure. The final product appeared as a yellow solid with a yield of 0.144 g (41%).

Anal. Calc. for $C_{24}H_{22}N_4O_2$; C, 72.34; H, 5.57; N, 14.06%; found: C, 72.47; H, 5.77; N, 14.35%.

^{1}H NMR ($CDCl_3$) δ: 1.37 (s, 3H), 3.78 (s, 3H), 6.62 (s, 2H), 7.13 (m, 3H), 7.19 (m, 2H), 7.47 (t, *J* = 7.4 Hz, 5 H), 7.51 (t, *J* = 7.5 Hz, 1H), 7.89 (d, *J* = 7.9 Hz, 2H), 12.42 (br s, OH).

^{13}C NMR ($CDCl_3$) δ: 26.5 (s, CH_3), 55.8 (OCH_3), 122.5, 126.2, 128.8, 129.2, 129.3, 131.0, 132.9, 137.5 (C of C_6H_5(C=N) and C_6H_5(N)), 115.6, 117.3, 135.6, 153.4 (C of C_6H_5(NH)), 104.0 (s, C3), 151.3 (s, C4), 159.3 (s, C5), 156.0 (s, C=N).

ESI-MS (−) CH_3OH (m/z, relative intensity %): 398.5 [100].

*2-((5-hydroxo-3-methyl-1-phenyl-1H-pyrazol-4-yl)(phenyl)methylene)-1-(4-nitro)phenylhydrazine) (PbH**07**)*

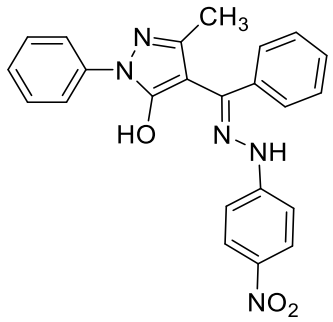

PbH**07** was synthesized by reaction of PP (700 mg, 2.515 mmol) and 4-nitrophenylhydrazine (472 mg, 2.49 mmol) in methanol (40 mL) as previously described. The product appeared as a brownish solid (yield 0.610 g, 59%).

Anal. Calc. for $C_{23}H_{19}N_5O_3$; C, 66.82; H, 4.63; N, 16.94%; found: C, 66.24; H, 4.91; N, 16.55%.

^{1}H NMR ($CDCl_3$) δ: 1.47 (s, 3H), 6.72 (s, 1H), 6.87 (d, *J* = 6.8 Hz, 2H), 7.14 (t, *J* = 7.3 Hz, 1H), 7.22 (t, *J* = 7.4 Hz, 1H), 7.43 (m, 4H), 7.66 (d, *J* = 7 Hz, 1H), 7.91 (d, *J* = 8 Hz, 1H), 7.97 (d, *J* = 8.3 Hz, 1H), 8.02 (d, *J* = 9.2 Hz, 1H), 8.13 (d, *J* = 9.3 Hz, 1H), 9.43 (s, 1H), 11.92 (br s, OH).

^{13}C NMR ($CDCl_3$) δ: 26.8 (s, CH_3), 122.5, 126.2, 128.8, 129.2, 129.3, 131.0, 132.9, 137.5 (C of C_6H_5(C=N) and C_6H_5(N)), 113.6, 124.8, 138.1, 149.1 (C of C_6H_5(NH)), 104.0 (s, C3), 151.3 (s, C4), 159.3 (s, C5), 155.6 (s, C=N).

ESI-MS (−) CH_3OH (m/z, relative intensity %): 413.4 [100].

*2-((5-hydroxo-3-methyl-1-phenyl-1H-pyrazol-4-yl)(phenyl)methylene)-1-(3-nitro)phenylhydrazine) (PbH**08**)*

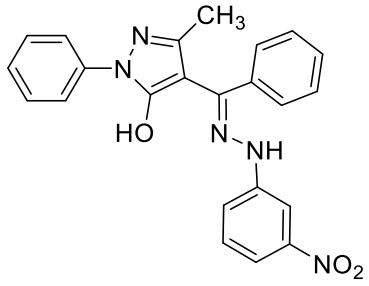

PP (350 mg, 1.258 mmol) and 3-nitrophenylhydrazine (236 mg, 1.245 mmol) were combined in 20 mL of methanol as described in general procedure, to give PbH**08** as a yellow solid (0.180 g, 35% yield).

Anal. Calc. for $C_{23}H_{19}N_5O_3$; C, 66.82; H, 4.63; N, 16.94%; found: C, 66.77; H, 4.53; N, 17.02%.

^{1}H NMR ($CDCl_3$) δ: 1.43 (s, 3H), 6.65 (s, 2H), 7.16 (s, 2H), 7.42 (t, *J* = 7.3 Hz, 2H), 7.43 (m, 3H), 7.55 (t, *J* = 7.5 Hz, 1H), 7.65 (t, *J* = 8.1 Hz, 1H), 8.01 (t, *J* = 8 Hz, 2H), 8.15 (s, 1H), 8.26 (d, *J* = 8.2 Hz, 1H), 12.52 (br s, OH).

^{13}C NMR ($CDCl_3$) δ: 26.8 (s, CH_3), 122.5, 126.2, 128.8, 129.2, 129.3, 131.0, 132.9, 137.5 (C of C_6H_5(C=N) and C_6H_5(N)), 109.3, 114.3, 120.2, 130.5, 144.1, 148.8 (C of C_6H_5(NH)), 104.0 (s, C3), 151.3 (s, C4), 159.3 (s, C5), 155.6 (s, C=N).

ESI-MS (−) CH_3OH (m/z, relative intensity %): 413.4 [100].

*2-((5-hydroxo-3-methyl-1-phenyl-1H-pyrazol-4-yl)(phenyl)methylene)-1-(2,4-dinitro)phenylhydrazine) (PbH**09**)*

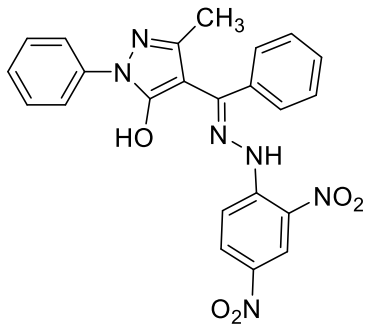

PbH**09** was afforded by the reaction of PP (800 mg, 2.874 mmol) and 2,4-dinitrophenylhydrazine (563 mg, 2.846 mmol) in 40 mL of methanol, at conditions described in the general procedure. The final product appeared as a red solid with a yield of 0.992 g (76%).

Anal. Calc. for $C_{23}H_{18}N_6O_5$; C, 60.26; H, 3.96; N, 18.33%; found: C, 60.24; H, 4.11; N, 18.54%.

^{1}H NMR ($CDCl_3$) δ: 1.43 (s, 3H), 6.65 (s, 2H), 6.78 (s, 1H), 7.16 (s, 2H), 7.42 (t, *J* = 7.3 Hz, 2H), 7.43 (m, 1H), 7.55 (t, *J* = 7.5 Hz, 1H), 7.65 (t, *J* = 8.1 Hz, 1H), 8.01 (d, *J* = 8 Hz, 2H), 8.15 (s, 1H), 8.26 (d, *J* = 8.2 Hz, 1H), 12.52 (br s, OH).

^{13}C NMR ($CDCl_3$) δ: 26.8 (s, CH_3), 122.5, 126.2, 128.8, 129.2, 129.3, 131.0, 132.9, 137.5 (C of C_6H_5(C=N) and C_6H_5(N)), 116.6, 123.3, 129.2, 130.7, 138.1, 145.4 (C of C_6H_5(NH)), 104.0 (s, C3), 151.3 (s, C4), 159.3 (s, C5), 155.6 (s, C=N).

ESI-MS (−) CH_3OH (m/z, relative intensity %): 458.4 [100].

*2-((5-hydroxo-3-methyl-1-phenyl-1H-pyrazol-4-yl)(phenyl)methylene)-1-(4-fluoro)phenylhydrazine) (PbH**10**)*

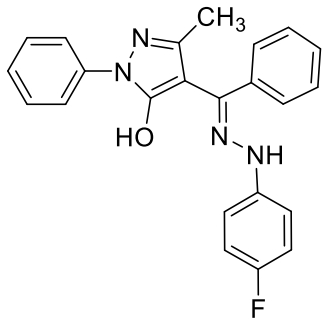

PP (350 mg, 1.258 mmol) and 4-fluorophenylhydrazine (202 mg, 1.245 mmol) were combined in methanol (20 mL) as described in the general procedure. PbH**10** was obtained as a yellow solid with a yield of 0.293 g (61%).

Anal. Calc. for $C_{23}H_{19}N_4OF$; C, 71.49; H, 4.96; N, 14.50%; found: C, 71.35; H, 5.18; N, 14.35%.

^{1}H NMR ($CDCl_3$) δ: 1.86 (s, 3H), 6.72 (s, 1H), 7.13 (s, 1H), 7.26 (t, *J* = 7.4 Hz, 3H), 7.44 (m, 6H), 7.52 (t, *J* = 7.5 Hz, 2H), 8.00 (d, *J* = 8 Hz, 2H), 12.52 (br s, OH).

^{13}C NMR ($CDCl_3$) δ: 26.8 (s, CH_3), 122.5, 126.2, 128.8, 129.2, 129.3, 131.0, 132.9, 137.5 (C of C_6H_5(C=N) and C_6H_5(N)), 115.6, 116.3, 138.1, 157.2 (C of C_6H_5(NH)), 104.0 (s, C3), 151.3 (s, C4), 159.3 (s, C5), 155.6 (s, C=N).

ESI-MS (−) CH_3OH (m/z, relative intensity %): 386.4 [100].

*2-((5-hydroxo-3-methyl-1-phenyl-1H-pyrazol-4-yl)(phenyl)methylene)-1-(4-chloro)phenylhydrazine) (PbH**11**)*

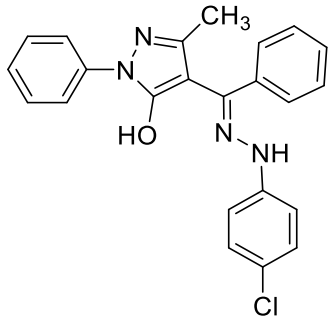

PbH**11** was synthesized by reaction of PP (250 mg, 0.898 mmol) and 4-chlorophenylhydrazine (170 mg, 0.949 mmol) in methanol (13 mL) as previously described. The product appeared as a yellow solid (yield 0.141g, 37%).

Anal. Calc. for $C_{23}H_{19}N_4OCl$; C, 68.57; H, 4.75; N, 13.91%; found: C, 68.24; H, 4.88; N, 13.14%.

^{1}H NMR ($CDCl_3$) δ: 1.33 (s, 3H), 6.61 (s, 1H), 7.17 (s, 2H), 7.19 (t, *J* = 7.4 Hz, 1H), 7.34 (m, 6H), 7.58 (t, *J* = 8.7 Hz, 1H), 7.62 (t, *J* = 8.7 Hz, 2H), 7.94 (d, *J* = 8 Hz, 2H), 12.43 (br s, OH).

^{13}C NMR ($CDCl_3$) δ: 26.8 (s, CH_3), 122.5, 126.2, 128.8, 129.2, 129.3, 131.0, 132.9, 137.5 (C of C_6H_5(C=N) and C_6H_5(N)), 117.6, 127.3, 129.5, 141.2 (C of C_6H_5(NH)), 104.0 (s, C3), 151.3 (s, C4), 159.3 (s, C5), 155.6 (s, C=N).

ESI-MS (−) CH_3OH (m/z, relative intensity %): 402.1 [100].

*2-((5-hydroxo-3-methyl-1-phenyl-1H-pyrazol-4-yl)(phenyl)methylene)-1-(4-bromo)phenylhydrazine) (PbH**12**)*

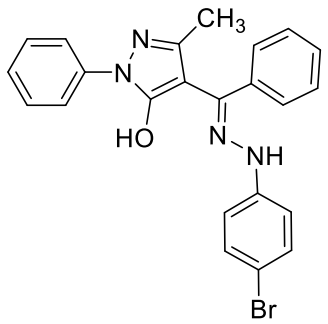

PbH**12** was afforded by the reaction of PP (250 mg, 0.899 mmol) and 4-bromophenylhydrazine (200 mg, 0.895 mmol) at conditions described in the general procedure. The final product appeared as a pale yellow solid with a yield of 0.222 g (55%).

Anal. Calc. for $C_{23}H_{19}N_4OBr$; C, 61.76; H, 4.28; N, 15.52%; found: C, 62.14; H, 4.67; N, 15.35%.

^{1}H NMR ($CDCl_3$) δ: 1.33 (s, 3H), 6.63 (s, 1H), 7.13 (s, 2H), 7.21 (t, *J* = 8.6 Hz, 1H), 7.33 (m, 6H), 7.56 (t, *J* = 8.6 Hz, 1 H), 7.66 (d, *J* = 8.6 Hz, 2H), 7.96 (d, *J* = 7.9 Hz, 2H), 12.42 (br s, 1H, OH).

^{13}C NMR ($CDCl_3$) δ: 26.8 (s, CH_3), 122.5, 126.2, 128.8, 129.2, 129.3, 131.0, 132.9, 137.5 (C of C_6H_5(C=N) and C_6H_5(N)), 116.8, 117.0, 133.2, 141.9 (C of C_6H_5(NH)), 104.0 (s, C3), 151.3 (s, C4), 159.3 (s, C5), 155.6 (s, C=N).

ESI-MS (−) CH_3OH (m/z, relative intensity %): 447.3 [100].

Thiophene series

*2-((5-hydroxo-3-methyl-1-phenyl-1H-pyrazol-4-yl)(thiophenyl)methylene)-1-phenylhydrazine) (PbH**13**)*

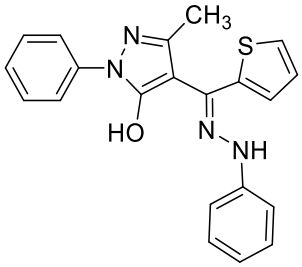

TP (300 mg, 1.055 mmol) and phenylhydrazine (104 µL, 1.066 mmol, d =1.099 g/mL) were combined in 20 mL of methanol at the conditions reported in the general procedure. PbH**13** precipitated as a brownish solid from the reaction mixture, accounting for 0.292 g (74%).

Anal. Calc. for $C_{21}H_{18}N_4OS$; C, 67.36; H, 4.85; N, 14.86%; found: C, 66.94; H, 5.04; N, 14.67%.

^{1}H NMR ($CDCl_3$) δ: 1.83 (s, 3H), 6.53 (s, 1H), 7.01 (t, *J* = 8.5 Hz, 1H), 7.06 (t, 1H), 7.15 (d, *J* = 7.7 Hz, 1H), 7.31 (t, *J* = 7.7 Hz, 2H), 7.34 (d, *J* = 8.6 Hz, 2H), 7.53 (d, *J* = 8.4 Hz, 1H), 7.54 (t, *J* = 8.6 Hz, 1H), 7.57 (m, 2H), 7.92 (d, *J* = 8.5 Hz, 2H), 11.61 (br s, 1H, OH).

^{13}C NMR ($CDCl_3$) δ: 26.8 (s, CH_3), 122.5, 124.4, 125.8, 126.2, 127.2, 127.4, 129.4, 137.4 (C of C_4H_3S(C=N) and C_6H_5(N)), 113.8, 122.4, 129.5, 143.0 (C of C_6H_5(NH)), 104.0, 151.3, 159.3 (C of pyrazolyl), 155.6 (s, C=N).

ESI-MS (−) CH_3OH (m/z, relative intensity %): 373.5 [100].

*2-((5-hydroxo-3-methyl-1-phenyl-1H-pyrazol-4-yl)(thiophenyl)methylene)-1-(2-pyridin)hydrazine) (PbH**14**)*

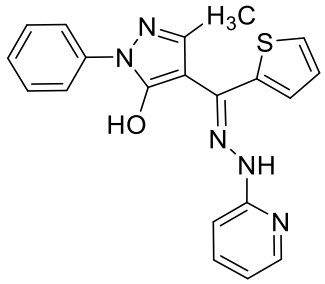

PbH**14** was afforded by the reaction of TP (300 mg, 1.055 mmol) and 2-pyridyl-hydrazine (115 mg, 1.066 mmol) in 25 mL of methanol as previously reported. The final product appeared as a yellow-brown solid (yield 0.204 g, 54%).

Anal. Calc. for $C_{20}H_{17}N_5OS$; C, 63.98; H, 4.56; N, 18.65%; found: C, 64.04; H, 4.73; N, 18.47%.

^{1}H NMR ($CDCl_3$) δ: 1.81 (s, 3H), 6.93 (t, *J* = 7.8 Hz, 1H), 7.08 (t, *J* = 8.5 Hz, 1H), 7.16 (t, *J* = 7.8 Hz, 3H), 7.41 (t, *J* = 8.5 Hz, 3H), 7.59 (d, *J* = 8.6 Hz, 1H), 7.76 (t, *J* = 8.5 Hz, 1H), 7.96 (m, 4H).

^{13}C NMR ($CDCl_3$) δ: 26.8 (s, CH_3), 122.5, 124.4, 125.8, 126.2, 127.2, 127.4, 129.4, 137.4 (C of C_4H_3S(C=N) and C_6H_5(N)), 108.8, 117.9, 138.2, 148.3, 152.9 (C of C_5H_4N(NH)), 104.0, 151.3, 159.3 (C of pyrazolyl), 155.6 (s, C=N).

ESI-MS (−) CH_3OH (m/z, relative intensity %): 374.4 [100].

*2-((5-hydroxo-3-methyl-1-phenyl-1H-pyrazol-4-yl)(thiophenyl)methylene)-1-(trifluormeth-4-yl)phenylhydrazine) (PbH**15**)*

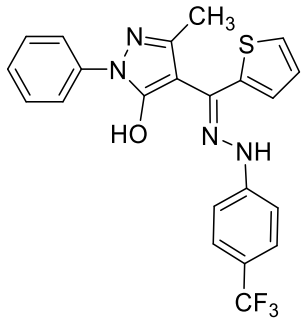

PbH**15** was synthesized by reaction of TP (300 mg, 1.055 mmol) and 4-(trifluoromethyl)phenylhydrazine (187 mg, 1.066 mmol) in methanol (25 mL) as previously described. The product appeared as a brownish solid (yield 0.420 g, 90%).

Anal. Calc. for $C_{22}H_{17}N_4OSF_3$; C, 59.72; H, 3.87; N, 12.66%; found: C, 59.16; H, 4.07; N, 12.67%.

^{1}H NMR ($CDCl_3$) δ: 1.82 (s, 3H), 6.53 (s, 1H), 7.01 (t, *J* = 8.5 Hz, 1H), 7.15 (d, *J* = 7.8 Hz, 1H), 7.41 (d, *J* = 7.9 Hz, 2H), 7.51 (t, *J* = 8.4 Hz, 1H), 7.53 (d, *J* = 8.4 Hz, 1H), 7.54 (t, *J* = 8.6 Hz, 2H), 7.77 (d, *J* = 8.6 Hz, 2H), 7.92 (d, *J* = 7.9 Hz, 2H), 12.01 (br s, 1H, OH).

^{13}C NMR ($CDCl_3$) δ: 26.8 (s, CH_3), 122.5, 124.4, 125.8, 126.2, 127.2, 127.4, 129.4, 137.4 (C of C_4H_3S(C=N) and C_6H_5(N)), 116.8, 120.4, 126.5, 146.2 (C of C_6H_4(NH)), 124.1 (CF_3), 104.0, 151.3, 159.3 (C of pyrazolyl), 155.6 (s, C=N).

ESI-MS (−) CH_3OH (m/z, relative intensity %): 441.4 [100].

*2-((5-hydroxo-3-methyl-1-phenyl-1H-pyrazol-4-yl)(thiophenyl)methylene)-1-(4-cyano)phenylhydrazine) (PbH**16**)*

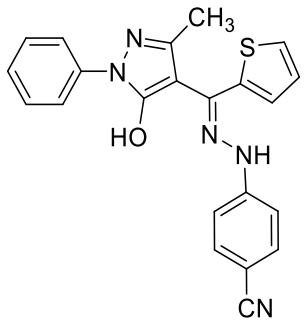

TP (300 mg, 1.055 mmol) and 4-cyanophenylhydrazine (180 mg, 1.066 mmol) were combined in methanol (30 mL) as described in the general procedure. PbH**16** was obtained as a yellow solid with a yield of 0.230 g (55%).

Anal. Calc. for $C_{22}H_{17}N_5OS$; C, 66.15; H, 4.29; N, 17.53%; found: C, 66.73; H, 4.68; N, 17.67%.

^{1}H NMR ($CDCl_3$) δ: 1.87 (s, 3H), 6.53 (s, 1H), 7.01 (t, *J* = 8.5 Hz, 1H), 7.15 (d, *J* = 7.8 Hz, 1H), 7.51 (t, *J* = 8.4 Hz, 1H), 7.53 (d, *J* = 8.4 Hz, 1H), 7.54 (t, *J* = 8.6 Hz, 2H), 7.68 (d, *J* = 8.5 Hz, 2H), 7.79 (d, *J* = 8.6 Hz, 2H), 7.92 (d, *J* = 7.9 Hz, 2H), 12.01 (br s, 1H, OH).

^{13}C NMR ($CDCl_3$) δ: 26.8 (s, CH_3), 122.5, 124.4, 125.8, 126.2, 127.2, 127.4, 129.4, 137.4 (C of C_4H_3S(C=N) and C_6H_5(N)), 102.8, 116.9, 118.8, 147.4 (C of C_6H_4(NH)), 118.5 (C≡N), 104.0, 151.3, 159.3 (C of pyrazolyl), 155.6 (s, C=N).

ESI-MS (−) CH_3OH (m/z, relative intensity %): 398.5 [100].

*2-((5-hydroxo-3-methyl-1-phenyl-1H-pyrazol-4-yl)(thiophenyl)methylene)-1-hydrazinyl)phenylic acid (PbH**17**)*

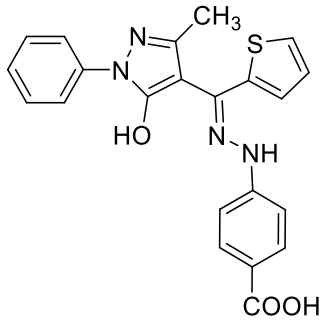

PbH**17** was afforded by the reaction of TP (300 mg, 1.055 mmol) and 4-hydrazinobenzoic acid (162 mg, 1.066 mmol) in 30 mL of methanol as previously reported. The final product appeared as a yellow solid (yield 0.232 g, 53%).

Anal. Calc. for $C_{22}H_{18}N_4O_3S$; C, 63.14; H, 4.34; N, 13.39%; found: C, 36.87; H, 4.46; N, 13.73%.

^{1}H NMR ($CDCl_3$) δ: 1.85 (s, 3H), 6.53 (s, 1H), 7.01 (t, *J* = 8.5 Hz, 1H), 7.15 (d, *J* = 7.8 Hz, 1H), 7.51 (t, *J* = 8.4 Hz, 1H), 7.53 (d, *J* = 8.4 Hz, 1H), 7.54 (t, *J* = 8.6 Hz, 2H), 7.71 (d, *J* = 8.6 Hz, 2H), 7.92 (d, *J* = 7.9 Hz, 2H), 8.28 (d, *J* = 8.5 Hz, 2H), 12.01 (br s, 1H, OH), 13 (br s, 1H, COOH).

^{13}C NMR ($CDCl_3$) δ: 26.8 (s, CH_3), 122.5, 124.4, 125.8, 126.2, 127.2, 127.4, 129.4, 137.4 (C of C_4H_3S(C=N) and C_6H_5(N)), 114.8, 120.4, 130.8, 148.1 (C of C_6H_4(NH)), 104.0, 151.3, 159.3 (C of pyrazolyl), 155.6 (s, C=N), 169.2 (COOH).

ESI-MS (−) CH_3OH (m/z, relative intensity %): 417.5 [100].

*2-((5-hydroxo-3-methyl-1-phenyl-1H-pyrazol-4-yl)(thiophenyl)methylene)-1-(4-methoxy)phenylhydrazine) (PbH**18**)*

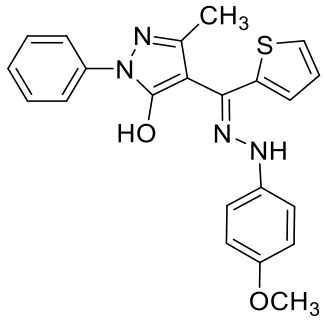

PbH**18** was synthesized by the reaction of TP (300 mg, 1.055 mmol) and 4-methoxyphenylhydrazine (136mg, 1.066 mmol) in methanol (20 mL) as previously described. The product appeared as a light brown solid (yield 0.187 g, 44%).

Anal. Calc. for $C_{25}H_{20}N_4O_2S$; C, 65.33; H, 4.98; N, 13.85%; found: C, 65.87; H, 5.06; N, 13.63%.

^{1}H NMR ($CDCl_3$) δ: 1.85 (s, 3H), 3.78 (s, 3H), 6.53 (s, 1H), 7.01 (t, *J* = 8.5 Hz, 1H), 7.05 (d, *J* = 8.4 Hz, 2H), 7.15 (d, *J* = 7.8 Hz, 1H), 7.51 (t, *J* = 8.4 Hz, 1H), 7.53 (m, 3H), 7.54 (d, *J* = 8.6 Hz, 2H), 7.92 (d, *J* = 7.9 Hz, 2H), 12.01 (br s, 1H, OH).

^{13}C NMR ($CDCl_3$) δ: 26.8 (s, CH_3), 56.0 (OCH_3), 122.5, 124.4, 125.8, 126.2, 127.2, 127.4, 129.4, 137.4 (C of C_4H_3S(C=N) and C_6H_5(N)), 115.0, 117.4, 135.5, 153.4 (C of C_6H_4(NH)), 104.0, 151.3, 159.3 (C of pyrazolyl), 155.6 (s, C=N).

ESI-MS (−) CH_3OH (m/z, relative intensity %): 403.5 [100].

*2-((5-hydroxo-3-methyl-1-phenyl-1H-pyrazol-4-yl)(thiophenyl)methylene)-1-(4-nitro)phenylhydrazine) (PbH**19**)*

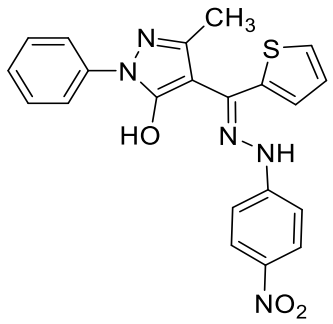

TP (300 mg, 1.055 mmol) and 4-nitrophenylhydrazine (202 mg, 1.066 mmol) were combined in methanol (30 mL) as described in the general procedure. PbH**19** was obtained as a red solid with a yield of 0.312 g (71%).

Anal. Calc. for $C_{24}H_{17}N_5O_3S$; C, 60.13; H, 4.09; N, 16.70%; found: C, 60.49; H, 4.04; N, 16.87%.

^{1}H NMR ($CDCl_3$) δ: 1.79 (s, 3H), 6.58 (s, 1H), 7.01 (t, *J* = 8.5 Hz, 1H), 7.15 (d, *J* = 7.8 Hz, 1H), 7.20 (d, *J* = 8.5 Hz, 2H), 7.51 (t, *J* = 8.2 Hz, 1H), 7.53 (d, *J* = 8.4 Hz, 1H), 7.54 (t, *J* = 8.6 Hz, 2H), 7.92 (d, *J* = 7.9 Hz, 2H), 8.17 (d, *J* = Hz, 2H), 12.01 (br s, 1H, OH).

^{13}C NMR ($CDCl_3$) δ: 26.8 (s, CH_3), 122.5, 124.4, 125.8, 126.2, 127.2, 127.4, 129.4, 137.4 (C of C_4H_3S(C=N) and C_6H_5(N)), 113.3, 124.5, 138.0, 148.9 (C of C_6H_4(NH)), 104.0, 151.3, 159.3 (C of pyrazolyl), 155.6 (s, C=N).

ESI-MS (−) CH_3OH (m/z, relative intensity %): 418.5 [100].

*2-((5-hydroxo-3-methyl-1-phenyl-1H-pyrazol-4-yl)(thiophenyl)methylene)-1-(3-nitro)phenylhydrazine) (PbH**20**)*

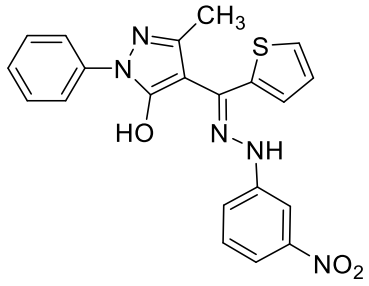

PbH**20** was afforded by reaction of TP (300 mg, 1.055 mmol) and 2,4-dinitrophenylhydrazine (202 mg, 1.066 mmol) in 30 mL of methanol, at conditions described in the general procedure. The final product appeared as an orange solid with a yield of 0.180 g (41%).

Anal. Calc. for $C_{24}H_{17}N_5O_3S$; C, 60.13; H, 4.09; N, 16.70%; found: C, 60.42; H, 4.18; N, 16.98%.

^{1}H NMR ($CDCl_3$) δ: 1.85 (s, 3H), 7.01 (t, *J* = 8.5 Hz, 1H), 7.15 (d, *J* = 7.8 Hz, 1H), 7.51 (d, *J* = 7.9 Hz, 2H), 7.53 (d, *J* = 8.4 Hz, 1H), 7.54 (t, *J* = 8.6 Hz, 1H), 7.73 (d, *J* = 8.5 Hz, 2H), 7.82 (t, *J* = 8.5 Hz, 1H), 7.92 (d, *J* = 8.5 Hz, 2H), 8.05 (d, *J* = 8.5 Hz, 1H), 8.42 (s, 1H), 12.01 (br s, 1H, OH).

^{13}C NMR ($CDCl_3$) δ: 26.8 (s, CH_3), 122.5, 124.4, 125.8, 126.2, 127.2, 127.4, 129.4, 137.4 (C of C_4H_3S(C=N) and C_6H_5(N)), 109.2, 113.9, 120.1, 130.4, 143.8, 149.0 (C of C_6H_4(NH)), 104.0, 151.3, 159.3 (C of pyrazolyl), 155.6 (s, C=N).

ESI-MS (−) CH_3OH (m/z, relative intensity %): 418.5 [100].

*2-((5-hydroxo-3-methyl-1-phenyl-1H-pyrazol-4-yl)(thiophenyl)methylene)-1-(2,4-dinitro)phenylhydrazine) (PbH**21**)*

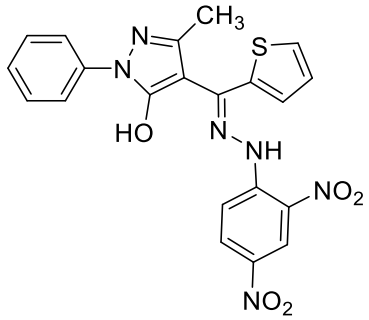

TP (300 mg, 1.055 mmol) and 2,4-dinitrophenylhydrazine (211 mg, 1.066 mmol) were combined in 20 mL of methanol as described in the general procedure, to give PbH**21** as an orange solid (0.285 g, 58% yield).

Anal. Calc. for $C_{21}H_{16}N_6O_5S$; C, 54.31; H, 3.47; N, 18.09%; found: C, 54.49; H, 3.51; N, 17.99%.

^{1}H NMR ($CDCl_3$) δ: 1.85 (s, 3H), 7.01 (t, *J* = 8.5 Hz, 1H), 7.15 (d, *J* = 7.8 Hz, 1H), 7.51 (d, *J* = 8.0 Hz, 2H), 7.53 (d, *J* = 8.4 Hz, 1H), 7.54 (t, *J* = 8.6 Hz, 2H), 7.92 (d, *J* = 7.9 Hz, 2H), 8.25 (d, *J* = 8.6 Hz, 1H), 8.36 (d, *J* = 8.6 Hz, 1H), 8.89 (s, 1H), 12.01 (br s, 1H, OH).

^{13}C NMR ($CDCl_3$) δ: 26.8 (s, CH_3), 122.5, 124.4, 125.8, 126.2, 127.2, 127.4, 129.4, 137.4 (C of C_4H_3S(C=N) and C_6H_5(N)), 116.8, 123.4, 129.2, 130.9, 145.1 (C of C_6H_3(NH)), 104.0, 151.3, 159.3 (C of pyrazolyl), 155.6 (s, C=N).

ESI-MS (−) CH_3OH (m/z, relative intensity %): 463.5 [100].

*2-((5-hydroxo-3-methyl-1-phenyl-1H-pyrazol-4-yl)(thiophenyl)methylene)-1-(4-fluoro)phenylhydrazine) (PbH**22**)*

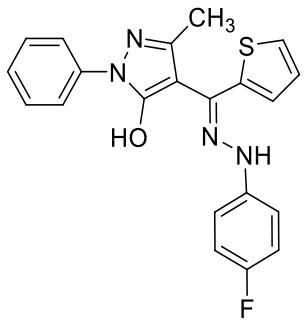

PbH**22** was synthesized by reaction of TP (630 mg, 2.216 mmol) and 4-fluorophenylhydrazine (357 mg, 2.194 mmol) in methanol (30 mL) as previously described. The product appeared as an intense yellow solid (yield 0.516 g, 60%).

Anal. Calc. for $C_{21}H_{17}N_4OSF$; C, 64.27; H, 4.37; N, 14.28%; found: C, 64.37; H, 4.48; N, 14.44%.

^{1}H NMR ($CDCl_3$) δ: 1.85 (s, 3H), 6.58 (s, 1H), 7.01 (t, *J* = 8.5 Hz, 1H), 7.15 (d, *J* = 7.8 Hz, 1H), 7.41 (d, *J* = 7.9 Hz, 2H), 7.48 (d, *J* = 8.4 Hz, 1H), 7.51 (d, *J* = 8.4 Hz, 2H), 7.53 (d, *J* = 8.4 Hz, 1H), 7.54 (t, *J* = 8.6 Hz, 2H), 7.92 (d, *J* = 7.9 Hz, 2H), 12.01 (br s, 1H, OH).

^{13}C NMR ($CDCl_3$) δ: 26.8 (s, CH_3), 122.5, 124.4, 125.8, 126.2, 127.2, 127.4, 129.4, 137.4 (C of C_4H_3S(C=N) and C_6H_5(N)), 115.4, 116.4, 138.5, 157.2 (C of C_6H_4(NH)), 104.0, 151.3, 159.3 (C of pyrazolyl), 155.6 (s, C=N).

ESI-MS (−) CH_3OH (m/z, relative intensity %): 391.5 [100].

*2-((5-hydroxo-3-methyl-1-phenyl-1H-pyrazol-4-yl)(thiophenyl)methylene)-1-(4-chloro)phenylhydrazine) (PbH**23**)*

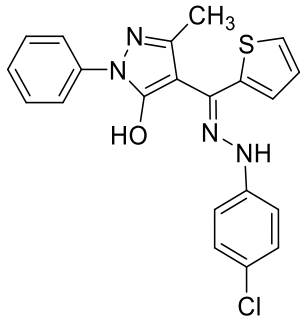

The same reaction was performed to obtain PbH**23** using 300 mg of TP (1.055 mmol) and 191 mg of 4-chlorophenylhydrazine (1.066 mmol) in methanol (20 mL). The product precipitated as a yellow powder (yield: 0.287 g, 67%).

Anal. Calc. for $C_{21}H_{17}N_4OSCl$; C, 61.68; H, 4.19; N, 13.70%; found: C, 61.76; H, 4.09; N, 13.55%.

^{1}H NMR ($CDCl_3$) δ: 1.85 (s, 3H), 6.58 (s, 1H), 7.01 (t, *J* = 8.5 Hz, 1H), 7.11 (d, *J* = 8.0 Hz, 1H), 7.15 (d, *J* = 7.8 Hz, 2H), 7.18 (d, *J* = 8.0 Hz, 1H), 7.51 (d, *J* = 8.4 Hz, 2H), 7.53 (d, *J* = 8.4 Hz, 1H), 7.54 (t, *J* = 8.6 Hz, 2H), 7.92 (d, *J* = 7.9 Hz, 2H), 12.01 (br s, 1H, OH).

^{13}C NMR ($CDCl_3$) δ: 26.8 (s, CH_3), 122.5, 124.4, 125.8, 126.2, 127.2, 127.4, 129.4, 137.4 (C of C_4H_3S(C=N) and C_6H_5(N)), 117.8, 127.9, 129.6, 141.1 (C of C_6H_5(NH)), 104.0, 151.3, 159.3 (C of pyrazolyl), 155.6 (s, C=N).

ESI-MS (−) CH_3OH (m/z, relative intensity %): 407.9 [100].

*2-((5-hydroxo-3-methyl-1-phenyl-1H-pyrazol-4-yl)(thiophenyl)methylene)-1-(4-bromo)phenylhydrazine) (PbH**24**)*

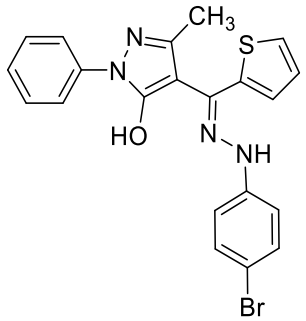

PbH**24** was synthesized by reaction of TP (300 mg, 1.055 mmol) and 4-bromophenylhydrazine (238 mg, 1.066 mmol) in methanol (20 mL) as previously described. The product appeared as a yellowish solid (yield 0.302 g, 63%).

Anal. Calc. for $C_{24}H_{17}N_4OS$; C, 55.64; H, 3.78; N, 12.36%; found: C, 55.30; H, 3.85; N, 12.33%.

^{1}H NMR ($CDCl_3$) δ: 1.85 (s, 3H), 6.58 (s, 1H), 7.01 (t, *J* = 8.5 Hz, 1H), 7.15 (d, *J* = 7.8 Hz, 1H), 7.40 (d, *J* = 7.9 Hz, 2H), 7.51 (d, *J* = 8.4 Hz, 2H), 7.53 (d, *J* = 8.4 Hz, 1H), 7.54 (t, *J* = 8.6 Hz, 1H), 7.68 (d, *J* = 8.5 Hz, 2H), 7.92 (d, *J* = 7.9 Hz, 2H), 12.01 (br s, 1H, OH).

^{13}C NMR ($CDCl_3$) δ: 26.8 (s, CH_3), 122.5, 124.4, 125.8, 126.2, 127.2, 127.4, 129.4, 137.4 (C of C_4H_3S(C=N) and C_6H_5(N)), 116.8, 117.4, 132.5, 142.1 (C of C_6H_5(NH)), 104.0, 151.3, 159.3 (C of pyrazolyl), 155.6 (s, C=N).

ESI-MS (−) CH_3OH (m/z, relative intensity %): 452.4 [100].

Benzyl series

*2-((5-hydroxo-3-methyl-1-phenyl-1H-pyrazol-4-yl)(benzyl)methylene)-1-phenylhydrazine) (PbH**25**)*

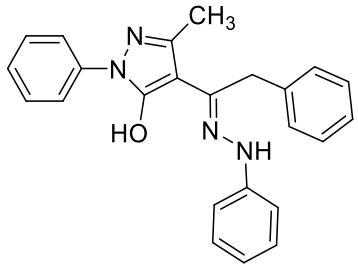

PbH**25** was synthesized by combining BP (300 mg, 1.027 mmol) and phenylhydrazine (100 µL, 1.027 mmol, d =1.099 g/mL) in 20 mL of methanol following the general procedure conditions. The final product appeared as a bright yellow powder with a yield of 0.310 g (79 %).

Anal. Calc. for $C_{24}H_{22}N_4O$; C, 75.37; H, 5.80; N, 14.65%; found: C, 75.01; H, 5.77; N, 14.52%.

^{1}H NMR ($CDCl_3$) δ: 2.48 (s, 3H), 3.62 (s, 2H), 6.56 (d, *J* = 8.3 Hz, 1H), 6.82 (t, *J* = 7.3 Hz, 1H), 7.08 (t, *J* = 7.2 Hz, 1H), 7.19 (t, *J* = 7.5 Hz, 1H), 7.26–7.21 (m, 3H), 7.34 (t, *J* = 7.6 Hz, 2H), 7.38 (d, *J* = 7.8 Hz, 2H), 7.49 (t, *J* = 7.4 Hz, 1H), 7.66 (d, *J* = 5.0 Hz, 2H), 7.98 (d, *J* = 7.8 Hz, 2H), 12.54 (br s, OH).

^{13}C NMR ($CDCl_3$) δ: 16.8 (CH_3), 33.6 (CH_2), 124.6, 127.3, 128.1, 128.8, 129.2, 134.6, 138.5, 138.9 (C of C_6H_5(CH_2C=N) and C_6H_5(N)), 113.8, 122.2, 129.4, 145.0 (C of C_6H_5(NH)), 100.2, 119.3, 167.1 (C of pyrazolyl), 165.7 (C=N).

ESI-MS (−) CH_3OH (m/z, relative intensity %): 381.3[100].

*2-((5-hydroxo-3-methyl-1-phenyl-1H-pyrazol-4-yl)(benzyl)methylene)-1-(pyridin-2-yl)hydrazine) (PbH**26**)*

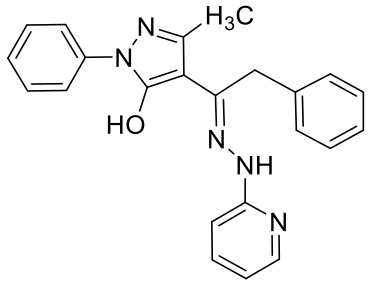

PbH**26** was synthesized from BP (385 mg, 1.374 mmol) and 2-hydrazinopyridine (150 mg, 1.374 mmol) following the general procedure previously described (80 °C, reaction time 2 h). Yield 65%, 0.333 g. PbH**26** is a brown powder soluble in DMSO, acetone, acetonitrile, alcohols, diethyl ether and chlorinated solvents.

Anal. Calc. for $C_{23}H_{21}N_5O$; C, 72.04; H, 5.52; N, 18.26%; found: C, 71.96; H, 5.41; N, 18.33%.

^{1}H NMR ($CDCl_3$) δ: 2.42 (s, 3H), 4.22 (s, 2H), 6.56 (d, *J* = 8.3 Hz, 1H), 6.82 (t, *J* = 7.3 Hz, 1H), 7.19 (t, *J* = 7.5 Hz, 1H), 7.26–7.21 (m, 4H), 7.31 (t, *J* = 7.6 Hz, 2H), 7.42 (t, *J* = 7.8 Hz, 2H), 7.49 (t, *J* = 7.4 Hz, 1H), 8.10 (d, *J* = 5.0 Hz, 1H), 8.04 (d, *J* = 7.8 Hz, 2H), 12.54 (br s, OH).

^{13}C NMR ($CDCl_3$) δ: 16.8 (CH_3), 33.6 (CH_2), 124.6, 127.3, 128.1, 128.8, 129.2, 134.6, 138.5, 138.9 (C of C_6H_5(CH_2C=N) and C_6H_5(N)), 106.8, 117.2, 147.0, 148.2, 157.9 (C of C_6H_4N(NH)), 100.2, 119.3, 167.1 (C of pyrazolyl), 165.7 (C=N).

ESI-MS (−) CH_3CN (m/z, relative intensity %): 382 [100].

*2-((5-hydroxo-3-methyl-1-phenyl-1H-pyrazol-4-yl)(benzyl)methylene)-1-(trifluormeth-4-yl)phenylhydrazine) (PbH**27**)*

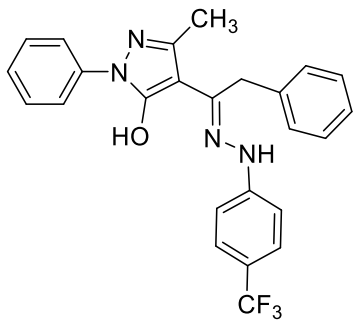

PbH**27** was synthesized from BP (500 mg, 1.710 mmol) and 4-trifluormethylphenylhydrazine (301 mg, 1.710 mmol) following the general procedure previously described (80 °C, reaction time 2 h). Yield 68%,

0.531 mg. PbH**27** is a yellow powder soluble in DMSO, acetone, acetonitrile, alcohols, diethyl ether and chlorinated solvents.

Anal. Calc. for $C_{25}H_{21}F_3N_4O$; C, 66.66; H, 4.70; N, 12.65%; found: C, 66.20; H, 4.60; N, 12.77%.

^{1}H NMR ($CDCl_3$) δ: 2.38 (s, 3H), 4.13 (s, 2H), 6.36 (s, 1H), 6.66 (d, *J* = 8.2 Hz, 1H), 7.16 – 7.10 (m, 2H), 7.22 – 7.17 (m, 1H), 7.27 – 7.22 (m, 4H), 7.50 – 7.35 (m, 4H), 7.97 (d, *J* = 8.7 Hz, 2H), 12.39 (br s, OH).

^{13}C NMR ($CDCl_3$) δ: 16.8 (CH_3), 33.6 (CH_2), 124.6, 127.3, 128.1, 128.8, 129.2, 134.6, 138.5, 138.9 (C of $C_6H_5(CH_2C{=}N)$ and $C_6H_5(N)$), 116.7, 120.2, 126.8, 148.1 (C of $C_6H_4(NH)$), 123.8 (CF_3) 100.2, 119.3, 167.1 (C of pyrazolyl), 165.7 (C=N).

^{19}F{^{1}H} NMR ($CDCl_3$, 125 MHz, with 0.05% v/v TMS, 298): δF 61.7.

{^{1}H,^{15}N}gs- HSQC NMR ($CDCl_3$, 51 MHz, 3J(N-H) = 3 Hz, 298 K): δN 96.2 (N4).

{^{1}H,^{15}N} gs-HMBC NMR ($CDCl_3$, 51 MHz, 3J(N-H) = 3 Hz, 298 K): δN 284.9 (N2), 140.6 (N3), 96.2 (N4), N1 not observed.

ESI-MS (−) CH_3CN (m/z, relative intensity %): 449 [100].

*2-((5-hydroxo-3-methyl-1-phenyl-1H-pyrazol-4-yl)(benzyl)methylene)-1-(4-cyano)phenylhydrazine) (PbH**28**)*

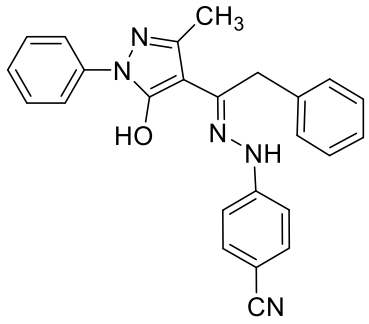

300 mg of BP (1.027 mmol) and 137 mg of 4-cyanophenylhydrazine were combined in 20 mL of methanol in the presence of glacial acetic acid to afford PbH**28** as a light yellow solid (yield 0.236 g, 57 %).

Anal. Calc. for $C_{25}H_{21}N_5O$; C, 73.69; H, 5.19; N, 17.19%; found: C, 73.51; H, 5.10; N, 17.33%.

^{1}H NMR ($CDCl_3$) δ: 2.48 (s, 3H), 3.62 (s, 2H), 6.56 (d, *J* = 8.3 Hz, 1H), 6.82 (t, *J* = 7.3 Hz, 1H), 7.19 (t, *J* = 7.5 Hz, 1H), 7.26–7.21 (m, 3H), 7.34 (t, *J* = 7.5 Hz, 2H), 7.49 (t, *J* = 7.4 Hz, 1H), 7.68 (d, *J* = 5.5 Hz, 2H), 7.83 (d, *J* = 8.0 Hz, 2H), 7.98 (d, *J* = 8.0 Hz, 2H), 12.54 (br s, OH).

^{13}C NMR ($CDCl_3$) δ: 16.8 (CH_3), 33.6 (CH_2), 124.6, 127.3, 128.1, 128.8, 129.2, 134.6, 138.5, 138.9 (C of $C_6H_5(CH_2C{=}N)$ and $C_6H_5(N)$), 102.8, 116.9, 118.7, 148.0 (C of $C_6H_4(NH)$), 118.9 (C≡N), 100.2, 119.3, 167.1 (C of pyrazolyl), 165.7 (C=N).

ESI-MS (−) CH_3OH (m/z, relative intensity %): 406.7 [100].

*2-((5-hydroxo-3-methyl-1-phenyl-1H-pyrazol-4-yl)(benzyl)methylene)-1-hydrazinil)phenylic acid (PbH**29**)*

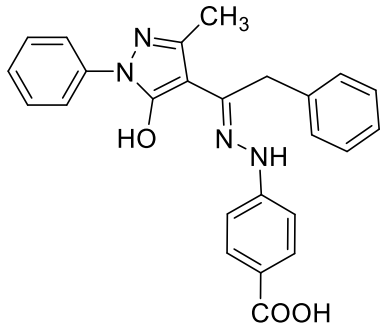

PbH**29** was synthesized by reaction of 300 mg of BP (1.027 mmol) and 156 mg of 4-hydrazinobenzoic acid (1.027 mmol) in methanol (20 mL) as described in general procedure. An off-white was obtained with a yield of 0.273 g (62 %).

Anal. Calc. for $C_{25}H_{22}N_4O_3$; C, 70.41; H, 5.20; N, 13.14%; found: C, 71.02; H, 5.18; N, 13.55%.

^{1}H NMR ($CDCl_3$) δ: 2.48 (s, 3H), 3.62 (s, 2H), 6.56 (d, *J* = 8.3 Hz, 1H), 6.82 (t, *J* = 7.3 Hz, 1H), 7.19 (t, *J* = 7.4 Hz, 1H), 7.26–7.21 (m, 3H), 7.34 (t, *J* = 7.8 Hz, 2H), 7.49 (t, *J* = 7.6 Hz, 1H), 7.88 (d, *J* = 8.3 Hz, 2H), 7.98 (d, *J* = 7.8 Hz, 2H), 8.28 (d, *J* = 8.0 Hz, 2H), 12.54 (br s, OH), 12.80 (br s, COOH).

^{13}C NMR ($CDCl_3$) δ: 16.8 (CH_3), 33.6 (CH_2), 124.6, 127.3, 128.1, 128.8, 129.2, 134.6, 138.5, 138.9 (C of $C_6H_5(CH_2C{=}N)$ and $C_6H_5(N)$), 114.8, 120.7, 131.9, 147.7 (C of $C_6H_4(NH)$), 169.8 (COOH), 100.2, 119.3, 167.1 (C of pyrazolyl), 165.7 (C=N).

ESI-MS (−) CH_3OH (m/z, relative intensity %): 425.6 [100].

*2-((5-hydroxo-3-methyl-1-phenyl-1H-pyrazol-4-yl)(benzyl)methylene)-1-(4-methoxy)phenylhydrazine) (PbH**30**)*

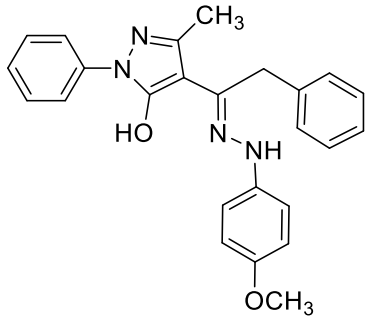

300 mg of BP (1.027 mmol) and 142 mg of 4-methoxyphenylhydrazine (1.027 mmol) were combined in 20 mL of methanol to obtain PbH**30** following the general procedure. PbH**30** appeared as a light yellow solid (yield 0.144 g, 34%).

Anal. Calc. for $C_{25}H_{24}N_4O_2$; C, 72.80; H, 5.86; N, 13.58%; found: C, 72.74; H, 5.61; N, 13.82%.

^{1}H NMR ($CDCl_3$) δ: 2.48 (s, 3H), 3.62 (s, 2H), 4.21 (s, 3H), 6.56 (d, *J* = 8.3 Hz, 1H), 6.82 (t, *J* = 7.3 Hz, 1H), 7.05 (d, *J* = 7.6 Hz, 2H), 7.19 (t, *J* = 7.5 Hz, 1H), 7.26–7.21 (m, 3H), 7.34 (t, *J* = 7.6 Hz, 2H), 7.49 (t, *J* = 7.4 Hz, 1H), 7.54 (d, *J* = 7.0 Hz, 2H), 7.98 (d, *J* = 7.9 Hz, 2H), 12.54 (br s, OH).

^{13}C NMR ($CDCl_3$) δ: 16.8 (CH_3), 33.6 (CH_2), 55.7 (OCH_3), 124.6, 127.3, 128.1, 128.8, 129.2, 134.6, 138.5, 138.9 (C of $C_6H_5(CH_2C{=}N)$ and $C_6H_5(N)$), 114.9, 117.2, 135.1, 153.0 (C of $C_6H_4(NH)$), 100.2, 119.3, 167.1 (C of pyrazolyl), 165.7 (C=N).

ESI-MS (−) CH_3OH (m/z, relative intensity %): 411.2 [100].

*2-((5-hydroxo-3-methyl-1-phenyl-1H-pyrazol-4-yl)(benzyl)methylene)-1-(4-nitro)phenylhydrazine) (PbH**31**)*

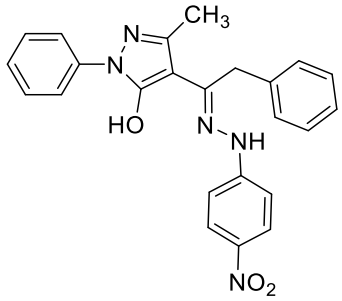

PbH**31** was synthesized by reaction of BP (300 mg, 1.027 mmol) and 4-nitrophenylhydrazine (157 mg, 1.027 mmol) in methanol (20 mL) as previously described. The product appeared as a light brown solid (yield 0.269 g, 61%).

Anal. Calc. for $C_{24}H_{21}N_5O_3$; C, 67.44; H, 4.95; N, 16.38%; found: C, 67.90; H, 5.02; N, 16.18%.

^{1}H NMR ($CDCl_3$) δ: 2.48 (s, 3H), 3.62 (s, 2H), 6.56 (d, *J* = 8.3 Hz, 1H), 6.82 (t, *J* = 7.3 Hz, 1H), 7.17 (t, *J* = 7.6 Hz, 1H), 7.19 (d, *J* = 7.5 Hz, 2H), 7.26–7.21 (m, 3H), 7.34 (t, *J* = 7.6 Hz, 2H), 7.49 (t, *J* = 7.4 Hz, 1H), 7.98 (d, *J* = 7.8 Hz, 2H), 8.23 (d, *J* = 7.8 Hz, 2H), 12.54 (br s, OH).

^{13}C NMR ($CDCl_3$) δ: 16.8 (CH_3), 33.6 (CH_2), 124.6, 127.3, 128.1, 128.8, 129.2, 134.6, 138.5, 138.9 (C of $C_6H_5(CH_2C{=}N)$ and $C_6H_5(N)$), 113.8, 127.2, 137.0, 148.9 (C of $C_6H_4(NH)$), 100.2, 119.3, 167.1 (C of pyrazolyl), 165.7 (C=N).

ESI-MS (−) CH_3OH (m/z, relative intensity %): 426.1 [100].

*2-((5-hydroxo-3-methyl-1-phenyl-1H-pyrazol-4-yl)(benzyl)methylene)-1-(3-nitro)phenylhydrazine) (PbH**32**)*

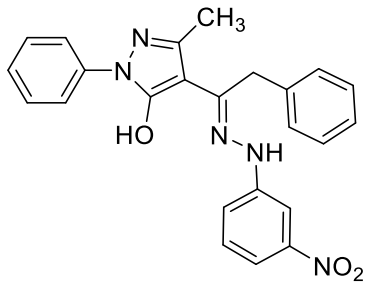

The reaction of 300 mg of BP (1.027 mmol) and 157 mg of 3-nitrophenylhydrazine (1.027 mmol) in 20 mL methanol following the general described procedure, afforded PbH**32**. The product appeared as a light brown powder with a yield of 0.209 g (48%).

Anal. Calc. for $C_{24}H_{21}N_5O_3$; C, 67.44; H, 4.95; N, 16.38%; found: C, 67.11; H, 5.13; N, 16.17%.

^{1}H NMR ($CDCl_3$) δ: 2.48 (s, 3H), 3.75 (s, 2H), 6.56 (d, *J* = 8.3 Hz, 1H), 6.82 (t, *J* = 7.3 Hz, 1H), 7.19 (t, *J* = 7.5 Hz, 1H), 7.26–7.21 (m, 3H), 7.34 (t, *J* = 7.6 Hz, 2H), 7.49 (t, *J* = 7.4 Hz, 1H), 7.78 (d, *J* = 8.0 Hz, 1H), 7.84 (t, *J* = 8.0 Hz, 1H), 7.98 (d, *J* = 7.8 Hz, 2H), 8.11 (d, *J* = 7.8 Hz, 1H), 8.47 (s, 1H), 12.54 (br s, OH).

^{13}C NMR ($CDCl_3$) δ: 16.8 (CH_3), 33.6 (CH_2), 124.6, 127.3, 128.1, 128.8, 129.2, 134.6, 138.5, 138.9 (C of $C_6H_5(CH_2C{=}N)$ and $C_6H_5(N)$), 109.7, 114.8, 120.2, 130.7, 143.5, 148.8 (C of $C_6H_4(NH)$), 100.2, 119.3, 167.1 (C of pyrazolyl), 165.7 (C=N).

ESI-MS (−) CH_3OH (m/z, relative intensity %): 426.4 [100].

*2-((5-hydroxo-3-methyl-1-phenyl-1H-pyrazol-4-yl)(benzyl)methylene)-1-(2,4-dinitro)phenylhydrazine) (PbH**33**)*

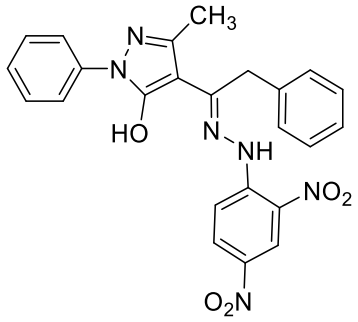

300 mg of BP (1.027 mmol) and 203 mg of 2,4-dinitrophenylhydrazine (1.027 mmol) in 20 mL of methanol and in the presence of catalytic amounts of glacial acetic acid gave PbH**33** as a bright yellow solid (yield 0.288 g, 59%).

Anal. Calc. for $C_{24}H_{20}N_6O_5$; C, 61.01; H, 4.27; N, 17.79%; found: C, 60.89; H, 4.38; N, 18.03%.

^{1}H NMR ($CDCl_3$) δ: 2.48 (s, 3H), 3.62 (s, 2H), 6.56 (d, *J* = 8.3 Hz, 1H), 6.82 (t, *J* = 7.3 Hz, 1H), 7.19 (t, *J* = 7.5 Hz, 1H), 7.26–7.21 (m, 3H), 7.34 (t, *J* = 7.6 Hz, 2H), 7.49 (t, *J* = 7.4 Hz, 1H), 7.98 (d, *J* = 7.8 Hz, 1H), 8.05 (d, *J* = 7.8 Hz, 1H), 8.38 (d, *J* = 7.9 Hz, 2H), 9.01 (s, 1H), 12.54 (br s, OH).

^{13}C NMR ($CDCl_3$) δ: 16.8 (CH_3), 33.6 (CH_2), 124.6, 127.3, 128.1, 128.8, 129.2, 134.6, 138.5, 138.9 (C of $C_6H_5(CH_2C{=}N)$ and $C_6H_5(N)$), 116.8, 123.2, 130.0, 137.4, 145.6 (C of $C_6H_3(NH)$), 100.2, 119.3, 167.1 (C of pyrazolyl), 165.7 (C=N).

ESI-MS (−) CH_3OH (m/z, relative intensity %): 471.7 [100].

*2-((5-hydroxo-3-methyl-1-phenyl-1H-pyrazol-4-yl)(benzyl)methylene)-1-(4-fluoro) phenylhydrazine) (PbH**34**)*

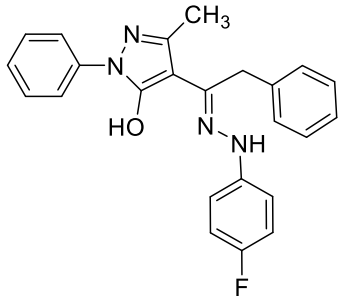

PbH**34** was obtained by reaction of BP (300 mg, 1.027 mmol) and 4-fluorophenylhydrazine (130 mg, 1.027 mmol) in methanol (20 mL) following the general procedure. The product appeared as a yellow solid (yield 0.260 g, 63%).

Anal. Calc. for $C_{24}H_{21}N_4OF$; C, 71.98; H, 5.29; N, 13.99%; found: C, 72.14; H, 5.47; N, 14.09%.

^{1}H NMR ($CDCl_3$) δ: 2.48 (s, 3H), 3.62 (s, 2H), 6.56 (d, *J* = 8.3 Hz, 1H), 6.82 (t, *J* = 7.3 Hz, 1H), 7.19 (t, *J* = 7.5 Hz, 1H), 7.26–7.21 (m, 3H), 7.34 (t, *J* = 7.6 Hz, 2H), 7.39 (d, *J* = 7.8 Hz, 2H), 7.46 (d, *J* = 8.0 Hz, 2H), 7.49 (t, *J* = 7.4 Hz, 1H), 7.98 (d, *J* = 7.8 Hz, 2H), 12.54 (br s, OH).

^{13}C NMR ($CDCl_3$) δ: 16.8 (CH_3), 33.6 (CH_2), 124.6, 127.3, 128.1, 128.8, 129.2, 134.6, 138.5, 138.9 (C of $C_6H_5(CH_2C{=}N)$ and $C_6H_5(N)$), 115.7, 116.6, 138.4, 157.2 (C of $C_6H_4N(NH)$), 100.2, 119.3, 167.1 (C of pyrazolyl), 165.7 (C=N).

ESI-MS (−) CH_3OH (m/z, relative intensity %): 399.1 [100].

*2-((5-hydroxo-3-methyl-1-phenyl-1H-pyrazol-4-yl)(benzyl)methylene)-1-(4-chloro)phenylhydrazine) (PbH**35**)*

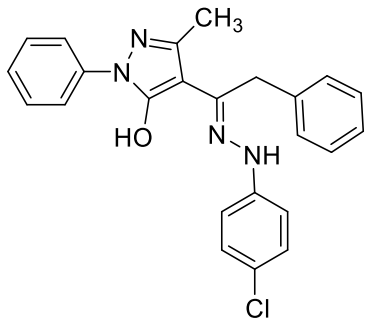

The same reaction was performed to obtain PbH**35**, using 300 mg of BP (1.027 mmol) and 146 mg of 4-chlorophenylhydrazine (1.027 mmol) in 20 mL of methanol. A yellow solid was afforded as the final product with a yield of 0.187 g (44 %).

Anal. Calc. for $C_{24}H_{21}N_4OCl$; C, 69.14; H, 5.08; N, 13.44%; found: C, 70.05; H, 5.17; N, 13.49%.

^{1}H NMR ($CDCl_3$) δ: 2.48 (s, 3H), 3.62 (s, 2H), 6.56 (d, *J* = 8.3 Hz, 1H), 6.82 (t, *J* = 7.3 Hz, 1H), 7.09 (d, *J* = 7.4 Hz, 2H), 7.15 (d, *J* = 7.9 Hz, 2H), 7.19 (t, *J* = 7.5 Hz, 1H), 7.26–7.21 (m, 3H), 7.34 (t, *J* = 7.6 Hz, 2H), 7.49 (t, *J* = 7.4 Hz, 1H), 7.98 (d, *J* = 7.8 Hz, 2H), 12.54 (br s, OH).

^{13}C NMR ($CDCl_3$) δ: 16.8 (CH_3), 33.6 (CH_2), 124.6, 127.3, 128.1, 128.8, 129.2, 134.6, 138.5, 138.9 (C of $C_6H_5(CH_2C{=}N)$ and $C_6H_5(N)$), 117.6, 128.0, 129.7, 141.3 (C of $C_6H_4(NH)$), 100.2, 119.3, 167.1 (C of pyrazolyl), 165.7 (C=N).

ESI-MS (−) CH_3OH (m/z, relative intensity %): 415.9 [100].

*2-((5-hydroxy-3-methyl-1-phenyl-1H-pyrazol-4-yl)(benzyl)methylene)-1-(4-bromo)phenylhydrazine) (PbH**36**)*

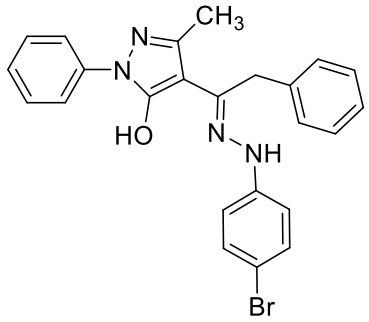

PbH**36** was prepared by reaction of BP (300 mg, 1.027 mmol) and 4-bromophenylhydrazine (191 mg, 1.027 mmol) in 20 mL methanol following the general procedure. The final product resulted as a light-yellow powder (yield 0.267 g, 56%).

Anal. Calc. for $C_{24}H_{21}N_4OBr$; C, 62.48; H, 4.59; N, 12.14%; found: C, 62.87; H, 5.11; N, 12.57%.

^{1}H NMR ($CDCl_3$) δ: 2.48 (s, 3H), 3.62 (s, 2H), 6.56 (d, *J* = 8.3 Hz, 1H), 6.82 (t, *J* = 7.3 Hz, 1H), 7.19 (t, *J* = 7.5 Hz, 1H), 7.26–7.21 (m, 3H), 7.34 (t, *J* = 7.6 Hz, 2H), 7.41 (d, *J* = 8.0 Hz, 2H), 7.49 (t, *J* = 7.4 Hz, 1H), 7.76 (d, *J* = 7.0 Hz, 2H), 7.98 (d, *J* = 7.8 Hz, 2H), 12.54 (br s, OH).

^{13}C NMR ($CDCl_3$) δ: 16.8 (CH_3), 33.6 (CH_2), 124.6, 127.3, 128.1, 128.8, 129.2, 134.6, 138.5, 138.9 (C of $C_6H_5(CH_2C{=}N)$ and $C_6H_5(N)$), 116.8, 118.2, 133.7, 142.7 (C of $C_6H_4(NH)$), 100.2, 119.3, 167.1 (C of pyrazolyl), 165.7 (C=N).

ESI-MS (−) CH_3OH (m/z, relative intensity %): 460.3 [100].

4.5.2 Synthesis of metal complexes

*[Zn(PbH26)$_2$] (**C1**)*

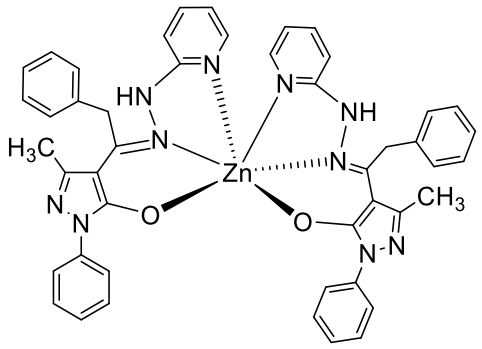

A solution of $Zn(OOCCH_3)_2 \cdot 2H_2O$ (29 mg, 0.133 mmol) in water (5 mL) was added to a solution of PbH**26** (120 mg, 0.313 mmol) dissolved in methanol (15 mL). The mixture was stirred at room temperature, and within an hour a light yellow precipitate formed, which was removed by filtration, washed with a EtOH/H_2O (60:40 v/v) solution, and shown to be **C1**. Yield = 78%, 102 mg. It is soluble in DMSO, DMF, acetone, acetonitrile, and chlorinated solvents.

Anal. Calc. for $C_{46}H_{40}N_{10}O_2Zn$; C, 66.55; H, 4.86; N, 16.87%; found: C, 63.65; H, 4.72; N, 15.64%.

^{1}H NMR ($CDCl_3$) δ: 8.05 (d, *J* = 8.0 Hz, 1H), 7.73 (d, *J* = 8.0 Hz, 2H), 7.55 (s, 1H,), 7.50 (d, *J* = 7.8 Hz, 2H), 7.44 (m, 3H), 7.38 (d, *J* = 7.6 Hz, 2H), 7.15 (t, *J* = 8.0 Hz, 2H), 6.99 (t, *J* = 8.0 Hz, 1H), 6.52 (t, *J* = 7.6 Hz, 1H), 6.33 (, d, *J* = 8.0 Hz, 1H), 4.41 (s, 2H), 2.42 (s, 3H).

^{13}C NMR ($CDCl_3$) δ: 165.5 (C5), 162.2 (C10), 152.6 (C16), 146.7 (C20), 144.6 (C3), 139.0 (C6), 138.5 (C18), 134.6 (C12), 129.8 (C15), 128.8 (C14,14'), 128.2 (C8,8'), 128.0 (C13,13'), 124.6 (C9), 119.3 (C7,7'), 115.4 (C19), 109.3 (C17), 97.6 (C4), 35.4 (C11), 17.2 (C21).

{^{1}H,^{15}N}gs- HSQC NMR ($CDCl_3$, 51 MHz, 3J(N-H) = 3 Hz, 298 K): δN 130.2 (N4).

{^{1}H,^{15}N} gs-HMBC NMR ($CDCl_3$, 51 MHz, 3J(N-H) = 3 Hz, 298 K): δN 51.2 (N5), N3, N2, and N1 not observed.

ESI-MS (+) CH_3CN (m/z, relative intensity %): 829 [70] $[Zn(PbH26)_2]^+$; 851 [100] $[Zn(PbH26)_2+Na]^+$; 1276 [55] $[Zn_2(PbH26)_3]^+$.

*[Zn(PbH27)$_2$(MeOH)$_2$] (**C2**)*

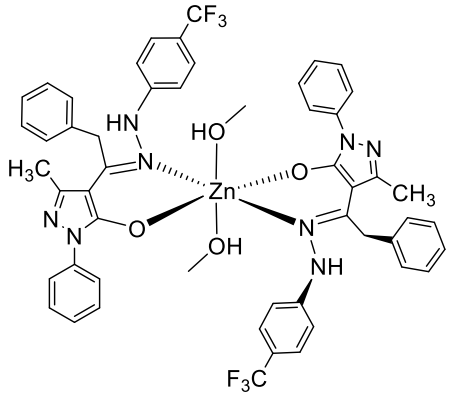

A solution of $Zn(OOCCH_3)_2{\cdot}2H_2O$ (29 mg, 0.133 mmol) in water (5 mL) was added to a solution of PbH**27** (120 mg, 0.166 mmol) dissolved in methanol (15 mL). The mixture was stirred at reflux and within an hour a light yellow precipitate formed, which was removed by filtration, washed with a EtOH/H_2O (60 : 40 v/v) solution, and shown to be **C2**. It is soluble in DMSO, DMF, acetonitrile, acetone, diethyl ether, and chlorinated solvents. Yield = 86%, 118 mg.

Anal. Calc. for $C_{52}H_{48}F_6N_8O_4Zn$; C, 60.73; H, 4.70; N, 10.90%; found: C, 60.68; H, 4.67; N, 10.81%.

^{1}H NMR ($CDCl_3$) δ: 7.84 (d, *J* = 8.0 Hz, 4H), 7.43 (t, *J* = 7.8 Hz, 4H), 7.34-7.23 (m, 12H), 7.03 (d, *J* = 6.6 Hz, 4H), 6.46 (d, *J* = 8.3 Hz, 4H), 5.98 (s, 2H), 4.17 (s, 4H), 3.44 (s, 6H), 2.28 (s, 6H), 1.30 (s, 4H).

^{13}C NMR ($CDCl_3$) δ: 177.7 (C5), 162.6 (C10), 149.1 (C3), 148.1 (C16), 138.5 (C6), 135.3 (C12), 129.1 (C14 and C14'), 128.7 (C8 and C8'), 127.9 (C13 and C13'), 127.0 (C15), 126.3q (3JC-F = 3.4 Hz, C18 and C18'), 125.6 (C9), 124.3q (1JC-F = 271.3 Hz, C20), 123.1q (2JC-F = 32.3 Hz, C19), 119.5 (C7 and C7'), 114.1 (C17 and C7'), 98.3 (C4), 35.7 (C11), 17.3 (C21).

^{19}F NMR ($CDCl_3$) δ: F 61.4.

{^{1}H,^{15}N}gs- HSQC NMR ($CDCl_3$, 51 MHz, 3J(N-H) = 3 Hz, 298 K): δN 117.3 (N4).

{^{1}H,^{15}N} gs-HMBC NMR ($CDCl_3$, 51 MHz, 3J(N-H) = 3 Hz, 298 K): δN 276.4 (N2), N3, N4, N1 not observed.

ESI-MS (+) CH_3CN (m/z, relative intensity %): 965 [100] $[Zn(PbH27)_2]^+$; 987 [40] $[Zn(PbH27)_2+Na]^+$; 1479 [30] $[Zn_2(PbH27)^3]^+$.

*[Cu(PbH26)$_2$] (**C3**)*

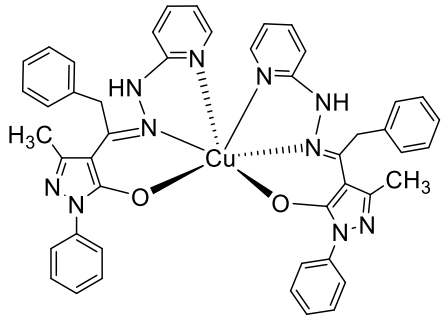

A solution of Cu(OOCCH$_3$)$_2$·2H$_2$O (31 mg, 0.157 mmol) in water (5 mL) was added to a solution of PbH**26** (120 mg, 0.313 mmol) dissolved in methanol (15 mL).). The mixture was stirred at room temperature and immediately, a brown green precipitate formed, which was removed by filtration, washed with a EtOH/H$_2$O (60 : 40 v/v) solution, and shown to be complex **C3**. It is soluble in DMSO, DMF, acetone, acetonitrile, and chlorinated solvents.

Anal. Calc. for $C_{46}H_{40}CuN_{10}O_2$; C, 66.69; H, 4.87; N, 16.91%; Found: C, 66.23; H, 4.75; N, 16.86%.

IR (Nujol cm^{-1}): 3297w br ν(N−H), 3062w ν(N−H), 3030w ν(C−H aromatic), 1617m ν(C=N), 1588m ν(C=N), 1572 ν(C=N), 1528m, 1508m ν(C=C), 1071m ν(N-N), 546m ν(Cu−N), 508s ν(Cu−O).

ESI-MS (+) CH$_3$CN (m/z, relative intensity %): 828 [100] [Cu(PbH26)$_2$]$^+$; 1274 [75] [Cu$_2$(PbH26)$_3$]$^+$.

UV-Visible (CH$_3$CN, 10^{-5} M): 256 nm (π–π*), 305 nm (n–π*, >C=N-), 378 nm (n–π*, py), 414 nm sh (LMCT).

*[Cu(PbH27)$_2$] (**C4**)*

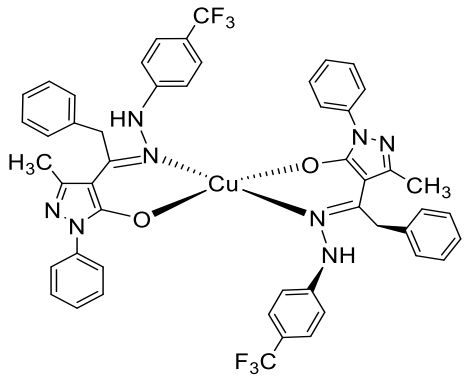

A solution of Cu(OOCCH$_3$)$_2$·2H$_2$O (26 mg, 0.133 mmol) in water (5 mL) was added to a solution of PbH**27** (120 mg, 0.166 mmol) dissolved in methanol (15 mL). The mixture was stirred at room temperature and immediately a red precipitate formed, which was removed by filtration, washed with

a EtOH/H_2O (60 : 40 v/v) solution, and shown to be **C4**. It is soluble in DMSO, DMF, acetone, and chlorinated solvents. Yield = 63%, 80 mg.

Anal. calcd. for $C_{50}H_{40}CuF_6N_8O_2$; C, 62.40; H, 4.19; N, 11.64%; Found: C, 62.19; H, 4.24; N, 11.32%.

IR (Nujol cm^{-1}): 3294m ν(N−H), 3026w ν(Carom-H), 3028w ν(Carom-H), 1614m ν(C=N), 1601m ν(C=N), 1588m ν(C=N), 1575m ν(C=C), 1516vs ν(C=C), 1489vs ν(C=C), 1327vs ν(C−F), 1103vs ν(C−F), 1065s ν(N−N), 540m ν(Cu−N), 510s ν(Cu−O).

ESI-MS (+) CH_3CN (m/z, relative intensity %): 963 [15] $[Cu(PbH27)_2]^+$; 1067 [20] $[Cu(PbH27)_2(MeOH)_2(MeCN)]^+$.

UV-Visible (CH_3CN, 10-5 M): 259 nm (π–π*), 278 nm (n–π*), 392 nm sh (LMCT).

*$[Cu(PP)_2]$ (**C5**)*

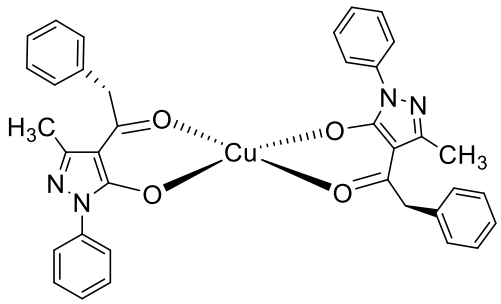

C5 is obtained with a procedure similar to that of **C4**, but leaving the reaction mixture under stirring for 24 hours, during which the red precipitate slowly converts to a dark green. It is soluble in DMSO, DMF, acetone, and chlorinated solvents. Yield = 86%, 74 mg.

Anal. Calc. for $C_{36}H_{30}CuN_4O_4$; C, 66.91; H, 4.68; N, 8.67%; Found: C, 66.55; H, 4.57; N, 8.71%.

IR (Nujol cm^{-1}): 3065w ν(Carom-H), 3037w ν(Carom-H), 1604s ν(C=O), 1590s ν(C=N), 1575vs ν(C=C), 1532m ν(C=C), 1486vs ν(C=C), 510s, 400m ν(Cu−O).

ESI-MS (+) CH_3CN (m/z, relative intensity %): 647 [100] $[Cu(PP)_2]+$.

4.5.3 Crystallography

Single-crystal X-ray diffraction data of PbH27 and complex **C2** were collected at room temperature with a Bruker-Nonius X8APEXII CCD area detector system equipped with a graphite monochromator with radiation Mo Kα (λ = 0.71073 Å). Data were processed through the SAINT reduction and SADABS absorption software (Bruker, 2008; Sheldrick, 1996). Structures were solved by direct methods and refined by full-matrix least-squares based on F2 through the SHELX and SHELXTL structure de-termination package (Sheldrick, 1996). All non-hydrogen atoms were refined anisotropically. Fluorine atoms F(2) and F(3) of the -CF_3 group in **C2** are found disordered in two positions and refined with occupancy factors of 0.80 and 0.20. Both sets of atoms were refined anisotropically. Hydrogen atoms were included as idealized atoms riding on the respective carbon, nitrogen, and oxygen atoms with bond lengths appropriate to the hybridization. All graphical representations have been obtained by using Olex2 software package (Dolomanov et al., 2009). Details of data and structural refinements are reported in supporting information.

4.5.4 DFT analysis

The electronic structure and geometries of PbH**27**, its tautomers and anion, [PbH**27**]$^-$, and zinc complex **C2** were investigated by using density functional theory at the B3LYP level (Lee et al., 1988; Beck, 1993). For the ligand and its corresponding anion the 6-311G** basis set was used for the optimization, while for the Zn complex the optimization was carried out using 6-311G*. Molecular geometries were optimized without symmetry restrictions. Frequency calculations were carried out at the same level of theory to identify all of the stationary points as minima (zero imaginary frequencies) and to provide the thermal correction to free energies at 298.15 K and 1 atm. Solution-phase SCF energies were calculated by a single-point calculation on the in vacuum optimized structure using the CPCM solvation model in chloroform (Cossi et al., 2003). Gibbs free energies in chloroform solution were estimated from the equation Gsolv = Esolv + (Ggas– Egas). The GIAO method was used for the NMR calculations (^{1}H-, ^{13}C- and ^{15}N-NMR isotropic shielding tensors), which were carried out at the 6-311++G** level of theory. The computed IR spectra were scaled by a factor of 0.96 (Wong, 1996; Scott and Radom, 1996). The DFT calculations were executed using the Gaussian 09 program package (Frisch et al., 2016). Coordinates of all optimized compounds are collected in the Supporting Information.

4.5.5 T. brucei, multi-drug resistant and animal strains and HFF cell culture

Biological assays have been conducted in collaboration with Prof. Harry de-Koning (School of Infection and Immunity, Parasitology, University of Glasgow, Glasgow, Scotland, UK). *T. b. brucei* s427 bloodstream forms, resistant *T. b. brucei* strains (*T. b.* B48 and *T. b.* SUR10), animal Trypanosoma strains (*T. equiperdum* and *T. evansi*), and HFF cells were cultivated in vented plastic flask at 37 °C with 5% CO_2. For *Trypanosoma* strains, the growth medium was Hirumi's modified Iscoves Medium (HMI)-9 supplemented with 10% (v/v) fetal bovine serum (Thermo Fischer Scientific Gibco, Waltham, MA, USA), whereas HFF cells were grown in Dulbecco's Modified Eagle's Medium (Sigma-Aldrich) supplemented with 10% (v/v) heat-inactivated fetal bovine serum, glutamine (0.584 g/L), and 10 mL/L 100×penicillin-streptomycin (Gibco) (Petrelli et al, 2016; Petrelli et al., 2017).

4.5.6 Growth inhibition assay on T. brucei, multi-drug resistant, Trypanosoma animal strains, and HFF cells

The synthetic compounds tested were dissolved in dimethyl sulfoxide (DMSO) and serially diluted with growth medium in white 96-well microtiter plates. 20,000 bloodstream forms of *T. brucei* cells, were added to each well to reach a final volume of 200 µL. In the case of mammalian cells (HFF cells), we added 2000 cells/well with similar results. To avoid any damage to the cells, the concentration of DMSO in the solution was never higher than 1% (no cell growth inhibition was observed with this concentration of DMSO). Cell viability was verified by a drug-free control for each compound. The plates were incubated for 48 h in the 5% CO_2 incubator; then 20 µL of 0.5 mM resazurine (Sigma Aldrich) was added to each well, and the plates were incubated for an additional 24 h before the fluorescence was measured with a FLUOstar Optima (BMG Labtech, Durham, NC, USA) at wavelengths of 544 nm for excitation and 590 nm for emission. The half-maximal efficacious concentration values (EC_{50}) were calculated on a log inhibitor versus the response curves by non-linear regression using the GraphPad prism 8 software (GraphPad Software, Inc., La Jol-la, CA, USA). The procedure was repeated in three independent experiments to make data reliable.

4.5.7 Drug sensitivity assay using cell counts

Compounds of varying concentrations were tested on trypanosomes for determination of *in vitro* cell growth using cell counts. Trypanosomes at their mid logarithmic phase of growth were taken from cultures and cell density was determined using a haemocytometer. The cell density was adjusted to 2 x 10^5 with fresh HMI-9 medium. After predetermined periods of exposure to the test compound, cell

counts were taken in triplicate, for each concentration of the compounds, for up to 32 hrs. The experiment was repeated two more times and the average counts were used for plotting the growth curve against time in hours.

4.5.8 Assessment of cell cycle (DNA content assay) using flow cytometry

Fluorescence Activated Cell Sorting Technology (FACS) was also used to study the effects of test compounds on DNA content in *Trypanosoma brucei brucei* s427 WT. Cell density was adjusted to 1×100 cells/mL with and without test compounds for the duration of the experiment. 1 mL of sample was transferred at each time point into microfuge tubes and centrifuged at 1620 × g for 10 min at 4 °C, washed once in PBS containing 5 mM of EDTA and re-suspended and fixed in 1 mL of 70% methanol and 30% PBS/EDTA. The tube with the cells was left at 4 °C overnight in the dark, and the samples were subsequently washed once with 1 mL PBS/EDTA, re-suspended in 1 mL PBS/EDTA containing 10 µg/mL propidium iodide and incubated at 37 °C for 45 minutes. RNase A (10 µg/mL) was added before the samples were analysed by a Becton Dickinson FACS Calibur using the FL2-Area detector and CellQuest software. The data obtained were analysed using FlowJo software (FlowJo LLC, Ashland, OR, USA).

4.5.9 Assessment of DNA configuration using fluorescence microscopy

The configuration of nuclei and kinetoplast DNA of treated and untreated *T. brucei* was visualised using a vectashield mounting medium with the dye 4,6-diamidino-2-phenylindole (DAPI) (Vector Lab. CA, USA), which fluoresces when bound to DNA, while the mitochondrial integrity was examined using the Mito-Tracker Orange CMTMRos staining dye (ThermoFisher Scientific, UK), which is a cationic fluorophore that accumulates in the mitochondria due to the highly negative mitochondrial membrane (Gile et al., 2015). First, a stock solution of 100 µM was made by adding 10 µL of a 1 mM Mito-tracker stock to 90 µL DMSO. From this solution, 1 µL was added to 1 mL of sample at each time point to make a final concentration of 100 nM of Mito-tracker. The sample was then incubated at 37 ºC and 5% CO_2 for 10 minutes. The incubated sample was washed in filter-sterilized 1× PBS and spun at 2,600 rpm for 10 minutes. After the final wash step, the sample was re-suspended in 1 mL of 1 x PBS. 50 µl of the re-suspended cells were spread onto a glass microscope slide, and were left to air dry, the cells were then fixed in methanol overnight at -20 ºC. The following day, the slides were rehydrated using 1 mL of PBS and allowed to rehydrate for 10 minutes after which it was then allowed to evaporate but not completely. A drop of Vectashield antifade mounting medium with DAPI (Vector Laboratories, USA) was added to the slides and spread by a coverslip; the coverslip was then applied, and the edges were sealed with nail varnish. DNA configuration was

assessed using a Zeiss Axioplan microscope using Hamamatso digital camera and Openlab software. A total of 200 cells per slide were counted for each sample using a cell counter, and scores for DNA configuration were given following these groups: 1N1K, 1N2K, 2N2K, where N is nuclear DNA; and K is kinetoplast DNA.

4.5.10 Determination of NTP and dNTP pools by HPLC

The bloodstream form of *T. brucei* (s427) was maintained at 37 °C and 5% CO_2 in Hirumi's modified Iscove's Medium (HMI)-9 medium and Serum Plus but containing 10% fetal bovine serum. Following the procedure from Ranjbarian and colleagues (2022), trypanosomes (50 mL), harvested in late logarithmic phase, were chilled on ice for 5 min before being collected and centrifuged at 4000 rpm for 5 min at 4 °C. Subsequently, the pellet was resuspended in 1 mL of culture medium, transferred to an Eppendorf tube, and centrifuged at 14000 rpm for 1 min at 4 °C. The NTP, NDP, dNDP, and dNTP pools were not affected by the time on ice (5 minutes), the centrifugation time (varied between 5 and 15 min), the centrifugation speed (varied between 4000 and 14000 rpm) or how many washings in culture medium that were made (3 times). After the medium wash, the collected trypanosomes were disintegrated by pipetting them up and down in 720 µL of ice-cold 0.6 M trichloroacetic acid containing 15 mM $MgCl_2$. The resultant solution was centrifuged at 14000 rpm for 1 min at 4 °C, and the supernatant was extracted twice with 1.13 the volume of Freon (78% v/v) trioctylamine (22% v/v). 400 µL of the resulting solution was transferred and centrifuged in a pre-washed Eppendorf tube with a 5 kDa filter (Nanosep 3k Omega, Pall Life Sciences). The sample was purified on a WAX cartridge properly pre-washed, and the collected solution was evaporated to dryness in a Speedvac (Savant) and dissolved in 200 µL of water. This fraction was used for the quantification of nucleotides, deoxynucleotides, diphosphates, and triphosphates by a 150 x 3 mm C18-WP HPLC column (Chromanik Sunshell). Samples ran in 27% of 23g/L KH_2PO_4 pH = 6.2 in 7% ACN (A); 53% of 7% ACN (B) and 20% of 3,52 g/L TBA in 7% ACN (C). Nucleotides were quantified by measuring peak heights and areas and comparing them to a standard curve.

4.6 References

Acharya, B.N., Saraswat, D., Kaushik, M.P. (2008). Pharmacophore based discovery of potential antimalarial agent targeting haem detoxification pathway. European Journal of Medicinal Chemistry, 43, 2840-52.

Adams, J.B. (2001). Bonding energy models. Encyclopedia of materials: science and technology, 763-767.

Barrett, M.P., Boykin, D.W., Brun, R., Tidwell, R.R. (2007). Human African trypanosomiasis: pharmacological re-engagement with a neglected disease. British Journal of Pharmacology, 152, 1155–1171.

Beck, A.D. (1993). Density-functional thermochemistry. III. The role of exact exchange. Journal of Chemical Physics, 98(7), 5648-6.

Bruker, A.P.E.X. (2008). SAINT; Bruker AXS Inc.: Madison, Wisconsin, USA.(b) Sheldrick, GM A short history ofSHELX. Acta Crystallogr., Sect. A: Found. Crystallogr, 64, 112.

Caputto, M.E., Fabian, L.E., Benítez, D., Merlino, A., Ríos, N., Cerecetto, H., Moltrasio, G.Y., Moglioni, A.G., González, M., Finkielsztein, L.M. (2011). Thiosemicarbazones derived from 1-indanones as new anti-*Trypanosoma cruzi* agents. Bioorganic & medicinal chemistry, 19(22), 6818-6826.

Chohan, Z.H., Hernandes, M.Z., Sensato, F.R., Moreira, D.R.M., Alves Pereira, V.R., Neves, J.K.D.A.L., De Oliveira, A.P., De Oliveira, B.C., Lima Leite, A.C. (2014). Sulfonamide–metal complexes endowed with potent anti-*Trypanosoma cruzi* activity. Journal of Enzyme Inhibition and Medicinal Chemistry, 29(2), 230-236.

Cossi, M., Rega, N., Scalmani, G., Barone, V. (2003). Energies, structures, and electronic properties of molecules in solution with the C-PCM solvation model. Journal of computational chemistry, 24(6), 669-681.

Cuccioloni, M., Bonfili, L., Cecarini, V., Nabissi, M., Pettinari, R., Marchetti, F., Petrelli, R., Cappellacci, L., Angeletti, M., Eleuteri, A.M. (2020). Exploring the Molecular Mechanisms Underlying the in vitro Anticancer Effects of Multitarget-Directed Hydrazone Ruthenium- (II)-Arene Complexes. ChemMedChem, 15, 105−113.

Cuevas-Hernández, R.I., Girard, R.M., Krstulović, L., Bajić, M., Silber, A.M. (2021). An aromatic imidazoline derived from chloroquinoline triggers cell cycle arrest and inhibits with high selectivity the *Trypanosoma cruzi* mammalian host-cells infection. PLoS Neglected Tropical Diseases, 15(11), e0009994.

Cuevas-Hernández, R.I., Girard, R.M., Martínez-Cerón, S., Santos da Silva, M., Elias, M.C., Crispim, M., Trujillo-Ferrara, J., Silber, A.M. (2020). A fluorinated phenylbenzothiazole arrests the *Trypanosoma cruzi* cell cycle and diminishes the infection of mammalian host cells. Antimicrobial Agents and Chemotherapy, 64(2), 10-1128.

Dolomanov, O.V., Bourhis, L.J., Gildea, R.J., Howard, J.A., Puschmann, H. (2009). OLEX2: a complete structure solution, refinement and analysis program. Journal of applied crystallography, 42(2), 339-341.

dos Santos Filho, J.M., Leite, A.C.L., de Oliveira, B.G., Moreira, D.R.M., Lima, M.S., Soares, M.B.P., Leite, L.F.C. (2009). Design, synthesis and cruzain docking of 3-(4-substituted-aryl)-1, 2, 4-oxadiazole-N-acylhydrazones as anti-*Trypanosoma cruzi* agents. Bioorganic & medicinal chemistry, 17(18), 6682-6691.

Fattorusso, C., Campiani, G., Kukreja, G., Persico, M., Butini, S., Romano, M.P., Altarelli, M., Ros, S., Brindisi, M., Savini, L., Novellino, E., Nacci, V., Fattorusso, E., Parapini, S., Basilico, N., Taramelli, D., Yardley, V., Croft, S., Borriello, M., Gemma, S. (2008). Design, synthesis, and structure–activity relationship studies of 4-quinolinyl-and 9-acrydinylhydrazones as potent antimalarial agents. Journal of medicinal chemistry, 51(5), 1333-1343.

Franco, J., Scarone, L., Comini, M.A. (2020). Novel distamycin analogues that block the cell cycle of African trypanosomes with high selectivity and potency. European Journal of Medicinal Chemistry, 189, 112043.

Frisch, M. E., Trucks, G. W., Schlegel, H. B., Scuseria, G. E., Robb, M., Cheeseman, J. R., Scalmani, G., Barone, V., Petersson, G.A., Nakatsuji, H., Li, X., Caricato, M., Marenich, A., Bloino, J., Janesko, B.G., Gomperts, R., Mennucci, B., Hratchian, H.P., Ortiz, J.V., Izmaylov, A.F., Sonnenberg, J.L., Williams-Young, D., Ding, F., Lipparini, F., Egidi, F., Goings, J., Peng, B., Petrone, A., Henderson, T., Ranasinghe, D., Zakrzewski, V.G., Gao, J., Rega, N., Zheng, G., Liang, W., Hada, M., Ehara, M., Toyota, K., Fukuda, R., Hasegawa, J., Ishida, M., Nakajima, T., Honda, Y., Kitao, O., Nakai, H., Vreven, T., Throssell, K., Montgomery, J.A.J., Peralta, J.E., Ogliaro, F., Bearpark, M., Heyd, J.J., Brothers, E., Kudin, K.N., Staroverov, V.N., Keith, T., Kobayashi, R., Normand, J., Raghavachari,

K., Rendell, A., Burant, J.C., Iyengar, S.S., Tomasi, J., Cossi, M., Millam, J.M., Klene, M., Adamo, C., Cammi, R., Ochterski, J.W., Martin, R.L., Morokuma, K., Farkas, O., Foresman, J.B., Fox, D.J. (2016). Gaussian, 9, 227.

Gerpe, A., Álvarez, G., Benítez, D., Boiani, L., Quiroga, M., Hernández, P., Sortino, M., Zacchino, S., González, M., Cerecetto, H. (2009). 5-Nitrofuranes and 5-nitrothiophenes with anti-*Trypanosoma cruzi* activity and ability to accumulate squalene. Bioorganic & medicinal chemistry, 17(21), 7500-7509.

Gile, G.H., Moog, D., Slamovits, C.H., Maier, U.G., Archibald, J.M. (2015). Dual organellar targeting of aminoacyl-tRNA synthetases in diatoms and cryptophytes. Genome biology and evolution, 7(6), 1728-1742.

Hammond, D.J., Gutteridge, W.E. (1982). UMP synthesis in the kinetoplastida. Biochimica et Biophysica Acta (BBA)-General Subjects, 718(1), 1-10.

Hofer, A., Steverding, D., Chabes, A., Brun, R., Thelander, L. (2001). *Trypanosoma brucei* CTP synthetase: a target for the treatment of African sleeping sickness. Proceedings of the National Academy of Sciences, 98(11), 6412-6416.

Lee, C., Yang, W., Parr, R.G. (1988). Development of the Colle-Salvetti correlation-energy formula into a functional of the electron density. Physical review B, 37(2), 785.

Marchetti, F., Nicola, C., Pettinari, R., Pettinari, C., Aiello, I., Deda, M., Candreva, A., Morelli, S., Bartolo, L., Crispini, A. (2019). Zinc(II) Complexes of Acylpyrazolones Decorated with a Cyclohexyl Group Display Antiproliferative Activity Against Human Breast Cancer Cells. European Journal of Inorganic Chemistry, 1027−1039.

Marchetti, F., Pettinari, C., Di Nicola, C., Tombesi, A., Pettinari, R. (2019). Coordination chemistry of pyrazolone-based ligands and applications of their metal complexes. Coordination Chemistry Reviews, 401, 213069.

Marchetti, F., Pettinari, C., Pettinari, R. (2005). Acylpyrazolone ligands: Synthesis, structures, metal coordination chemistry and applications. Coordination Chemistry Reviews, 249(24), 2909-2945.

Marchetti, F., Pettinari, R., Pettinari, C. (2015). Recent advances in acylpyrazolone metal complexes and their potential applications. Coordination Chemistry Reviews, 303, 1-31.

Marr, J., Muller, M. (Eds.). (1995). Biochemistry and molecular biology of parasites. Elsevier. London, 89-117.

McKinnon, K.M. (2018). Flow cytometry: an overview. Current protocols in immunology, 120(1), 5-1.

Petrelli, R., Orsomando, G., Sorci, L., Maggi, F., Ranjbarian, F., Biapa Nya, P.C., Petrelli, D., Vitali, L.A., Lupidi, G., Quassinti, L., Bramucci, M., Hofer, A., Cappellacci, L. (2016). Biological activities of the essential oil from *Erigeron floribundus*. Molecules, 21(8), 1065.

Petrelli, R., Ranjbarian, F., Dall'Acqua, S., Papa, F., Iannarelli, R., Kamte, S.L.N., Vittori, S., Benelli, G., Maggi, F., Hofer, A., Cappellacci, L. (2017). An overlooked horticultural crop, *Smyrnium olusatrum*, as a potential source of compounds effective against African trypanosomiasis. Parasitology international, 66(2), 146-151.

Pettinari, R., Marchetti, F., Di Nicola, C., Pettinari, C., Galindo, A., Petrelli, R., Cappellacci, L., Cuccioloni, M., Bonfili, L., Eleuteri, A.M., Guedes da Silva, M., Pombeiro, A.J.L. (2018). Ligand Design for N,O- or N,N-Pyrazolone-Based Hydrazones Ruthenium(II)-Arene Complexes and Investigation of Their Anticancer Activity. Inorganic Chemistry, 57, 14123−14133.

Portes, M.C., De Moraes, J., Véras, L.M.C., Leite, J.R., Mafud, A.C., Mascarenhas, Y.P., Luz, A.E.V., Alves De Lima, F.C.D.A., Do Nascimento, R.R., Petrilli, H.M., Silva Pinto, P.L., Althoff, G., Ferreira, A.M.D.C. (2016). Structural and spectroscopic characterization of epiisopiloturine-metal complexes, and anthelmintic activity vs. *S. mansoni*. Journal of Coordination Chemistry, 69(10), 1663-1683.

Ranjbarian, F., Sharma, S., Falappa, G., Taruschio, W., Chabes, A., Hofer, A. (2022). Isocratic HPLC analysis for the simultaneous determination of dNTPs, rNTPs and ADP in biological samples. Nucleic Acids Research, 50(3), e18-e18.

Reddy, A., Sangenito, L. S., de Azevedo Guedes, A., Branquinha, M. H., Kavanagh, K., McGinley, J., dos Santos, A.L.S., Velasco-Torrijos, T. (2017). Glycosylated metal chelators as anti-parasitic agents with tunable selectivity. Dalton Transactions, 46(16), 5297-5307.

Rice, D.R., Vacchina, P., Norris-Mullins, B., Morales, M.A., Smith, B.D. (2016). Zinc (II)-dipicolylamine coordination complexes as targeting and chemotherapeutic agents for *Leishmania major*. Antimicrobial agents and chemotherapy, 60(5), 2932-2940.

Rodríguez-Hernández, K.D., Martínez, I., Reyes-Chilpa, R., Espinoza, B. (2020). Mammea type coumarins isolated from *Calophyllum brasiliense* induced apoptotic cell death of *Trypanosoma cruzi* through mitochondrial dysfunction, ROS production and cell cycle alterations. Bioorganic Chemistry, 100, 103894.

Scott, A.P., Radom, L. (1996). Harmonic vibrational frequencies: an evaluation of Hartree− Fock, Møller− Plesset, quadratic configuration interaction, density functional theory, and semiempirical scale factors. The Journal of Physical Chemistry, 100(41), 16502-16513.

Shaikh, I., Jadeja, R.N., Patel, R. (2020). Three Mixed Ligand Mononuclear Zn(II) Complexes of 4-Acyl Pyrazolones: Synthesis, Characterization, Crystal Study and Anti-Malarial Activity. Polyhedron, 183, 114528.

Shaikh, I., Jadeja, R.N., Patel, R., Mevada, V., Gupta, V.K. (2021). 4-Acylhydrazone-5-pyrazolones and their zinc (II) metal complexes: synthesis, characterization, crystal feature and antimalarial activity. Journal of Molecular Structure, 1232, 130051.

Shaikh, I.U., Patel, R.K., Mevada, V.A., Gupta, V.K., Jadeja, R.N. (2019). Binary and Ternary Zinc(II) Complexes of Acyl Pyrazolones: Synthesis, Spectroscopic Analysis, Crystal Structure and Antimalarial Activity. ChemistrySelect, 4, 8286−8294.

Sheldrick, G.M. (1996). Program for empirical absorption correction of area detector data. Sadabs.

Verma, G., Marella, A., Shaquiquzzaman, M., Akhtar, M., Ali, M.R., Alam, M.M. (2014). A review exploring biological activities of hydrazones. Journal of pharmacy & bioallied sciences, 6(2), 69.

Wong, M.W. (1996). Vibrational frequency prediction using density functional theory. Chemical Physics Letters, 256(4-5), 391-399.

Zhang, L., Xu, G.C., Yang, Y., Guo, J.X., Jia, D.Z. (2013). Syntheses, structure diversity and properties of complexes with 4-acyl pyrazolone salicylidene hydrazide derivatives. Dalton Transactions, 42(12), 4248-4257.

Zhao, Z., Dai, X., Li, C., Wang, X., Tian, J., Feng, Y., Xie, J., Ma, C., Nie, Z., Fan, P., Qian, M., He, X., Wu, S., Zhang, Y., Zheng, X. (2020). Pyrazolone Structural Motif in Medicinal Chemistry: Retrospect and Prospect. European Journal of Medicinal Chemistry, 186, 111893.

4.7 Supporting information

Table S1. Details of data collection and structure refinements for PbH**27** and **C2**.

Formula	**PbH27**	**C2**
Formula	$C_{25}\,H_{21}\,N_4\,O\,F_3$	$C_{54}\,H_{56}\,F_6\,N_8\,O_6\,Zn$
Mr	450.56	1092.43
crystal size [mm]	0.40 x 0.20 x 0.04	0.40 x 0.20 x 0.06
crystal system	Monoclinic	Triclinic
space group	$P2_{1/c}$	*P*-1
a [Å]	11.153(3)	9.941(3)
b [Å]	22.940(6)	11.872(4)
c [Å]	9.084(3)	12.109(5)
α [°]	90	95.200(17)
β [°]	97.324(16)	101.884(17)
γ [°]	90	105.333(16)
V [Å3]	2305.1(11)	1332.6(8)
Z	4	1
ρ cald [gcm^{-3}]	1.295	1.361
μ [mm^{-1}]	0.098	0.539
θ range [°]	2.429 to 24.974	2.303 to 25.678
data collected	33167	11965
unique data, *Rint*	4001, 0.0758	5012, 0.0642
obs. data [$I > 2\sigma(I)$]	2155	2600
no. Parameters	326	362
restraints	0	0
R_1 [$I > 2\sigma(I)$]	0.0543	0.0543
wR_2 [all data]	0.1455	0.1314
GOF	1.001	0.942

Table S2. Energies for the tautomer of PbH**27**.

	PbH27	
	Tautomer I	**Tautomer II**
	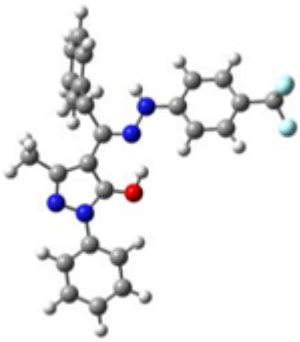	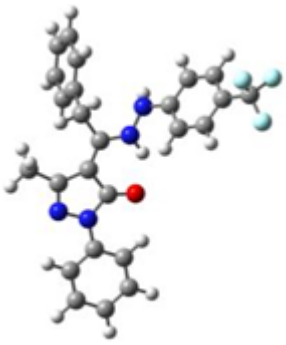
E	-1559.445250	-1559.449708
E_D	-1559.028991	-1559.032877
E_t	-1559.000852	-1559.004778
H	-1558.999908	-1559.003833
G	-1559.093531	-1559.097074
ΔE	0.0	-2.8
ΔG	0.0	-2.2
$\Delta E(CHCl_3)$	0.0	-4.4
$\Delta G(CHCl_3)$	0.0	-3.8

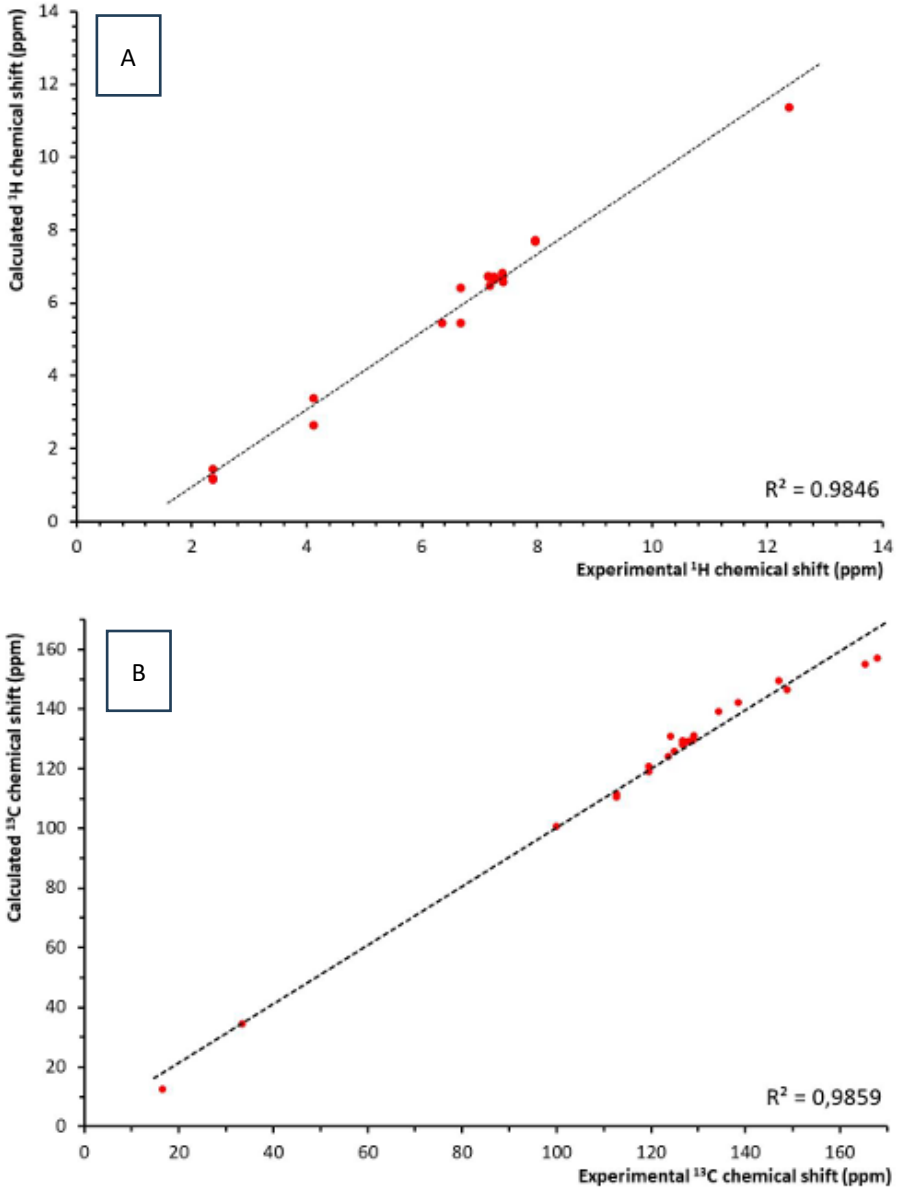

Figure S1. Comparison of the calculated (tautomer I) and experimental A) ^{1}H NMR and B) ^{13}C NMR spectra of PbH**27**.

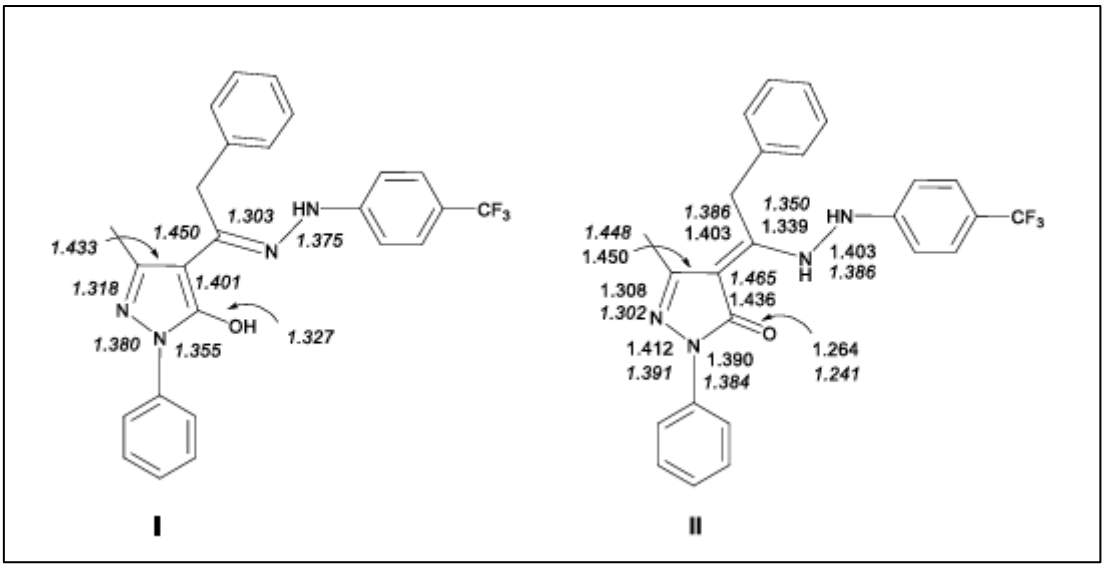

Figure S2. Comparison of selected bond distances of PbH**27**: calculated tautomers I and II (*italic*) and experimental.

Table S3. Comparison of selected experimental and calculated structural parameters of **C2**.

Bond distances (Å) and angles (°)	**Experimental**	**Calculated**
Zn-O	1.989	2.050
Zn-N	2.116	2.088
Zn-O_{MeOH}	2.285	2.270
C=O	1.277	1.279
C-N	1.303	1.315
N-N	1.444	1.424
C-C	1.445	1.432
C-$C_{pyrazol}$	1.430	1.430
O-Zn-O	180.0	180.0
N-Zn-N	180.0	180.0
O_{MeOH}-Zn-O_{MeOH}	180.0	180.0

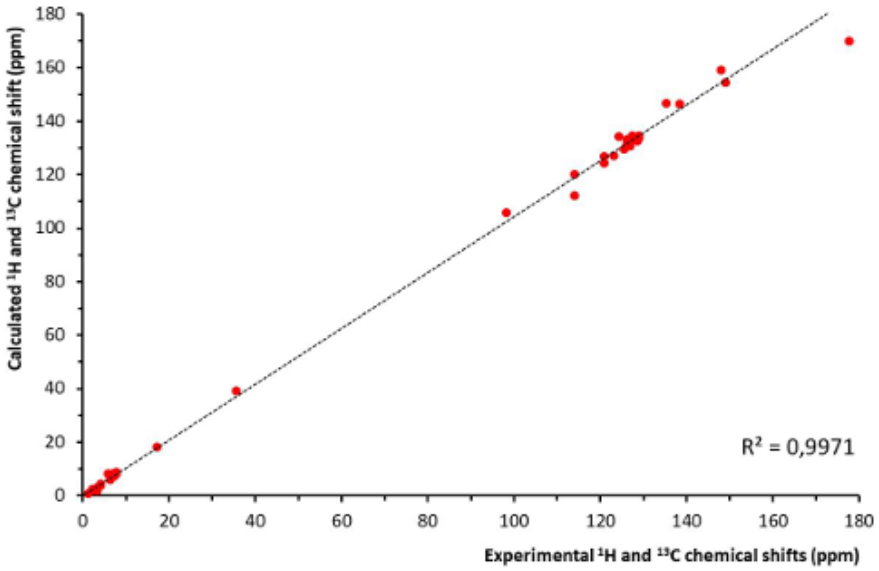

Figure S3. Comparison of the calculated and experimental ^{1}H and ^{13}C NMR spectra of **C2**.

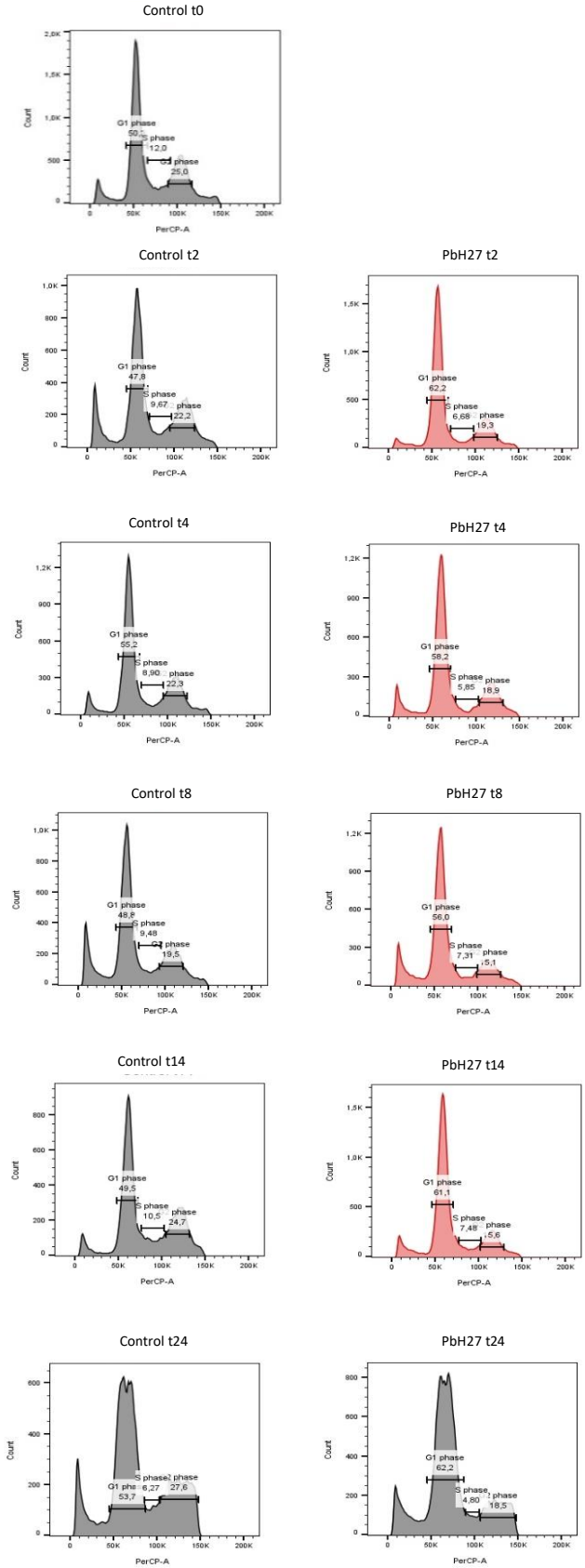

Figure S4. Flow cytometry for cell cycle assessment histogram plot of treated (PbH**27**) and untreated (control) *T. brucei* s427 WT cells.

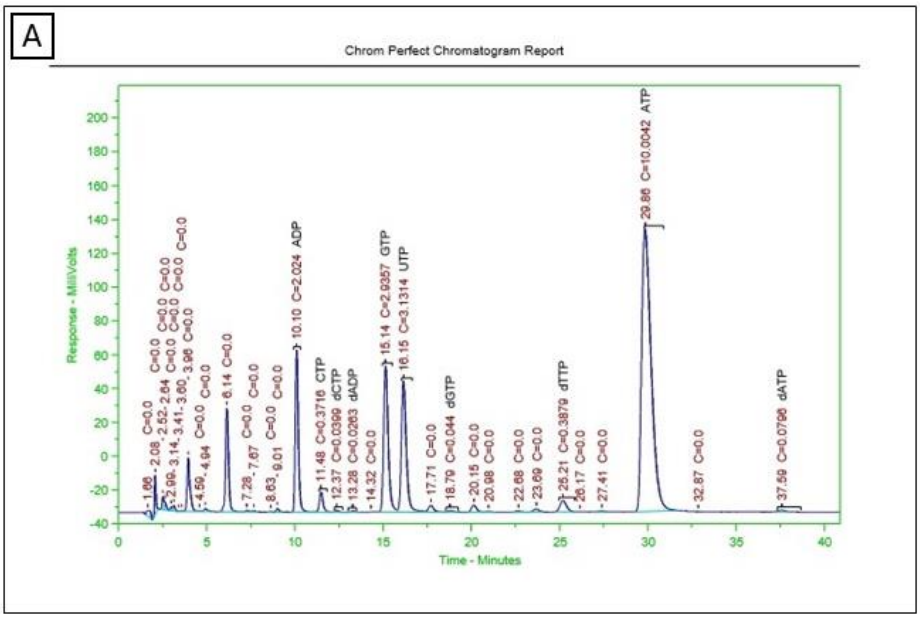
A
Chrom Perfect Chromatogram Report
Response - MilliVolts
Time - Minutes
10.10 C=2.024 ADP
15.14 C=2.9357 GTP
16.15 C=3.1314 UTP
29.86 C=10.0042 ATP
37.59 C=0.0796 dATP

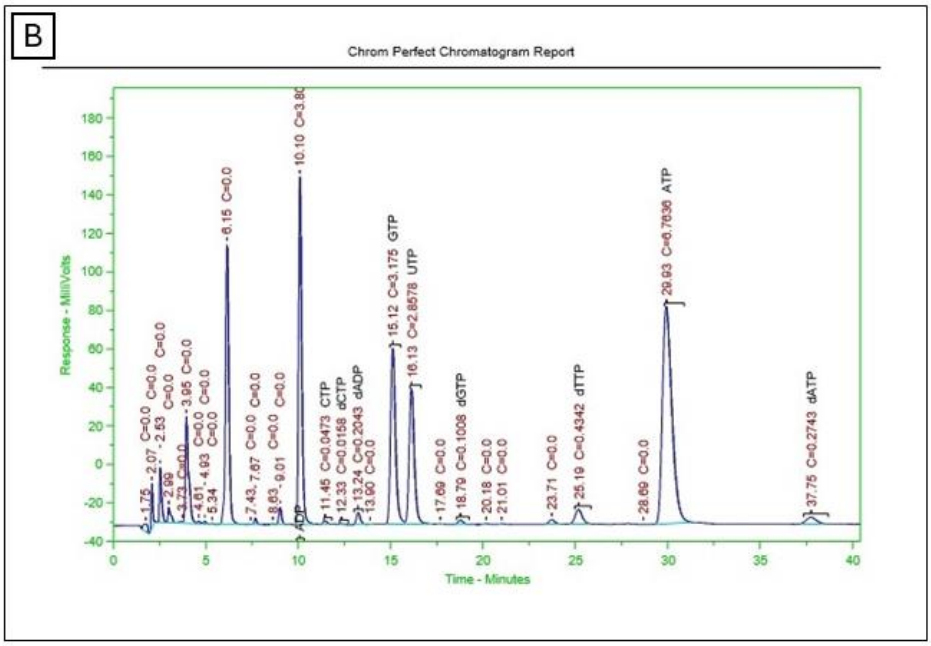
B
Chrom Perfect Chromatogram Report
Response - MilliVolts
Time - Minutes
6.15 C=0.0
10.10 C=3.80
15.12 C=3.175 GTP
16.13 C=2.8578 UTP
29.93 C=6.7636 ATP
37.75 C=0.2743 dATP

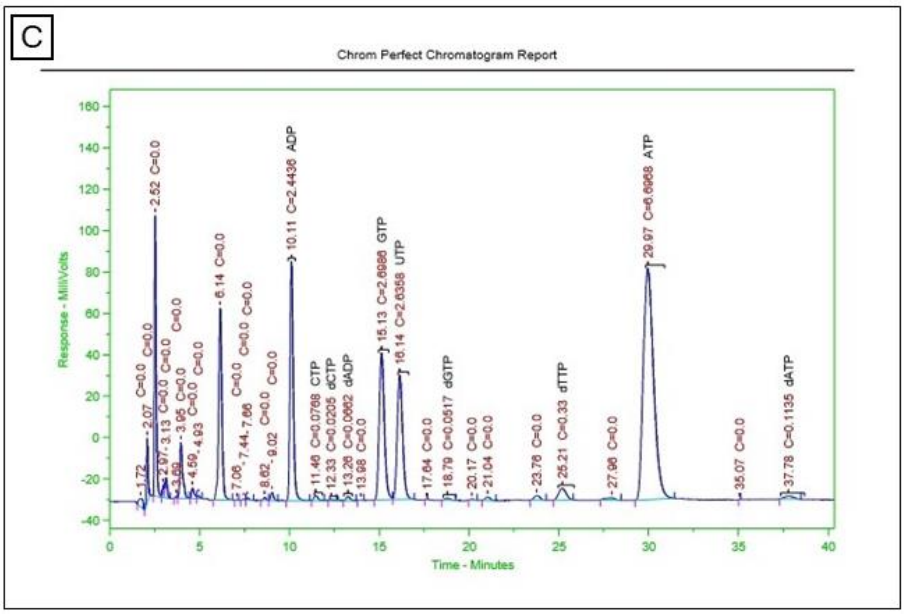

Figure S5. HPLC chromatograms showing NTPs, dNTPs, NDPs, and dNDPs. From the top: A) untreated cells; B) cells treated with PbH**27** (5 µM) and C) cells treated with **C2** (5 µM).

CONCLUSIONS

Trypanosomiases are spread all over the world causing great social and economic issues in the poorest countries. This thesis work was an attempt to face this important concern by exploiting different sources and approaches. First, it was possible to evaluate the advantages and disadvantages of using natural sources to obtain valuable antitrypanosomal products. Notoriously, plants possess antibacterial, antimycotic, and antiparasitic potential, being naturally characterized by the presence of many bioactive compounds that protect the plant itself from external harmful agents.

The extraction of volatile and non-volatile fractions from plant matrices yields highly complex products with diverse compositions. This diversity is both advantageous and challenging. On one hand, it adds value to these products by incorporating bioactive compounds that may synergize with each other. On the other hand, it can diminish their potential effectiveness due to potential antagonism among components and the potential toxicity of some compounds.

Moreover, affording these products requires considerable effort in terms both of time and costs, further complicating the task. However, there is also a social aspect that mustn't be overlooked; the affected local population hardly accepts synthetic drugs, and Western medicine is viewed with suspicion. For this reason, synthetic therapies are often discontinuously followed and due to insufficient compliance, their efficiency suffers. Natural products could be a valuable alternative resembling the traditional medicine used for centuries by the local ethnic groups. Despite the fact that plants represent a good source of new and effective antitrypanosomal agents, synthetic drugs remain the most studied, efficient, safe, and currently the only ones approved by the healthcare systems. The great issue related to synthetic drugs is the insurgence of resistance in trypanosomes. Parasites are indeed highly variable due to the continuously changing surface glycoprotein characterizing them. Thus, there is the urgency for new and structurally different compounds to overcome this resistance issue.

In this regard, my research focused on studying both natural and synthetic compounds against *T. brucei* taking into account the limits of these two approaches and trying to exalt their advantages. In detail, the study of *Anthriscus nemorosa* and *Cannabis sativa* gave us the possibility to explore the potential of different compounds and blends derived from these two plants. The studied products were selected isolating and subsequently possibly mixing the most active and safe components for the treatment of trypanosomiases. For some of them, encapsulation was also performed, in order to ease the administration and to drive down costs of a hypothetical different pharmaceutical form.

Formulation of micro- and nanoemulsions is indeed easy and economically advantageous. Concerning synthetic products, instead, the pyrazolone-based hydrazone series were prepared after a screening of already existing precursors that demonstrated activity towards the parasite. Being the structures of these synthetic compounds considerably different from those of current drugs approved for antitrypanosomal use, it was supposed that PbH**01**-**36** and the metal complexes derived from the most active among them could act on different mechanisms for which the parasites haven't shown resistance yet. The most active analogs were tested against resistant strains of the parasites assessing the absence of cross-resistance with current treatments. The mechanism of action of the most promising compounds was also investigated through a series of tests on treated cells. Additionally, a possible enzymatic target, CTPS, was hypothesized.

In light of the results of this thesis, the next steps of this research project will focus on different tasks. First of all, less expensive and more performant techniques for the isolation of compounds of interest from the two natural matrices need to be developed. Isolation through silica-gel and preparative HPLC are certainly successful but expensive and not easily scalable, and there is an urge for new and green processes. Additionally, it would be auspicable to favour an easy and economically convenient way of administration for the most promising isolated compounds and blends derived from volatile and non-volatile fractions of *A. nemorosa* and *C. sativa*. This task has been partially accomplished by formulating nanoemulsions of the EO from aerial parts of *A. nemorosa*, but the next steps in this direction include formulation of nanoemulsions or liposomes even for mixes and non-volatile extracts of both the considered plants. Regarding synthetic products, instead, the proposed target needs to be confirmed through a direct assay on the identified enzyme. Moreover, further studies are needed to determine the transport mechanism of the molecules inside the target cellular district to verify if the presence of the zinc atom in the complex **C2** influences the transport with respect to its ligand precursor PbH**27** and, consequently, the efficiency of the drug.

The overall results of this thesis lay the foundation for the development of new and innovative drugs for the eradication of trypanosomiases, both considering natural sources and synthetic products with a particular attention to the issues related to these two approaches. However, the way to the completion of new innovative drugs for trypanosomiases is long and not free from hurdles. The hope is that governments, healthcare systems, and private investors keep investing and trusting research to reach the aim of eradicating these severe pathologies.